# Structural Investigations Using Small Angle Scattering Techniques and Contrast Variation

D I S S E R T A T I O N

Zur Erlangung des akademischen Grades

d o c t o r  r e r u m  n a t u r a l i u m

- Dr. rer. nat. -

im Fach Chemie

Physikalische und Theoretische Chemie

eingereicht an der

Mathematisch-Naturwissenschaftlichen Fakultät I

der Humboldt-Universität zu Berlin

von

**Dipl. Chem. Christian Rabe**

Präsident der Humboldt-Universität zu Berlin:
Prof. Dr. Jan-Hendrik Olbertz

Dekan der Mathematisch-Naturwissenschaftlichen Fakultät I:
Prof. Stefan Hecht PhD

Gutachter: 1. Prof. Dr. Matthias Ballauff

2. Prof. Dr. Klaus Rademann

Datum der Einreichung: 21. Januar 2014

Datum der Promotion: 26. November 2014

„Das lebhafteste Vergnügen, das ein Mensch in der Welt haben kann, ist neue Wahrheiten zu entdecken; das nächste von diesem ist, alte Vorurteile loszuwerden.“

Friedrich II., “der Große”, preußischer König (1712 – 1768)

*meiner Familie*

# Abstract

The analysis of the small angel X-Ray and neutron scattering is an ideal tool for the discussion of the structure and interactions of submicroscopic particles. Herein, the variation of the scattering contrast enlarges the spectrum of information, additionally. As shown in the presented work, complementary probes give a detailed picture of the investigated systems. The focal point of the discussion is set on polyethylene nanoparticles and structures based on hyperbranched polyglycerol. The analyses provide, for instance, information on the mechanism that leads to an ideal arrangement of the non-branched polymer chains during the formation of the platelet-like polyethylene nanoparticles. The amorphous phase exclusively hosts the redirection of the polymer chains into the crystalline domain. This allows the unimpeded chain diffusion. The effect of defects along the polymer chain on the particle structure was studied by the analyses of polyethylene with precisely placed methyl groups. Analyses of aqueous dispersions of hyperbranched polyglycerol reveal the fractal-like character of the global molecule structure. Additionally, the significant contribution of the molecule's microstructure to the corresponding small angle scattering was considered. The analyses of molecules composed of the hyperbranched core and a complete functionalisation with bipolar chains profited from these results. Hereby, the molecule structure in polar and non-polar media was identified. In polar surrounding the formation of well-defined aggregates was described. This provides essential information for a further discussion of this type of molecules as drug delivery platform.

# Zusammenfassung

Die Analyse der Röntgen- und Neutronenkleinwinkelstreuung stellt ein ideales Werkzeug für Untersuchungen der Struktur submikroskopischer Teilchen und deren Wechselwirkungen dar. Hierbei eröffnet die Variation des Streukontrastes ein zusätzliches Spektrum an Informationen. Wie in der vorliegenden Arbeit gezeigt wird, kann durch die Verwendung komplementäre Verfahren ein detailliertes Bild der untersuchten Systeme erarbeitet werden. Im Fokus der Diskussion stehen Polyethylennanopartikel und Strukturen basierend auf hyperverzweigtem Polyglycerol. Die durchgeführten Untersuchungen liefern beispielsweise Rückschlüsse auf den Mechanismus, der zu einer nahezu idealen Anordnung unverzweigter Polymerketten, während der Bildung der Polyethylennanopartikel, führt. Im amorphen Anteil dieser plättchenförmigen Partikel findet demnach ausschließlich eine Richtungsänderung beim Wiedereintritt der Polymerketten in die kristalline Phase statt, wodurch eine ungehinderte Kettendiffusion möglich ist. Der Einfluss von Defekten entlang der Polymerkette auf die Partikelstruktur konnte durch Untersuchungen eines präzise verzweigten Polyethylens ermittelt werden. Bei weiteren Untersuchungen von wässrigen Dispersionen eines hyperverzweigten Polyglycerols konnte die übergeordnete Struktur als Fraktal beschrieben werden. Der signifikante Beitrag der Mikrostrukturierung des Moleküls zu dessen Kleinwinkelstreuung wurde in den Analysen berücksichtigt. Die Strukturuntersuchungen von Molekülen mit dem polaren hyperverzweigten Kern und einer nahezu vollständigen Funktionalisierung durch bipolare Ketten profitierte von diesen Ergebnissen. Hierbei wurde die Struktur dieser Moleküle in polaren und unpolaren Medien ermittelt. In einer polaren Umgebung wurde die Bildung von Assoziaten beschrieben. Dies liefert wertvolle Hinweise auf die Wirkungsweise als Wirkstofftransportsystem liefert.

# Table of content

# 1. Introduction

Polymers represent one of the most important classes of synthetic products with a wide variety of applications [1,2]. Hereby, their versatile and tuneable properties can be generated by a large number of available low-molecular repeating units and different chain architectures [1,2]. Nevertheless, the important processes being the origin of their characteristic properties are still under intense discussion. This is not at least an issue of great importance inquired by the chemical industry for optimising manufacturing processes of common bulk polymers, for example. In fact, the relationship between the structure and the corresponding properties are of outstanding importance for complex polymer systems that are addressed, for instance, for medical applications. Hereinafter, two rather different polymer systems will be the focal point of investigation. This includes, on the one hand, a discussion of the structure of nanoparticles composed of polyethylene in the context of chain arrangements to form semi-crystalline nanoparticles. On the other hand, a core-multishell architecture was studied to reveal its spatial structure under different experimental conditions.

The linking key for the investigations is the analysis of the small angle scattering (SAS) in combination with contrast variation. The conjunction with further complementary techniques reveals the morphological features of these rather different polymer structures. The variation of the scattering contrast due to the addition of contrast agents or the chemical modification of the probed structures became a common method for structural analyses in the sub-microscopic regime by SAS techniques [3,4,5]. Moreover, this discussion should prove that this combination is a versatile and likewise a powerful approach for a detailed structural analysis of the investigated nanoparticles.

## 1.1. Nanoparticles of linear and precisely branched polyethylene

Polyethylene (PE) is a common and omnipresent polymer in a variety of applications in everyday life. The straightforward production associated with low costs, excellent, and tuneable mechanical properties led to a market share of around 30 %, which amounts to a production of 60 million tons per year [1]. This benefits from the development of the *Ziegler-Natta* process using transition metals as catalysts [1,2,6]. This procedure allows the polymerisation of ethylene at mild conditions and opens up a variety of different polymer morphologies. Polyethylene has long been in the focus of academic research to gain understanding of the polymerisation process itself, but also on issues concerning the ordering of the polymer segments (Fig. 1) [7,8,9,10,11,12,13,14]. Highly ordered crystalline phases, along with amorphous domains hosting non or weakly ordered domains, govern the macroscopic properties of the polymer. The crystalline arrangement is assigned to interactions between the chain segments benefitting from *van der Waals* (vdW) interactions. Moreover, the thickness of the folded lamellae has an important impact on the melting properties of semi-crystalline polymers, which are of great importance for different applications and manufacturing processes. The relation between the thickness of the crystalline lamella and the corresponding thermodynamic properties is described by the *Gibbs-Thompson* equation [12,15]. It has been used for the determination of the melting point of polymers in the thermodynamic equilibrium, which is not accessible by experimental methods. Additionally, the glass transition temperature, where the molecular mobility becomes arrested, can be extrapolated from an extension of this relation [16]. The polymer crystallites display an anisotropic growth at their crystallographic planes [17,18,19]. At

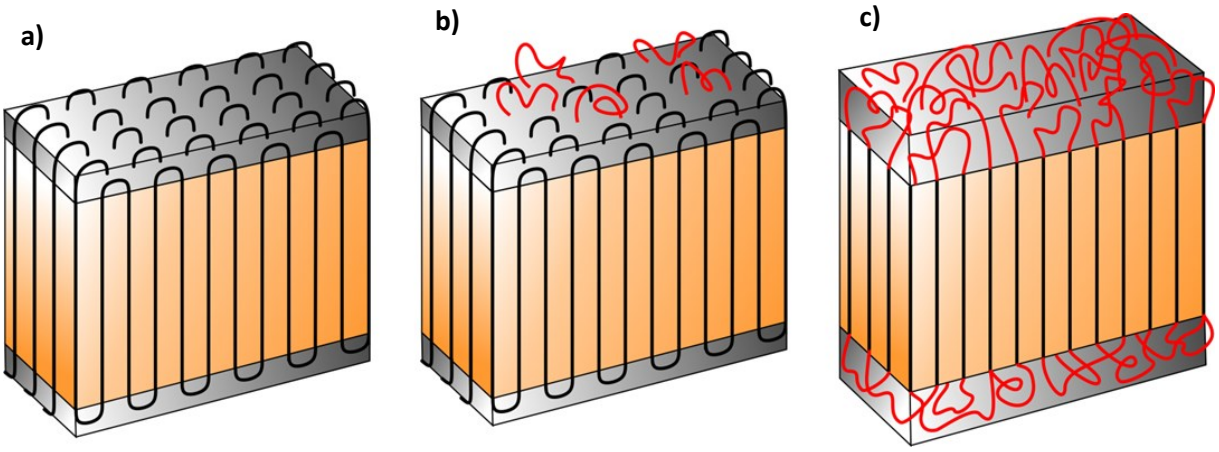


**Fig. 1: Illustration of the suggested chain folding for a) high order crystallisation from solution, b) partially disordering, and c) recrystallisation from the melt [14]. The crystalline phase is represented by the orange region, whereas the amorphous phase is respectively symbolised by the grey domains.**

the crystal surface the formation of loops and entanglements leads to less ordered amorphous domains [13,14,20,21]. A maximum of the growth rate is observed for polymer crystals with a thickness near to the stability limit, as this is described by the *Gibbs-Thomson* relationship [15].

During the last decade improvements of the emulsion polymerisation procedures using highly active Ni(II)-complexes [22,23,24,25,26] led to stable single nanoparticles of PE [27,28,29]. However, most of these synthetic approaches yielded multilamellar PE-particles [28,29]. Nanoparticles consisting of a single lamella were first discussed by Weber et al. [30] and were commented by Cheng shortly afterwards [16]. The nanoparticles with a platelet-like shape were studied using complementary methods of cryogenic transmission electron microscopy (cryo-TEM) and small angle X-ray scattering (SAXS) in conjunction with contrast variation. The nanoparticle formation was assigned to occur right after the catalytic polymerisation of ethylene in the aqueous solution. This process occurs under mild conditions of temperature and pressure in the confined matrix of emulsion droplets [28]. The crystallisation to thin lamellae was ascribed to the supercooling conditions of more than 100 °C below the melting temperature of the respective bulk material. Thin films that consist of these particles were studied using atomic force microscopy (AFM) [31,32], whereas the annealing of the dispersed particles was reported by Rochette and co-workers [33]. By means of SAXS analyses combined with contrast variation the particle structure and the thickening of the crystalline lamella due to a preceding temperature treatment was studied and discussed with respect to the observations made from the bulk material. Furthermore, this kind of particles is discussed in the context of metastability and can thus easily switch between one metastable state to another upon heating [34].

The macroscopic polymer properties can be tuned in an extended range by various chain microstructures, which are not at least of upmost importance for their large scale applications [1,2]. For instance, the crystallinity of the polymers is influenced by the chain branching to which recent attention was addressed [35,36,37,38,39,40,41]. From the acyclic diene metathesis (ADMET) polymerisation [1,42,43,44,45] a large number of polymers with a precise microstructure is accessible. To date, however, research was mostly focused on the corresponding bulk materials [35,36,37,38,39,40,41,46,47,48], whereas publications dealing with nanoparticles are seldom. The influence of the sequence length between the positions of the branches along the polymer backbone was reported by Hosoda et al. [39,46]. The morphological chances due to the variation of the alkyl

branch size were intensively studied by Wagener and co-workers [35,38,40,41]. Moreover, the insertion of precisely placed carboxylic moieties along the chain was presented by Baughman et al. [48]. Prior to this, polymers with a random distribution of carboxylic groups forming thermoresponsive and stable surfactant-free nanoparticles were reported by Kryuchkov et al. [49]. Recently, nanoparticles with precisely placed carboxylic groups obtained by ADMET polymerisation were reported by the Mecking group [50].

## 1.2. Core-multishell structures

The development of new, high efficient and innovative drugs is one of the most important goals of science. Nevertheless, most of the recent pharmaceutical agents also require innovative ways of application to unfold their full medical activity. This often reduces the doses needed for the intended medical purpose, as well as the risk of potential harmful side effects. Direct targeting the site of action and the controlled release of the active compounds are just a few of the requirements to modern drug delivery systems [51,52,53,54,55]. For this reason, the development of innovative drug delivery agents is of the same importance as the development of new active compounds [55,56]. For this purpose, Haag presented the principle of dendritic core-shell structures acting as responsive nanocarriers for drug delivery applications [57].

The current generation of liposome-like core-multishell (CMS) nanoparticles is built up from a polar core of hyperbranched polyglycerol (hPG). The core molecules are linked to linear chains composed of a hydrophobic $C_{18}$-segment and a polar outermost monomethyl (polyethylene oxide) block (Fig. 2). Radowski and co-workers showed, with their studies on this kind of pseudo-dendritic scaffold architectures, that the first generation of CMS-molecules display a promising approach to proof the principle suggested by Haag [58]. By using different dye molecules as model guests, they observed the solubilisation of the dyes in their appropriate non-solvents. Furthermore, the influence of the

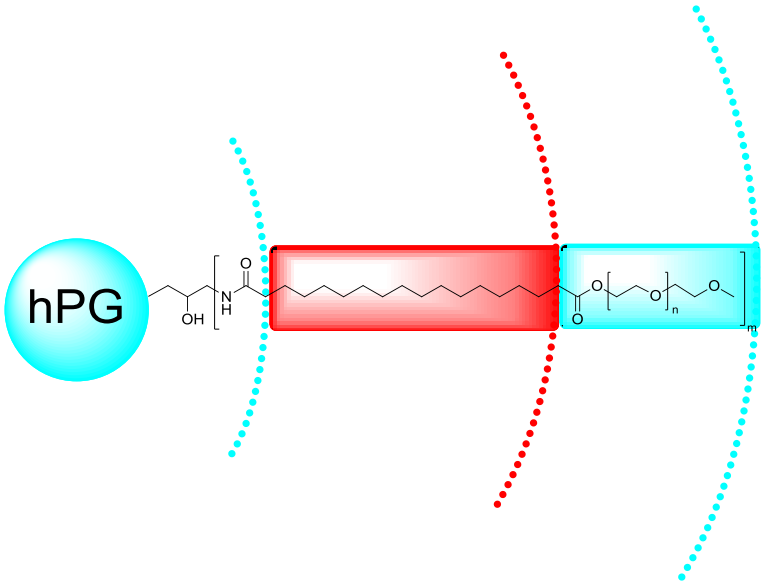


**Fig. 2: Schematic drawing of the chemical structure of a core-multishell (CMS) nanoparticle. The blue sections represent the hydrophilic regions within the molecule. The red coloured section represents the hydrophobic domain.**

core sizes and the length of the aliphatic block were studied with respect to the uptake capacity of the host structure for polar and non-polar molecules. First general structural investigations were conducted using dynamic light scattering (DLS) and cryo-TEM. The size of the CMS-molecules was determined to be 5 nm to 10 nm. The structure size after the embedding of the guest molecules was found to be in the range between 30 nm and 50 nm. By means of surface tension measurements a critical aggregation concentration (CAC) could be observed during the encapsulation process. This was assigned to the formation of well-defined supramolecular aggregates.

A number of reports concerning the potential application as a drug delivery system followed: Quadir et al. focused their studies on the transport properties of dye molecules and antitumor drugs [59]. Küchler et al. presented studies to the skin penetration ability of the CMS-structures [60,61]. The skin penetration of the current CMS-nanocarrier system was studied by electron paramagnetic resonance (EPR) spectroscopy by Haag et al. [62]. Wolf and co-workers embedded opioids and studied the effects using CMS-molecules in in-vitro wound healing models [63]. CMS-nanocarriers were also tested for their transport properties of copper ions [64]. Bio-available copper is discussed as playing an important role in the treatment of accompanying symptoms of *Alzheimer*'s disease (pathological plaque). Current in vitro tests of CMS-nanocarriers confirmed their non-toxicity to living cells. All studies agree on the point that CMS-structures based on hyperbranched polymers could enhance the transport and the availability of potential active agents in future pharmaceutical applications.

Another feature of the CMS-structures was studied by Keilitz and co-workers [65,66,67,68]. They reported the formation and stabilisation of noble metal nanoparticles by CMS-molecules and tested subsequently their catalytic activity. Furthermore, the CMS-system was used as a template phase for the formation of porous silica, loaded with catalytic active platinum nanoparticles [69].

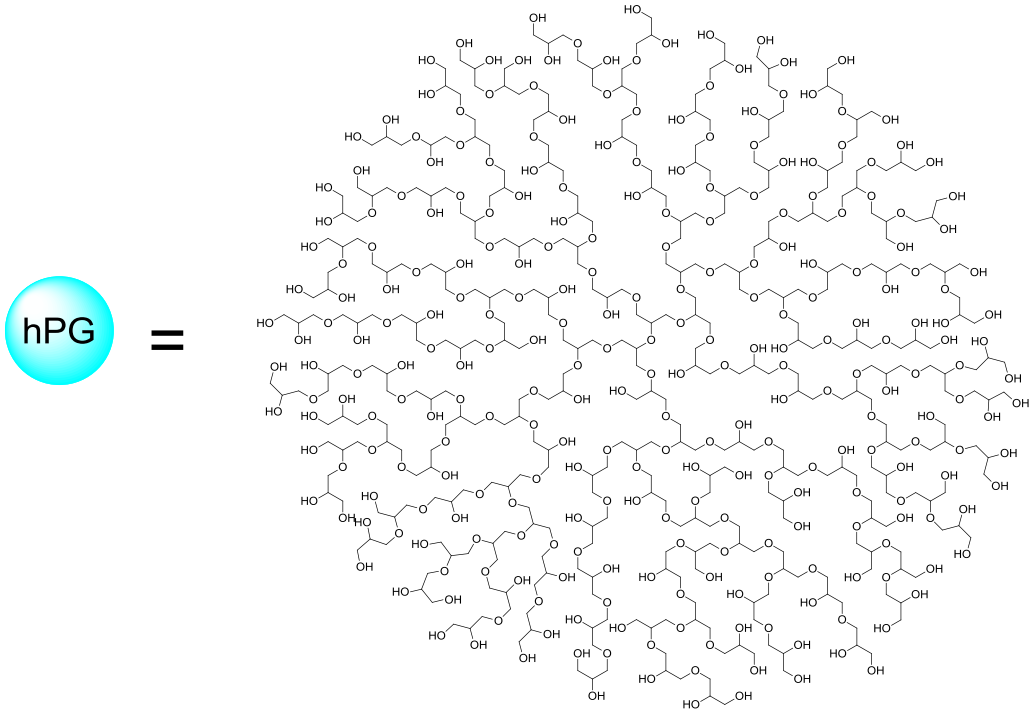


**Fig. 3: Schematic structure of a conformer of the hyperbranched polyglycerol (hPG) building block ($M_w$ ≈ 10 kg mol$^{-1}$, $n_{OH}$ = 137). This conformer structure was used for complementary molecular dynamic (MD) simulations.**

The hyperbranched polyglycerol (Fig. 3) being the major building block of the investigated CMS-carrier system is on its own in the focus of various studies. Unlike dendrimers, having a well-defined molecular architecture deriving from a step-wise growth from a central core molecule, hyperbranched molecules can be generated in a one-step polycondensation of $AB_f$ monomers [70,71,72,73]. Although hyperbranched molecules exhibit a less perfect structure, these molecules do display certain similarities in the manner in which they are obtained for dendrimers,. They benefit from the absence of chain entanglements, a large number of end group functionalities, as well as a globular structure [70,72]. The high degree of functionality allows the design of molecules with a diversified spectrum of properties and therefore versatile applications [74,75,76,77,78]. Especially, pharmacological applications were discussed [79,80,81,82,83]. The concept of the polycondensation of monomers with a multiple functionality was already introduced by Flory [84]. A corresponding particle scattering factor for the hyperbranched structures based on principles from polymer statistics was developed by Burchard [85,86]. However, only a few studies on the structural characteristics of hyperbranched polymers using small angle scattering methods (SAS) were available so far [87,88,89,90]. Moreover, the authors failed to model the observed small angle scattering in necessary detail. The comprehensive report by Burchard and his colleague could reveal the globular and microscopic structure of a hyperbranched structure using the combination of small angle neutron scattering (SANS) experiments and molecular dynamic (MD) simulation [91].

# 2. Motivation

Despite of various studies on polymer morphologies undertaken in the last decades, the processes taking place during the formation of ordered domains are still under discussion. The analyses of bulk polymers were mostly accompanied by undesired side effects, such as multilamellar phases being embedded in an amorphous matrix [13,14], for example. The growth of polymer single crystals was another challenge. Using suspensions of single crystal nanoparticles avoid some of these concomitants. Thus, further understanding of the crystallisation process itself is obtained. The current generation of semi-crystalline nanoparticles composed of linear PE is seen as highly useful to attain further insight into the process of chain folding within a polymer crystallite [30,33]. The synthesis of these particles in a low-temperature process using a novel Ni(II)-complex as catalyst led to PE that consists of virtually non-branched chains. Therefore, the nanoparticles formed by such ideal PE were supposed to have excellent crystalline properties. In this context, the thickening of the crystalline lamellae due to the annealing of the nanoparticles at different temperatures will be discussed in more detail. Of particular interest is the guiding function of the amorphous phase wherein the polymer chains fold and re-enter the crystalline phase. Further investigations will focus upon the microstructural characteristics of the nanocrystals.

Polymers having a precise branching along their backbone are seen as a further step towards a deeper understanding of the crystallisation process. As these polymers carry precisely placed defects, the influences on the chain folding and on the formation of crystalline domains is of particular interest. Based on the prior studies on bulk materials [35,36,37,38,39,40,41,46,47,48,92,93,94,95] the synthesis of corresponding stable nanoparticles was encouraged. Semi-crystalline nanoparticles were obtained in a secondary dispersion polymerisation of precisely branched monomers, synthesised by the ADMET procedure [42,43,44,45]. In our specific case, this procedure yields a polymer carrying methyl groups at every 21$^{st}$ carbon along the backbone.

Apart from the various reports on the properties and potential applications of the CMS-architecture, no studies are available at the moment dealing with a comprehensive structural analysis of the CMS-nanoparticle system. For this reason the spatial structure and the structural changes under different experimental conditions are of upmost interest. These will provide insight into the

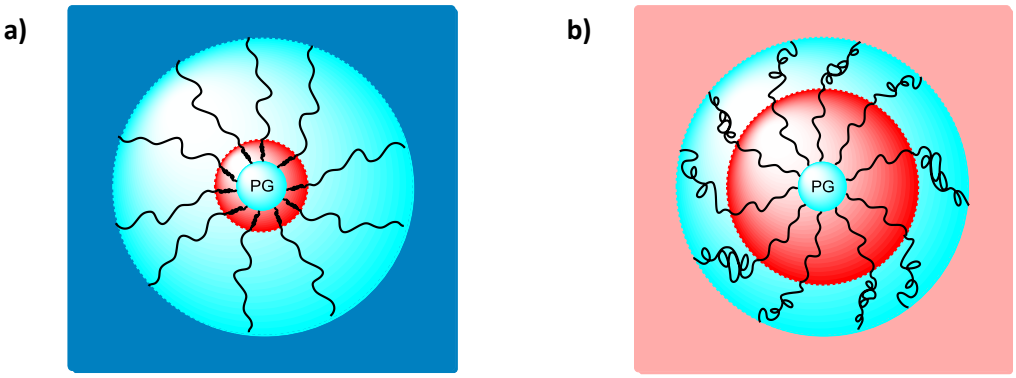


**Fig. 4: Suggestions for the structure of the CMS-molecule dispersed in a polar (a) and in a non-polar medium (b). The hydrophilic polyglycerol core and the outermost polyethylene oxide shell are blue coloured. The region of the joining hydrophobic alkyl segments is coloured in red.**

processes that allow the system to be solubilised in polar and non-polar media equally (Fig. 4) and which also play an important role during the embedding of guest molecules in the host structure. The interactions of the CMS-particles with lipid membranes and the corresponding transport mechanism have not been fully understood to date. Due to this fact, the major goal of this discussion is a detailed structural analysis of the structure of CMS-nanoparticles. An improved understanding of these issues will help gain insight into the mechanism guiding the transport and release process of guest molecules in the context of a potential pharmaceutical application. Moreover, this will benefit the development of future CMS-molecule generations towards a responsive drug delivery system. Furthermore, the routine presented for the comprehensive structural analysis might lead to the reduction of cost-intensive pharmaceutical studies on new active structures and agent delivery systems to a minimum. In addition, the structure attributes of the hyperbranched polyglycerol being the scaffold of the CMS architecture are of particular interest. The structure will be discussed in the context of the recent developments in the analyses of hyperbranched polymers using scattering methods in combination with theoretical calculations [91].

The analysis of structural characteristics of particles in the submicrometer regime requires suitable methods. In this context cryogenic sample preparation techniques used for electron microscopy were at first applied for issues questioned by bio scientists [96,97,98]. This method became as well a frequently used tool as a complementary probe for the analyses of synthetic colloidal samples [99,100,101]. It takes advantage of probing the native state of the analysed specimen due to the extreme supercooling by a plunge freezing process. This inhibits the appearance of artefacts and damages due to the freezing process itself. The application of imaging techniques in combination with small angle scattering is considered a highly suitable approach for the analyses of polymer nanoparticles. This method was already successfully applied in the analysis of semi-crystalline latex particles [102]. Furthermore, the combination of SAS and contrast variation provide detailed insight into the structure of polymer nanoparticles [5,30,33,102]. This method was also used by different authors to analyse the structure of dendritic molecules and their specific interactions [103,104,105,106,107,108,109,110,111,112]. By probing the atom nuclei during a SANS experiment, changes within a structure element can be analysed. For instance, this provides access to the location of guest molecules within a host structure formed by CMS-nanoparticles. To gain insight into the crystalline microstructure of the polymer nanoparticles, the analyses of the corresponding wide angle diffraction (WAXD) will be discussed as well [113].

The combination of scattering experiments along with imagining techniques and complementary methods has been verified as a versatile and powerful approach for the analysis of structures on the nanoscopic scale. The discussion will demonstrate that comprehensive structural studies are highly relevant for the understanding of the corresponding properties of the analysed molecules. This becomes especially important in the complex context of pharmaceutical applications.

# 3. Theory

## 3.1. Scattering in soft matter science

Scattering techniques are useful tools for probing the structure of matter. The analysis of the respective small angle scattering is a method frequently used in order to study structures and phenomena in the size domain between several Angstroms and the micrometre regime. This involves various colloidal species like micelles, polymers and liquid crystals as well as gel networks and the large class of nanocomposite materials [4,114,115,116].

The general setup of a small angle scattering experiment is illustrated in Fig. 5. In this section, the basic components will be discussed in a general way [3,4,114,117]. The classical SAS-setup consists of a radiation source, a monochromator, collimation elements, the sample, and the detector. The common X-ray source for lab applications is the copper target equipped X-ray tube emitting the characteristic *K-*$\alpha$ radiation [114,117]. Nevertheless, synchrotron sources gain more importance for modern scientific issues, due to offering a broad wavelength spectrum, low angular divergence, and high photon flux [114,117]. Neutrons are generated by a fission reaction in a nuclear reactor or by the bombardment of heavy metal targets with accelerated protons [114]. The monochromator processes the emitted radiation to a single wavelength or narrow distributed bands of wavelengths. For X-rays this could be realised by the reflection on single crystals [117], whereas for SANS setups velocity selectors [114,118] or chopper arrays (refer to section 4.1) are used. The optical profile of the beam is defined by a subsequent collimation trough variable guide elements, slit or pinhole optics [114,117,118]. The irradiated area of the sample is provided by the sample aperture. The sample environment for small angle scattering experiments is versatile and depends on the sample's properties and scientific issues. Simple liquid cells, used for basic analyses, are complemented by sample environments designed for extreme temperatures or pressures, as well as for electric or magnetic fields. For the sake of absolute calibration, information on the intensity of the incident radiation is needed as well. Therefore, monitor elements measuring the incident flux are located in

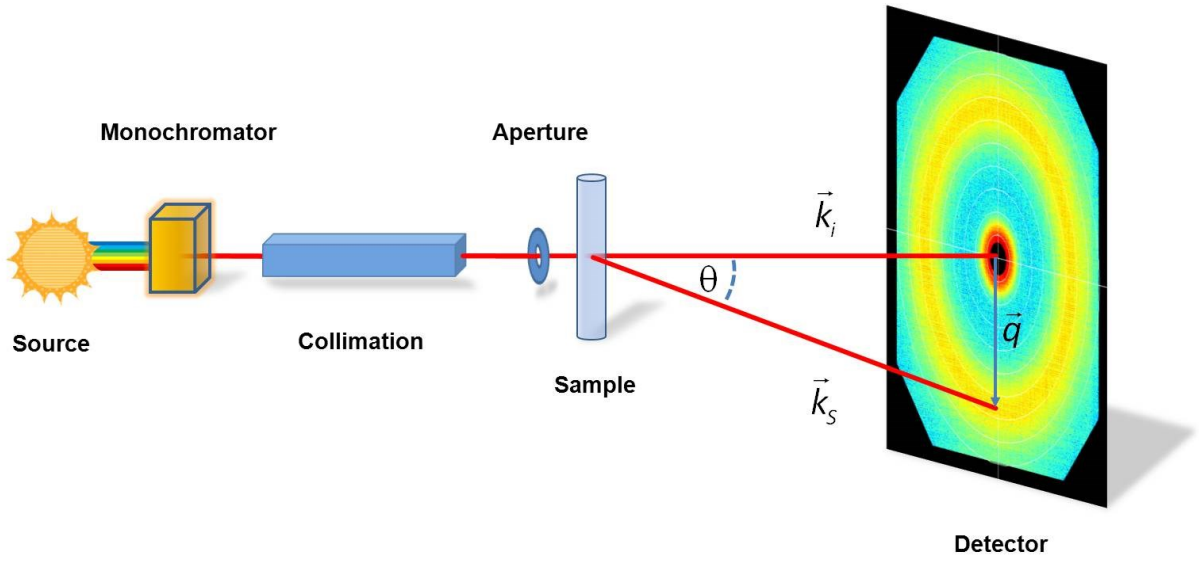


**Fig. 5: Scheme of the general setup of a small angle scattering experiment.**

front of the sample. The incident radiation is characteristically scattered by the investigated specimen and is measured with a position sensitive detector located at a certain distance from the sample. The detection of neutrons and X-rays differs in certain ways. In a nuclear reaction of neutrons with $^{3}$He gas, charged particles are generated that can be detected at the detector electrodes [114,118]. The X-ray photon detection follows a similar principle as incident photons are able to ionise rare gas molecules like Argon or Xenon [114,118]. This process leaves a trail of charged and therefore detectable particles. An alternative for the detection of neutrons is provided by scintillation detectors, equipped with a $^{6}$Li doped glass matrix [114,119]. Here, photons are generated by the incident neutrons, which can then be measured by photosensor elements.

## 3.2. General terms of the scattering theory

The scattering mechanism of neutrons and X-rays is quite different, but the general ideas concerning the interference of scattered waves are in both cases the same. Thus, the general principles will be outlined in the following section. The basic consideration will take some general assumptions into account [3,4]:

1. The incident radiation is monochromatic and coherent.
2. The magnitude of the wave vector is not changed during the elastic scattering process.
3. In order to fulfil the interference condition, the incoming and the scattered wave have a defined phase relation.
4. The scattered and interfering waves are detected in a far distance from the scattering centres. Therefore, a plane wave front is assumed. This is known as the *Fraunhofer*-approximation.
5. The *Born*-approximation assumes that within the studied isotropic system the incident plane wave is only scattered once. Multiple scattering is not considered.

The scattering of the incident wave takes place at individual scattering centres. The relative position of the individual scatterers is provided by a radial distribution function. The scattering length density (SLD) distribution $\rho(r)$ is the direct link to the structure of the probed sample.

$$\rho(r) = \sum_i \rho_i(r) b_i \tag{1}$$

Herein, $b_i$ is the scattering length of the different species embodied in the sample and their density distribution $\rho_i(r)$ with respect to the number of individual scatterers per volume unit. The scattering length quantifies interaction between radiation and matter. It is characteristic for the different scattering specimen and the radiation. The average scattering length density of a sample with a known composition is calculated as follows [3]:

$$b = \frac{\sum b_i}{V_m} \tag{2}$$

Here, $V_m$ is the molar volume, accessible via measurements of the macroscopic density of the sample. Further details on the scattering of neutrons and X-rays are provided in the appendix.

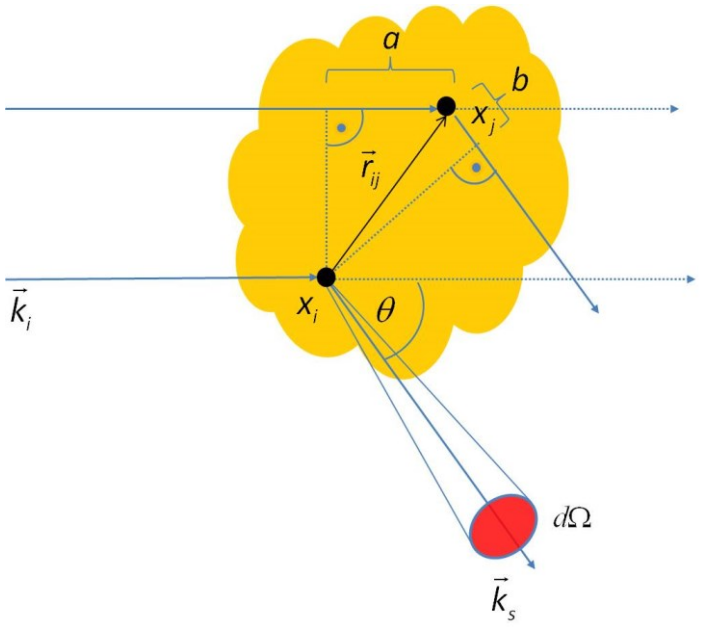


**Fig. 6: Schematic drawing of a basic scattering geometry. The incident plane wave ( $\vec{k}_i$ ) is scattered at $X_i$ and $X_j$. A spherical wave ( $\vec{k}_s$ ) propagates into the direction of $\theta$. Due to the path difference of the scattered waves interference takes place. The scattering intensity is detected in a certain distance on the detector plane within an area defined by the solid angle $\Omega$.**

The simplified scheme in Fig. 6 illustrates the basic scattering geometry. The detected scattering intensity results from the interference of the scattered waves propagating from the different scattering centres $X_i$ and $X_j$ and having a phase difference $\delta$. These individual scatterers are linked by the vector $\vec{r}_{ij}$.

The scattering vector $\vec{q}$ is defined by the following relation and describes the momentum transfer during the scattering process [3].

$$|\vec{q}| = |\vec{k}_s - \vec{k}_i| = q = \frac{4\pi}{\lambda}\sin\left(\frac{\theta}{2}\right) \tag{3}$$

Here, $\vec{k}_i$ ($\vec{k}_i = 2\pi\lambda^{-1}$) is the modulus of the incident wave vector with the wavelength $\lambda$ and $\vec{k}_s$ is the one of scattered wave. The enclosed angle is called the scattering angle $\theta$. For an elastic small angle scattering experiment only the magnitude of the scattering vector is considered, which is related to a length in the reciprocal space. In the following discussion it will be assigned the unit $nm^{-1}$. For the summation of the individual scattered waves $\delta$ between incident and scattered waves has to be taken into account and is provided by formula (4) [3]:

$$\delta \equiv \vec{k}_i \cdot \vec{r}_{ij} - \vec{k}_s \cdot \vec{r}_{ij} = \vec{q} \cdot \vec{r}_{ij} \tag{4}$$

The total amplitude of the three-dimensional *Fourier* transform of $\rho(r)$ of the scattering ensemble is provided by [4]:

$$A(q) = \sum_i b_i \, e^{-i\vec{q}\vec{r}} = \iiint_V \rho(\vec{r}) e^{-i\vec{q}\vec{r}} d^3\vec{r} = \int_V \rho(\vec{r}) e^{-i\vec{q}\vec{r}} d^3\vec{r} \tag{5}$$

Herein, the vector $\vec{r}$ results from $\vec{r} = \vec{r}_{ij} = \vec{r}_i - \vec{r}_j$. This relation takes into account that the integration is done over the total scattering volume *V*.

The detector signal correlates with the absolute squared amplitude of the scattered wave. The differential scattering cross section is an adequate quantitative expression for the ratio between incident and scattered radiation [4].

$$I(q) = \frac{d\sigma}{d\Omega} = \left\langle A(q)\, A^*(q) \right\rangle = \int_V \int_V \rho(\vec{r}_i)\, \rho(\vec{r}_j)\, e^{-i\vec{q}\left(\vec{r}_i - \vec{r}_j\right)} d^3\vec{r}_{\mathrm{i}}\, d^3\vec{r}_{\mathrm{j}} \tag{6}$$

Here, $\sigma$ defines the cross section, which represents the fraction of the scattered radiation from the incident one. The area where the phenomenon is observed in a certain distance to the scattering centres is defined by the solid angle $\Omega$. The experimental access to differential scattering cross section is provided by the number of events on the position sensitive detector with respect to the incident number of photons or neutrons. The bracket notation $\langle ... \rangle$ refers to the thermal average.

For randomly oriented isotropic scatterers and for spherical symmetry, *Debye* established the following relation employing the magnitude *r* of the vector $\vec{r}$ [4,120]:

$$I(q) = 4\pi \int_0^\infty r^2 \rho(r) \frac{\sin(qr)}{qr} dr \tag{7}$$

Until this point, only single objects non-affected by their surrounding matrix have been discussed. Hereinafter, an object with a homogeneous scattering length density $b_p$ embedded in a continuous surrounding and with a scattering length density $b_m$ will be considered. The difference between the scattering powers arising from the particle and the matrix is called the scattering contrast $\Delta b$. Thus, equation (6) in combination with the *Debye* formula (7) can be written as [121]:

$$I(q) = 4\pi \int_0^\infty \int_0^\infty \left(b(\vec{r}_{\mathrm{i}}) - b_m\right)\left(b(\vec{r}_{\mathrm{j}}) - b_m\right) \frac{\sin\left(q\left|\vec{r}_{\mathrm{i}} - \vec{r}_{\mathrm{j}}\right|\right)}{q\left|\vec{r}_{\mathrm{i}} - \vec{r}_{\mathrm{j}}\right|} d\vec{r}_i\, d\vec{r}_j \tag{8}$$

$$I(q) = \frac{1}{V} I_0(q) = \frac{1}{V} \Delta b^2 F(q) \tag{9}$$

Herein, $I_0(q)$ displays the scattering intensity of a single particle and $F(q)$ is the particle form factor describing its corresponding spatial geometry. For specimen with an inhomogeneous scattering length density distribution, as for instance in case of core-shell architectures, the particle scattering factor has to be expressed as a function of the scattering contrasts.

## 3.3. Scattering of particles in solution

Considering that *N* particles are dispersed in a continuous volume *V* equation (9) is completed by the particle number density and gives an expression with the unit of an inverse length. In the following discussion, the unit $cm^{-1}$ will be used.

$$I(q) = \frac{N}{V} \Delta b^2 F(q) \tag{10}$$

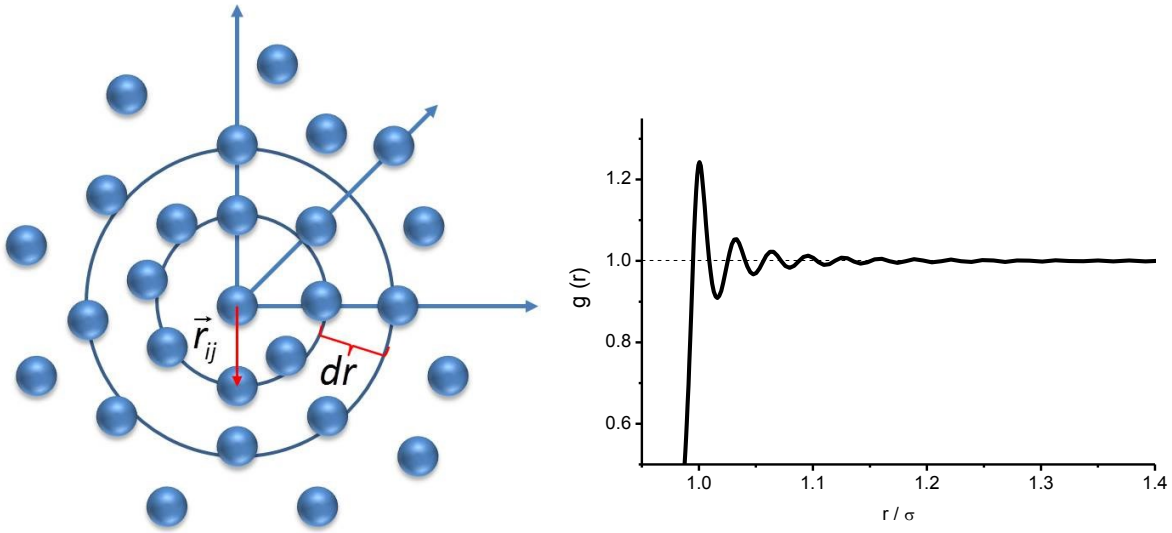


**Fig. 7: Scheme of the radial distribution of particles in concentrated dispersion. The graph displays the corresponding radial correlation function *g*(*r*).**

The simplest case is limited to single scatterer within a matrix or for high dilution. This approximation assumes that there is no correlation between the positions of the particles and thus there is no phase relation between the scattered waves. Increasing the number density causes a spatial correlation and the scattered waves interfere. The correlation of the dispersed particles is provided by the structure factor *S*(*q*) [4].

$$I(q) = \frac{N}{V} \Delta b^2 F(q) S(q) \tag{11}$$

The spatial correlation between the individual scatterer $X_i$ and $X_j$, which are connected by the vector $\vec{r}_{ij}$, can be written as follows [3]:

$$S(q) = 1 + \frac{1}{N} \left\langle \sum_{i=1}^{N} \sum_{j \neq i}^{N} e^{-iq\vec{r}_{ij}} \right\rangle = 1 + 4\pi \frac{N}{V} \int_0^{\infty} \left(g(r) - 1\right) e^{-iqr} dr \tag{12}$$

Here, *g*(*r*) is the pair correlation function. This aspect leads to the final summarising equation describing the basic scattering aspects of a small angle scattering experiment:

$$I(q) = \phi V_P \Delta b^2 F(q) S(q) \tag{13}$$

Here, $\phi$ is the volume fraction and $V_P$ the respective particle volume.

In summarising this important section concerning the basics of the scattering theory, one can conclude as follows: The geometry of the probed particles can be described by the form factor *F*(*q*). The spatial correlation between the individual particles is described by the structure factor *S*(*q*). The observed scattering intensity is thus proportional to product of the form factor and the structure factor, whereas the form factor is related to the *Fourier* transform of the scattering length density distribution $\rho(r)$ of the probed structure. The corresponding transformation of *S*(*q*) leads to the pair correlation function *g*(*r*). For dilute systems the structure factor becomes unity.

## 3.4. Scattering at small scattering angles

The analysis of the scattering intensities at small scattering angles $\theta$ is useful in obtaining general model independent information on the investigated structure. It reveals the radius of gyration $R_G$, which is a measure for the density distribution around the centre of mass [3,4]. It can also be used for the determination of the particle volume $V_P$. Both values together allow drawing basic ideas on the geometry of the probed specimen. Equation (14) is known as the *Guinier*-equation [3]:

$$I(q) \approx \phi \, V_P^2 \Delta b^2 \left(1 - q^2 \frac{R_G}{3}\right) \approx I_0(q) \exp\left(-\frac{(q\,R_G)^2}{3}\right) \tag{14}$$

The approximation is restricted to the following assumptions:

1) The relation is only valid for small scattering angles to fulfil $R_G \cdot q << 1$.

2) An isotropic system without inter-particle interactions is considered. Thus, the structure factor becomes unity.

3) The particles are randomly oriented and isotropically distributed.

From the linearised *Guinier*-equation, $R_G$ can be extracted from the slope of the function correlating with squared magnitude of the scattering vector, whereas the intercept reveals the forward scattering intensity $I(q \rightarrow 0)$. The respective plot of $q^2$ vs. ln $[I(q \rightarrow 0)]$ is commonly known as the *Guinier*–plot.

The correlation between the radius of gyration and the dimensions of a few common geometrical bodies can be calculated as follows from [122]:

Spheres: $$R_G{}^2 = \frac{3}{5} R^2 \tag{15}$$

Cylinders: $$R_G{}^2 = \frac{R^2}{2} + \frac{L^2}{12} \tag{16}$$

Ellipses: $$R_G{}^2 = \frac{a^2 + b^2 + c^2}{5} \tag{17}$$

## 3.5. Contrast variation

Contrast variation analysis is a powerful tool for revealing the particle shape and inner structure [4,5,117,123,124]. In general, this method uses a variation of the analyst's scattering length density or of the surrounding matrix. Neutron scattering, for instance, takes advantage of the great difference between the coherent scattering lengths of hydrogen and deuterium. By means of a simple exchange of a certain amount of hydrogenated solvent by its respective deuterated equivalent, it is possible to cover a large range of scattering contrasts for the analysis of liquid suspensions [114]. This general idea is illustrated in the scheme provide by Fig. 8. The analysis of the scattering intensities at different scattering contrasts is thus a frequently employed procedure to gain additional information on structural characteristics of the investigated species (Fig. 8 a), b), c) ).

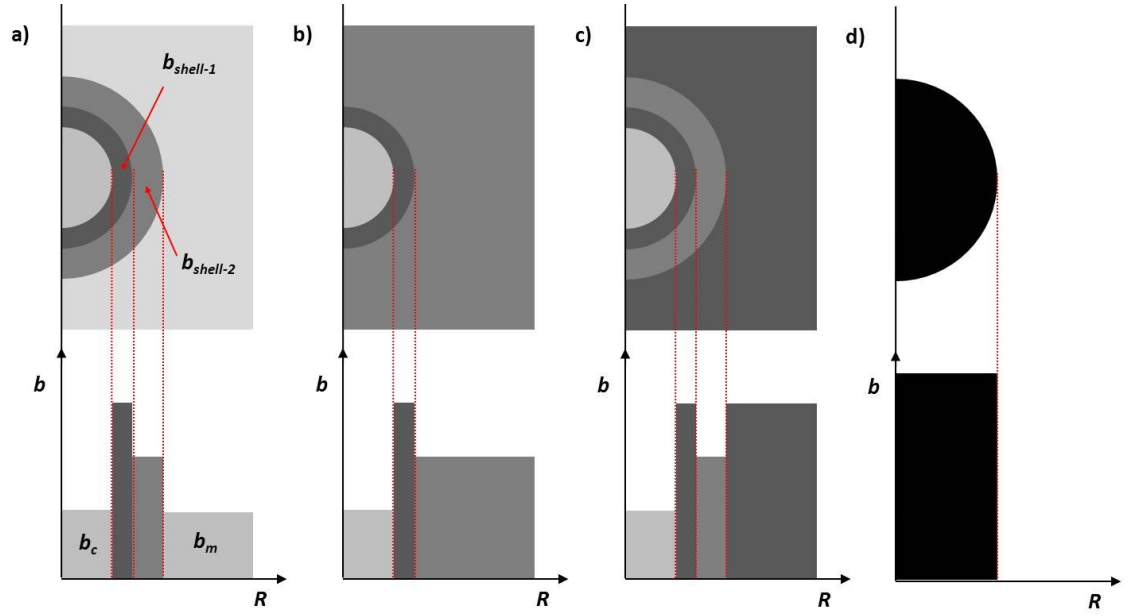


**Fig. 8: Scheme illustrating the principle of contrast variation for structural analysis. The structure of a core-shell particle having different scattering length densities within the different parts of the particle ($b_c$ – SLD-core, $b_{shell-1}$ – SLD-shell 1, $b_{shell-2}$ – SLD-shell 2) can be analysed by the variation of the scattering length density of the surrounding matrix $b_m$. The scattering length densities are illustrated by different shades of grey. The corresponding scattering length density profile is illustrated below.**

A contrast match can be realised by adjusting the matrix scattering length density $b_m$ to the requested one of the probed structure. Thus, case a) represents the core-match conditions with $b_m = b_c$, whereas cases b) and c) show the shell-match conditions, where either $b_{shell-1}$ or $b_{shell-2}$ is equal to $b_m$. The case of infinite contrast ($\Delta b = \pm \infty$) is illustrated in Fig. 8 d). Here, only the particle shape contributes to the scattering intensity, whereby the information arising from the inner structure vanishes. In order to obtain independent information on the shape and the inner structure of a particle, the scattering intensities, measured during a contrast variation series, are decomposed into contrast dependent and contrast independent terms. Through an extrapolation to infinite contrast, the particle shape function $T(\vec{r})$ can be extracted. This correlates with the radial distribution function of a particle with a homogenous scattering length density $b_P$ (Fig. 8 c) ). For this reason, there are two limiting cases. The measure $T(\vec{r})$ provides 1 only within the particle or 0 elsewhere. Therefore, $T(\vec{r})$ is directly connected to the particle volume $V_P$ and can be assigned to the volume not accessible to the dispersion medium [5,125].

$$V_P = \int_0^\infty T(\vec{r})\, d\vec{r} \tag{18}$$

The average scattering length density of the particle $b_P$ is provided by:

$$b_P = \frac{1}{V_P} \int_0^\infty T(\vec{r}) b(\vec{r}) d\vec{r} \tag{19}$$

The decomposition of the local scattering length density $b(\vec{r})$ into a contrast dependent and independent term reveals [125]:

$$b(\vec{r})-b_m = T(\vec{r})\left(b(\vec{r})-b_m\right)-T(\vec{r})\Delta b(\vec{r}) \tag{20}$$

The second term of equation (20) $\Delta b(\vec{r})$ depicts the radial difference of the scattering length density to the average value $b_P$. It has to be considered that:

$$\int_0^\infty T(\vec{r})\,\Delta b(\vec{r})\,d\vec{r} = 0 \tag{21}$$

Hereinafter, the normalisation of the scattering intensity to the one of a single particle $I_0(q)$ will be considered. A more general expression is provided by [3]:

$$I_0(q) = \int_V\int_V [b(\vec{r}_i)-b_m][b(\vec{r}_j)-b_m]\frac{\sin\left(q\left|\vec{r}_i-\vec{r}_j\right|\right)}{q\left|\vec{r}_i-\vec{r}_j\right|}d\vec{r}_i d\vec{r}_j \tag{22}$$

The intensity $I_0(q)$ can be decomposed into [5,117]*:*

$$I_0(q) = \Delta b^2\, I_S(q) + \Delta b\, I_{SI}(q) + I_I(q) \tag{23}$$

Here, $I_S(q)$ is the contrast dependent shape-term. Scaling with the squared contrast, it is also the leading term of the decomposition. The scattering contribution deriving from the particles inner structure is provided by the contrast independent inner-term $I_I(q)$. The second contrast dependent term is the cross-term $I_{SI}(q)$.The corresponding relations follow [5]:

$$I_S(q) = \int_V\int_V T(\vec{r}_i)T(\vec{r}_j)\frac{\sin\left(q\left|\vec{r}_i-\vec{r}_j\right|\right)}{q\left|\vec{r}_i-\vec{r}_j\right|}d\vec{r}_i d\vec{r}_j \tag{24}$$

$$I_{SI}(q) = \int_V\int_V T(\vec{r}_i)T(\vec{r}_j)\Delta b(\vec{r}_j)\frac{\sin\left(q\left|\vec{r}_i-\vec{r}_j\right|\right)}{q\left|\vec{r}_i-\vec{r}_j\right|}d\vec{r}_i d\vec{r}_j \tag{25}$$

$$I_I(q) = \int_V\int_V T(\vec{r}_i)\Delta b(\vec{r}_j)T(\vec{r}_i)\Delta b(\vec{r}_j)\frac{\sin\left(q\left|\vec{r}_i-\vec{r}_j\right|\right)}{q\left|\vec{r}_i-\vec{r}_j\right|}d\vec{r}_i d\vec{r}_j \tag{26}$$

The analysis of the scattering intensities at vanishing $q$-values, obtained from measurements at different scattering contrasts, reveals model independent parameters. The extrapolated forward scattering intensity $I(q \rightarrow 0)$ at different scattering contrasts $\Delta b$ is used for the determination of the particles average scattering lengths density $b_P$ and their respective volume $V_P$ [117].

$$\sqrt{\frac{I(q\rightarrow 0)}{\phi}} = \sqrt{V_P}\left(b_P - b_m\right) \tag{27}$$

In this case, $V_P$ results from the squared slope of the linear function, whereas $b_P$ is provided by a function of its intercept. This correlation is commonly known as the *'square root'* relation.

Moreover, form the absolute scaled scattering intensity extrapolated to vanishing scattering angles the determination of the apparent molecular weight of a dispersed molecule is possible [3]:

$$M_{W-app} = \frac{I(q\rightarrow 0)\,\rho^2 N_A}{\Delta b^2 c} \tag{28}$$

Herein, $\rho$ is the macroscopic mass density of the molecules and *c* its respective concentration. An extrapolation for infinite dilution revealing $I_0(q)$ can be used for the calculation of the weight averaged molecular weight of the probed specimen by analysis of its respective forward scattering intensity using equation (14).

The correlation between $R_G$ and $\Delta b$ can be used for the extrapolation of the respective radius at infinite contrast $R_{G\infty}$ [117,124]. The corresponding plot illustrating this relation is also known as the *Stuhrmann*-plot.

$$R_G^2 = R_{G\infty}^2 + \frac{\alpha}{\Delta b} - \frac{\beta}{\Delta b^2} \tag{29}$$

with:

$$R_{G\infty}^2 = \frac{1}{V_P}\int_0^\infty T(\vec{r})\, r^2 d\vec{r} \tag{30}$$

$$\alpha = \frac{1}{V_P}\int_0^\infty T(\vec{r})\Delta b(\vec{r})\, r^2 d\vec{r} \tag{31}$$

$$\beta = \frac{1}{V_P^2}\left[\int_0^\infty T(\vec{r})\Delta b(\vec{r})\, \vec{r}\, d\vec{r}\right]^2 \tag{32}$$

Here, $R_{G\infty}$ is provided as a function of the slope from the linear correlation. The respective intercept reveals the parameter $\alpha$, that is a measure for the spatial distribution of inhomogeneity within the analysed species. A positive value of $\alpha$ is an evidence for an increased scattering length density of the exterior parts of the particle, whereas a negative value indicates an increased scattering length density around the particles centre. The value of $\beta$ is related to the squared distance between the centre of gravity of the shape function $T(\vec{r})$ and the internal inhomogeneity $T(\vec{r})\Delta b(\vec{r})$ that vanishes for centrosymmetric structures [5].

## 3.6. Polydispersity

Analyses of polymer samples must take polydispersity aspects into consideration that, for instance, arise from molecular mass distributions. The obtained scattering intensities however are summation of all individual scatterers of the probed sample and therefore display the average of the analysed specimen. This has a certain influence on the analysis of scattering data, which can lead to a loss of information on structural characteristics (Fig. 9). To a certain extent, polydispersity can be considered by distribution functions adapted to the scattering intensities of monodisperse geometries [117,126].

$$I_{poly}(q, R_0) = \int_0^\infty G(R, R_0, x)\, I(q, R) dR \tag{33}$$

Here, $R_0$ represents the mean value of the distribution, whereas *x* characterises the distributions width. The influence of the polydispersitiy on the scattering and the corresponding size distribution is

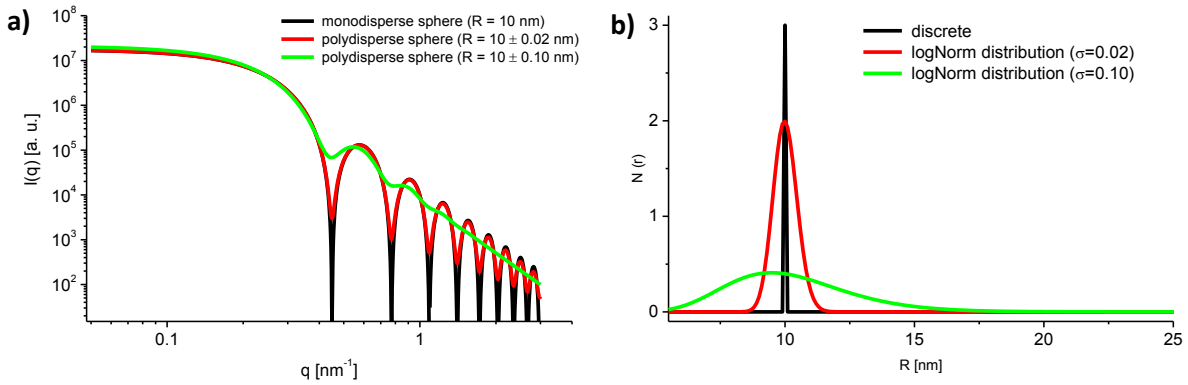


**Fig. 9: a) Scattering intensities simulated for spheres with a radius of $R_0$ = 10 nm. The coloured lines represent the corresponding scattering intensities of polydisperse spheres assuming a logarithmic normal distribution of 2 % (red curve) and 10 % (green curve) of *R*. b) The corresponding size distribution of R.**

illustrated in Fig. 9 using the example of a homogeneous sphere. It is therefore clearly demonstrated that a broadening in the size distribution leads to a significant smearing of the scattering intensities. Conclusively, this could lead to a controversy interpretation of the scattering data using different geometrical approaches.

Common distribution functions are the Log-normal and the *Gaussian* or Normal distributions, which are equal to [126]:

$$G_{Gauss}(R,R_0,\Delta R)=\frac{1}{\Delta R\sqrt{2\pi}}\exp\left(\frac{(R-R_0)^2}{2\Delta R^2}\right) \tag{34}$$

$$G_{LogNorm}(R,R_0,\sigma_{LogNorm})=\frac{1}{R\sigma_{LogNorm}\sqrt{2\pi}}\exp\left(-\frac{1}{2\sigma_{LogNorm}^2}\left(\ln\frac{R_0}{R}\right)^2\right) \tag{35}$$

Here, $\Delta R$ is the half-width of the *Gaussian* function and $\sigma_{LogNorm}$ describes the standard mean deviation from $R_0$ in the LogNorm-distribution.

# 4. Time of Flight Small Angle Neutron Scattering

The rapidly growing need for the analysis of scientific issues in the sub-micrometre regime especially from soft matter science intensified the development of new and innovative SANS instrumentation [115,127]. Herein, the requested issues range from probing large spatial structures simultaneously with small specimen being several orders smaller, over kinetic analyses, or to the studies on the influence of external fields on the sub-microscopic arrangement. Furthermore, spallation sources like the European Spallation Source (ESS) planned in Lund (Sweden) are dealt as the future alternative to reactor based sources providing neutrons for science. Spallation sources use accelerated protons for the bombardment of heavy metal targets for the generation of thermal neutrons [114]. This process is commonly pulsed and therefore requires adapted techniques and instrumentation.

The time of flight (TOF) method employs a neutron spectrum with respect to the neutron velocity, which is related to the time the neutrons need to travel along a certain distance. Therefore, the corresponding neutron wavelength is determined by their respective time of flight. TOF-SANS does not only support pulsed sources, it also represents an alternative for the classical monochromatic instruments at reactor based neutron sources [128]. Here, the pulsed neutron beam is generated by a set of choppers. The TOF-technique opens up different advantages. In contrast to the classical SANS setup using velocity selectors for the definition of narrow distributed wavelengths, with the TOF-method variable wavelength bands can be used. This enlarges the accessible momentum transfer adjusted to the experimental requirements. Additionally, the commonly compact design of

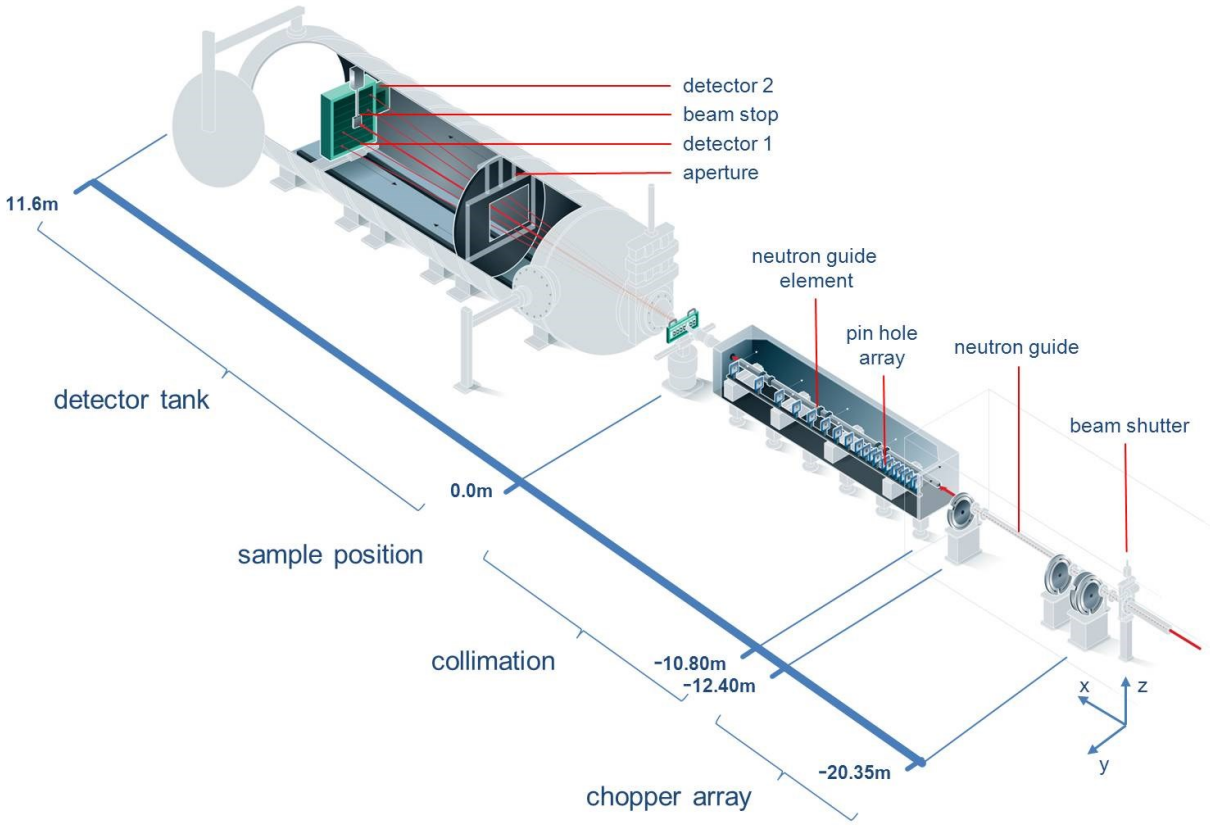


**Fig. 10: Experimental setup of the very small angle neutron scattering instrument V16-VSANS at the BER-II reactor of the HZB in Berlin (Germany).**

TOF-SANS instruments reduces the influence of the neutron gravity effect. So far, this effect had to be carefully considered at the classical SANS-setups for the longest sample-detector distances [129]. Nevertheless, neutron TOF-experiments demand excellent resources for the data acquisition as the amount of data obtained by a single experiment is large in comparison to the data amount obtained from the classical monochromatic setups.

In this section, the TOF-SANS instrument V16-VSANS at the BER-II neutron source in Berlin (Germany) will be introduced in more detail. The instrument is especially developed for the analysis of issues from soft matter science. The abbreviation VSANS stands for very small angle neutron scattering implying an accessible $q$-range of $8 > q > 10^{-4}$ nm$^{-1}$. The instrument has a total length of just 32.45 m and is located at the NL4C neutron guide behind a supermirror coated multichannel bender. The final cross section at the entrance to the instrument is 80 x 80 mm$^2$ emitting an average neutron flux of $8.5 \cdot 10^7$ cm$^{-2}$ s$^{-1}$. The general experimental setup is illustrated by the scheme illustrated in Fig. 10. The major instrument-axis pointing towards the neutron source is named $x$-axis. The horizontal direction is represented by the $y$-axis and consequently the vertical direction is provided by the $z$-axis.

## 4.1. Wave band definition

The cold “white”! neutron spectrum emitted from the BER-II reactor is processed by a set of four choppers to the experimental requirements (Fig. 11). The first two choppers are located right behind the instrument entrance at 20.35 m and 20.325 m in front of the sample having an opening aperture of $\varphi_1 = 11.1°$ and $\varphi_2 = 22.2°$ respectively. They can be operated in parallel and anti-parallel rotation mode. The combination of these two choppers allows tuning the pulse length, momentum transfer resolution, and neutron flux available at the sample. By setting the first chopper as pulse chopper, the generation of short pulses with good time resolution $\Delta t / t$ is realised and thus the resolution in

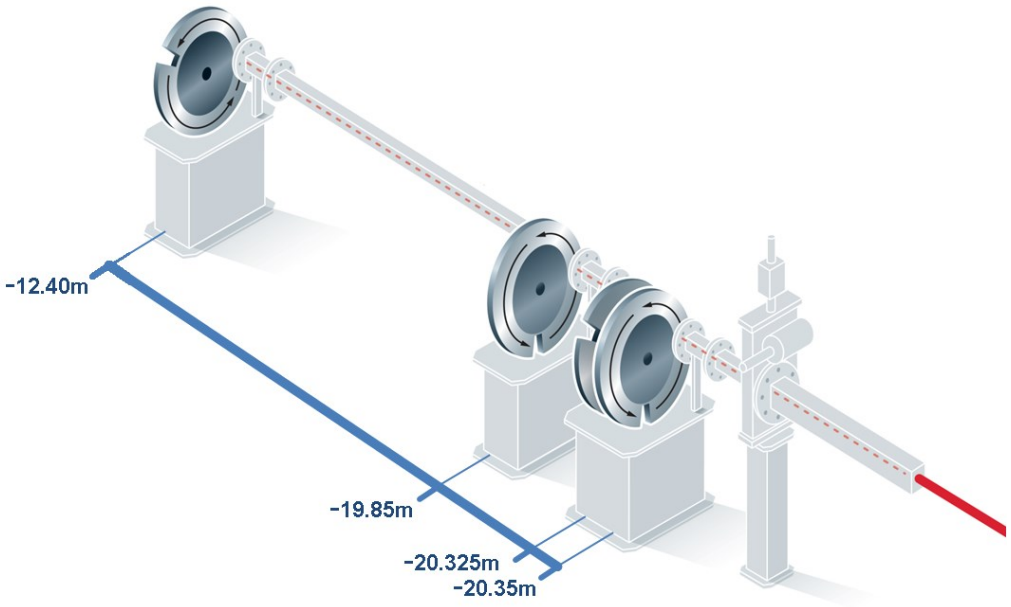


**Fig. 11: Schematic drawing of the chopper setup for the wave band definition located in the casemate. Chopper 1 (-20.35 m) and chopper 2 (-20.325 m) act as pulse chopper. Chopper 3 at -19.85 m is used to avoid frame overlap. At 12.40 m the waveband chopper is located defining the transmitted waveband.**

the momentum transfer $\Delta q / q$ is enhanced. This can even be improved by combining chopper 1 and 2. This option is of special interest for samples having fine structured scattering patterns. Even so, the number of available neutrons at the sample is low and therefore it is challenging to investigate weakly scattering samples in a limited time frame with the needed accuracy. Using chopper 2 for the generation of the neutron pulses, yield longer pulses with an increased number of available neutrons. Thus, this is the option of choice for weakly scattering samples without significantly structured scattering patterns, as this is the case for polymer coils, for instance. The rotation frequency $\nu$ of the pulse chopper thus defines the available waveband frame provided by $\lambda_{min}$ and $\lambda_{max}$. At the same time, the pulse choppers set the starting time for the determination of the individual TOF of the transmitted neutrons. The pulse length can be tuned from 0.62 to 1.24 ms operating the choppers with a respective speed of up to 3000 rounds per minute (rpm). To tailor the generated neutron pulse, chopper 3 located at 19.85 m and chopper 4 at 12.4 m in front of the sample are used (Fig. 11). Their respective opening apertures are $\varphi_3$ = 16.72° and $\varphi_4$ = 60.0°. Chopper 4 in is called waveband chopper which defines the widths of the transmitted waveband and therefore the position of $\lambda_{min}$ and $\lambda_{max}$. To avoid the overtaking of slow neutrons by fast neutrons of the following pulse, chopper *3* serves to cut off the neutrons with high wavelengths of the previous pulse. This so-called frame overlap would lead to falsified TOF-correlations and must therefore be very carefully avoided. A monitor element counting the neutrons after passing the chopper array is located right behind the waveband chopper at ≈ 12.4 m. The monitor signal is used for the normalisation of the neutrons counted by the detector.

Hereinafter, the generation of neutron pulses with well-defined properties will be discussed in a theoretical context. The transmitted neutron velocity spectrum $N(\lambda)$ is normalised with respect to the number of incident neutrons $N_0(\lambda)$. It can be expressed as a function of the transmission of the individual choppers $T_i(\lambda, \Delta s_i)$ and thus can be written as:

$$T(\lambda) = \frac{N_0(\lambda) K \prod_{i=1}^{N_c} T_i(\lambda, \Delta s_i)}{N_0(\lambda)} = K^* \prod_{i=1}^{N_c} T_i(\lambda, \Delta s_i) \tag{36}$$

Here, the total number of choppers to be passed is $N_c$, whereas $K^*$ is a normalisation constant. Furthermore, $\Delta s_i$ is the respective distance of the individual choppers to the pulse source. For setups using a continuous source this value is calculated with respect to the distance to the pulse chopper. The transmission of the pulse chopper is thus provided as the ratio of the opening aperture over the full angle. As already noted, by passing the pulse chopper, the transmitted neutron spectrum becomes wavelength dependent due to the different neutron velocities as a distinct time domain is defined.

The phase shift of a chopper with respect to the pulse source is provided by $\phi_i$. The individual chopper transmission is a function of time, its opening aperture, as well as its corresponding rotation frequency, and phase shift. Therefore, the boundaries for the transmission of neutrons by a chopper are provided with respect to the neutron wavelength and time by:

$$T_i(\lambda, t) = \begin{cases} \upsilon_i \ for\ 0 \le \left| 2\pi \upsilon_i t + \phi_i \right| mod\ 2\pi \le \varphi_i \\ 0 \ for\ all\ other\ values\ (2\pi \upsilon_i t + \phi_i) \end{cases} \tag{37}$$

These conditions reveal the time frame of the choppers in the open state. The moment, in which the pulse chopper reaches the open state, is defined as the starting time $t_0$. Until the pulse chopper closes after $\tau$ an ensemble of neutrons with different velocities, which correspond to the "white" spectrum of the source, have passed the chopper. For the further treatment, the time parameter provided by (37) is transformed into the wavelength domain employing the well-known *de Broglie* relation (38).

$$\lambda = \frac{h}{p} = \frac{h}{m_n v} = \frac{h\,t}{m_n s} \tag{38}$$

The momentum of the neutrons is provided by *p*, whereas *h* refers to the *Planck*-constant. The neutron mass is represented by $m_n$ and *s* equals $\Delta s_i$, which is again the distance to the pulse source. This gives the transformed boundaries:

$$T_i(\lambda, \Delta s_i, t_0) = \begin{array}{l} \upsilon_i \;\; for\; 0 \le \left| 2\pi\left( t_0 + \lambda \Delta s_i \frac{m_n}{h} \right) + \phi_i \right| mod\; 2\pi \le \varphi_i \;, 0 \le t_0 \le \tau \\ 0 \;\; for\; all\; other\; values \left| 2\pi\left( t_0 + \lambda \Delta s_i \frac{m_n}{h} \right) + \phi_i \right| , 0 \le t_0 \le \tau \end{array} \tag{39}$$

The individual chopper transmission can be solved by the following integral, corresponding to all the neutrons that passed the respective chopper:

$$T_i(\lambda, \Delta s_i) = \int_0^{\tau} T_i(\lambda, \Delta s_i, t_0)\, dt_0 \tag{40}$$

Between two choppers a phase shift $\phi_{i,j}$ is defined by the angular difference between the centres of the opening apertures $\varphi_i$ and $\varphi_j$. Consequently, the previously introduced $\phi_i$ embodies the different opening apertures and phase shifts $\phi_{i,j}$ respectively.

$$\phi_i = \frac{\varphi_j - \varphi_i}{2} - \phi_{j,i} \tag{41}$$

The calculation of the total transmission provided by equation (36) includes the normalisation regarding to the loss of neutrons at the pulse chopper by *K*.* This is required as the calculated $T_i$ only considers the additional loss of neutrons at the following choppers.

$$K^* = \left( \frac{\varphi_0}{\varphi_1} \right)^{N_c - 1} \tag{42}$$

A sufficient resolution in the *q*-domain is one of the basic requirements for a SANS experiment. As can be learned from the discussion above, this is closely related to wavelength resolution and therefore to the resolution in the time domain. The accuracy in the time domain $\Delta t$ is provided by $\pm\, \tau / 2$. An enhanced time resolution is obtained for wavelength with a lower transmission [130].

$$\Delta t = \tau \frac{\varphi_0}{\varphi_1} T(\lambda) \tag{43}$$

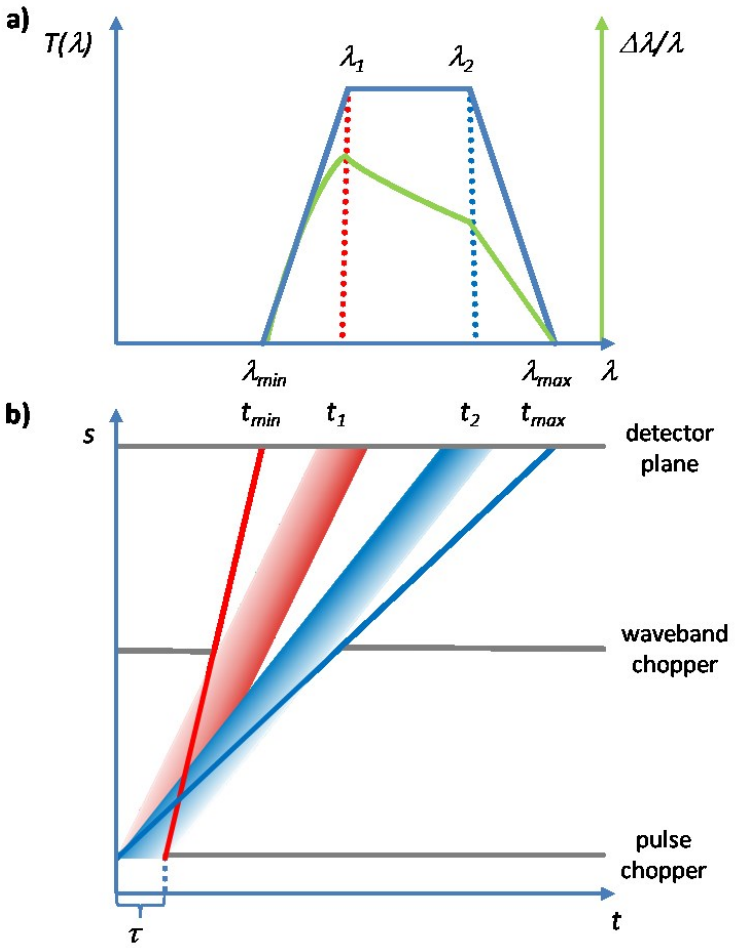


**Fig. 12: The lowermost sketch b) represents the path-time scheme of a TOF-experiment. The pulse chopper generates the pulse and the waveband chopper tailors its width. The time frames of the choppers in the closed state are represented by the solid grey lines. Neutrons with the highest velocity reach the detector with $t_{min}$ representing the lowest accessible wavelength $\lambda_{min}$ and vice versa. The waveband passing the chopper array within the full pulse frame contribute to the transmission spectrum $T(\lambda)$, which is confined by $\lambda_{min}$ and $\lambda_{max}$. The transmission $T(\lambda)$ as observed at the detector plane and corresponding resolution $\Delta\lambda / \lambda$ are depicted in scheme a).**

An illustrative scheme is provided by the path-time diagram of a chopper array illustrated in Fig. 12 b). The time frame of the pulse chopper in the open state is represented by $\tau$. Here, the closed state of the respective choppers is indicated by the solid grey lines along the time-axis. The neutron trajectories are represented by straight lines with a slope corresponding to their respective velocity and thus their corresponding wavelengths. The transmitted neutrons waveband is tailored by the waveband chopper defining the available neutron waveband (Fig. 12 a) ). Neutrons with the highest velocity reach the detector plane at $t_{min}$. Nevertheless, these neutrons exhibit a low transmission $T(\lambda_{min})$. Thus, slow neutrons representing the highest wavelengths $\lambda_{max}$ of the transmitted "white" spectrum require the time $t_{max}$ for the same distance, but also exhibit a low transmission $T(\lambda_{max})$. These issues are illustrated in Fig. 12 a). These values are of certain interest for the further data processing and can be calculated as follows:

$$t_{\min} = \frac{\left(\frac{\varphi_1}{2} + \phi - \frac{\varphi_4}{2}\right) - \varphi_1}{2\pi\,\upsilon_1} \tag{44}$$

$$\lambda_{min} = \frac{h\,t_{min}}{2\pi\,m\,\upsilon_1\,\Delta s_4} \tag{45}$$

$$t_{\max} = \frac{\left(\frac{\varphi_1}{2} + \phi + \frac{\varphi_4}{2}\right)}{2\pi\,\upsilon_1} \tag{46}$$

$$\lambda_{min} = \frac{h\,t_{max}}{2\pi\,m\,\upsilon_1\,\Delta s_4} \tag{47}$$

Here, $\nu_1$ is the frequency of the pulse chopper and $\varphi_1$ the respective opening aperture. The waveband chopper is $\varphi_4$ and its respective distance to the pulse source is $\Delta s$.

Those neutrons passing the pulse chopper during the full time frame of the neutron pulse represent the available waveband between $\lambda_1$ and $\lambda_2$ with a maximum transmission. Below and above these values the transmission decreases linearly to zero. The corresponding values needed for the data treatment can be determined with the following equations.

$$\lambda_1 = \frac{h}{2\pi\,m\,\upsilon_1\,\Delta s_4}\left(\frac{\varphi_1}{2} + \phi - \frac{\varphi_4}{2}\right) \tag{48}$$

$$\lambda_2 = \frac{h}{2\pi\,m\,\upsilon_1\,\Delta s_4}\left(-\frac{\varphi_1}{2} + \phi + \frac{\varphi_4}{2}\right) \tag{49}$$

## 4.2. Detection

The neutron detection in the classical mode is realised by a 0.9 x 1 $m^2$ $^3$He-tube detector hosting 112 tubes with a length of 1 m and a diameter of 8.3 mm each [114]. The tubes are each virtually subdivided into 100 cells. Consequently, the detector area is represented trough a pixel array of 112 x 100 elements. The distance between detector and sample can be varied continuously from 1.7 m to 11.23 m. The classical mode employing the common neutron guide collimation (Fig. 10) and the complete accessible neutron velocity spectrum, covers a $q$-range of $3\cdot10^{-2}$ $nm^{-1} < q < 6$ $nm^{-1}$. By rotation of the detector at the smallest sample-detector distance, the $q$-range can even be extended to $q \approx 8$ $nm^{-1}$. The spatial resolution along the $y$-axis of the detector plane is mainly provided by the fixed arrangement of the detector tubes. Along the $z$-axis, the calibration is accomplished by measurements of a homogeneous scattering pattern using a grid in front of the detector with defined dimensions. Thus, the complete detector plane can be described by a well-defined pixel array that encodes the spatial information. This, however, is an essential source of information for the data acquisition in the classical SAS-instruments, where for every pixel the number of detected neutrons is summed up. Due to the TOF-mode, an additional time component is recorded for every

pixel. Every detected neutron is correlated with the distinct detection time and therefore every pixel contains an entire TOF-spectrum. In other words, neutrons with a certain momentum transfer and well-defined TOF are summed in a TOF-spectrum by a certain group of detector pixels. Herein, the position of the pixel is related to $\theta$ and the respective TOF gives access to $\lambda$. Consequently, the set of information provided by a single detector pixel is significantly increased compared to the classic detection. Nevertheless, the TOF-detection mode demands special requirements with respect to the hardware and the data processing. Furthermore, the amount of data is much higher and is stored in a binary format. To prevent so-called "dead time" effects, originating in the neutron detection process itself and caused by the detector electronic, the amount of neutrons per pixel and time is restricted and has to be taken into consideration during the experiments.

A second detector (Fig. 10) can be used for the detection of the scattered neutrons with lowest momentum transfers. This is realised by adjusting this detector in front of the tube detector. The 30 x 30 $cm^2$ cross-wire detection unit has a spatial resolution of about 2 mm using as well $^3He$ for the detection process. It is reserved for the low-*q* analysis using the multi-pinhole grid-collimation providing a well-focused neutron beam. This option additionally extends the accessible *q*-range down to $q > 10^{-4}$ $nm^{-1}$

## 4.3. Data acquisition

The V16-VSANS instrument is operated by the *CARESS* software developed for controlling the instrumentation at the BER-II neutron source. It makes communication to the electronic devices possible, such as motors and sensor elements, for example. It also enables the transcription of the device specific code into a short cut syntax that can be easily understood by the operator and therefore simplifies the instrument operation. The instrument parameters are controlled using a terminal interface input. Moreover, this makes it easy for the operator to develop script files including all relevant parameters for an experiment. These can be adapted to the experimental requirements and can be saved and executed by the CARESS input shell.

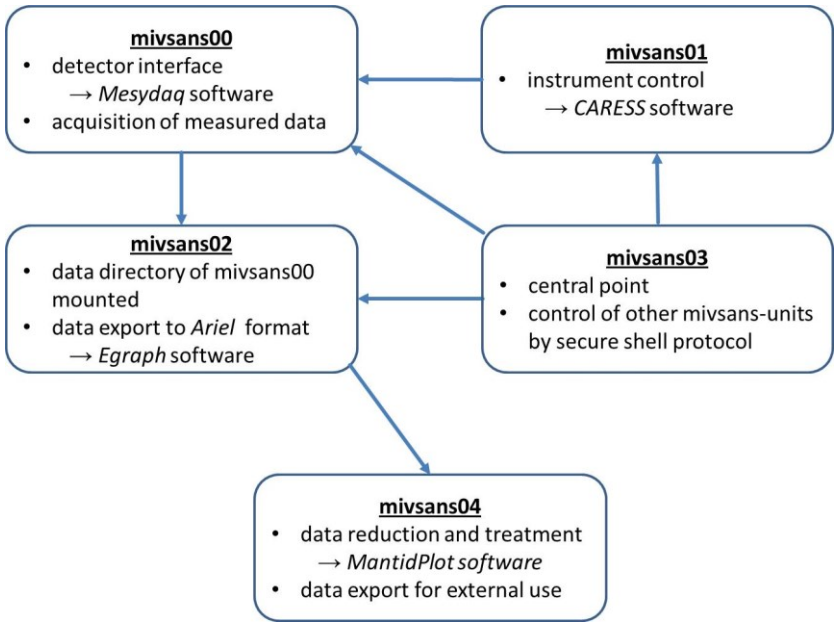


**Fig. 13: Schematically representation of the computer systems used for the operation of the V16-VSANS instrument, data acquisition, and further data treatment.**

Five individual computer systems are used to control the instrument, the data acquisition, the data storage, and the final data treatment (Fig. 13). These computers are connected within a self-contained computer network integrated and secured by the local network of the instrumentation at the BER-II.

The central unit of the *VSANS*-network enables control of the other components of this local network by *secure shell* protocol. The acquisition of the measured detector signals is done by the software *Mesydaq* and is stored separately. For security reasons, the raw data are stored in the read-only-mode that secure the data from being manipulated. For further treatment, the raw-data have to be transformed into the *ARIEL* format including additional measurement information, such as relevant instrument parameters, for example. The raw data visualisation and export is realised by the *Egraph*-software. Furthermore, the software allows monitoring the recorded detector data even for individual pixels of the different detector tubes.

## 4.4. Data treatment

The TOF-data collected in the pixel array of either one of the two detectors are processed by the detector software *Mesydaq*. The data are stored as binary files that can be rendered graphically by the software *Egraph*. This software also enables the data export to the *ARIEL* format that can be imported to the *MantidPlot*-software. This software was developed for the treatment of neutron and muon data and is highly useful for the reduction, transformation and visualisation of TOF-SANS data sets [131]. It is an open source program utilising the *Pythons* syntax and is under permanent advancement by the SAS-community. A general overview on the data treatment procedure is provided in the schematic flow diagram provided in Fig. 14. The export of the measurement data using *Egraph* generates two file-formats. One contains the measurement data encoded in a binary file. The other one, the header file, incorporates the instrument parameters of the specific measurements. This includes all detector specific parameters, like detector distance, for instance, or the detector tube alignment, and information concerning the sample.

For the analysis of absolute calibrated SANS-intensities the following measurements additionally to the measurement of the sample itself are required. Measurements of the empty beam (EB) and of the empty cell (EC) are performed as reference. A measurement of cadmium (CD) is used for the correction of the background noise of the measured detector signal. The transmission of the samples and the respective references is of particular importance for the final data processing and is therefore determined by measurements with the attenuated direct beam and without beam stop in front of the detector. For the calibration of the scattering intensities of the sample measurements of reference samples with a homogenous scattering pattern are performed. Commonly, the isotropic scattering of water is used for this purpose [118,132]. Nevertheless, the scattering intensity of water depends on the neutron wavelength and therefore has to be recalibrated by a less wavelength-dependent isotropically scattering sample. This is done by cross-calibrated glassy carbon for instance. Furthermore, the calibration of the scattering intensities can be checked by measurements of samples with known physical properties as for example polymer standards. The *MantidPlot* software allows the data processing by command line input using an appropriate *Python* syntax. Furthermore, the whole reduction procedure can be prepared by adapting *Python*-script files, which includes all relevant steps and parameters. Most of the data processing steps can be visualised by respective

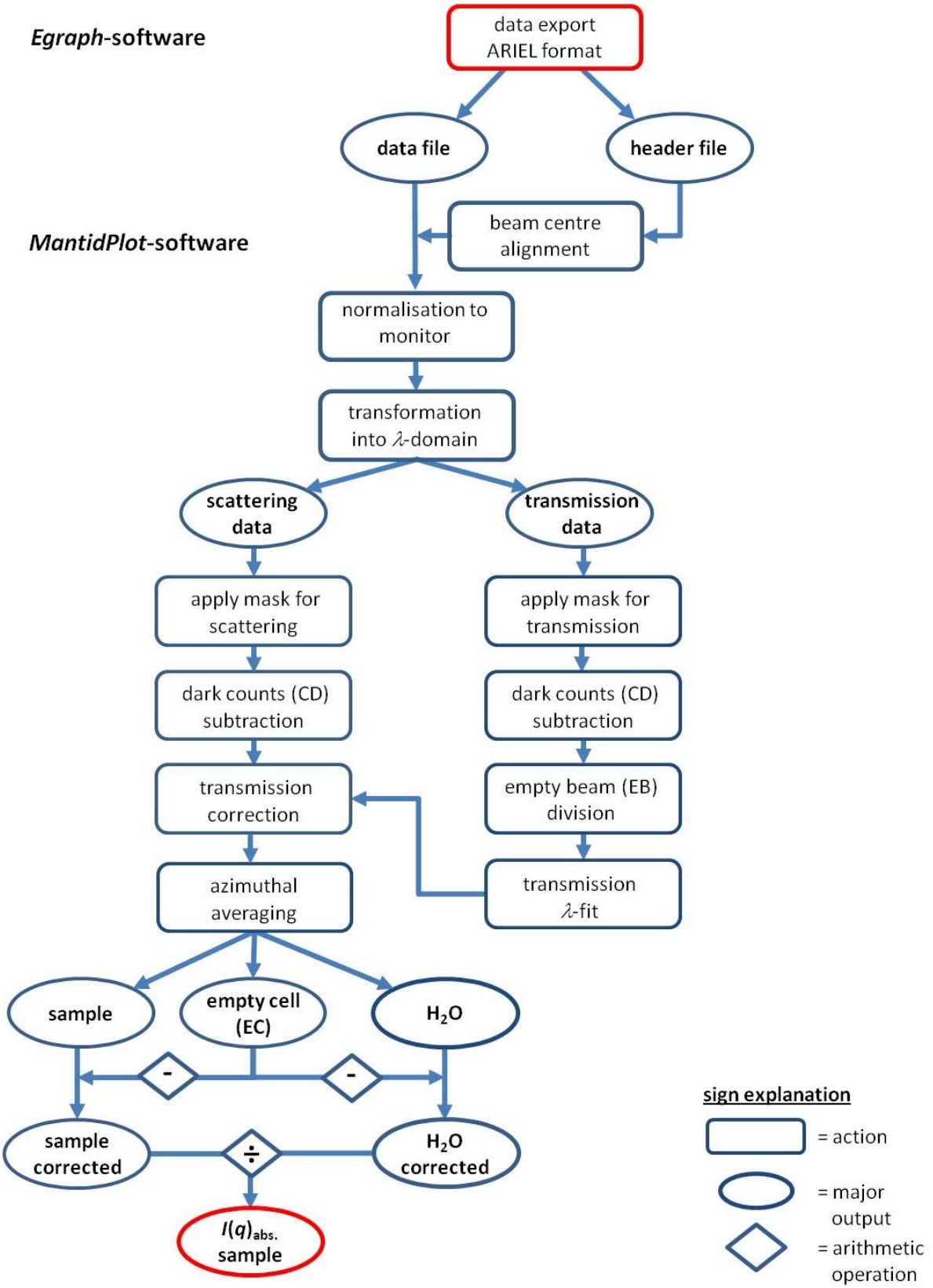


**Fig. 14: Schematic representation of the data treatment of the TOF-SANS data format provided by the *Egraph*-software to yield the absolute calibrated scattering intensities *I*(*q*).**

plots and therefore allows the user an easy access to the obtained data and to the individual steps of the reduction process. Hence, a brief outline trough a common data reduction process will be provided.

For the reduction process certain instrument specific parameters are needed from the instrument file that is commonly used for all measurements of the same set. This file contains for instance information on the detector pixel array. By checking the position of the primary beam from transmission measurements for instance the alignment of this array could be refined, if necessary. Its correct positioning is of high relevance for the azimuthal averaging of the measured scattering intensities as the position of the primary beam defines the origin of the scattering vector. Initially, the summation of the individual TOF spectra recorded by the detector provide a first overview regarding the measurement and the respective data quality. Furthermore, these summed up spectra can be subsequently used for the calculation of the respective transmission values. The measured data are normalised to the monitor counts for the comparison of different sets of data and for the transformation from the time into the wavelength domain. The respective monitor spectrum measured right behind the chopper array at approximately -12.4 m is additionally encoded in the data files. The data sets are rebinned afterwards. Here, a linear or logarithmic binning scheme can be applied within the binning boundaries defined by the user. The summed up spectra from transmission measurements of samples, empty cell, and water are corrected by subtraction of the cadmium spectrum. The transmission as a function of the wavelength is obtained by division of the data sets by the respective set of the empty beam. Due to the lower data statistics, the transmission data are refined by a linear or logarithmic fit algorithm. Individual masks can be applied for the requirements of transmission or respective scattering measurements. For the transmission measurements, just the pixel within the range of ten cells from the centre are considered. Furthermore, an individual wavelength band for the data evaluation can be defined for refinement of the measured scattering data. This can differ from the waveband transmitted by the chopper array, but allows the adaption of the data reduction routine to the scientific issue. The data sets of the scattering measurements are corrected by the wavelength dependent fit of the transmission value and the *Poisson* errors, which are later on used for the calculation of the correct scattering intensities. In the next step, the corrected data sets from the scattering measurements of the empty cell are subtracted from those of the water reference and the sample data sets. This yields the respective corrected scattering intensities as a function of the momentum transfer. Finally, the normalisation to the scattering of a reference sample is done revealing the absolute scattering intensities that can be used for the further analysis. Most of the basic routines are implemented in the *MantidPlot* software and are automatically applied using the respective syntax during the reduction process manually or using the script option.

## 4.5. Reference measurements

To verify the performance of the V16-VSANS instrument, different sets of reference measurements were performed. For this purpose, for instance, a water-soluble polyethylene oxide sample (PEO) was purchased from Polymer Standard Service – Mainz as reference material. The polymer was dissolved in pure $D_2O$ to yield a concentration series with a respective polymer weight fractions $\omega$ of 3 wt%, 2 wt%, 1 wt%, and 0.5 wt%. The samples were measured at a sample detector distance of 6 m and 2 m with a respective collimation of 12 m and 6 m. The corresponding chopper setups were

adjusted to the experimental requirements to yield a $q$-range of 0.12 $nm^{-1} < q < 3.4\ nm^{-1}$. The scattering intensities displayed in Fig. 15 were corrected by the contribution of $D_2O$.

Basic structural parameters of polymer samples, such as the molar mass $M_w$, for instance, the radius of gyration $R_{G,}$ as well as the second and third osmotic virial coefficients, $B_{app}$ and $C_{app}$ are accessible by the *Zimm*-equation (50) [117,133]:

$$\frac{Kc}{R(q,c)} = \frac{1}{M_w} + \frac{R_G\, q^2}{3M_w} + 2B_{app}c + 3C_{app}c^2 + \ldots \tag{50}$$

Here, $K$ is the contrast factor, which scales as a function of $\Delta b$ and the polymer density in solution. The scattering ratio $R(q, c)$ is directly related to the absolute scattering intensity $I(q)$ measured by TOF-SANS. The *Zimm*-equation displays a two-fold dependence of the scattering function on $q^2$ and $c$. Therefore, *Zimm* developed a plot, where $K{\cdot}c{\cdot}R(q, c)^{-1}$ is plotted against $q^2 + k{\cdot}c$, with $k$ being a constant shifting the intensities measured for different polymer concentrations along the $q^2$-axis (Fig. 16). The extrapolation towards $q^2 = 0$ is of particular interest as it represents the dependence of the apparent reciprocal molar mass $M_{w\text{-}app}^{-1}$ on the polymer concentration. It furthermore reveals the influence of the second and third osmotic virial coefficients $B_{app}$ and $C_{app}$ of the dissolved polymer.

The radius of gyration of the investigated PEO sample determined by the *Zimm*-equation is $R_G$ =5.8 ± 0.1 nm. The analysis revealed a weight averaged molecular weight of $M_w$= 12.4 ± 0.1 kg $mol^{-1}$. The reference certificate provided by Polymer Standard Service – Mainz quotes a molecular weight of $M_w(q^2)$ = 13.7 kg $mol^{-1}$ determined by static light scattering. The second virial coefficient was determined to be $B_{app} = 4.3 \pm 0.1{\cdot}10^{-4}$ $cm^3\ mol\ g^{-2}$, which corresponds to a polymer dissolved in a corresponding good solvent.

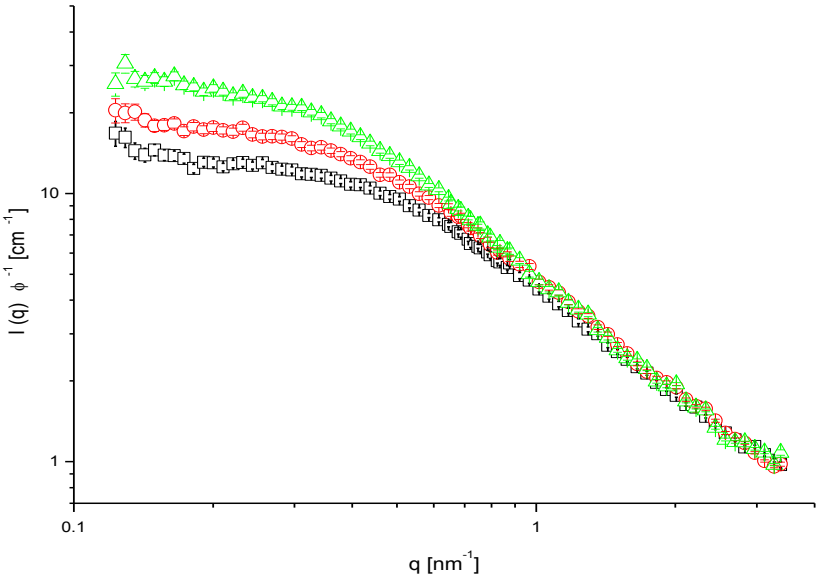


**Fig. 15: TOF-SANS intensities obtained from measurements of a PEO reference sample dissolved in $D_2O$. The measured scattering intensities $I(q)$ were corrected by the contribution of $D_2O$ and normalised by the polymer volume fraction $\phi$ (concentration series: - black squares, 2 wt% - red circles, and 1 wt% - green up triangles). The measurement of polymer solution with $\omega$ = 0.5 wt% was not considered.**

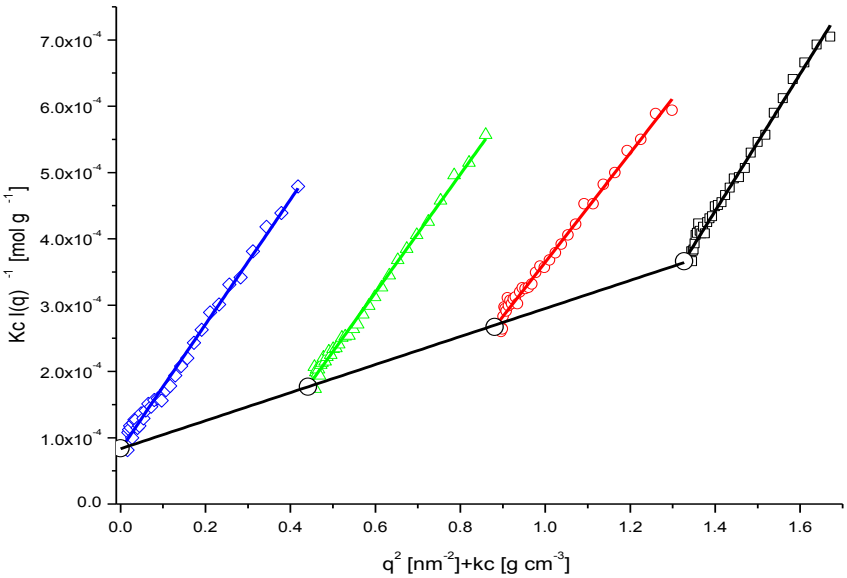


**Fig. 16. *Zimm*-plot obtained from the concentration series of a PEO reference sample. The colour and symbol code was adapted from Fig. 15. The blue diamonds represent the extrapolated scattering intensities to a vanishing polymer concentration. The coloured solid lines represent the fit according to the $q^2$-dependence provided by equation (50). The black open circles represent the extrapolated scattering intensity for $q^2 \rightarrow 0$, which can be used for the determination of $M_w$ and $B_{app}$.**

# 5. Experimental section

## 5.1. Sample preparation

### 5.1.1. Linear polyethylene nanoparticles

The semi-crystalline nanoparticles composed of linear PE were synthesised by Anna Osichow in the group of Prof. Stefan Mecking at the University of Konstanz.

The particles were prepared in a low-temperature emulsion polymerisation procedure employing the nickel complex displayed in Fig. 17 [134]. The PE content of the received nanoparticle dispersion was $\omega_{PE}$ = 2.6 wt%. The dispersion remained stable over months. For the stabilisation of the dispersion, the ionic surfactant sodium dodecylsulfate (SDS) was employed. The dispersion contained $\omega_{SDS}$ = 0.13 wt% of the surfactant and $\omega_{PEG}$ = 0.37 wt% of polyethylene glycol (PEG, $M_w$ = 5000 g mol$^{-1}$) as a further additive. Differential scanning calorimetry (DSC) reveal a crystalline fraction of $\chi_{c\text{-}DSC}$ > 90 % and a melting temperature of $T_m$ = 144 °C. The hydrodynamic properties were analysed by means of DLS and analytical ultra-centrifuge. Details are provided in the appendix. The evaluation of gel permeation chromatography (GPC) measurements revealed a molecular weight of $M_n = 4.2 \cdot 10^5$ g mol$^{-1}$ with a polydispersity of $M_w$ / $M_n$ = $D$ = 1.4. $^{13}$C-NMR analysis demonstrates the almost complete absence of methyl branching with less than one methyl-branch per 1000 carbon atoms. From density measurements of a concentration series the corresponding particle mass density including the adsorbed additives was determined with $\rho$ = 1.0024 ± 0.001 g cm$^{-3}$.

For the contrast variation series analysed by SAXS, the samples were diluted with an SDS containing solution to keep the surfactant concentration constant. The final polymer content was $\omega_{PE}$ = 0.87 wt%. The nanoparticles dispersions and the corresponding background solutions were prepared by the addition of glucose. The prepared mixtures contained sugar weight fractions of 4.5 wt%, 7 wt%, 15 wt%, and 22 wt%. Additionally, PE-nanocrystals dispersed in water were annealed at 100 °C, 115 °C, 125 °C, 130 °C and 150 °C in sealed glass vials for 15 minutes and were studied by SAXS measurements. Those samples had a polymer weight fraction of $\omega_{PE}$ = 2.6 wt%.

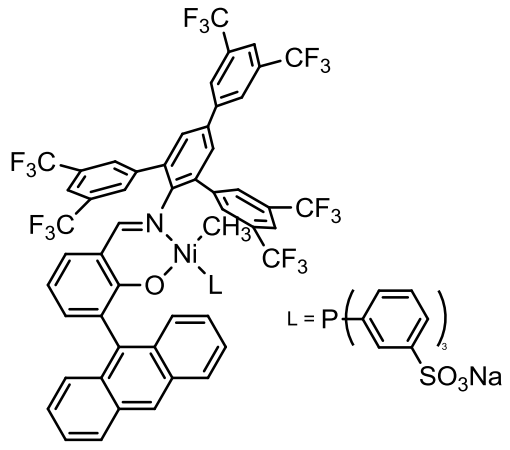


**Fig. 17: Chemical structure of the catalytic active complex salicylaldiminato nickel methyl phosphine TPPTS for the low-temperature synthesis of nascent high order polyethylene.**

For the analysis by TOF-SANS, a different batch of the PE-nanoparticle dispersion with a polymer weight content of $\omega_{PE}$ = 1.9 wt% was employed, as received. The dispersion was diluted with $D_2O$ to yield the final polymer weight fraction of approximately $\omega_{PE} \approx 1$ wt%. Furthermore, the sample contained PEG with $\omega_{PEG}$ = 0.26 wt% and SDS with $\omega_{SDS}$ = 0.39 wt%. Complementary DSC measurements revealed a crystal fraction of $\chi_{C\text{-}DSC} \approx 84$ %.

### 5.1.2. Precisely branched polyethylene nanoparticles

The nanoparticles of well-defined methyl-branched PE were synthesised by Justyna Trzaskowski in the group of Prof. Stefan Mecking at the University of Konstanz.

The received dispersion contained nanoparticles of branched PE carrying precisely placed methyl groups at every 21$^{st}$ carbon. The polymer had been prepared by an acyclic diene metathesis (ADMET) polymerisation of α,ω-diene monomers [46]. The nanoparticles particles formed in a secondary dispersion approach as indicated in Fig. 18 [135]. The dispersions had a total polymer weight fraction of $\omega_{PE}$ = 0.96 wt% and furthermore contained 1.5 wt% of dodecyltrimethylammonium chloride (DTAC) as stabilising surfactant.

For the SAXS-analysis of a contrast variation series, glucose was added to tune the scattering contrast. Thus, the dispersions contained 4.5 wt%, 7 wt%, 15 wt%, and 22 wt% glucose. For a proper background subtraction, solutions with appropriate sugar and surfactant content were prepared and measured under equivalent conditions. Additionally, references with adequate sugar content but without surfactant were analysed.

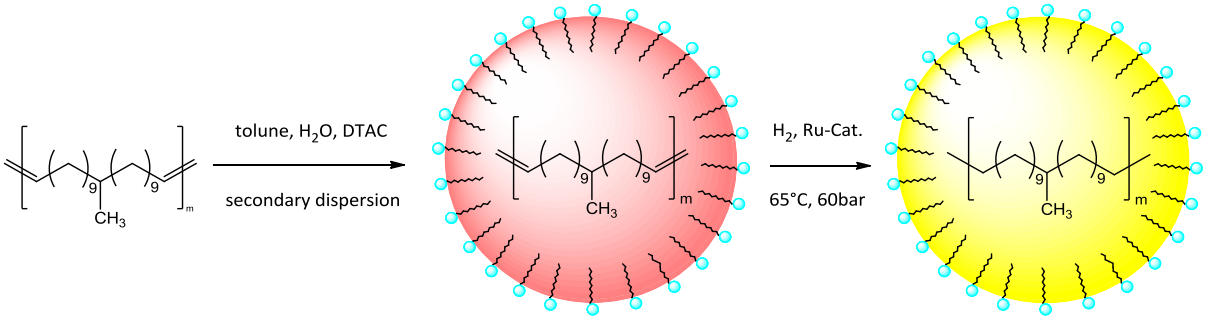


**Fig. 18: Scheme of the preparation of nanoparticles of precisely methyl-branched polyethylene in a secondary dispersion process.**

### 5.1.3. CMS-molecules based on hyperbranched polyglycerol

The core-multishell nanoparticles as well as samples of the hyperbranched polyglycerol were synthesised in the group of Prof. Rainer Haag at the Free University Berlin (FUB).

The received samples of the hyperbranched polyglycerol (hPG) were synthesised following the procedure reported by Paulus [136]. This is based on the protocol introduced by Sunder and co-worker [137,138]. Herein, 1, 1, 1-Trimethylolpropane (TMP) with a molecular weight of $M_{TMP}$ = 134.18 g mol$^{-1}$ was used as initial unit. The monomer unit is represented by glycidol having a corresponding molecular weight of $M_{glycidol}$ = 74.08 g mol$^{-1}$. $^{1}$H and $^{13}$C-NMR were used to analyse the microscopic structure. The GPC-analysis of the investigated sample revealed a molecular weight of $M_W$ = 10.4 kg mol$^{-1}$ with $D$ = 1.85 (solvent: $H_2O$, polymer standard: pullulan). The mass density of the

dispersed polymer was extrapolated in a concentration series to be $\rho$ = 1.253 ± 0.001 g cm$^{-3}$. The purified and lyophilised product was used as received.

The hPG sample was diluted with $H_2O$ for the DLS and SAXS investigations. Here, for the DLS experiments the polymer weight fraction was adjusted to $\omega_{hPG\text{-}DLS}$ < 0.1 wt% and for the SAXS-analysis to $\omega_{hPG\text{-}SAXS}$ ≈ 1 wt%. For the analysis of a concentration series by SANS the polymer was diluted with $D_2O$ to prepare solution containing 3 wt%, 2 wt%, 1 wt%, and 0.5 wt% of the polymer.

The received sample of the CMS-molecules was prepared by the adapted routine reported by Radowski [58]. Here, an hPG molecule was aminised to receive a degree of terminal ammination of approximatly 70 % ($hPG_{10kDA}$ $(\text{-}NH_2)_{0.7}$). The outer double layer was prepared by the reaction of 1, 18-octadecandioic acid with monomethyl-poly(ethylene oxide) having an molecular weight of approximately $M_n$ ≈ 350 g mol$^{-1}$ (mPEG350) and linked to the hyperbranched core (Fig. 2). All the structural investigations were carried out with the purified bulk material from a single batch of CMS-molecules. The macroscopic mass density of the CMS-nanocarriers dispersed in water was determined from a concentration series with $\rho_{CMS\text{-}H2O}$ = 1.111 ± 0.02 g cm$^{-3}$. A corresponding value of $\rho_{CMS\text{-}C7H8}$ = 1.043 ± 0.002 g cm$^{-3}$ was obtained for dispersions containing toluene.

For the preparation of the stock solutions the freeze-dried CMS-particles were dissolved in the respective solvent and stored in the refrigerator over months. The recovery of CMS-molecules from non-polar dispersions was realised from mixtures containing water and a respective evaporation of the organic phase. The reuse of the purified and freeze-dried samples did not change the sample properties. The samples were additionally filtered through membranes with pore size of 100 nm or 200 nm if necessary.

The variation of the scattering contrast in the small angle scattering experiments were realised by dissolving the CMS-structures in sucrose solutions with varying sugar content in the case of SAXS and for SANS in mixtures of water ($H_2O$) and heavy water ($D_2O$) respectively. Additionally contrast variation series were carried out using mixtures of toluene ($C_7H_8$) and toluene D-8 ($C_7H_8$) as non-polar dispersion media. The specific compositions of the dispersions are provided in the corresponding sections of the discussion.

All chemicals and solvents of analytical grade were purchased from respective suppliers and were used as received.

## 5.2. Methods

### 5.2.1. Light scattering

Dynamic light scattering measurements were conducted using the Malvern Zetasizer Nano ZS. The device is equipped with a 50 mW laser operating at $\lambda$ = 532 nm. The instrument allows the determination of the auto-correlation function of the scattered light at $\theta$ = 178° (backscattering mode) and $\theta$ = 12° (forward scattering). The detector signal is processed by a digital correlator unit being able to process intensity correlations down into the nanosecond regime. All measurements were performed in 10 mm quartz cells. The sample was thermostated by a *Peltier* element with $\Delta T$ = 0.1 K. Temperature dependent measurements were performed with steps of 0.5 K or 1 K and an equilibration of at least 10 minutes per step. The obtained data were treated with the CONTIN-

algorithm [139] implemented in the instrument software (version 6.01). For all DLS measurements samples with a total weight fraction of $\omega < 0.1$ wt% were used.

For angular dependent, DLS measurements in the range between 20° < $\theta$ < 150°, an ALV goniometer system was used. It is equipped with a 22.5 mW He-Ne laser emitting a polarised beam at $\lambda$ = 632 nm. The detection system is linked to a Perkin Elmer SPCM-CD2969 photodiode by fibre optics. The signal processing is realised by an ALV – LSE 5004 correlator unit. The correlation functions were treated with the ALV correlator software (version V4.0) using the CONTIN option. For an additional evaluation step of angular dependent measurements a custom-made *C++* - routine implementing the non-linear fit algorithm based on exponential fit functions was employed [140].

### 5.2.2. Density measurements

The density measurements were performed with a Anton Paar density meter DMA 60 with the oscillating U-tube system DMA 602. The temperature was controlled by a thermostat with an external temperature sensor near the sample. The cycle duration of the oscillation was recorded by a custom-made *LabView*-tool and converted into density values using dry air and neat water as references. The extrapolations of the macroscopic mass densities of the samples were done from concentration series.

### 5.2.3. Cryogenic Transmission Electron Microscopy

For cryo-TEM analysis, the aqueous dispersions with a weight fraction of $\omega < 0.1$ wt% were placed on a copper TEM grid. Most of the liquid was removed by blotting paper to leave a thin film. The specimens were vitrified by rapid plunging into liquid ethane and cooled to approximately 90 K. The frozen samples were transferred in a cryo-transfer holder to the Zeiss EM922 OMEGA EFTEM instrument. All examinations were carried out at an acceleration voltage of 200 kV. Zero-loss filtered images ($\Delta E$ = 0 eV) were obtained from reduced dose conditions [141].

### 5.2.4. Small Angle X-ray Scattering – SAXS

The small angle X-ray scattering was measured at the ASAXS beamline at the BESSY-II storage ring in Berlin (Germany) and at the ID02 beamline at the European Synchrotron Radiation Facility (ESRF) in Grenoble (France).

The small angle scattering experiments at the SAXS instrument located at the 7T MPW beam line at the BESSY-II was performed with a 200 x 200 mm² gas detector with a spatial resolution of 200 µm. The photon energy was selected with a silicon (111) double crystal monochromator to 12 keV corresponding to a wavelength of $\lambda$ = 1 Å. Two sample detector distances of 1 m and 3.4 m cover the $q$-range of 0.1 < nm$^{-1}$ $q$ < 4.5 nm$^{-1}$. The acquisition time for every sample and detector position was 10 minutes. As the experiments were run under fine vacuum conditions the samples were enclosed in 2 mm mark tubes purchased by Müller&Müller-Berlin OHG and from Hilgenberg GmbH. For the sake of absolute calibration, the individual sample path length was determined by transmission measurements moving the capillary holder perpendicular to the incident beam. Glassy carbon with a thickness of 90 µm was used as reference for absolute calibration and silver behenate as the

standard for the azimuthal averaging. The data reduction was done with the software package *SASRedTool* developed by Haas [142].

The measurements at the ID02 beamline of the ESRF were performed using the 2D FReLoN Kodak CCD-detector. With a photon energy of 12.5 keV corresponding to a wavelength of $\lambda = 1$ Å and detector positions between 1.2 m and 10 m a $q$-range of 0.01 $nm^{-1} < q < 4.5$ $nm^{-1}$ was accessible. The samples were measured in a tempered polycarbonate flow capillary at 25 °C. The acquisition time per photon shot was 100 µs. For every sample, at least 10 single measurements were performed and averaged during the data reduction process. To prevent radiation damages the sample was automatically pushed through the capillary. The data reduction, including absolute calibration and circular averaging, was directly performed during the measurements by an online data reduction routine. Further data treatment was performed using the software package *SAXSutilities* by Sztucki [143].

### 5.2.5. Wide Angle X-ray Scattering – WAXS

For the wide angle diffraction of dried bulk material the Bruker AXS D8 Advance diffractometer equipped with a copper X-ray tube, emitting the Cu-$\alpha$ line at $\lambda = 1.541$ Å, was applied. The diffraction intensities were measured between 10°< $2\theta$ < 80° in the reflective mode.

The WAXS-intensities of nanoparticles in dispersion was simultaneously measured during the SAXS experiments at the ID02 beam line. The instrument is equipped with an AVIEX PCCD-4284 detector covering the $q$-range between 3.5 < $q$ < 35 $nm^{-1}$.

### 5.2.6. Small Angle Neutron Scattering – SANS

The analyses of the CMS-molecules under different experimental conditions were carried out during beam time at the SANS-II instrument located at the SINQ spallation source of the Paul Scherrer Institute (PSI) in Villigen (Switzerland). The experiment with an overall length of 12 m and a standard pinhole optic is equipped with a $^3$He area-sensitive wire detector developed by the Risø National Laboratory. A velocity selector is used to select the wavelength and the beam is collimated by the individual insertion of six neutron guides. For the 1 m and 5 m detector position a wavelength of $\lambda = 4.5$ Å was used. For reasons of efficiency and to gain the full accessible $q$-range, the wavelength for the 6 m detector position was set to 10.6 Å. For absolute calibration, neat water, and for the subtraction of the dark current, cadmium, were measured in addition [132]. The data reduction was done using the *BERSANS* tool by Keiderling [144].

Contrast variation experiments in aqueous media were carried out at the D11 small angle diffractometer at the Institut Laue-Langevin (ILL) in Grenoble (France). The classical pinhole instrument with a total length of about 80 m is equipped with a $^3$He multi-detector. The sample-to-detector distance can be varied between 1.2 m and 40 m. The movable neutron guides allow the collimation of the neutron beam at 12 discrete distances. The wavelength is selected with a mechanical velocity selector with a spread in wavelength ($d\lambda / \lambda$) of approximately 9 %. For the experiments, a wavelength of $\lambda = 6$ Å was selected and the scattering was measured at 1.2 m, 8 m, and 13.5 m detector position and respective collimation of 8 m, 8 m, and 13.5 m. The data reduction and calibration was done with the tool *LAMP* by Richard et al. offered by the ILL [145]. As calibrating

standards neat water for absolute calibration and cadmium for the background determination were used.

Contrast variation experiments in non-polar media were carried out at the KWS 1 at the FRM II neutron source in Garching. The instrument with pinhole optics has a total length of 40 m and is equipped with a detector system using the Anger principle [119]. The 8x8 photomultiplier array uses a 60 x 60cm$^2$ $^6$Li-glass scintillator with an efficiency > 95% for $\lambda > 4.5$ Å neutrons [146]. A light disperser glass spreads the light produced by a neutron event to an array of 3 x 3 photomultipliers [147]. The collimation is realised by 18 individual neutron guide segments. The wavelength is selected by a Dornier velocity selector with a spread in wavelength of approximately $\Delta\lambda / \lambda \approx 10$ %. For the performed measurements the wavelength was set to $\lambda = 6$ Å. The scattering intensities were recorded at 1.5 m and 8 m detector position and a respective collimation of 8 m. For absolute calibration, vanadium-cross-calibrated Plexiglas and boron carbide for the dark count subtraction were used. The data reduction was performed with the tool *QTIKWS* developed by Pipich [148].

The V16 instrument is located at the BER-II reactor in Berlin. The principle of time of flight, neutron scattering and the essential components of the instrument were introduced in section 4. The measurements were performed using variable wavelength bands from different chopper setups suitable for the experimental requirements. Together with the sample-to-detector distances at 1.2 m and 6 m and the corresponding collimation, the experimental parameter were adjusted to cover the required *q*-range and resolution. The collimation in the standard mode is realised by insertion of up to six neutron guides having an aperture of 40 × 40 mm². The collimation was adapted to the utilised chopper setups and the different sample to detector distances. The data processing was realised by a modified routine of the software *MantidPlot.* For the dark current subtraction and for absolute calibration, respective measurements of cadmium and water were performed. The measurements of water for absolute calibration in the probed *q*-regime was suitable [132]. For the evaluation of the scattering data different bands of wavelengths out of the detected neutron spectrum were used to optimise the data resolution.

All SANS-experiments were carried out at 25 °C in standard Hellma cuvettes type 120 having a path length of 1 mm.

# 6. Results and Discussion

## 6.1. Crystalline polyethylene nanoparticles

The following sections deals with the analyses of PE-nanoparticles which recently attracted attention in the debate on the polymer crystallisation process [25,26,28,30,33]. The isolation of the crystalline phase was one of the major challenges of recent synthetic work. It was realised with the preparation of semi-crystalline particles in the nanometre scale by catalysed emulsion polymerisation. An excellent approach for a comprehensive structural analysis of the PE-nanoparticles is the combination of imaging techniques, such as TEM and cryo-TEM, for instance, and scattering methods like SAXS and SANS, as well as WAXS.

### 6.1.1. Crystalline nanoparticles of linear polyethylene

Nanoparticles composed of linear PE were synthesised by an emulsion polymerisation process [134]. As demonstrated in the schematic illustration in Fig. 19 the Ni-complex is activated by the absorption of ethylene at increased pressure. Hence, the catalyst becomes lyophilic and needs to be stabilised by SDS surfactant molecules in the aqueous dispersion. The synthesis was carried out at 10 °C, which requires the addition of ethylene glycol for stabilisation. Furthermore, the addition of polyethylene glycol ($M_{w\text{-}PEG} \approx 5$ kg mol$^{-1}$) disables the formation of ethylene glycol superstructures. It is supposed to stabilise the emulsion during the polymerisation at low temperatures. It could not be removed during the purification by dialysis.

The nanoparticle morphology was studied by cryo-TEM from highly diluted dispersions (refer to section 5.2.3). The representative micrographs shown in Fig. 20 display particles with a facetted shape in different orientations to the electron beam (Fig. 20 a) ) revealing the platelet-like character of the nanoparticles. The single particle shown in Fig. 20 b) is oriented planar to the incident beam, so that the top of the platelet is visible. The particle shape underlines the discussion on the growth of the nanocrystals as provided by Weber and co-worker [30]. The truncated lozenge shape is thus a rather late state of the crystal growth compared to the lozenge shape of macroscopic PE-crystals [149,150,151,152]. Furthermore, particles with an almost rectangular shape indicate the presence of monoclinic crystallites. The narrow rod-like shape illustrated in Fig. 20 c) can be associated with particles whose planar orientation is perpendicular to the direction of the probing beam. The light amorphous material topping the dense crystalline phase could not be visualised by cryo-TEM. It is contrast matched by the vitrified ice of the dispersions medium [153]. The statistical evaluation of

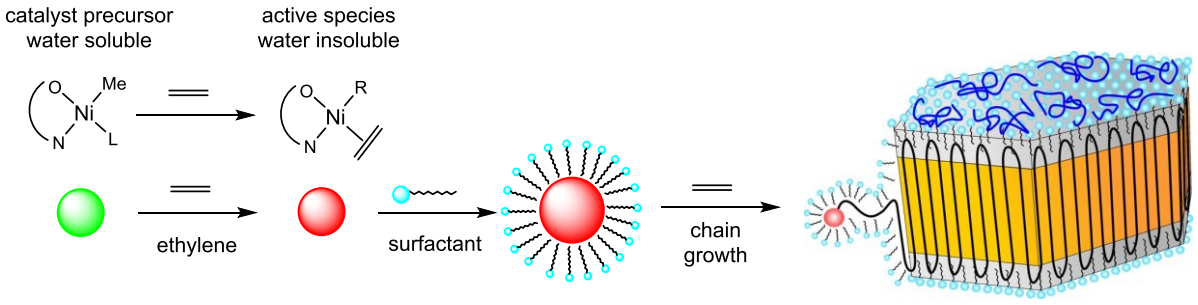


**Fig. 19: Schematic drawing of the formation of nanoparticles of linear PE by the catalytic active Ni-complex.**

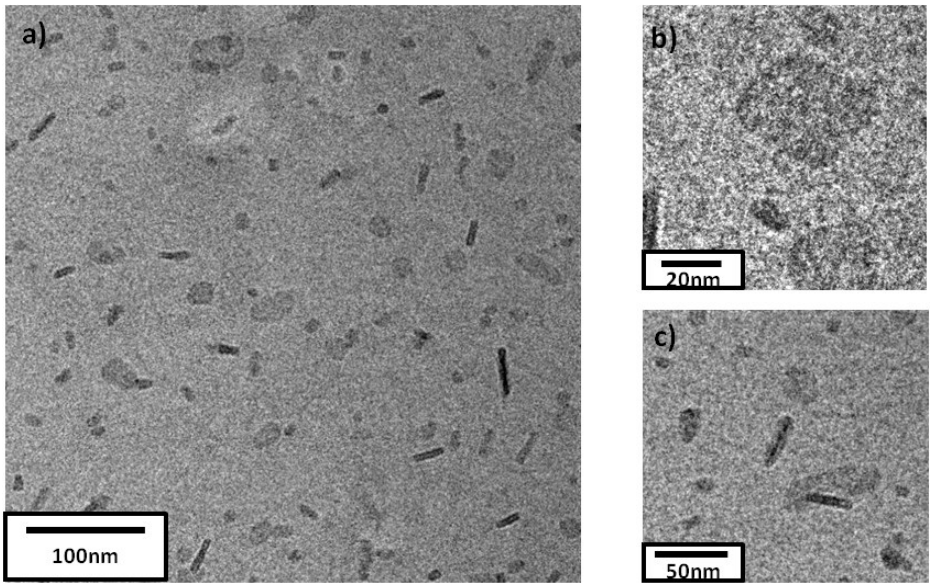


**Fig. 20: a) Cryo-TEM micrograph of semi-crystalline PE-nanoparticles. b) The magnification shows the top view of the facetted platelets. c) The detail shows the respective side view. The amorphous phase is not visible due to contrast match conditions t.**

cryo-TEM micrographs should be regarded with caution in the case of anisotropic particles. The random orientation of the particles towards the probing beam can impede the correct determination of the particle dimensions. The particle diameter was found to be approximately 20 nm having a likewise bimodal distribution, whereas the lateral dimension of the platelets is around 6 nm. Moreover, the investigated cryo-TEM micrographs reveal a certain polydispersity of the investigated sample.

The measurements of the particle small angle X-Ray scattering were performed at the ID02 beamline at the ESRF in Grenoble (France). In the respective contrast variation series, glucose was used as contrast agent for increasing the electron density of the dispersion medium. The particle concentration was decreased to $\omega_{PE} < 1$ wt % to reduce the influence of inter-particle interactions that are assigned to repulsive forces caused by the adsorbed surfactant molecules at the particle surfaces [30,33]. The compositions of the measured samples are provided in Tab. 1.

The SAXS-intensities obtained from the PE-nanoparticles dispersions were corrected from the contribution deriving from the dispersion media. This was realised by the subtraction of the scattering intensities of the respective sugar solutions with consideration of the nanoparticle volume fraction $\phi_{PE}$ according to [103]:

$$I(q) = I_{dispersion}(q) - (1-\phi)\, I_{solvent}(q) \tag{51}$$

The corrected scattering intensities solely deriving from the PE-nanoparticles are represented by the open symbols depicted in Fig. 21. The evaluation of the forward scattering intensities revealed a non-negligible influence of inter-particle correlations. This was concluded from the two regimes found for the slope of the linearised scattering intensities, which were analysed with the *Guinier*-relation provided by equation (14). Therefore, essential parameters like the particle volume $V_P$ and the particle average scattering length density $b_P$ could not be extrapolated with the needed accuracy. As a consequence the decomposition of the scattering intensities as a function of the scattering contrast as designated by equation (23) could not be realised.

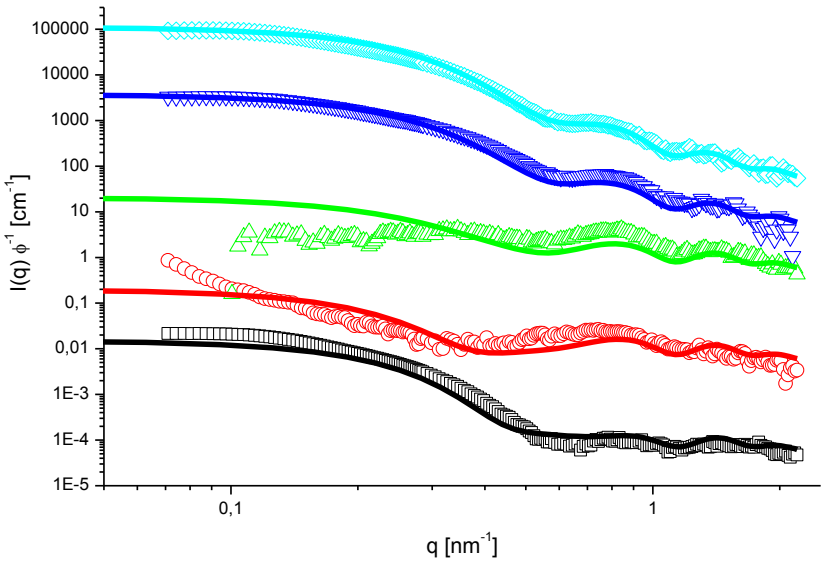


**Fig. 21: SAXS-intensities normalised by $\phi$ as obtained from a contrast variation series of PE-nanoparticle dispersions using glucose as contrast agent. The scattering intensities were corrected by the scattering contributions of the dispersion media. From bottom to top the sugar content was increased (0 wt% - black squares, 4.5 wt% - red circles, 7 wt% - green up triangles, 13 wt% - blue down triangles, and 22 wt% - cyan diamonds). The fits utilising the particle scattering factor provided by equation (53) are represented by the solid lines. For reason of clarity the curves are shifted vertically from bottom to top by $10^{-3}$, $10^{-1}$, 10, and $10^{3}$.**

**Tab. 1: Overview on the samples composition and corresponding $b_m$ used for the contrast variation series with nanoparticles composed of linear PE.**

| $\omega$ glucose | $\omega$ PE | $\phi$ PE | $b_m$ | $\rho_m$ |
|---|---|---|---|---|
| wt% | wt% | | $10^{10}$cm$^{-2}$ | g cm$^{-3}$ |
| 0 | 0.87 | 0.0090 | 9.42 | 0.9974 |
| 4.5 | 0.87 | 0.0096 | 9.55 | 1.0164 |
| 7 | 0.87 | 0.0097 | 9.63 | 1.0315 |
| 15 | 0.87 | 0.0097 | 9.91 | 1.0503 |
| 22 | 0.87 | 0.0098 | 10.16 | 1.0503 |

The particle scattering factor used for the analysis of the corrected SAXS-intensities is expressed by equation (53) [33]. It represents a platelet-like body carrying two topping layers on each side as this is illustrated in Fig. 22.

$$I_0(q) = \int_0^1 F^2(q,x)\,dx \tag{52}$$

$$F(q,x) = 2\pi R \frac{J_1\left(qR\sqrt{1-x^2}\right)}{q\sqrt{1-x^2}} \left( \Delta b_{SDS/PEG} \frac{\sin\left(\frac{qxL}{2}\right)}{\left(\frac{qx}{2}\right)} + \Delta b_a \frac{\sin\left(\frac{qxL_a + L_c}{2}\right)}{\left(\frac{qx}{2}\right)} + \Delta b_c \frac{\sin\left(\frac{qxL_c}{2}\right)}{\left(\frac{qx}{2}\right)} \right) \tag{53}$$

Here, $R$ is the particle radius, whereas $L$ is the corresponding overall height. The platelet-like character is described by the first order cylindrical *Bessel* function $J_1$. The thickness of the crystalline phase is denoted by $L_c$ and this of the amorphous layer $L_a$, respectively. The outermost layer contains the adsorbed surfactant molecules stabilising the particles. The thickness of the SDS / PEG layer is respectively calculated from the overall height of the platelets and the heights of the two other phases. The appropriate scattering contrasts are represented by $\Delta b_{SDS/PEG} = b_{SDS} - b_m$ for the outermost shell, $\Delta b_a = b_a - b_{SDS/PEG}$ for the amorphous layer, and $\Delta b_c = b_c - b_a$ for the crystalline phase. All dimension parameters were analysed employing *Gaussian* distribution functions.

From the contrast variation series these structural parameters could be calculated using a global fit routine. A bimodal *Gaussian* distribution of the particles' mean radius served for the calculation of the fits depicted in Fig. 21. The applied distribution was developed according to the bimodal distribution found by measurements of the hydrodynamic radii using an analytical ultracentrifuge [154]. The corresponding data (Fig. S 1) are provided in the appendix. The two centres of the distribution were found at $R_1 \approx 5.4$ nm and $R_2 \approx 8.4$ nm. The thickness of the crystalline phase was fitted with $L_c = 8.8 \pm 1$ nm and the corresponding scattering length density was determined with $b_c = 9.57 \cdot 10^{10}$ cm$^{-1}$. This refers to a macroscopic density of the crystalline phase of $\rho_c = 0.991$ g cm$^{-3}$. The thickness of the topping amorphous layer having a scattering length density of $b_a = 8.50 \cdot 10^{10}$ cm$^{-2}$ was calculated with $½L_a = 1.1 \pm 0.5$ nm. The scattering length density correlates with a macroscopic packing density of $\rho_a = 0.880$ g cm$^{-3}$. The density values correspond to those determined by Rochette [33]. The outermost layer has a thickness of $½L_{SDS/PEG} = 0.7 \pm 0.1$ nm and a corresponding scattering length density of $b_{SDS/PEG} = 11.20 \cdot 10^{10}$ cm$^{-2}$. From the calculated dimensions of the phases by volume the crystallinity could be determined to be $\chi_{C\text{-}SAXS} = 83$ %.

The estimation of the average molecular weight of the nanoparticles by equation (28) was accomplished using the fitted scattering intensities. Comparing the molecular weight of the nanoparticles with the one determined by GPC ($M_{w\text{-}GPC} = 5.9 \cdot 10^5$ g mol$^{-1}$) demonstrates that the PE-nanoparticles are formed in average by two polymer chains at the most. Together with virtual absence of branching along the polymer backbone, the nanoparticles are nearly free of defects, leading to a well-behaved crystallisation of the PE-chains.

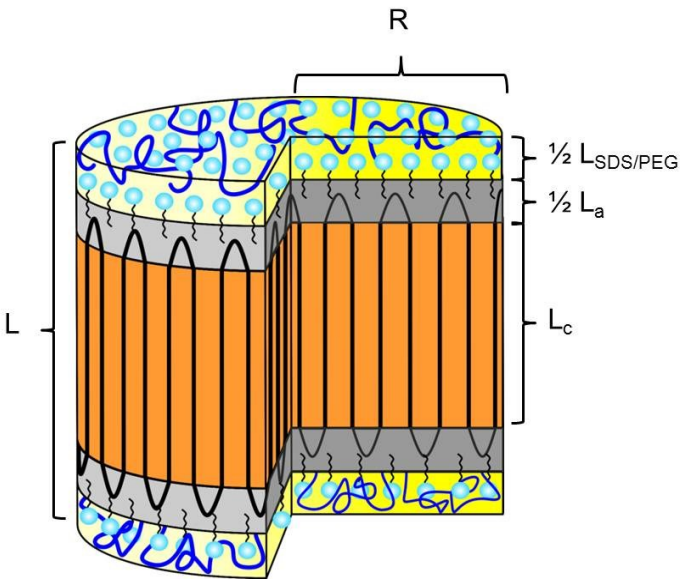

**Fig. 22: Scheme of the cylindrical platelet model with two topping layers on each side.**

## Analysis by TOF-SANS measurements

Further analysis of the spatial structure of the PE-nanocrystals was performed with TOF-SANS measurements. The sample investigated by neutrons scattering was synthesised under equivalent experimental conditions as used for the sample studied with X-rays. The nanoparticle dispersion was diluted with $D_2O$ to tune the scattering contrast. Thus, the final polymer weight fraction was approximately $\omega_{PE} \approx 1$ wt%. The corresponding scattering length density of the dispersions medium was calculated with $b_m = 2.75 \cdot 10^{10}$ cm$^{-2}$. The measured scattering intensities were corrected by the scattering contribution of an appropriate mixture of $D_2O$ and $H_2O$ employing equation (51). This yielded the SANS intensities displayed by the open symbols in Fig. 23. The data were modelled employing the platelet model provided by equation (53). The thickness of the crystalline phase was

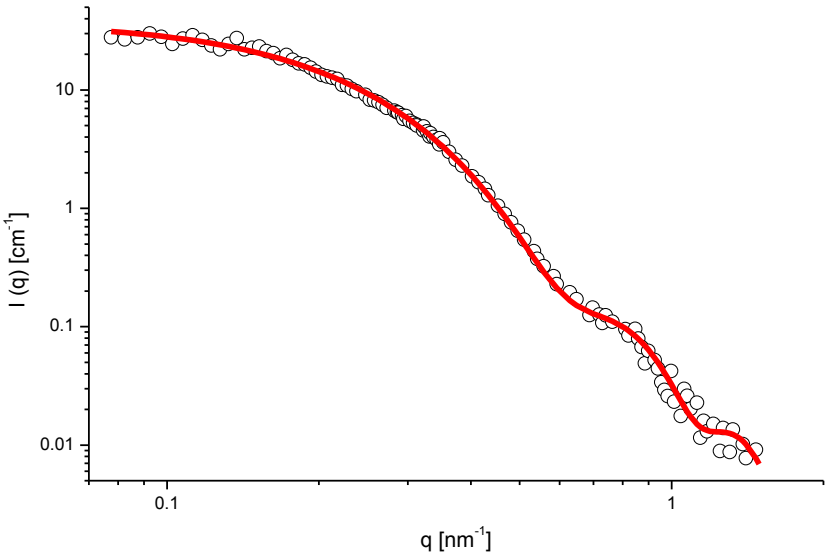


**Fig. 23: TOF-SANS intensities obtained from a dispersion of crystalline nanoparticles composed of linear PE. The solid line represents the result of the fit according to equation (53).**

**Tab. 2: Overview on the parameters used for the analyses of PE nanoparticles by SAXS and SANS measurements. *) A bimodal *Gaussian* distribution for *R* was applied. **) The sample was taken from different synthetic batch.**

| | | SAXS* | SANS** |
|---|---|---|---|
| $R$ | nm | $R_1 \approx 5.4$<br>$R_2 \approx 8.4$ | 5.7 ± 2.3 |
| $L_c$ | nm | 8.8 ± 1 | 7.8 ± 1 |
| ½ $L_a$ | nm | 1.1 ± 0.5 | 1.1 |
| ½$L_{SDS/PEG}$ | nm | 0.7 ± 0.1 | 1.0 |
| $b_c$ | $10^{10}$ cm$^{-2}$ | 9.57 | -0.33 |
| $b_a$ | $10^{10}$ cm$^{-2}$ | 8.50 | -0.31 |

| | | | |
|---|---|---|---|
| $b_{SDS/PEG}$ | $10^{10}$ cm$^{-2}$ | 11.20 | 0.49 |

fitted with $L_c$ = 7.8 ± 1 nm and the corresponding scattering length density was determined with $b_c$ = -0.33·$10^{10}$ cm$^{-2}$. The fit represented by the solid red line in Fig. 21 was calculated using a particle mean radius of $R$ = 5.7 ± 2.3 nm. Here, a monomodal *Gaussian* distribution for $R$ served for the calculation. This value correlates with a macroscopic density of the crystalline phase being $\rho$ = 0.991 g cm$^{-3}$, which is the same as used for the evaluation of the SAXS data (Tab. 2). The thickness of the amorphous layer having a scattering length density of $b_a$ = -0.31·$10^{10}$ cm$^{-2}$ was determined with ½$L_a$ = 1.1 nm. The amorphous structure is thus related to a corresponding macroscopic density of $\rho$ = 0.880 g cm$^{-3}$, which is similar to the results obtained by SAXS (Tab. 2). The difference between scattering length densities of the amorphous and the crystalline phase thus results only from the different packing densities of the PE-chains. The topping layer containing SDS and PEG has a thickness of ½$L_{SDS\,/\,PEG}$ = 1.0 nm. As corresponding scattering length density $b_{SDS\,/\,PEG}$ = 0.49·$10^{10}$ cm$^{-1}$ was used [155]. Consequently, the crystallinity could be estimated from the dimensions of the specific phases by volume by approximately $\chi_{C\text{-}SANS}$ ≈ 78 %.

## Analysis of WAXS measurements

Furthermore, the structure of the PE-nanoparticles was examined by WAXS measurements from a precipitated sample. The observed scattering intensities are related to the inter-planar spacing between the crystallographic planes within the crystallite. This is expressed by the modified *Bragg*-equation (54) [113].

$$d = \frac{n\lambda}{2\sin\theta} = \frac{2\pi}{q} \tag{54}$$

Here, $d$ represents the distance between the atomic planes and $n$ is the order of the observed reflection. The diffraction intensities of the major reflections are shown in Fig. 24. An additional overview on the observable reflections is provided in Tab. 3. The major reflections at $2\theta$ = 21.4° and $2\theta$ = 23.8° were ascribed to orthorhombic PE [156]. The diffraction signal at $2\theta$ = 19.42° refers to the monoclinic PE modification [157]. This modification was reported for samples of mechanically strained PE or for samples having an ultra-high molecular weight (UHMW) [158,159,160,161,162]. The analysis of the diffraction pattern followed the procedure reported by Russell [159,163] and is illustrated in Fig. 24. The scattering intensities were decomposed into the contributions of the orthorhombic (long dashed, cyan coloured line) and monoclinic (solid green line) PE crystal modification. The diffraction intensities were fitted using *Gaussian-Lorentzian* profiles and their respective summation lead to the scattering intensities represented by the solid red line. The determination of the crystal fraction considers an amorphous phase (dashed blue line) represented by a broad signal below the reflections of the crystalline domains. Here, the maximum of the amorphous halo was located at $2\theta$ = 19.7° [161]. The determination of the crystal fraction and the correlating purpose of the amorphous phase has also been the subject of intensive discussions in the literature over years [163,164,165,166]. The analysis of the WAXS-intensities reveals a crystallinity of $\chi_{C\text{-}WAXS}$ = 86 %, whereby the total crystal fraction contains 14 % of the monoclinic PE modification. As a consequence of the low-temperature emulsion polymerisation of ethylene utilising the recent Ni-catalyst, the monoclinic crystal structure can be observed with nanoparticles of average molecular weight PE (refer to chapter 5.1.). This observation has not been reported for PE-nanoparticles to

date. One reason for this can be attributed to the mechanical strain from the rapid crystallisation of the polymer chain during the nanoparticle formation.

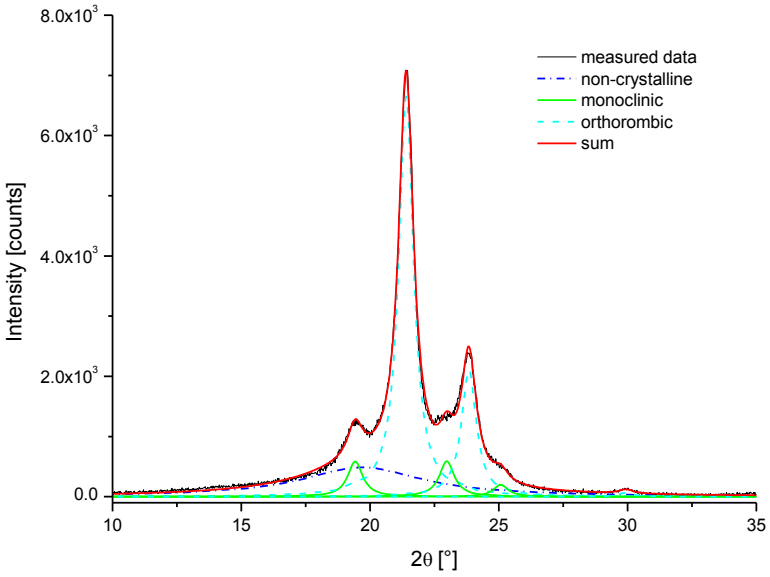


**Fig. 24: WAXS-intensities of PE-nanoparticles measured as precipitated sample. The plot illustrates the decomposition of the diffraction signal into contribution of orthorhombic (dashed cyan coloured line) and monoclinic (solid green line) PE [159,163]. An additional signal of the amorphous phase (dashed blue line) was fitted as a broad halo signal. The red line represents the summation of the different contributions [161].**

**Tab. 3: Position and relative intensities for the observed WAXS-signals from precipitated crystalline nanoparticles of linear PE.**

| $2\theta$ | $d_{exp}$ | relative intensity |
|---|---|---|
| ° | Å | % |
| 19.42 | 4.57 | 19 |
| 21.40 | 4.15 | 100 |
| 23.82 | 3.73 | 35 |
| 29.92 | 2.98 | 4 |
| 36.18 | 2.48 | 5 |
| 39.76 | 2.27 | 5 |
| 40.52 | 2.23 | 5 |
| 41.40 | 2.18 | 5 |
| 43.06 | 2.10 | 5 |
| 46.68 | 1.94 | 3 |
| 52.60 | 1.74 | 3 |
| 54.90 | 1.67 | 2 |
| 57.02 | 1.61 | 2 |

Wide angle powder diffraction reveals only an average of the existing crystalline units within the investigated sample. One method of gaining insight into the specific crystal structure is single crystal diffraction [113]. Unfortunately, it is not the method of choice for the analysis of isolated PE-nanocrystals, since the technique is limited by the size of the investigated sample. To overcome this problem, TEM-analysis accompanied with selected area electron diffraction (SEAD) experiments from assorted regions of a dried nanoparticle dispersion were performed [167]. Due to the fast appearance of radiation damages and amorphisation of the particles, it was only possible to probe the sample using short-time exposures illuminating large sample areas. These observations must be ascribed to the high-energy input caused by the probing electron beam. Hence, the differentiation between nanoparticles having either a monoclinic or an orthorhombic lattice structure was not successful. The weak diffraction signals did not reveal the monoclinic crystal structure of the PE sample, but confirmed the orthorhombic modification. Therefore, the monoclinic PE appears to be rapidly converted into the stable orthorhombic modification by just the thermal energy of the probing electrons.

## Analysis of annealed samples by SAXS measurements

The morphological changes due to the annealing of the PE-crystallites were studied by respective SAXS measurements. The samples of the annealing series having a polymer weight fraction of $\omega_{PE}$ = 2.6 wt% were tempered for 15 minutes in sealed tubes. It was shown by Davis and colleagues that the major morphological changes take place within the first minutes of the temperature treatment [168]. Hence, the nanoparticles were completely converted to the thermodynamic equilibrium morphology during the exposure. Formula (51) served for the background correction of the SAXS-intensities, which are represented by the open symbols in Fig. 25. The data were fitted using the model provided by equation (53) describing the platelet-like shape and layered microstructure of the PE-nanoparticles. This approach refers to non-interacting particles and is represented by the dashed lines in the corresponding plot. In contrast to the dispersions used for the contrast variation series the polymer weight fraction used for the annealing series was approximately threefold higher. This becomes obvious especially for small magnitudes of the scattering vector, where the scattering intensities significantly deviate from the model. This is ascribed to the repulsive, electrostatic interactions between the platelets [30,33]. The pair correlation of the dispersed nanoparticles is comparable to the one of hard spheres having a repulsion radius of $R_{HS}$ = 18.8 nm and can be associated with the counter ion diffusive layer around the platelets. Steric interactions between the platelets are seen to have a minor influence at low particle concentrations [33]. This can be deduced from earlier reports to the influence of the particle structure factor for dispersions of the platelet-like stilbenoid dendrimers [111] and other platelet-like structures [169,170]. The influence of the inter-particles correlations is considered by the fits represented by the solid lines in Fig. 25.

The fitted SAXS-intensities reveal substantial morphological changes of the PE-nanoparticles due to the temperature treatment. An overview on the parameters used for fitting the data of the annealing series is provided in Tab. 4. The evaluation reveals a thickening of the crystalline phase until the annealing temperature of 115 °C. Here, $L_c$ increases from $L_c$ = 8.8 ± 1 nm for native PE-nanoparticles over $L_c$ = 11.5 ± 1 nm for nanoplatelets annealed at 100 °C to $L_c$ = 13.7 ± 1 nm at 115 °C. The scattering length density of the crystalline phase at 100 °C and 115 °C was fitted with

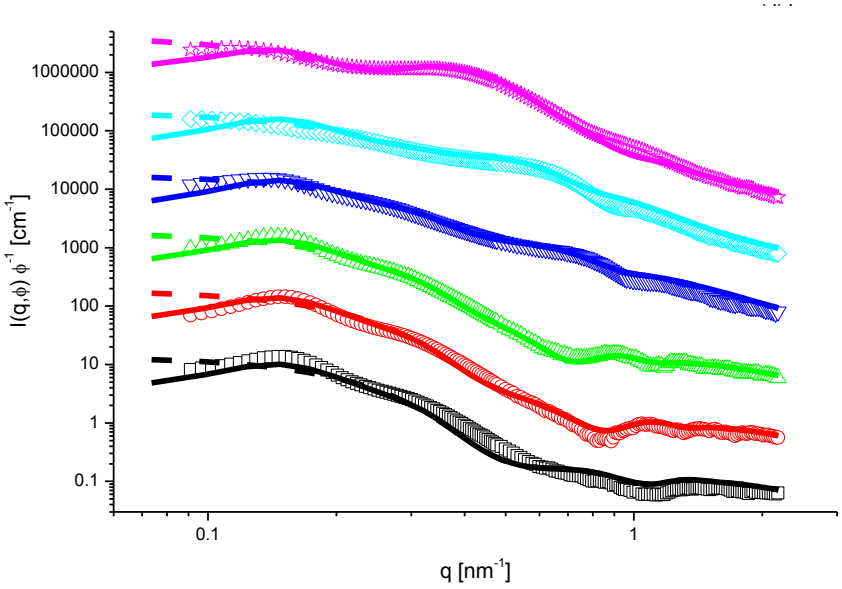


**Fig. 25: SAXS-intensities normalised by $\phi$ as obtained from annealed nanoparticles composed of linear PE. From bottom to top the annealing temperature was increased (black squares no temperature treatment, red circles : 100 °C, green triangles : 115 °C, blue triangles : 125 °C, cyan diamonds : 130 °C, and magenta stars : 150 °C). The five intensities corresponding to the annealed samples were shifted upwards by the factor of $10^1$, $10^2$, $10^3$, $10^4$, and $10^5$. The dashed lines correspond to the fits according to equation (53) assuming no inter-particle correlation, the solid lines represent the calculated scattering intensities including repulsively interacting particles.**

**Tab. 4: Structural parameters of the PE-nanocrystals as derived from the fitted scattering intensities as shown in Fig. 25. The corresponding scattering length density of the amorphous PE-layers was $b_c = 8.50 \cdot 10^{10}$ cm$^{-2}$, whereas for the SDS / PEG layers $b_{SDS/PEG} = 11.20 \cdot 10^{10}$ cm$^{-2}$ was used. The respective standard deviation of the *Gaussian* size distributions is 1 nm for $L_C$ and 0.5 nm for $L_a$. These parameters were assumed to be independent of the annealing temperature.**

| T | $L_c$ | $L_a$ | $b_c$ |
|---|---|---|---|
| [ °C] | [nm] | [nm] | [$10^{10}$ cm$^{-2}$] |
| 25 | 8.8 | 2.1 | 9.57 |
| 100 | 11.5 | 2.1 | 9.57 |
| 115 | 13.7 | 2.1 | 9.57 |
| 125 | 7.8 | 3.2 | 9.76 |
| 130 | 8.5 | 4.4 | 9.76 |
| 150 | 9.8 | 16.0 | 9.57 |

$b_c = 9.57 \cdot 10^{10}$ cm$^{-2}$. The thickness of the amorphous phase was observed as remaining constant. As for the native PE-particles, a thickness of $½L_a = 1.1 \pm 0.25$ nm was found. This value indicates a rather thin phase, although, as already outlined before, a significant contribution arises from the aliphatic tail groups of the adsorbed SDS molecules. This notwithstanding, a well-defined re-entry of the PE-chains back into the crystalline domain by the formation of tight loops can be deduced. Theoretical studies on the structure of the amorphous phase have been reported by different authors

[171,172,173,174,175,176]. They claimed that the chain fold and re-entry can be realised by just a few repeating units and, therefore, a rather thin amorphous phase is formed. The thermal treatment enhances the polymer diffusion within the crystallite yielding the thermodynamically favoured state. Thus, the loops within the amorphous phase act as guide rollers, allowing the polymer chains to glide along each other during the thickening of the particles, as illustrated in Fig. 26. The size distribution of $R$ had to be adapted for the particle thickening as the scattering volume of the dispersed PE-particles is constant. A further increase of the annealing temperature to 125 °C leads to a shrinking of the crystalline phase to $L_c = 7.8 \pm 1$ nm, whereas the thickness of the amorphous phase increases to $½L_a = 1.6 \pm 0.25$ nm. For the respective dispersion annealed at 130 °C the height of the crystalline phase increases to $L_c = 8.5 \pm 1$ nm. For the amorphous layer, $½L_a = 2.2 \pm 0.25$ nm was found. According to these values, an additional increase of the amorphous phase by a factor of about two reveals a significant shrinking of the size of the ordered domain. The annealing at 125 °C and 130 °C is accompanied by an increase of the corresponding scattering length density to $b_c = 9.76 \cdot 10^{10}$ cm$^{-2}$. The increase of $b_c$ is directly related to an increased density of the crystalline phase as the composition of the incorporated material is not changed. The increase of the macroscopic density of PE-samples during annealing was reported by Davis and was assigned to a contraction of the crystal unit cells [168]. The increase of the amorphous fraction is supposed to be accompanied by the formation of entanglements between the chains re-entering the crystalline stem. Moreover, the adsorbed additives can be incorporated into the disordered domain. As a result, the unaffected diffusion of the PE-chain within the crystallite is not preserved and the lamella thickening does not follow the thermodynamic predictions.

The SAXS-intensities of a dispersion annealed at 150 °C, which is above the melting temperature of the PE- nanocrystallites, were measured additionally. The corresponding fit parameters of the platelets were $L_c = 9.8 \pm 1$ nm and $½L_a = 8 \pm 0.25$ nm. For the scattering length density for the crystalline phase $b_c = 9.57 \cdot 10^{10}$ cm$^{-1}$ was used to model the scattering intensities. The recrystallisation of the nanoparticles leads to a significant increase of the amorphous domain and a consequent loss of crystallinity. Furthermore, the calculated particle dimensions could result from a fusion of individual nanoparticles in the molten state.

Furthermore, the lamella thickening was analysed with respect to the thermodynamic properties of PE. Important work on this topic has been done by Strobl [12,15,177]. His studies cover the relation between the annealing temperatures of polymer crystallites and the corresponding crystal thickness.

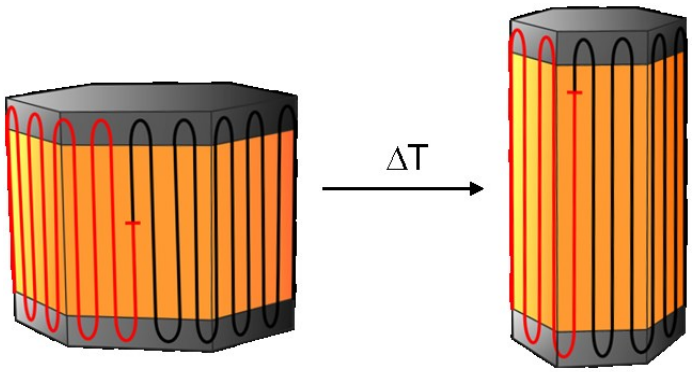


**Fig. 26: Scheme of the mechanism of the lamella thickening with the amorphous phase acting as "guide pulley" for the adjacent re-entry of the polymer chains.**

Hereby, the thickening due to a temperature treatment leads to the equilibrium crystal thickness that is related to the surface free energy of the crystallites. From this correlation the melting and crystallisation properties of PE crystallites with respect to the crystal thickness can be determined by the *Gibbs-Thomson* equation [12,177]:

$$T_m = T_m^{\infty}\left(1 - \frac{2\sigma^*}{\Delta H_{Surf} L_C}\right) \tag{55}$$

The value $L_C$ demonstrates the thickness of the crystalline lamella, whereas $T_m$ is the melting temperature and $\Delta H_{surf}$ the heat of fusion. The equilibrium melting temperature of PE-crystals of infinite size was determined by Wunderlich to be $T_m^{\infty}$ = 141.5 °C [178]. The value of $\sigma^*$ represents the surface free energy of the planes hosting the folded polymer chains. In the case of particles with a large lateral dimension, $\sigma^*$ becomes a function of the interfacial tension between the solvent and the amorphous polymer domain [179,180]. The plot in Fig. 27 illustrates the *Gibbs-Thomson* relation. Here, the red symbols represent the inverse lamella thicknesses obtained for the PE-nanoparticles analysed herein. The results reported by Rochette are indicated by the blue symbols [33]. For purposes of comparison, the predicted melting line for PE bulk material by Strobl is shown by the dashed line [177]. The slope of the correlation between $T$ and $1 / L_C$ is related to the surface free energy. Thus, the nanoparticles embodying higher order display a higher $\sigma^*$ (solid red line) than reported for the PE-nanocrystals investigated by Rochette et al. (solid blue line) [33]. This is due the absence of chain branching of the PE forming the high ordered crystallites discussed herein. The molecular stiffness and free energy needed for the stabilisation of amorphous loops increases with the degree of branches, which consequently limits the bending and rotation of the polymer

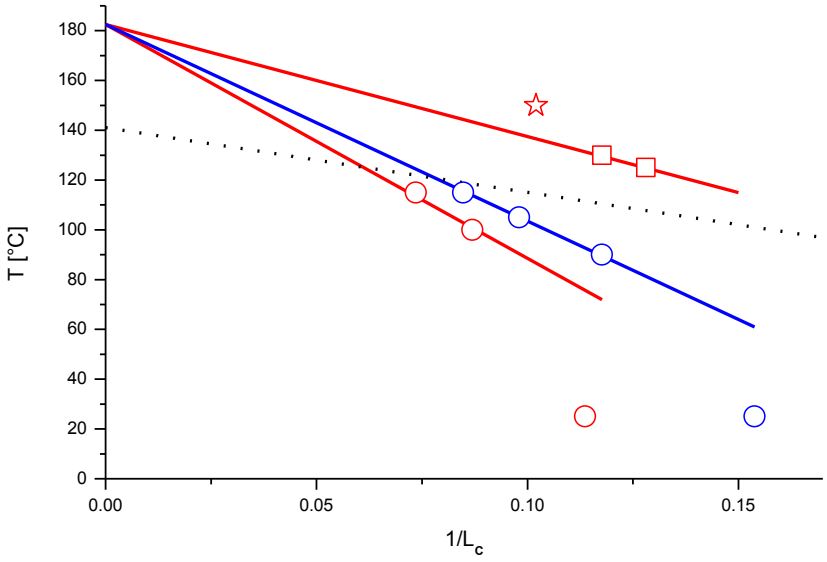


**Fig. 27: Variation of the crystal thickness as consequence of the annealing of the PE-nanoparticles at different temperatures (red symbols). The circles represent samples below the predicted melting line (dashed line) for PE-bulk material [177]. Respectively, samples above are provided by open squares. The red star corresponds to the sample tempered at 150 °C being above the melting temperature of the nanocrystals determined by DSC. For comparison the data from previous studies are shown (blue symbols) [33].**

backbone. The lowest annealing temperatures (circles) are located below the theoretical melting line, whereas the values of $1 / L_C$ observed for PE-nanoparticles annealed at 125 °C and 130 °C are located above (squares). Unfortunately, Rochette does not provide any data on the respective crystal thicknesses above 115 °C for comparison. The extrapolation represented by the solid lines in Fig. 27 leading to $T \approx 182$ °C correspond to infinitely long polymer chains, where the influence of the amorphous phase on the crystallisation vanishes [33]. The inverse crystal thickness for the sample annealed at 150 °C (star) does not follow these trends and the predictions made by the *Gibbs-Thomson* relation.

For a complementary analysis of the microstructural changes of PE-nanoparticles due to the annealing the WAXS intensities of respective dispersions were recorded at the ID02 beam line during the SAXS experiments. The plot in Fig. 28 displays the wide angle diffraction intensities of the investigated nano-platelets. The measured scattering intensities were corrected by the subtraction of the WAXS-intensities of a SDS-solution being the dispersion medium according to equation (51). This correction led to a significant over correction of the scattering intensities for $q > 17.5$ nm$^{-1}$. For this reason only a qualitative interpretation of the data sets can be discussed. The measured diffraction signal of native PE-particles (Fig. 28, black line) demonstrates the significant reflection of monoclinic PE at $q \approx 14.0$ nm$^{-1}$. The two major reflections at $q \approx 15.6$ nm$^{-1}$ and $q \approx 17.2$ nm$^{-1}$ are primarily assigned to the orthorhombic modification. The annealing at 100 °C (Fig. 28, red line) led to the disappearance of the monoclinic reflection and an increase of the signal intensities corresponding to the orthorhombic phase. The monoclinic order is thus completely transformed into the stable orthorhombic one upon mild annealing. The annealing at 125 °C shows a slight decrease of the scattering intensity related to the crystalline domain, accompanied with an increase of the scattering intensities of the amorphous domain (Fig. 28, green line). This can be associated with the increasing intensity of the broad scattering signal at lower scattering angles relative to the orthorhombic

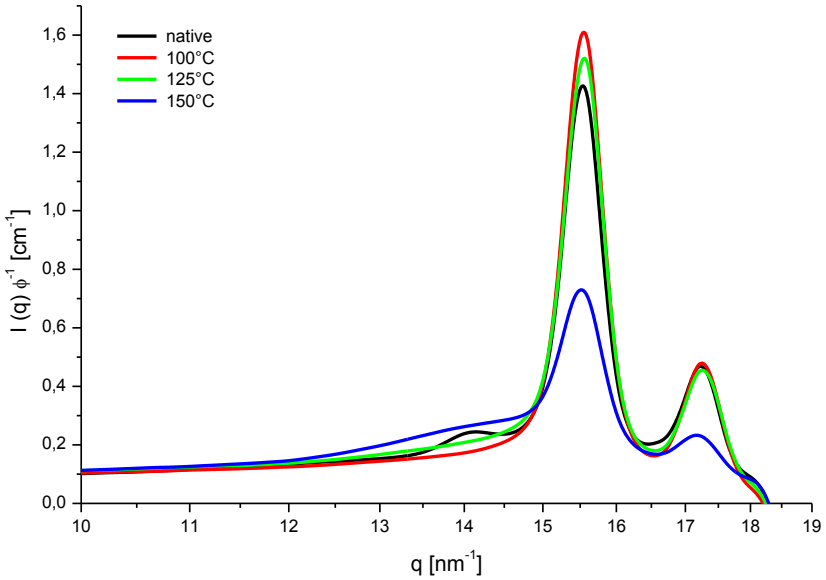


**Fig. 28: WAXS-intensities of PE-nanoparticles after correction of the scattering contribution of the dispersion medium. The black curve represents the diffraction signals of native PE-nanoparticles showing a significant reflection at $q \approx 14.0$ nm$^{-1}$ corresponding to monoclinic PE. The blue, red, and green curves represent the diffraction signals of annealed samples.**

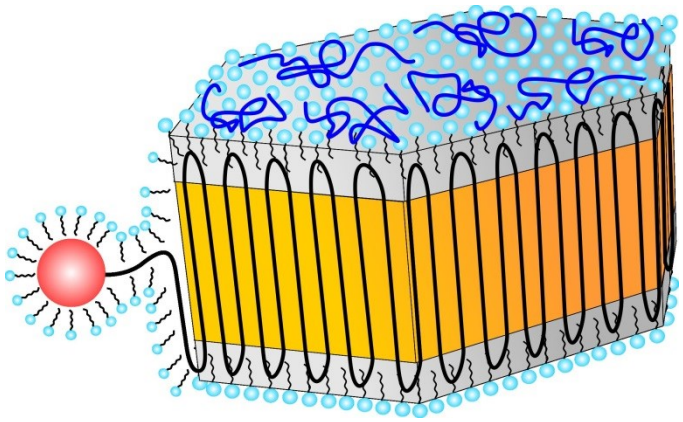

**Fig. 29: Schematic drawing representing a nanoparticle of linear PE formed by the catalytic active Ni-complex (red sphere). The polymer chain is stabilised by adsorbed SDS molecules and is rapidly added to the crystal growth front. The redirection and re-entry of the polymer chain takes place in the thin amorphous layer (grey layer) topping the crystalline domain (orange layer).**

150 °C, being above the melting temperature of the PE-crystallites, the signal intensity of the amorphous phase is significantly increased. The intensities corresponding to the crystalline reflections dropped contemporaneously (Fig. 28, blue line).

In conclusion, the crystalline structure of the investigated PE-nanoparticles results from the low-polymerisation temperature and the catalytic properties of the employed Ni-complex (Fig. 17). The crystallisation at low temperatures and within the confined space of the emulsion droplets differs significantly from the crystallisation due to the super cooling of polymer melts [1]. In the present case, the crystallisation occurs due to the rapid embedding of the growing chain directly into the crystalline growth front as this is schematically displayed in Fig. 29. Here, the crystallisation appears to be as fast as the chain growth. This could be estimated from an extrapolation of the initial growth rate of 10 monomer units per second forming the homogeneous nucleus [181,182,183]. However, the thickness of the crystals must be defined in a very early stage of the growing process. The first polymer stems attached to the growth front have to be longer than a critical value to overcome the nucleation barrier created by an excess surface energy to minimize the bulk energy [17]. Moreover, the confinement provided by the droplets during the emulsion polymerisation and the chain growth taking place at the emulsion droplets interfaces leads to nanocrystals with a single growth front. Therefore, the formation of disordered segments or chain entanglements is virtually avoided. These particles can thus be termed “ideal nanocrystal” as the polymer chains are arranged in highly ordered way having virtually no defects or entanglements. The growing polymer chain and consequently the formed nanoparticles are stabilised by the absorbed surfactant molecules as this is illustrated in Fig. 29. The PEG molecules represented by the blue coils in Fig. 29 are supposed to be attached to the particle surface contributing to the polar phase and consequently supporting the particle stabilisation.

## 6.1.2. Nanoparticles of precisely branched polyethylene

Semi-crystalline nanoparticles composed of precisely methyl-branched PE were obtained from the ADMET-polymerisation of branched monomers in a secondary emulsion process [135]. The polymer carries a single methyl group at every 21$^{st}$ carbon atom along the polymer backbone.

Studies of quick frozen dispersions were performed in order to reveal the morphological characteristics of nanoparticles formed by the branched PE TEM-analysis of the dried dispersions and respective cryo-TEM. The corresponding micrographs revealed anisotropic shaped particles with a high grade of polydispersity and a doubtless polymorphology (Fig. 30). However, these images display a core-shell architecture, where the particle centre exhibits a phase of denser material. This appears darker in the micrographs and can be associated with the crystalline core of the nanoparticles. This domain is surrounded by lighter material, which can be assigned to the amorphous arrangement of the polymer chains. The light amorphous PE is not contrast matched as discussed for the linear PE investigated under cryogenic conditions (refer to chapter 6.1.1). The particles possess an equatorial diameter of approximately 50 nm. The tilting of the samples by 60° reveals their oblate-like shape with a total height of approximately 10 nm to 20 nm. Moreover, the cryo-TEM micrograph in Fig. 30 d) shows an irregular particle with a central core exhibiting an increased electron density, similar to the observation made by TEM. The particle shell that is composed of light amorphous material is visible. The visibility of the amorphous domain results from a slightly increased electron density within the amorphous domain compared to the one found for non-branched PE (refer to section 6.1.1.).

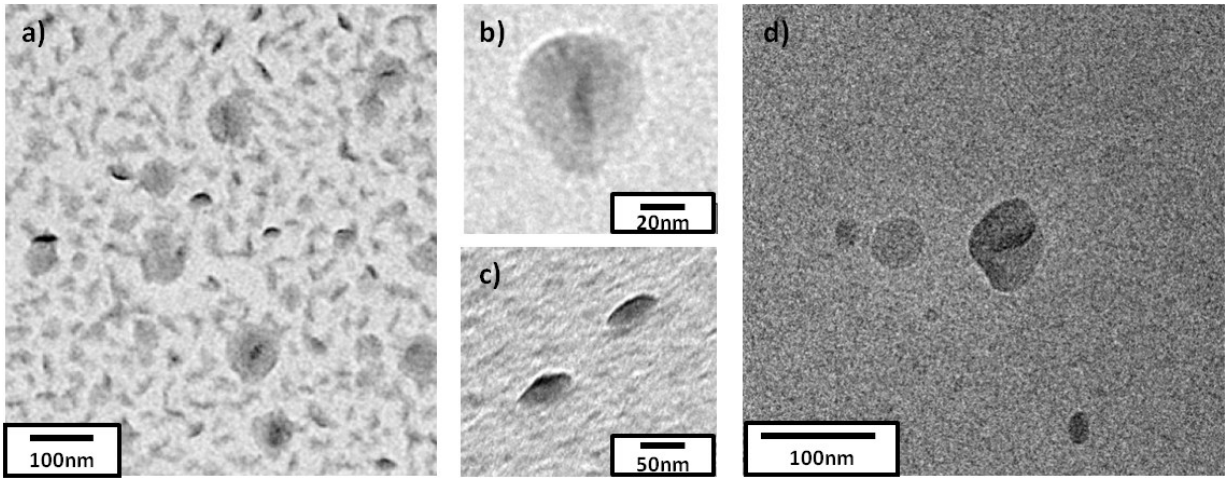


**Fig. 30: a) TEM micrographs of semi-crystalline nanoparticles from a dried dispersion of branched PE-nanoparticles. b) Magnification of a single PE-nanoparticle. c) Nanoparticles investigated by tilting the sample stage by 60° towards the probing electron beam. d) Cryo-TEM micrograph obtained from a plunge freeze PE-nanoparticle dispersions.**

### SAXS measurements

A contrast variation series analysed by SAXS was performed in order to confirm the core-shell structure found by electron microscopy. For this purpose, the scattering intensities of the nanoparticles dispersions containing different amounts of glucose were measured. Herein, the sugar

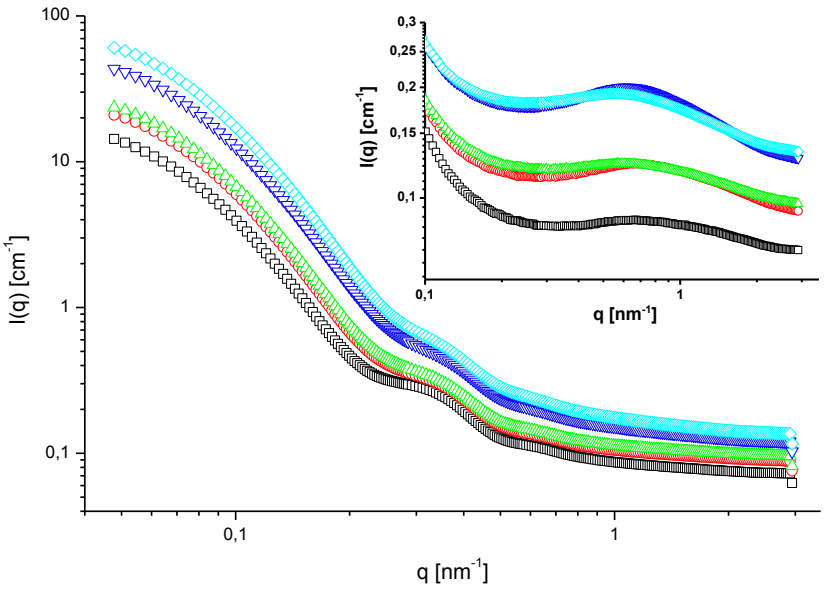


**Fig. 31: SAXS-intensities obtained from a contrast variation series of nanoparticles of precisely branched PE using glucose as contrast agent. The sugar concentration was increased from bottom to top from 0 wt%, 4.5 wt%, 7 wt%, 15 wt%, to 22 wt% glucose content. The inset shows the SAXS-intensities of sugar solutions containing 1.5 wt% of DTAC. The symbol and colour code for the respective glucose content is the same as used in the main graph. The surfactant content is appropriate to the one used for the nanoparticle dispersions. The absolute calibrated data are shown without further treatment.**

was used as contrast agent. Additionally, sugar solutions with an appropriate content of the surfactant DTAC were investigated for a sufficient background correction. The corresponding sample compositions are provided in Tab. 5 and the associated original SAXS-intensities are reflected in Fig. 31. The plot illustrates the scattering curves as obtained after the final data reduction. The inset displays the corresponding SAXS-intensities of sugar solution containing DTAC in appropriate amounts to those of the investigated nanoparticle dispersions. Here, a broadened scattering intensity signal around $q \approx 0.7\ nm^{-1}$ can be observed. This can be associated with the scattering contribution of DTAC-micelles. Furthermore, the shape of the scattering curves appears to be dependent on the scattering contrast. The small angle scattering of several commonly used surfactants was reported by Prevost [155]. Contrast variation studies using X-ray scattering of self-assembled systems were reported elsewhere but should not be the focus of the present investigations [184,185]. For the analysis of the scattering intensities deriving solely from the PE-particles, the contribution of the dispersions media, namely the glucose solutions had to be considered. In particular, the scattering intensities contributed by the surfactant molecules had to be taken into account. In the first instance, the scattering intensities of the sugar solutions were subtracted from the SAXS-intensities of the corresponding nanoparticle dispersions according to equation (51). This procedure led to a non-satisfying result, as the high-$q$ region was significantly influenced by the small angle scattering of the free DTAC-micelles. The structures formed by the self-assembling surfactant molecules and therefore their specific small angle scattering appeared to be strongly dependent on the composition of the dispersion. The subtraction following equation (51) led to an over-correction of the scattering intensities at larger $q$-vectors. In this case, one important issue is the different amount of free DTAC-micelles in the nanoparticle dispersions and in the solutions

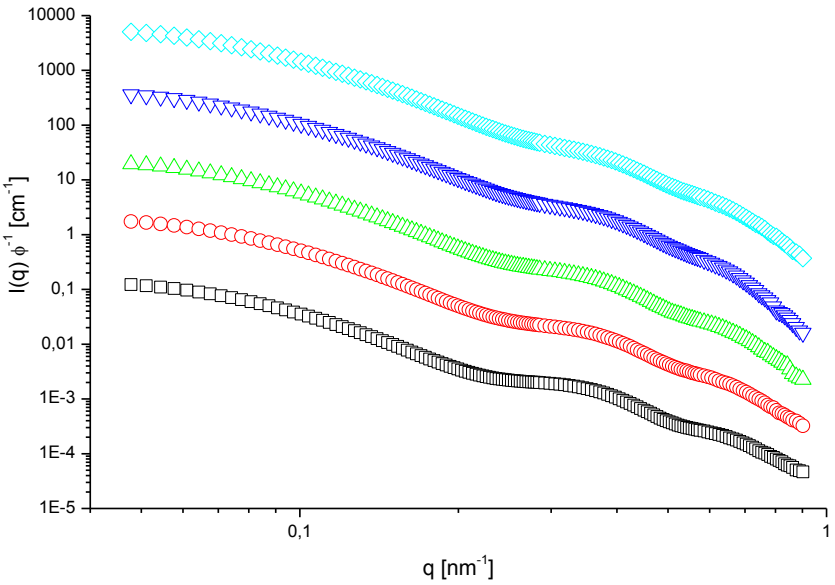


**Fig. 32: SAXS-intensities corrected by the contribution of the dispersion media normalised by $\phi$. The symbol and colour code is adapted from Fig. 31. For reasons of clarity the four lowermost intensities were downshifted by a factor of 10, $10^2$, $10^3$ and $10^4$.**

used for the correction of the respective particles. Hence, these molecules cannot contribute to the formation of free micelles. The employed surfactant concentration was tested to be the lowest concentration, suitable for the proper stabilisation of the dispersed nanoparticles. Therefore, the additional small angle scattering intensities generated by the self-assembled structures were corrected as follows. The scattering intensities beyond $q = 1\ nm^{-1}$ were fully assigned to those contributed by the DTAC-micelles. Thus, the scattering intensities of a DTAC-solutions at a provided contrast were multiplied by an arbitrary factor to match the scattering intensity of the respective nanoparticles dispersion above $q > 1\ nm^{-1}$. Nevertheless, only the evaluation of the corrected scattering intensities was suitable for values of the scattering vector of $q < 0.7\ nm^{-1}$, as this is illustrated in Fig. 32.

From the analysis of the scattering intensities at vanishing scattering angles, the initial molecular parameters were calculated using the *Guinier*-relation given by equation (14). The corresponding *Guinier*-plot is illustrated in Fig. 33, whereas the results of the analysis are tabulated in Tab. 5. From the variation of $b_m$ only a minor influence on $R_G$ was observed, whereas the intensities of the particle forward scattering reveal a significant trend. The correlation leading to $b_P$ and $V_P$ using equation (27) is illustrated in Fig. 34. The respective particle volume was determined with $V_P = 36000 \pm 3000\ nm^3$, whereas the correlation reveals an average particle scattering length density of $b_P = 8.71 \pm 0.04\ 10^{10}\ cm^{-2}$. The obtained $b_P$ is smaller than the value $b_m$ of neat water (Tab. 5). The low scattering length density indicates a low packing density of the PE-chains within the nanoparticles. Therefore, the precisely placed methyl branches along the chain significantly contribute to formation of a less dense packing than this is found for the bulk material of linear PE [186]. The influence of the branching on the polymer crystallisation was intensively discussed in the literature [38,39,48,95]. As the short methyl branches are supposed to be incorporated into the crystalline stack, they influence the order within semi-crystalline structure [35,38,92]. With $b_P$ the individual scattering contrasts $\Delta b$ were calculated.

**Tab. 5: Overview on the samples composition of the contrast variation series of nanoparticles composed of precisely branched PE. The results from the *Guinier*-analysis are tabulated in addition.**

| $\omega$ glucose | $\omega$ PE | $\phi$ PE | $b_m$ | $\rho_m$ | $R_G$ | $I(q \rightarrow 0)$ |
|---|---|---|---|---|---|---|
| wt% | wt% | | $10^{10}$cm$^{-2}$ | g cm$^3$ | nm | cm$^{-1}$ |
| 0 | 0.96 | 0.0107 | 9.42 | 0.9974 | 22.0 ± 2.3 | 19.2 ± 0.2 |
| 4.5 | 0.96 | 0.0109 | 9.55 | 1.0164 | 22.0 ± 2.4 | 29.1 ± 0.4 |
| 7 | 0.96 | 0.0110 | 9.63 | 1.0315 | 22.0 ± 2.4 | 32.7 ± 0.6 |
| 15 | 0.96 | 0.0113 | 9.91 | 1.0503 | 22.1 ± 2.5 | 61.2 ± 1.0 |
| 22 | 0.96 | 0.0116 | 10.16 | 1.0503 | 22.3 ± 2.6 | 86.3 ± 1.4 |

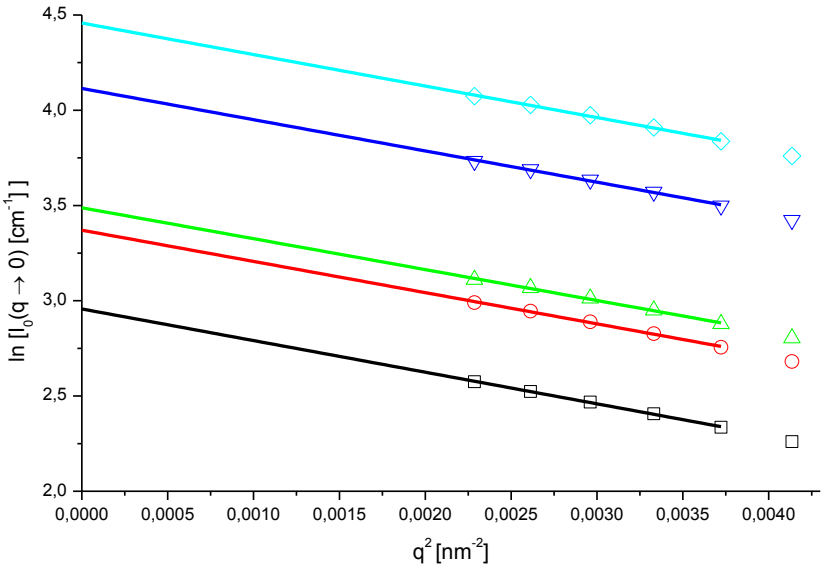


**Fig. 33: *Guinier*-plot: Linearised forward scattering intensities from the contrast variation series of nanoparticles formed by branched PE. The symbol and colour code is taken from Fig. 31.**

The particle dimensions at infinite contrast were determined from the extrapolation as a result of equation (29). This correlation is illustrated in Fig. 35. It leads to $R_{G\infty}$ = 22.4 ± 2.8 nm, which is in the range of the values obtained by the *Guinier*-analysis. A measure for the electron distribution within the nanoparticle is provided by the parameter $\alpha$ that is defined by equation (31). The corresponding value was determined with $\alpha$ = (1.20 ± 0.68) $10^{-3}$. The positive value indicates an increased electron density in the particle periphery [187]. The outermost part of the particles is composed out of light amorphous PE. Therefore, $\alpha$ correlates with the adsorbed surfactant molecules at the particle surface. These molecules contribute electron density deriving from their polar head groups [155]. To illustrate the influence of the scattering contrast Fig. 36 shows the scattering intensities normalised by $\phi$ and $\Delta b^2$. This correlation reveals the low-$q$ regime, which is related to the outermost regions of the particle, to be almost independent from the variation of $b_m$. The influence becomes more prominent for $q > 0.2$ nm$^{-1}$, where the scattering intensities vary significantly. The high-$q$ region correlating with shorter length scales in real space can be associated with the particles inner structure. Furthermore, the plot elucidate that the presence of the micellar structures influences the

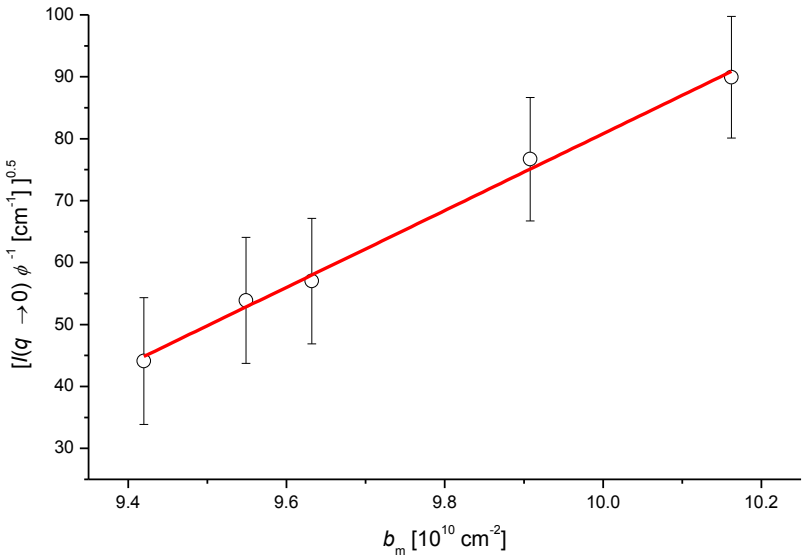


**Fig. 34: '*Square root*'-plot: Dependence of the forward scattering intensities as a function of the scattering length density of the dispersions medium $b_m$.**

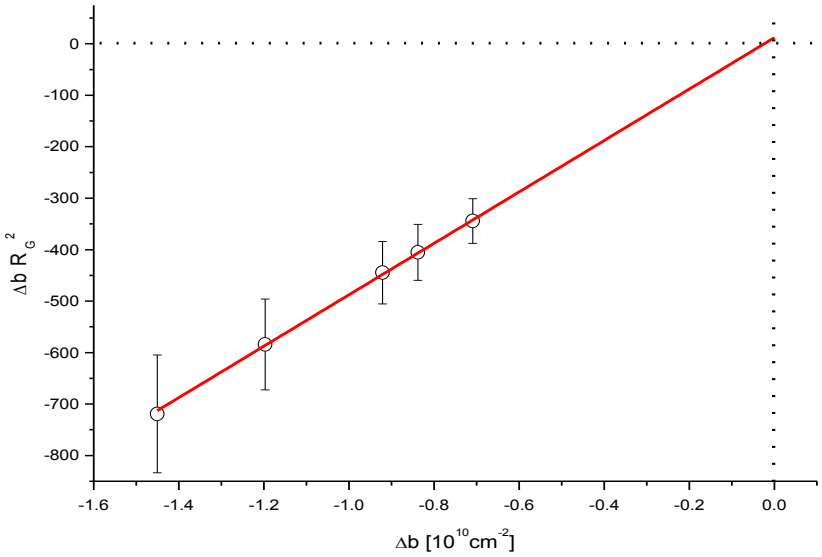


**Fig. 35: *Stuhrmann*-plot: Radius of gyration as a function of the scattering contrast $\Delta b$.**

angular regime above $q > 0.7\ nm^{-1}$. Here, the subtraction of the corresponding scattering contribution of the DTAC-micelles appears non-sufficiently realised.

For a more comprehensive determination of the particles shape and the internal structure the scattering intensities $I(q, \Delta b)$ were decomposed as a function of $\Delta b$. This method allows the determination of the particle shape by its specific scattering contribution unaffected by the contribution arising from the particles inner structure (refer to section 3.5). Employing equation (23) the parabolic fits lead to the contributions of $I_S(q)$, $I_{SI}(q)$, and $I_I(q)$ respectively. For selected $q$-values the scattering intensities normalised by $\phi$ and the fits corresponding to formula (23) are illustrated in Fig. 37. This illustrates the decomposition to be sensitive in the low-$q$ region, where the intensities

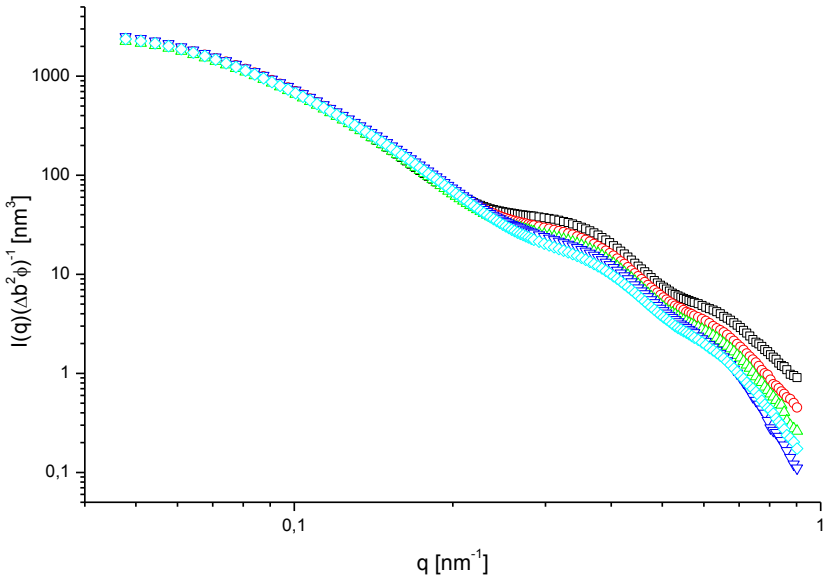


**Fig. 36: Scattering intensities of nanoparticles of branched PE normalised by $\phi$ and $\Delta b^2$. The symbol and colour code corresponds to Fig. 31.**

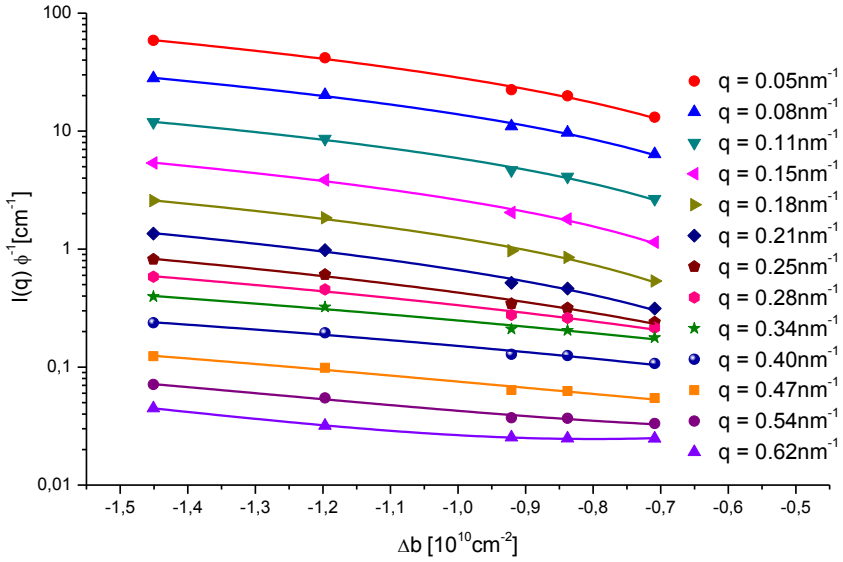


**Fig. 37: Scattering intensities for selected *q*-values as a function of the scattering contrast $\Delta b$. The solid lines represents the parabolic fit according to equation (23).**

tend to an intensity minimum. The correlation for $q$ = 0.62 nm$^{-1}$ shows a divergence from this trend, which becomes more dominant for higher $q$-vectors. For this region the decomposition must be seen as insecure for the reasons already outlined. However, the contrast decomposition processed over the total accessible $q$-range reveals the partial scattering intensity $I_S(q)$, which refers solely to the overall shape of the particles as illustrated in Fig. 38. Obviously, $I_S(q)$ display no characteristic $q$-dependence as this is known for common monodisperse spheroids [4,188]. This could be explained by a rather high polydispersitiy of the investigated sample that smear out these characteristics. The data of $I_S(q)$ were modelled best with the particle scattering factor of polydisperse oblate-like ellipsoids [189,190]. The length of the equatorial-axis was thus determined with $R_{eq}$ = 23.8 ± 8.8 nm

and the perpendicular semi-axis was found to be $R_p$ = 4.9 ± 1.8 nm. For the respective calculation a LogNorm size distribution was employed. These fit parameters also describe the calculated particles dimensions from the analysis of the scattering at vanishing *q*-values. Moreover, the dimensions are in the range of the values determined by electron microscopy. Additionally, other geometrical bodies were tested to fit the data of $I_S(q)$. The fit for a polydisperse sphere having a diameter *d* = 27 ± 10 nm shows significant deviation especially for higher *q*-vectors. The corresponding particle volume differs from the extracted values from the analysis of the low-*q* regime. The scattering contribution corresponding to the particles inner structure $I_I(q)$ and those of the cross-term $I_{SI}(q)$ were also

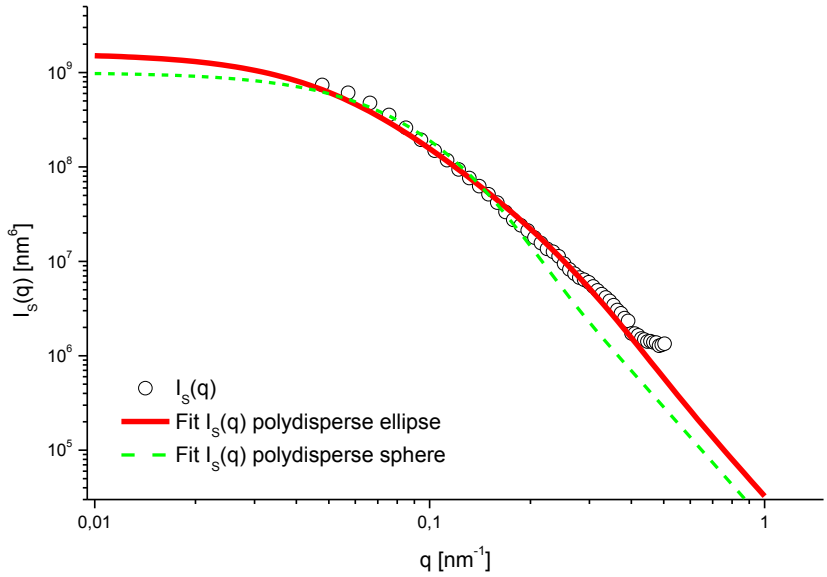


**Fig. 38: Scattering intensities $I_S(q)$ correlating with the particles shape as derived from the contrast decomposition procedure. The solid red line corresponds to the fit for an oblate-shaped ellipse, whereas the dashed line corresponds to a spherical particle.**

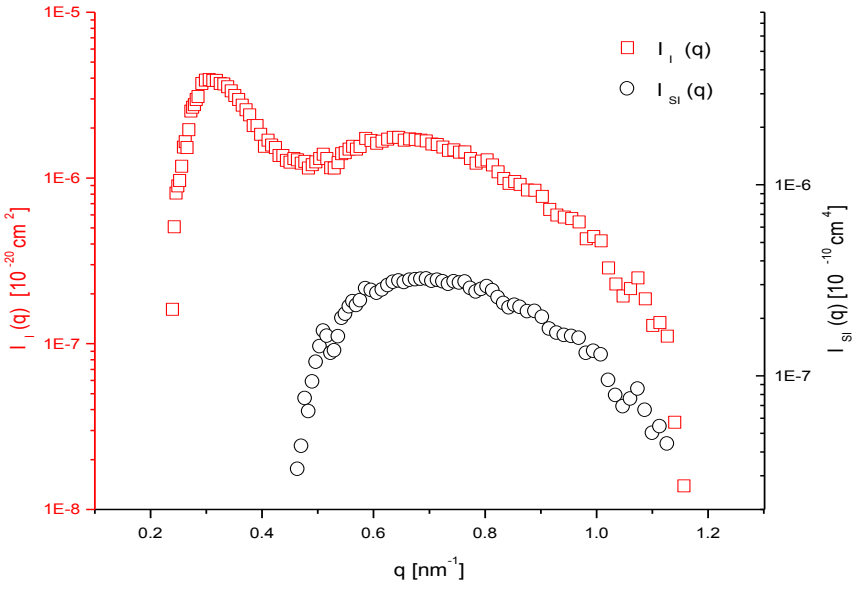


**Fig. 39: Scattering intensities corresponding to the inner-term $I_I(q)$ (red squares) and for the cross-term $I_{SI}(q)$ (black circles) as obtained from the contrast decomposition according to equation (23)**

extracted. The contribution of $I_I(q)$ shows the significant decrease of the scattering intensities towards low-$q$ values between $0.2\ nm^{-1} < q < 0.3\ nm^{-1}$. Therefore, the decomposed scattering intensities do not affect each other in this specific $q$-region. The further data analysis testing different geometrical bodies to model $I_I(q)$ could not reveal additional structural characteristics.

## WAXS measurements

The crystal structure of the nanoparticles was studied by WAXS measurements from a precipitated sample. The measured WAXS-intensities are provided in Fig. 40, whereas the position and relative intensity of the corresponding diffraction signals are tabulated in the Tab. 6. The analysis revealed the semi-crystalline structure of the investigated nanoparticles. The crystallinity of the investigated nanoparticles was estimated with $\chi_{C\text{-}WAXS} \approx 41\ \%$ by comparing the respective signal integrals with those of the molten sample. This value is in good agreement with the crystallinity determined by DSC-measurements, which reveals $\chi_{C\text{-}DSC} \approx 42\ \%$. The main diffraction signals for the PE-nanoparticles were observed at $2\theta = 19.17°$ and $2\theta = 21.92°$. These signals are shifted to smaller scattering angles compared to those of the classical orthorhombic phase observed for linear PE [156]. This can be explained by an expansion of the lattice cells due to the incorporation of the methyl branches into the crystalline domain. The presence of just a few further and rather weak diffraction signals impeded the evaluation of the diffraction data. Moreover, the evaluation of the crystal plane reflections from polymer crystals has to consider molar mass distribution effects that broaden or smear out diffraction signals, for example. The further analysis was performed using the *Crysfire Suite* developed by Shirley [191]. Herein, the procedures reported by Taupin [192], Werner [193], and Boultif [194] were tested with the extracted reflections. The procedure reveals crystal unit cells with a tendency towards the monoclinic crystal modification. The further refinement of the suggested unit cells step was performed with the program *CHECKCELL* by Laugier and Bochu [195].

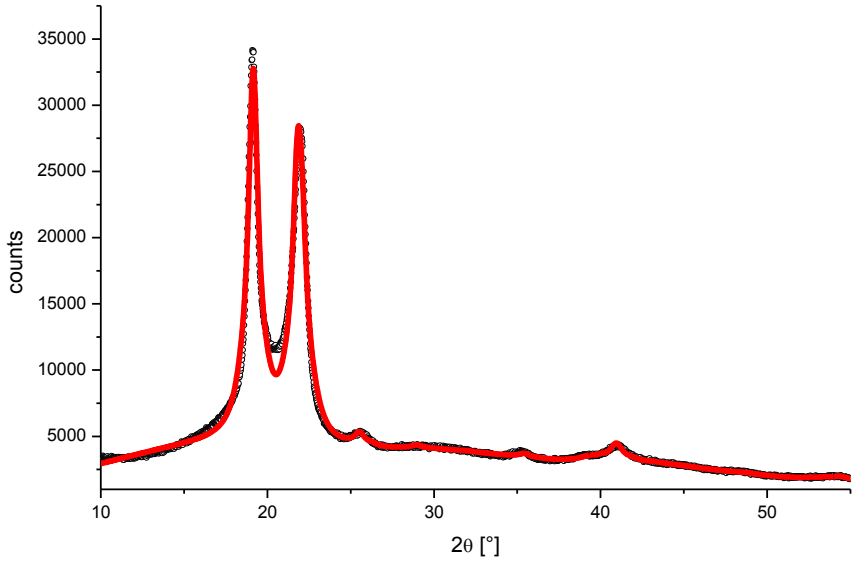


**Fig. 40: WAXS-intensities obtained from nanoparticles of precisely branched PE. The open black dots represent the measured scattering intensities. The solid red line corresponds to the fit calculated by the routine of "*Le Baile*" based on a monoclinic unit cell.**

**Tab. 6: Position and relative intensities of the diffraction signals of semi-crystalline nanoparticles of methyl-branched PE as revealed from the pattern shown by Fig. 40.**

| $2\theta$ | $d_{observed}$ | relative intensity |
|---|---|---|
| ° | Å | % |
| 19.17 | 4.63 | 100 |
| 21.92 | 4.05 | 86 |
| 25.72 | 3.46 | 2 |
| 35.31 | 2.54 | 2 |
| 39.20 | 2.30 | 1 |
| 41.08 | 2.20 | 5 |
| 54.16 | 1.69 | 1 |

Herein, the predicted cells and their corresponding reflection could be compared to the observed scattering pattern. The best match was obtained for a monoclinic cell from the space group P2 having the following parameters:

$a$ = 9.42 Å, $b$ = 2.64 Å, $c$ = 4.12 Å, $\alpha$ = 90°, $\beta$ = 101°, $\gamma$ = 90°

The density calculated for the crystalline phase composed out of these unit cells reveal a density of $\rho_{crys}$ = 0.93 g cm$^{-3}$. The refinement using the software *Fox* (version 1.9.7.0 R1312) by Favre-Nicolin and Černý [196,197] led to the fit provided by the red solid line in Fig. 40. Herein, the cell parameters were optimised based on the original dataset with respect to the contribution of the amorphous phase. The procedure reveals a slightly modified unit cell with:

$a$ = 9.38 Å, $b$ = 2.62 Å, $c$ = 4.13 Å, $\alpha$ = 90°, $\beta$ = 101°, $\gamma$ = 90°

The corresponding density of the unit cell was calculated using $\rho_{crys}$ = 0.93 g cm$^{-3}$. This value is significantly smaller than the values known for crystalline PE composed of non-branched chains [186]. Estimating that the average particle scattering length density determined from the contrast variation series by SAXS solely refers to the branched PE, leading to a corresponding mass density of $\rho$ = 0.9 ± 0.04 g cm$^{-3}$. Calculating the crystal fraction from the partial densities of the crystalline and amorphous phase resulted in $\chi_{C\text{-}density}$ ≈ 40 %. This value is within the range of the values determined by WAXS and DSC.

Similar results according to the crystalline structure of PE with precise branching had been reported previously. Lieser and co-worker assigned a triclinic unit cell according to Turner-Jones [198] to the wide angle reflections from a bulk material of PE carrying methyl groups at every 21$^{st}$ carbon [92]. The density of the crystalline phase was calculated with $\rho_{crys}$ = 0.91 g cm$^{-3}$. Compared to this, Qiu et al. determined a monoclinic unit cell for bulk sample having a similar microstructure [93]. A reduced lattice symmetry is considered to enhance the packing of the pendant groups. Herein, the methyl groups are supposed to redistribute to a defect plane within the lattice, consequently reducing the free volume. Wagener and co-worker discussed the influence of the length of the precisely placed branches [38,40]. They demonstrated that only methyl and ethyl branches are incorporated into the lattice cell, whereas longer ones are excluded from the unit cell. The branches are also preferred

position for chain folding. An induced chain fold was discussed for alkanes with precisely placed chlorines [199]. The voluminous amorphous phase observed by TEM, which was furthermore found by complementary WAXS-analysis and can be explained as the consequence of the reduced reordering ability of the polymer chains. This results from the steric hindrance arising from the branching along the polymer backbone. Thus, the redirection of the polymer chain towards the ordered phase is impeded due to the formation of loops and entanglements.

## 6.2. Core-multishell (CMS) nanoparticles

The focal point in the following section will be the analysis of the spatial structure of molecules based on hyperbranched polymers. Herein, hyperbranched polyglycerol is one of the most relevant and versatile representatives [75,80,81,82]. Moreover, it is the major building block of a variety of structures with versatile applications [200,201,202]. Thus, the detailed analysis of the hPG will further support the comprehensive investigations on the spatial structure of CMS-nanoparticles.

### 6.2.1. Hyperbranched polyglycerol

#### 6.2.1.1. Microstructure analysis

The investigated hyperbranched polyglycerol was obtained by the polycondensation of glycidol. The synthesis follows the protocol developed by Sunder and co-worker [138], which was recently modified by Paulus [136]. The analysis of the molecular microstructure was realised using $^{1}$H and $^{13}$C-NMR spectroscopy. The NMR spectra are illustrated in the appendix (Fig. S 2 and Fig. S 3). This procedure reveals the degree of branching (*DB*) and the degree of polymerisation (*DP*) from the relative signal intensities determined from the $^{13}$C-NMR spectra (Fig. S 2, Tab. 7) employing the correlations reported by Sunder [138].

$$DB \approx \frac{2D^*}{2D^* + L^*_{13} + L^*_{14}} \tag{56}$$

$$DP \approx \frac{T^* + L^*_{13} + L^*_{14} + D^*}{T^* - D^*} f \tag{57}$$

The signal intensities of the 1, 3 linear segments and those of the 1, 4 linear segments are provided by $L^*_{13}$ and $L^*_{14}$. The dendritic units are represented by $D^*$ and the terminal ones by $T^*$ respectively. The value of $f$ describes the functionality of the initial unit being TMP in the present case. These structure elements are schematically illustrated in Fig. 41.

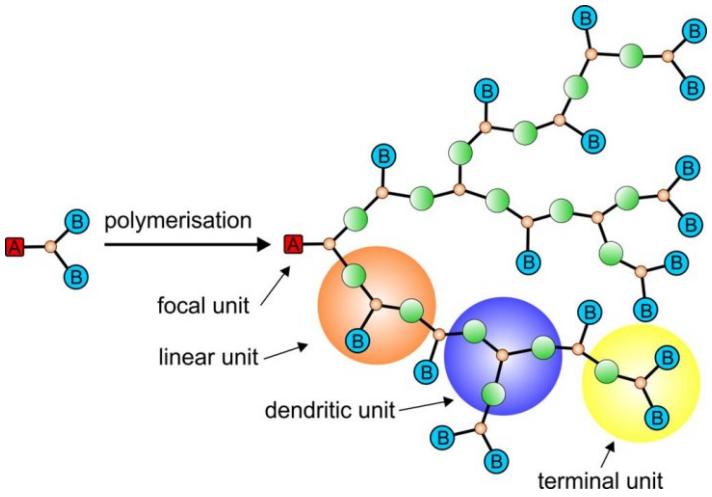


**Fig. 41: Schematic representation of the polycondensation of $AB_f$ - monomers forming hyperbranched architectures. The different structural units are highlighted.**

**Tab. 7: Analysis of microstructural characteristics of hPG from $^{13}$C-NMR spectra.**

| | shift | relative integral | structural unit | relative abundance |
|---|---|---|---|---|
| | ppm | | | % |
| $L^*_{13}$ | 82.0 – 81.0 | 1 | terminal (*T*) | 34 |
| D* | 80.5 – 79.5 | 2.22 | linear 1,3 ($L_{13}$) | 12 |
| 2 $L^*_{14}$ | 74.5 – 73.5 | 4.38 | linear 1,4 ($L_{14}$) | 27 |
| 2 D*, 2 T* | 73.5 – 72.0 | 9.41 | dendritic (*D*) | 27 |
| $L^*_{13}$, $L^*_{14}$ | 72.0 – 70.5 | 3.24 | | |
| T* | 65.0 – 64.0 | 2.72 | | |
| $L^*_{13}$ | 63.5 – 62.0 | 1.02 | | |

The corresponding values were determined with $DB = 0.59$ and $DP_n = 0.48$. With respect to the molecular weight of the monomer and the initial unit (refer to section 5.1.3), a number weighted molecular weight of $M_{n\text{-}NMR} = 3.69$ kg mol$^{-1}$ was calculated.

### 6.2.1.2. Small Angle Scattering

For the analysis by TOF-SANS, the hPG was dissolved in pure $D_2O$ and studied in a concentration series. The respective scattering contribution of the dispersion media was subtracted from the measured scattering intensities of the polymer dispersions employing equation (51). The corrected scattering intensities illustrated in Fig. 42 show a characteristic *q*-dependence that was also found in earlier studies on hyperbranched polymers [88,89,90]. Here, the scattering intensities show a variation in slope towards higher *q*-values, corresponding to short correlation length in real space.

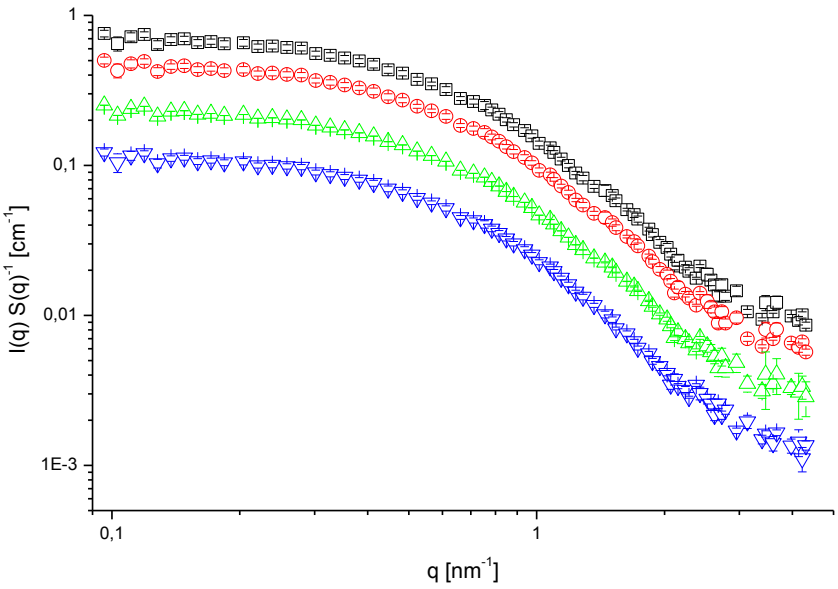


**Fig. 42: TOF-SANS-intensities as a function of *q* from a concentration series of hPG dispersed in $D_2O$. The SANS-data were corrected by the scattering contribution of the dispersion medium and *S*(*q*). From bottom to top: dispersions with increasing polymer weight fraction $\omega$ (0.5 wt%, 1 wt%, 2 wt%, and 3 wt%).**

However, this feature was not discussed in detail or was simply poorly resolved due to a limited instrumental resolution in the high-$q$ sector [89].

The concentration series served for the determination of the scattering intensities for infinite dilution $I_0(q)$ [103,105]. For the investigated concentration range $I_0(q)$ could be extrapolated with good accuracy from the linear correlation between $\phi / I(q, \phi)$ and $\phi$. For selected $q$-values this dependence is illustrated in Fig. 43. The scattering intensities normalised by $\phi$, as shown in Fig. 44 reveal the influence of the inter-particle correlation in the low-$q$ regime even for small particle volume

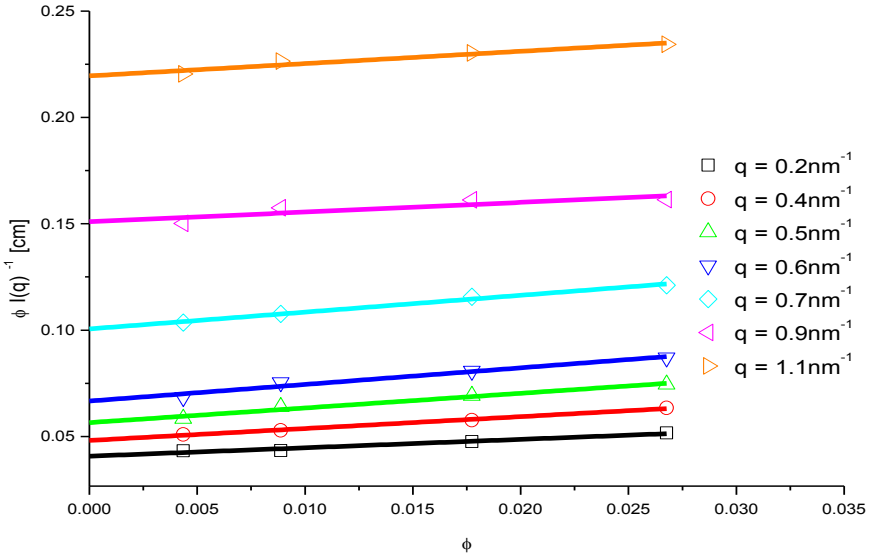


**Fig. 43: Correlation of the scattering intensities $I(q, \phi)$ and the polymer volume fraction $\phi$ for selected $q$-values. The solid lines represent the extrapolation for vanishing $\phi$.**

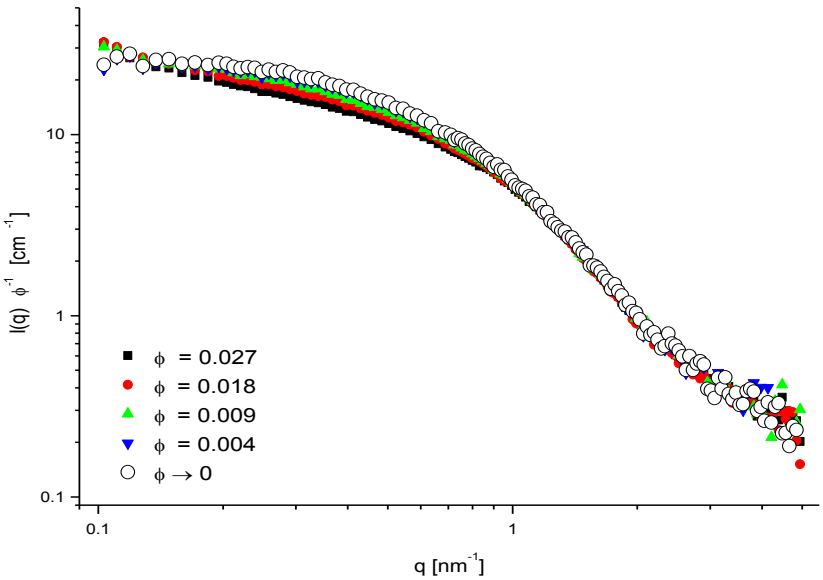


**Fig. 44: TOF-SANS-intensities normalised by $\phi$ as obtained from hPG dispersed in $D_2O$. The colour and symbol code is adapted from Fig. 42. The extrapolated scattering intensity for vanishing concentration $I_0(q)$ are represented by open circles.**

fractions, which can be deduced from the variation of the scattering intensities at small magnitudes of $q$. However, for the lowest measured $q$-values a slight increase of the intensities can be observed. The structure factor $S(q)$ was determined employing equation (13).

With respect to the limiting case of small $q$-values and finite volume fractions, $S(q)$ is a function of the osmotic compressibility. It can, therefore, be expanded as a function of the polymer volume fraction for the determination of an effective correlation distance $d_{eff}$ deriving from [5,105,111]:

$$\frac{1}{S(q)} \cong 1 + 2B_{app}\phi + 3C_{app}\phi^2 + \ldots \tag{58}$$

$$B_{app} = \frac{2\pi {d_{eff}}^3}{3V_P}\left(1 - \frac{1}{10}{d_{eff}}^2 q^2 + \ldots\right) \tag{59}$$

Here, $B_{app}$ and $C_{app}$ are the apparent second and third virial coefficient. The value of $d_{eff}$ is correlating with an effective distance between interacting particles in solution and can be determined from the linear correlation of $1 / S(q)$ and $q^2$ at small magnitudes of the scattering vector (Fig. 45). The correlation illustrated in Fig. 46 is used for the determination of $S(q)$ at vanishing scattering vectors $S(0)$ from the respective intercepts of the linear correlations. The corresponding results are provided in Tab. 8.

The theoretical neutron scattering length density of hPG was calculated by equation (2) to be $b_{neutrons} = 0.927 \cdot 10^{10}$ cm$^{-2}$. Hence, the scattering contrast for the molecules dispersed in $D_2O$ was calculated with $\Delta b = -5.431 \cdot 10^{10}$ cm$^{-2}$. The analysis of $I_0(q)$ by equation (14) reveals the dimension of the polymers in solution characterised by its *Guinier*-radius being $R_G = 2.7 \pm 0.1$ nm (Fig. 47). However, $R_G$ gives the radius of the polymer with respect to the centre of mass. These dimensions are smaller compared to the value of $R_H$ determined by angular dependent DLS from highly diluted dispersion [203,204]. Here, a hydrodynamic radius of $R_H = 3.8 \pm 0.1$ nm was obtained. Furthermore,

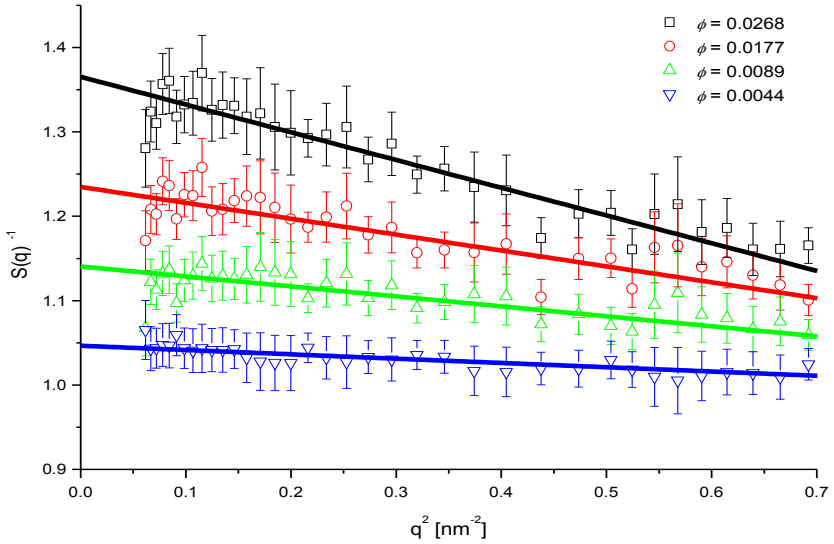


**Fig. 45: Correlation of $1 / S(q)$ and $q^2$ for the determination of the effective interaction diameter $d_{eff}$. The colour and symbol code is adapted from Fig. 42.**

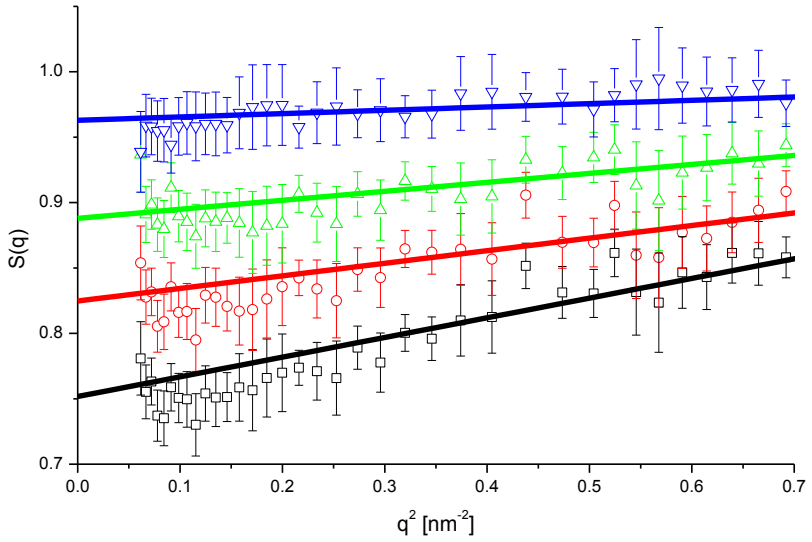


**Fig. 46: $S(q)$ as a function of $q^2$ used for calculating $S(0)$. The colours and symbols are taken from Fig. 42.**

**Tab. 8: Overview on the concentration series of the hPG dispersed in $D_2O$ as investigated by TOF-SANS.**

| $\omega$ | $\phi$ | $d_{eff}(S(0))$ | $d_{eff}(S(q^2))$ | $S(0)_{exp}$ |
|---|---|---|---|---|
| wt% | | nm | nm | |
| 3.04 | 00268 | 2.8 ± 1.0 | 2.9 ± 1.0 | 0.75 |
| 2.01 | 0.0177 | 2.9 ± 1.0 | 2.9 ± 1.0 | 0.82 |
| 1.01 | 0.0089 | 3.1 ± 1.0 | 3.0 ± 1.0 | 0.89 |
| 0.49 | 0.0044 | 2.8 ± 0.9 | 3.0 ± 1.0 | 0.96 |
| 0.17 | 0.0015 | - | - | - |

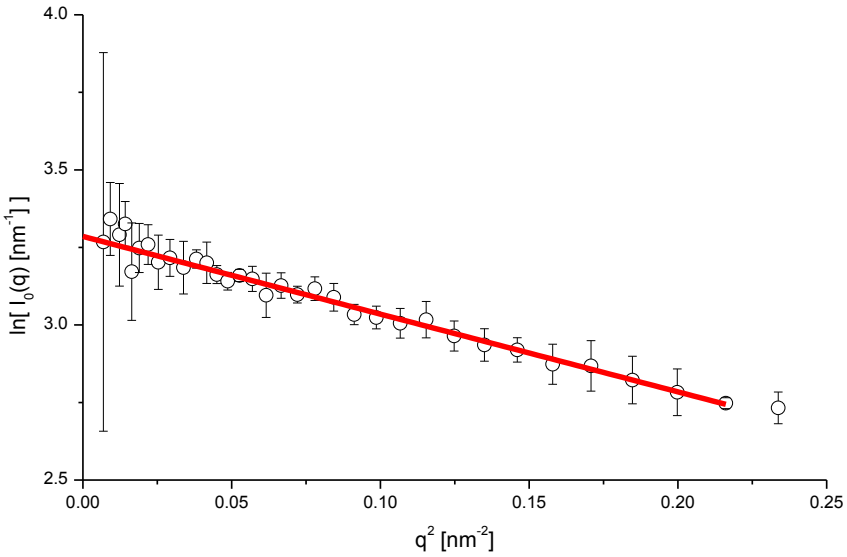


**Fig. 47: Linearised scattering intensities $I_0(q)$ of hPG dispersed in $D_2O$. The solid red line corresponds to the linear fit according to the *Guinier*-formula (14).**

a weight averaged molecular weight of $M_w$ = 6.8 ± 0.4 kg mol$^{-1}$ was determined from the *Guinier*-regime of $I_0(q)$. These values are important key parameters for the further evaluation of the CMS-nanoparticles. Comparing the values of $R_G$ and $d_{eff}$ demonstrates that the effective interaction distance is smaller as expected for non-charged hard spheres. For this limiting case, $d_{eff} \approx 2\ R_G$ holds [105,111].

A general approach to analyse the charcteristic scattering of the hyperbranched polymers is the decomposition of $I_0(q)$ with respect to the fractal-like structure of the hyperbranched scaffold. Meanwhile, the fractal approach for objects embodying self-similarity [205,206,207,208] became widely accepted for the characterisation of structural issues from polymer science [209,210,211,212,213]. The radial distance distribution *g(r)* of fractals was introduced by de Gennes [214]. The corresponding power law decay was established by Sinha and co-worker [205].

$$g_{fractal}(r) = A\, r^{(3-D_f)}\, h(r/\xi) \tag{60}$$

Here, $A$ is a scaling constant and $h(r/\xi)$ is the cut-off function that is related to the perimeter of the fractal structure. The correlation length $\xi$ represents the distance above which the mass distribution within the fractal structure is no longer described by the respective power law. The influence of different cut-off functions used for the analysis of fractal-like arrangements was reviewed by Sorensen [207,215]. Here, the exponential cut-off provided by equation (61) is one of the most frequently used ones [91,207,209,212,215].

$$h(r/\xi)_{exp} = exp\left(-\frac{r}{\xi}\right) \tag{61}$$

The corresponding analytical calculation of the *Fourier* transform of $g(r)$ was reported by Sinha revealing the particle scattering factor to be [205,207]:

$$F_{fractal}(q) = A\frac{\sin((D_f-1)\arctan(q\,\xi))}{(D_f-1)\,q\,\xi\left(1+q^2\,\xi^2\right)^{\frac{(D_f-1)}{2}}} \tag{62}$$

The relation between correlation length and radius of gyration is thus provided by [216]:

$$\xi = \sqrt{\frac{2}{D_f\left(D_f+1\right)}}R_{G-fractal} \tag{63}$$

The fractal dimension is related to the spatial distribution of the self-similar objects [217]. Usually, when it comes to dissolved polymers, a non-integer power law is found. This correlates with the well-defined decrease of the segment density emanating from the centre of mass. For polymers dissolved in their respective good solvent, low values of $D_f$ with $D_f > 2$ can be detected for the swollen structure. For the theta-solvent condition, $D_f$ = 2.3 is found. Polymers dissolved in their respective poor solvents or with increased branching reveal higher values of $D_f$ due to an increased space filling [87,212,218].

The decomposition according to the fractal approach illustrated by Fig. 48 is based on the recent discussion provided by Burchard [91]:

$$F(q)_{hb} = F(q)_{fractal} + \frac{1}{DP_w} F(q)_{segment} \tag{64}$$

Here, the decomposition into contributions arising from the fractal-like arrangement of the segmental sub-units and their specific scattering contribution was analysed. The weight averaged degree of polymerisation $DP_w$ was determined from the $M_{w\text{-}TOF\ SANS}$ and the molecular weight of the monomer unit to be $DP_w = 92.3$. The analysis revealed the fit illustrated by the solid red line

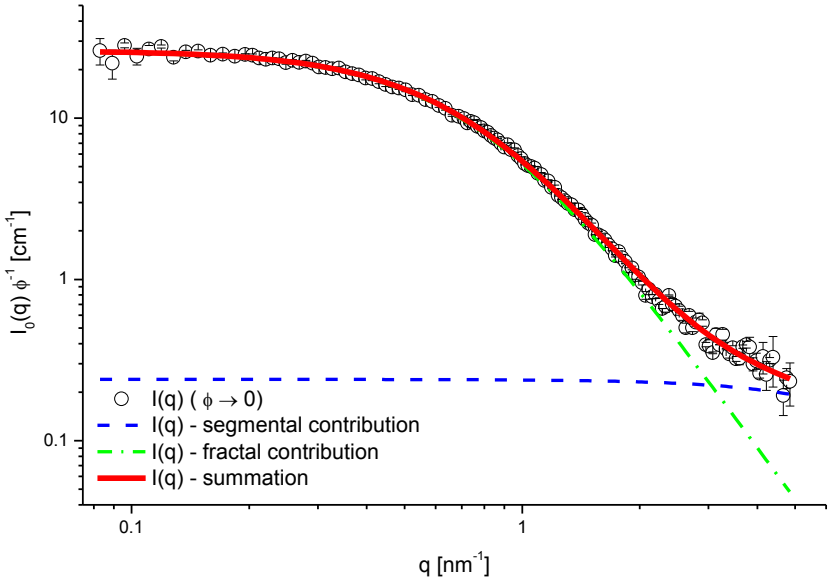


**Fig. 48: $I_0(q)$ as obtained by the analysis of the concentration series of hPG dispersed in $D_2O$ measured by SANS. The dashed green line represents the fit according to equation (62) related to a fractal structure with $D_f = 2.8$. The dashed blue line represents the contribution of the segmental structure. The solid red line corresponds to the summation as provided by formula (64).**

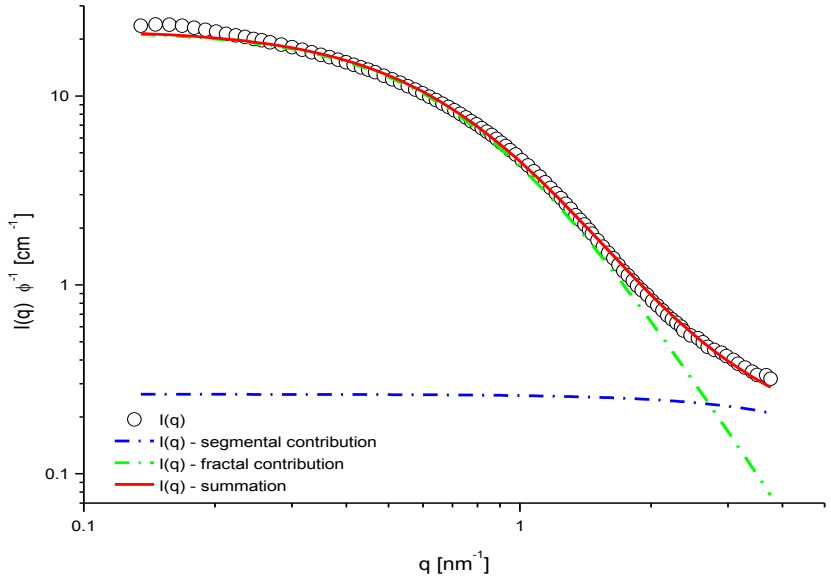


**Fig. 49: SAXS-intensities of the hyperbranched polyglycerol dispersed in $H_2O$. The solid line represents the fit according to equation (64).**

**Tab. 9: Overview on parameters employed for the analysis of hyperbranched polyglycerol by SANS and SAXS measurements. The data were obtained from the decomposition procedure provided by equation (64).**

| | | SAXS | SANS |
|---|---|---|---|
| $R_{G\text{-}fractal}$ | nm | 2.75 | 2.75 |
| $D$ | | 2.8 | 2.8 |
| $R_{G\text{-}segments}$ | nm | 0.3 | 0.3 |
| $\Delta b$ | $10^{10}$ cm$^{-2}$ | 2.06 | -5.431 |

in Fig. 48. Here, the scattering contribution of the fractal-like structure is illustrated by the dashed green line. The computation of equation (72) employs $R_{G\text{-}fractal}$ = 2.75 nm and a respective fractal dimension of $D_f$ = 2.8. This is related to a rather dense arrangement within the hyperbranched scaffold, consequently resulting from the high degree of branching (refer to section 6.2.1.1). The contribution of the segmental units normalised by $DP_w$ as represented by the dashed blue line in Fig. 48 revealed a respective radius of gyration of $R_{G\text{-}segments}$ = 0.3 nm.

Additionally, the hyperbranched polymer was analysed by SAXS measurements. Even then, the scattering contrasts are different for neutrons and X-rays, and the $q$-dependence of the scattering intensities appears similar (Fig. 49). The scattering length density of the hPG for X-ray photons was calculated to be $b_{X\text{-}ray} = 11.48 \cdot 10^{10}\text{cm}^{-2}$. This gives a scattering contrast of $\Delta b = 2.06 \cdot 10^{10}\text{cm}^{-2}$ for the particles dispersed in water. There were no data of concentration series available for the extrapolation of $I_0(q)$. Nevertheless, fitting the data applying equation (64) under consideration of the respective polymer volume fraction revealed the fit represented by the solid red line. The scattering contribution of the fractal-like structure is characterised by $R_{G\text{-}fractal}$ = 2.75 nm and a fractal dimension of $D_f$ = 2.8. The dashed blue line displays the contribution of the segmental units normalised by $DP_w$. Here, a radius of gyration of $R_{G\text{-}segments}$ = 0.3 nm was calculated. These structural parameters are in good agreement with the data obtained by SANS (Tab. 9).

## 6.2.2. Core-multishell (CMS) nanoparticles

### 6.2.2.1. Light scattering

The hydrodynamic dimensions of the CMS-molecules dispersed in aqueous surrounding were determined by DLS measurements [140]. The evaluation of the auto-correlation functions of highly diluted samples revealed the corresponding relaxation rates $\Gamma(q)$ at different scattering angles $\theta$. The correlation between $\Gamma$ and $q^2$ illustrated in Fig. 50 demonstrates a linear dependence [140]. The translational diffusion coefficient $D_T$ can be calculated from the slope of the correlation. The related hydrodynamic mean radius was determined from the *Stokes-Einstein* relation with $R_H$ = 8.9 ± 0.4 nm [140]. The evaluation of the auto-correlation functions for measurements carried out at $\theta$ = 90° and $T$ = 25 °C employing the CONTIN-algorithm [139] reveals the size distribution demonstrated by the blue line in Fig. 52 with a corresponding distribution width of approximately 5.0 nm.

Additionally, non-polar dispersions of the CMS-molecules were tested at $T$ = 25 °C. The molecules dispersed in chloroform revealed a hydrodynamic radius of $R_H$ = 6.1 ± 0.3 nm. This value is significantly smaller as the corresponding one obtained from the aqueous dispersion. This is an evidence for substantial structural changes of those molecules when being dispersed in non-polar media. For CMS-nanoparticles dispersed in toluene no evaluable auto-correlation functions were obtained.

The general hydrodynamic dimensions of the CMS-particle in polar and non-polar dispersions determined by DLS measurements are below 10 nm. Thus, these particles appear highly suitable for the purpose of pharmaceutical applications [52,57,59,200].

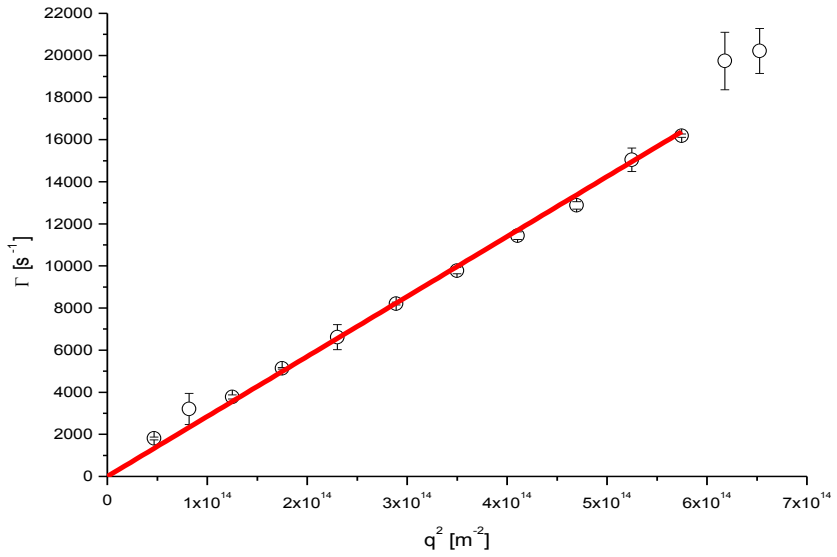


**Fig. 50: Relaxation rates $\Gamma$ as a function of $q^2$ as derived from CMS-nanoparticles dispersed in $H_2O$ and measured at 25°C (open symbols) and respective linear regression (red solid line).**

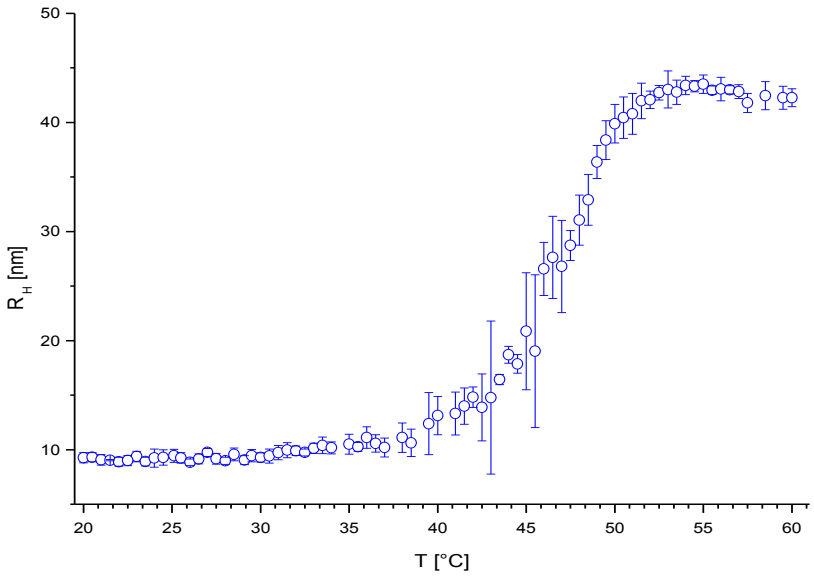


**Fig. 51: Temperature dependence of the hydrodynamic radius $R_H$ of CMS-nanoparticles dispersed in $H_2O$.**

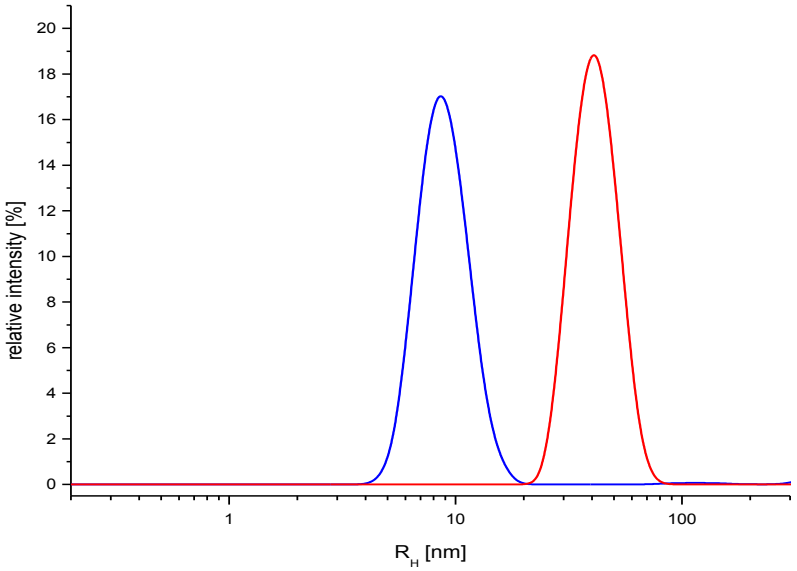


**Fig. 52: Results from the CONTIN-analysis of the auto-correlation functions ($\theta = 90°$) of CMS-nanoparticles dispersed in $H_2O$ at 25 °C (blue line) and 60 °C (red).**

The influence of the temperature on aqueous CMS-nanoparticles dispersions was examined in the range 20 °C < $T$ < 60 °C (Fig. 51). A significant size trend was observed. It reveals a considerable increase of the hydrodynamic particle size above 35 °C and a maximum size was reached at 55 °C. The CONTIN-analysis gave $R_H \approx 42$ nm with a corresponding distribution width of approximately 22 nm (Fig. 52, red line). The sample was measured several times and thus revealed a full reversibility. The size trend can be explained by coagulation of individual CMS-molecules to form a secondary structure of well-defined size during the heat treatment. The well-behaved formation of secondary structures might have a promising purpose in further studies of the encapsulation properties of the CMS-nanocarriers as their efficiency and capacity can significantly be influenced.

The effective encapsulation of guest molecules of different composition is one of the major advantages of this nanocarrier system [58,59,60,61,63]. To mimic common active agents, dye-molecules with a similar hydrophilicity were used. Furthermore, using dyes allowed their tracking by common lab instrumentation as for instance UV-Vis spectroscopy [58]. For the present investigations the azo-dye Congo red was used as polar guest molecule and the dye β-carotene as corresponding non-polar representative (Fig. 53). The measurements addressed to the embedding of the dyes were performed with suspensions of CMS-molecules with a weight fraction of approximately $\omega_{CMS} \approx 0.01$ wt%. The respective dye concentration was in the millimolar range. The measurements were performed in the solvent and additionally in the corresponding non-solvent of the dye molecules, realised by a preceding solvent exchange. The DLS measurements reveal a significant increase of the hydrodynamic radii after addition of the dye molecules to mixtures of the CMS-particles and the respective non-solvent of the dye (Fig. 54). The Congo red containing dispersion with chloroform as medium show a sharp peak at $R_H = 36 \pm 2$ nm. In comparison the $\beta$-carotene containing sample shows a broad size distribution with a maximum at $R_H = 46 \pm 5$ nm. A minor peak within this broadened distribution was found at approximately $R_H \approx 15$ nm. This can be explained with the encapsulation of the non-miscible dye molecules within a supramolecular host structure

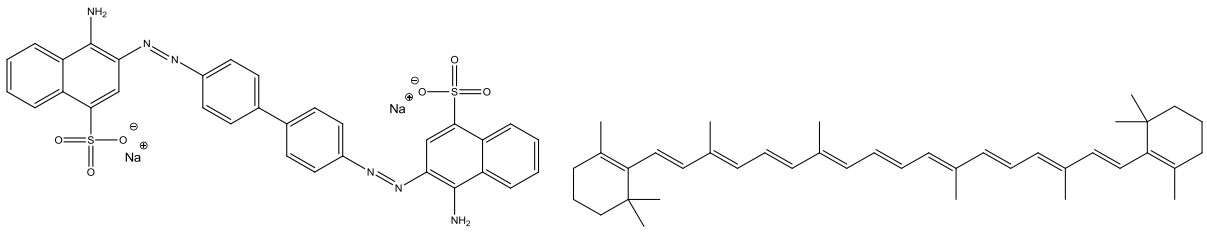


**Fig. 53: Chemical structure of the azo-dye Congo red (left) and the natural dye β-carotene (right).**

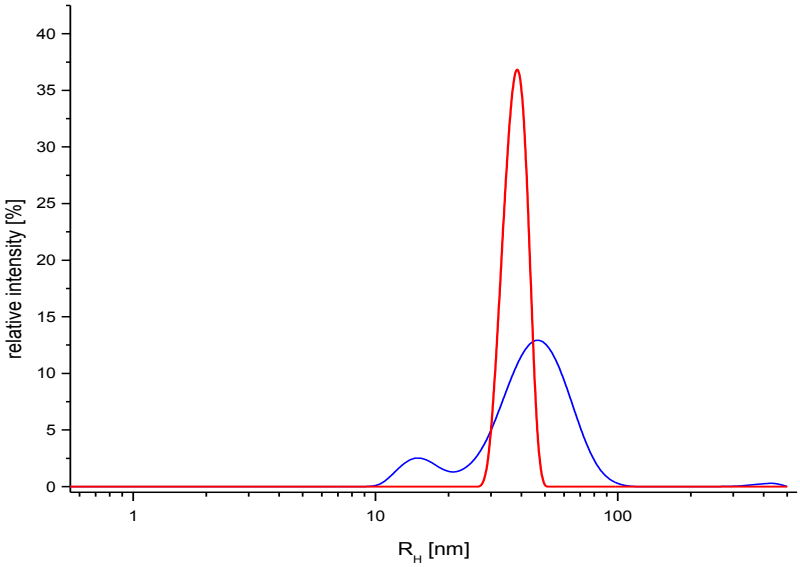


**Fig. 54: CONTIN-analysis of auto-correlation functions of CMS-molecules charged with the polar dye Congo red measured in chloroform (red curve) and respectively non-polar β-carotene (blue curve) in water. The measurements of the encapsulated dye molecules were carried out in the corresponding non-solvent of the dye molecules at 25 °C.**

formed by the CMS-unimers. The presence of the guest molecules initiates the formation of these superstructures [59,60,219]. The recent investigations underline the results from earlier reports. Nevertheless, the spatial distribution of the guest molecules within these aggregates cannot be investigated by DLS. For a clarification of the embedding mechanism further analyse of the CMS-nanocarrier structure and the structure of the supramolecular aggregates by complementary methods is essential.

### 6.2.2.2. Cryogenic Transmission Electron Microscopy – cryoTEM

Cryogenic sample preparation in conjunction with TEM analysis was already successfully accomplished by Radowski and co-worker in order to reveal the general morphology of their CMS-particles and to follow the formation of supramolecular aggregates by the encapsulation of model-guest molecules [58]. For the present analysis, the CMS-nanoparticles based on hPG were studied in a highly diluted aqueous dispersion. The representative micrographs illustrated in Fig. 55 depict the CMS-particles as dark shaded dots embedded in the matrix of vitrified amorphous ice. The shape of the dispersed molecules can be described as almost spherical. The statistical evaluation revealed a corresponding radius of these spheroids of $R$ = 5.3 ± 3.2 nm. These dimensions are in agreement with the data from the DLS experiments as the hydrodynamic radius is expected to be larger than the real dimensions of the probed structures. Nevertheless, the limited contrast of the polymer to the surrounding matrix and the limited resolution of the method for sizes below 10 nm should be taken into account. Moreover, this technique is not suitable to answer issues on the microstructure of the CMS-particles. The micrographs show the tendency of the CMS-nanoparticles to form anisotropic aggregates composed of just a few CMS-nanoparticle unimers.

For the verification of the temperature dependent size trend determined by DLS (refer to section 6.2.2.1) an aqueous dispersion of CMS-particles was slowly tempered to 60 °C and plunge freeze for the analysis by cryo-TEM (Fig. 56). The sample depicts the formation of supramolecular aggregates with a diameter between 100 nm and 200 nm. These dimensions are above the values determined by

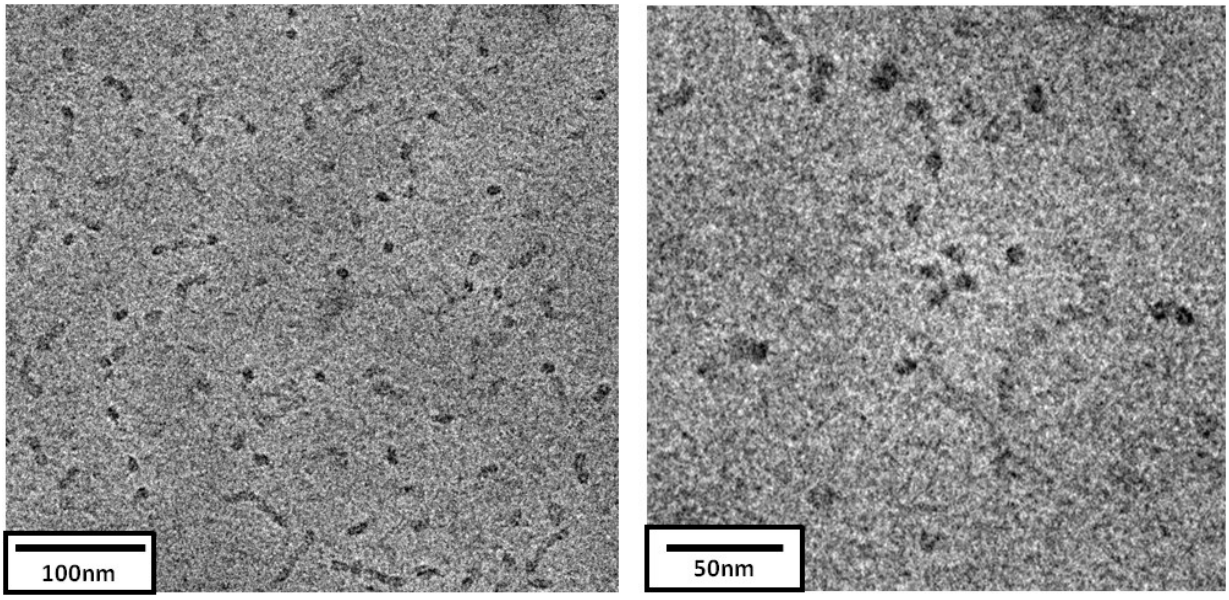


**Fig. 55: Cryo-TEM micrographs of diluted aqueous dispersions of CMS-nanoparticles.**

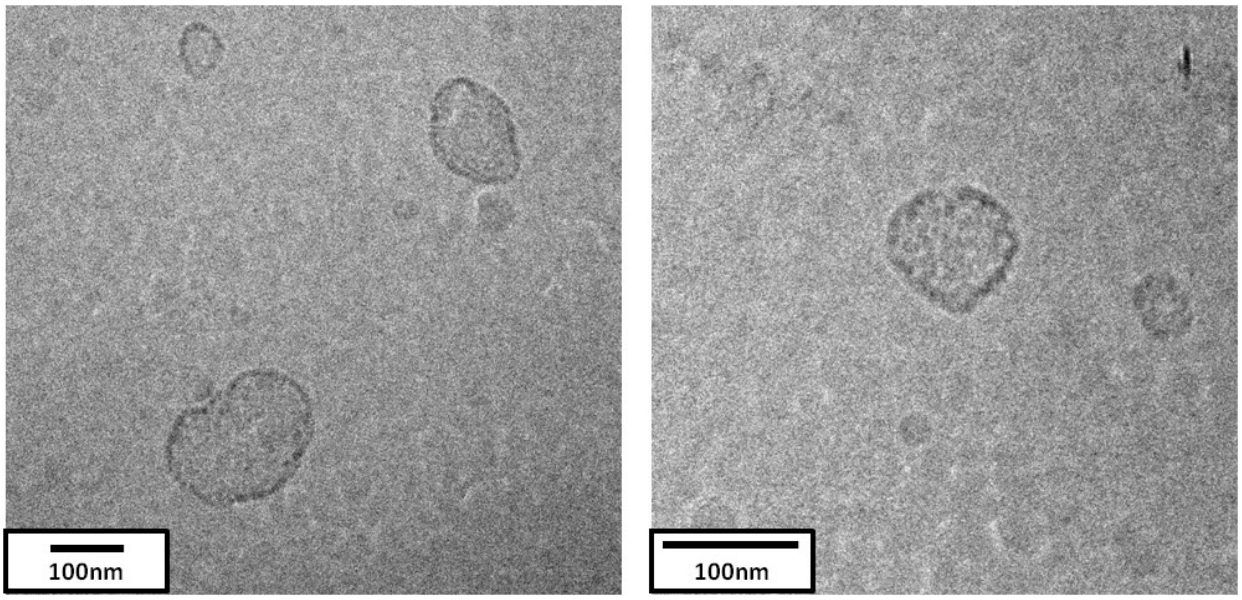


**Fig. 56: Cryo-TEM micrographs of a dispersion of CMS-nanoparticles tempered to 60 °C and plunge freeze after equilibration.**

the DLS analysis. Moreover, the micrographs reveal structures with a certain polydispersity and polymorphology. This must be explained by the preparation of the dispersions at increased temperatures. During the DLS experiments a continuous increase of the temperature of approximately 0.5 K to 1 K per ten minutes could be realised, leading to aggregates with a narrow size distribution whose formation could be followed online. During the sample preparation for investigations by cryo-TEM, this precise temperature control could not be realised.

### 6.2.2.3. Small Angle Neutron Scattering – SANS

### Non-polar CMS-nanoparticle dispersions

The analysis of the CMS-particles dispersed in non-polar surrounding are of particular interest for the evaluation of the basic molecular parameters. Furthermore, it will improve the understanding of the universal solubility of the CMS-structure and the host-guest process in a potential drug delivery application [58,59]. Furthermore, this opens up insight into the processes that permit the CMS-particles to interact with lipid membranes during the transport of active agents to the site of action [59,60,61,62].

#### *Variation of the CMS-nanoparticle concentration*

To validate the influence of inter-particle correlations between the CMS-particles, a concentration series using pure toluene D-8 as dispersion medium was analysed. The respective compositions of the samples are provided in Tab. 10. The correcting of the SANS-intensities employing equation (51) yielded the intensities displayed by the solid symbols in Fig. 57. From the normalised scattering intensities, the influence of the inter-particle interactions appear less prominent as this was found for the hyperbranched scaffold molecules dispersed in $D_2O$ (refer to section 6.2.1.2).

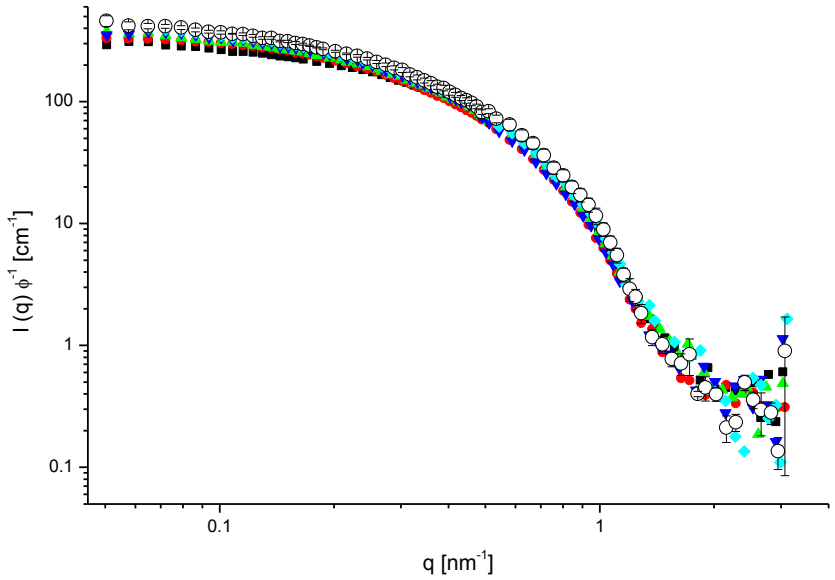


**Fig. 57: SANS-intensities of CMS-nanoparticles dispersed in toluene D-8 normalised by $\phi$ as obtained from a concentration series. The extrapolated SANS-intensities for vanishing particle volume fraction $I_0(q)$ are provided by respective open symbols.**

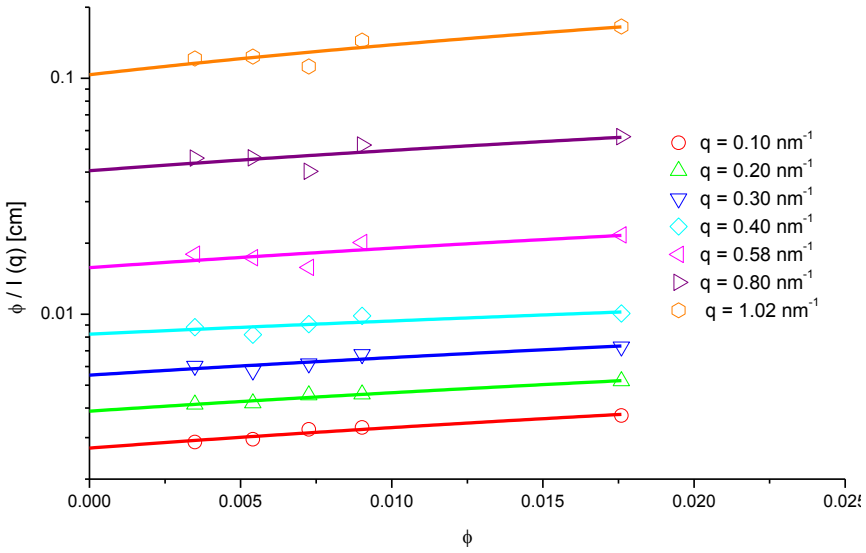


**Fig. 58: Correlation between $I(q, \phi)$ and $\phi$ for selected $q$-values. The solid lines represent the extrapolation for vanishing $\phi$.**

The scattering intensities at infinite dilution $I_0(q)$ were extrapolated from the correlation between $\phi / I(q, \phi)$ and $\phi$ (Fig. 58), which are respectively provided by the open symbols in Fig. 57. Only at the highest $q$-values this extrapolation is affected by poor statistics of the measured small angle scattering. With respect to equation (13) the structure factor $S(q)$ was calculated.

The analysis of $S(q)$ at small $q$-values was used for the determination of the effective inter-particle distance and $S(0)$ by the equations (58) and (59). From the correlation between $1 / S(q)$ and $q^2$ the corresponding $d_{eff}$ was determined to be approximately $d_{eff} \approx 9$ nm (Fig. 59). The analysis of the

**Tab. 10: Overview on the concentration series of CMS-nanoparticles in non-polar dispersions analysed by SANS. The scattering intensities were analysed with respect to the influence of inter-particle correlations using equations (58) and (59).**

| $\omega$ | $\phi$ | $d_{eff}(S(0))$ | $d_{eff}(S(q^2))$ | $S(0)_{exp}$ |
|---|---|---|---|---|
| wt% | | nm | nm | |
| 1.95 | 0.0176 | 9.3 ± 0.6 | 7.1 ± 0.4 | 0.73 |
| 1.00 | 0.0090 | - | - | - |
| 0.80 | 0.0073 | 9.9 ± 0.6 | 8.1 ± 0.1 | 0.84 |
| 0.60 | 0.0054 | 9.3 ± 0.6 | 8.7 ± 0.1 | 0.89 |
| 0.39 | 0.0035 | - | - | - |

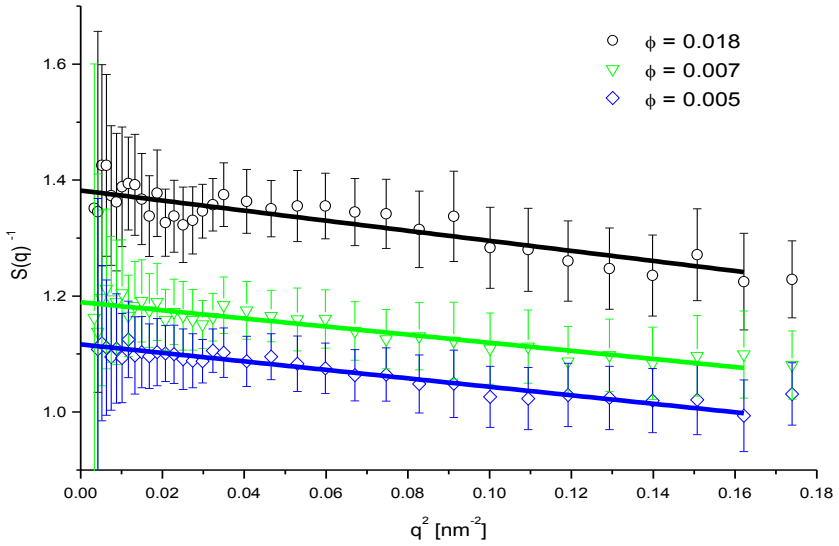


**Fig. 59: 1 / $S(q)$ as a function of $q^2$ for the calculation of $d_{eff}$ according to equation (58).**

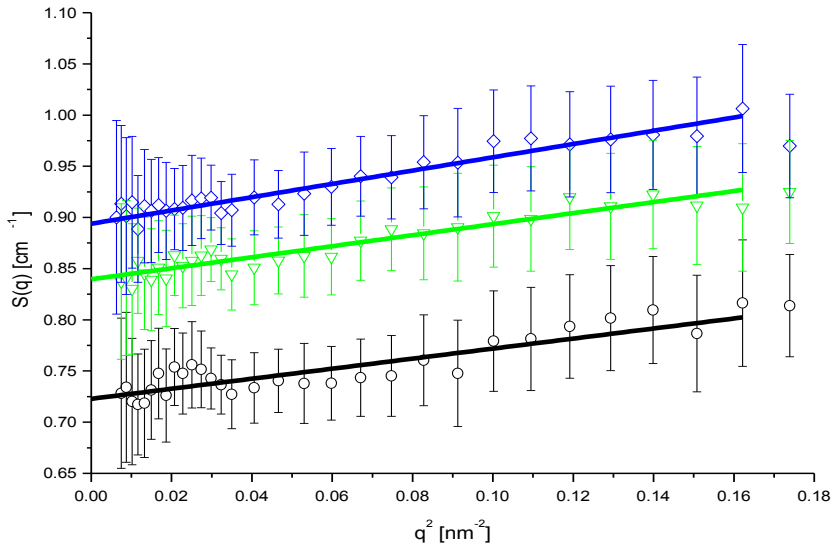


**Fig. 60: Extrapolation towards vanishing $q^2$ of the scattering vector for the determination of $S(0)$.**

forward-scattering regime of $I_0(q)$ (Fig. 61) using the *Guinier*-equation (14) reveal the particle dimension with $R_G = 5.9 \pm 0.2$ nm. Comparing $d_{eff}$ and $R_G$ shows $d_{eff}$ to be in the range expected for non-charged hard spheres for which $2R_G \approx d_{eff}$ is valid. The extrapolation of $S(q)$ toward vanishing $q$-values is illustrated in Fig. 60 and the corresponding results concerning $S(0)$ are provided in Tab. 10.

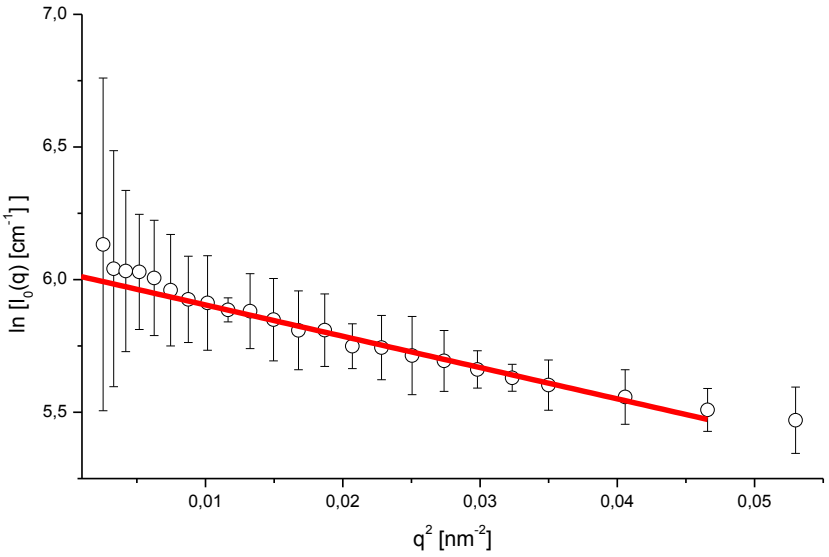


**Fig. 61: Linearised SANS-intensities $I_0(q)$ of the CMS-particles dispersed in toluene D-8. The solid red line corresponds to the linear fit according to the *Guinier*-formula (14).**

### *Variation of the scattering contrast*

Further insight into the spatial structure of the CMS-nanoparticles in a non-polar environment is gained by contrast variation experiments. Therefore, mixtures of toluene ($C_6H_5CH_3$) and its deuterated analogon toluene D-8 ($C_6D_5CD_3$) were used as dispersions media. The hereby accessible scattering length density ranges from $b_m = 0.935 \cdot 10^{10}$ cm$^{-2}$ for hydrogenated toluene to $b_m = 5.662 \cdot 10^{10}$ cm$^{-2}$ for toluene D-8. The scattering intensities of the CMS-molecules dispersed in mixtures containing different amounts of the deuterated toluene are provided in Fig. 62. These were

**Tab. 11: Overview on the contrast variation experiments in non-polar media and the results corresponding to the *Guinier*-analysis based on equation (14).**

| $C_6H_5CH_3 : C_6D_5CD_3$ | $\omega$ | $\phi$ | $b_m$ | $\rho_m$ | $R_G$ |
|---|---|---|---|---|---|
| | wt% | | $10^{10}$ cm$^{-2}$ | g cm$^{-3}$ | nm |
| 0 : 1 | 1.00 | 0.0090 | 5.66 | 0.943 | 5.8 ± 0.3 |
| 12 : 35 | 1.00 | 0.0088 | 4.45 | 0.922 | 5.8 ± 0.2 |
| 7 : 43 | 0.99 | 0.0088 | 5.00 | 0.932 | 5.5 ± 0.2 |
| 23 : 18 | 1.00 | 0.0086 | 3.00 | 0.898 | 5.8 ± 0.2 |
| 99 : 29 | 0.99 | 0.0084 | 2.00 | 0.881 | 5.8 ± 0.4 |

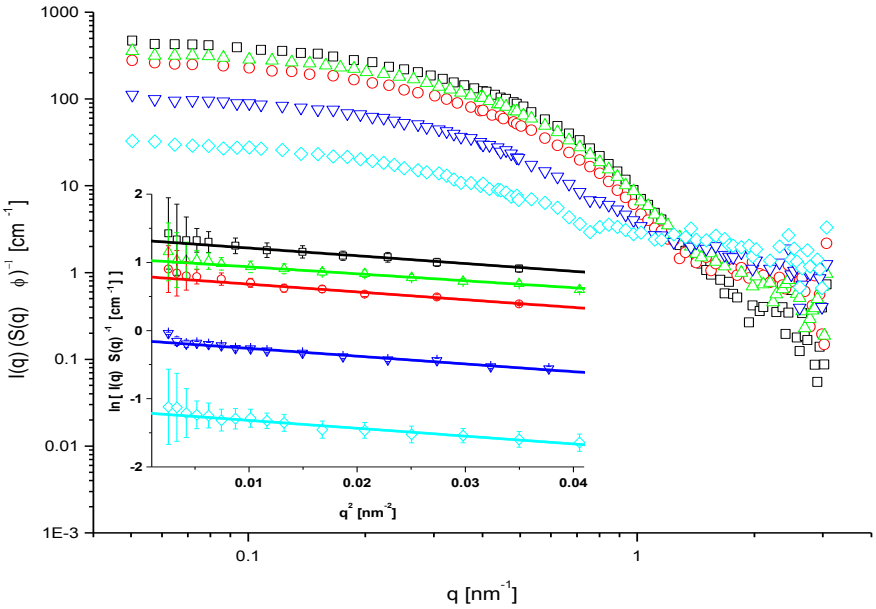


**Fig. 62: SANS-intensities from contrast variation experiments with CMS-molecules dispersed in non-polar media. The scattering intensities are normalised by volume fraction. (contrast media – $C_6H_5CH_3$ : $C_6D_5CD_3$ = 1 : 0 – black squares, 12 : 35 – red circles, 7 : 43 – green triangles, 23 : 18 – cyan diamonds, 99 : 29 – blue triangles). The inset displays the *Guinier*-plot of the linearised scattering intensities. The solid lines correspond to linear fits using equation (14).**

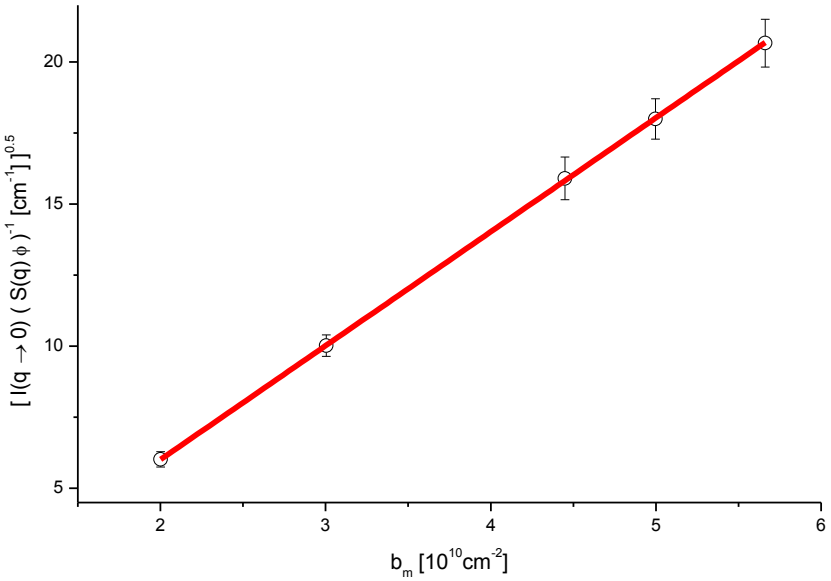


**Fig. 63: Forward scattering intensities $I(q \rightarrow 0)$ as a function of the scattering length density of the dispersion medium $b_m$ according to equation (27).**

obtained by the subtraction of the scattering contribution of the corresponding dispersion media employing equation (51). Here, also $S(q)$ as determined from the analysis of the concentration series was considered. The relevant parameters of the investigated dispersions are provided in Tab. 11, which includes the results from the *Guinier*-analysis by equation (14). The corresponding linearised scattering intensities at vanishing $q$-vectors are illustrated by the inset of Fig. 62. The values of the forward scattering intensities determined from this procedure were used for the calculation of $b_p$, as

well as for the extrapolation of the respective average particle volume by equation (27). The correlation employing $I(q \rightarrow 0)$ as a function of $b_m$ is displayed in Fig. 63. Hence, an average particle volume of $V_P = 161 \pm 1$ nm$^3$ was determined and the corresponding value of $b_P$ was extrapolated with $b_P = 0.50 \pm 0.01 \cdot 10^{10}$ cm$^{-2}$. This value is not covered by the accessible SLD-range from mixtures of toluene and toluene D-8.

The average particle scattering length density leads to the scattering contrast $\Delta b$, which furthermore allows the calculation of the molecular weight to be $M_w = 96.7 \pm 8.0$ kg mol$^{-1}$. The following assumption was based on the molecular parameters of the hyperbranched scaffold molecule (refer to chapter 6.2.1) and the attached di-block segments. The hPG carries in average 134 hydroxyl-groups, which could be functionalised in the following steps of the synthesis (refer to section 6.2.1.1). The molecular weight of the CMS-molecules of approximately 97 kg mol$^{-1}$ is obtained for an entire functionalised hPG with $C_{18}$-mPEG$_7$ blocks, each having a molecular weight of approximately $M_{w\,shell} \approx 620$ g mol$^{-1}$. This finding is in contrast to the prediction from the synthesis protocol as only 70 % of the functional groups are supposed to be reactive for further coupling reactions (refer to section 5.1.3.). The theoretical molecular weight of the CMS particles is 69.4 kg mol$^{-1}$.

The scattering intensities with respect to the individual scattering contrasts $\Delta b$ as illustrated in Fig. 64. The plot demonstrates that the variation of the scattering contrast does not lead to a significant variation of the scattering intensities in the low-$q$ region. Notwithstanding, for values of the scattering vector above 0.3 nm$^{-1}$ the scattering intensities diversify significantly. The overall shape of the particles, which correlates with the respective scattering at small $q$-values therefore appears independent from contrast variation.

The radius of gyration at infinite contrast $R_{G\infty}$ is a direct measure for the particle dimensions. By employing the *Stuhrmann*-relation provided by equation (29) $R_{G\infty}$ and the quantity $\alpha$ were extracted to be $R_{G\infty} = 6.1 \pm 0.3$ nm$^{-1}$ and $\alpha = (4.09 \pm 4.78)\ 10^{-4}$ (Fig. 65). Hence, $\alpha$ indicate a homogeneous

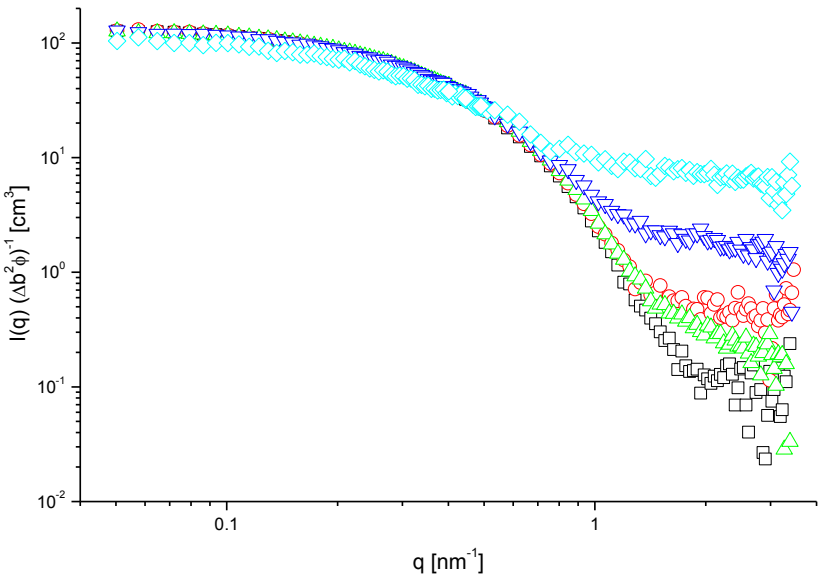


**Fig. 64: Scattering intensities from contrast variation series in non-polar environment normalised by the scattering contrast $\Delta b$ and the volume fraction $\phi$. The respective colour and symbol code refers to Fig. 62.**

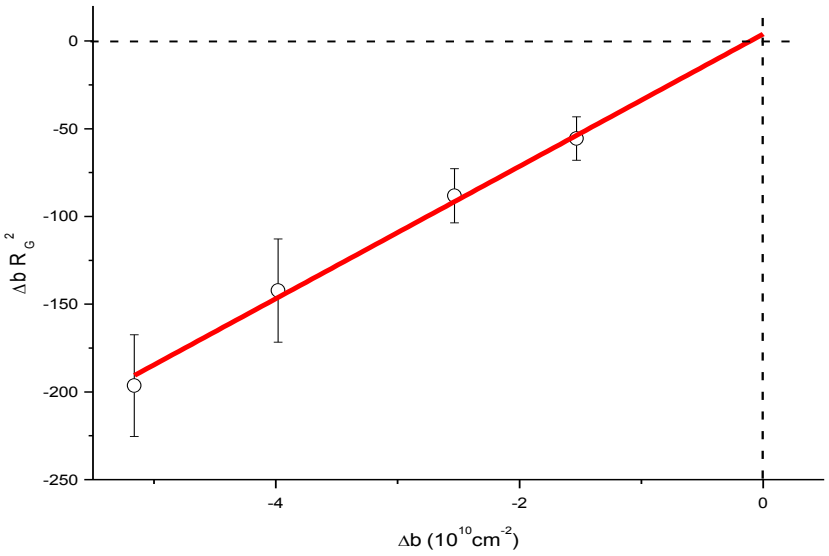


**Fig. 65: *Stuhrmann*-plot: *Guinier*-radius $R_G$ as a function of the scattering contrast $\Delta b$. The solid line represents the fit corresponding to equation (29).**

distribution of the scattering length density within the CMS-particles. Therefore, there is no distinct evidence for a core-shell structure. Spatial inhomogeneity only contributes for smaller length scales probed beyond 1 $nm^{-1}$. The particle dimension determined from the *Stuhrmann*-relation is almost in the range of $R_G$ obtained from the *Guinier*-analysis of the concentration series in $D_2O$. Furthermore, the calculated $R_G$ is in the range of the hydrodynamic radius determined by DLS (refer to section 6.2.2.1) [204].

Further insight into the spatial structure can be gained by employing the contrast decomposition procedure provided by equation (23). For selected $q$-values, the results of the parabolic fit algorithm are illustrated in Fig. 66. Here, especially the low-$q$ region is suitable, as described in this procedure. Nevertheless, for $q > 1.5\ nm^{-1}$ the fit becomes less distinct. The normalised scattering intensities corresponding to the particle shape $I_S(q)$ are represented by the open symbols in Fig. 67. Modelling $I_S(q)$ with common geometrical bodies did not lead to a sufficient matching. For comparison the shape function found for fourth-generation dendrimers was tested on $I_s(q)$ with respect to the molecular key parameters $V_P$ and $R_{G\infty}$ [106,107]. For these regular branched structures, the particle shape function could be described by a *Gaussian* over the entire $q$-range. As demonstrated by the dashed green line in Fig. 67, this approach could not describe $I_s(q)$ found for the CMS-particles. The best fit was obtained using the fractal concept [205,206,215]. Thus, the solid red line in Fig. 67 represents the fractal approach provided by equation (62). The fractal dimension was determined with $D_f = 3$ according to the characteristic slope of the scattering intensities. The corresponding particle dimension was calculated with $R_{G\text{-}fractal} = 6.1 \pm 0.2$ nm, which is in good agreement with the results from the analysis of the *Guinier*-regime. The fractal dimension indicates a space filling structure with a corresponding rough surface and which thus correlates with the poor solvent conditions. Furthermore, this is supposed to be accompanied by a backfold of the outermost polar PEO segments towards the polar hPG-core due to their limited miscibility in the non-polar surrounding. The folding of the bridging alkyl segments can be discussed in the same way as done for

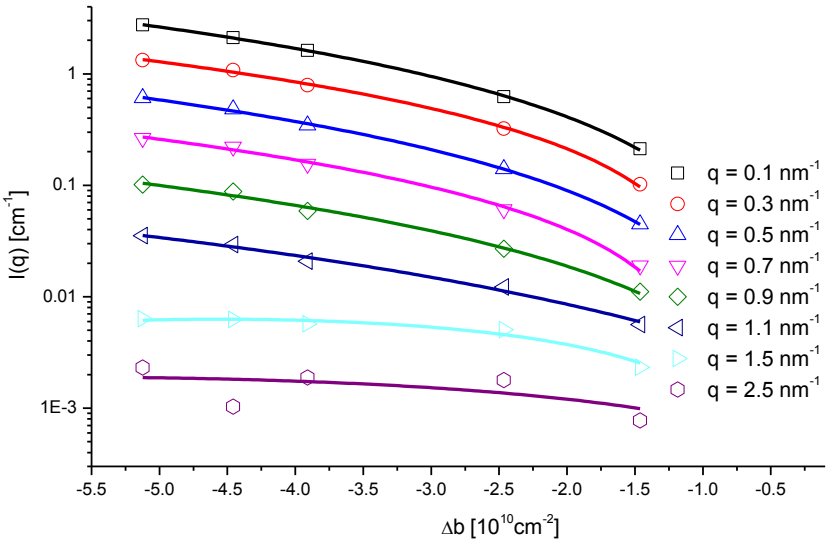


**Fig. 66: Scattering intensities for selected *q*-values as a function of *Δb*. The solid lines represent the results of a parabolic fit algorithm according to equation (23).**

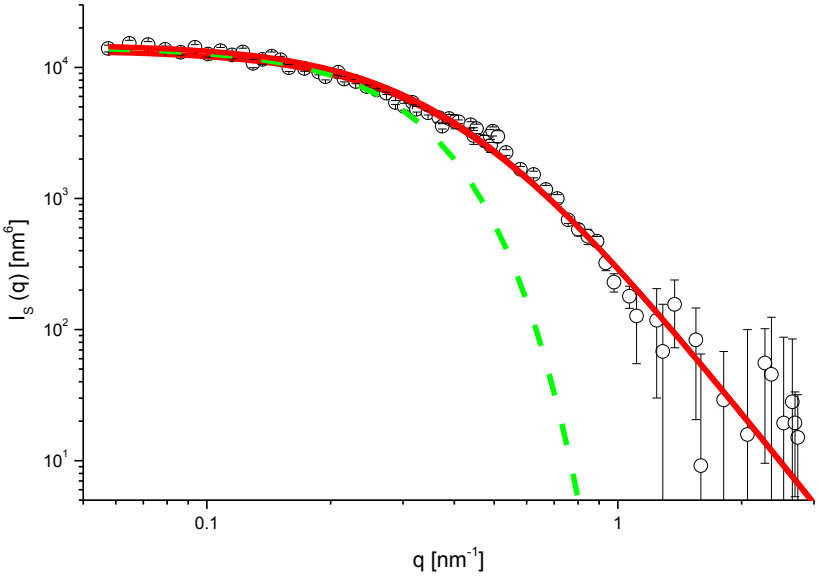


**Fig. 67: Scattering intensities corresponding to the shape term $I_S(q)$ arising from a single particle as obtained from the contrast decomposition of the scattering intensities at varying scattering contrasts by equation (23). The solid line represents the best fit according to the fractal approach [207]. For comparison, the shape function found for dendrimers (dashed green line) was calculated with the extracted molecular key parameters of $V_P$ and $R_{G\infty}$ [106,107].**

alkyl chains in polymers forming narrow loops by just a few monomer units [176]. Moreover, the high degree of functionalisation additionally contributes to the space filling of the architecture. In conclusion, the small and compact structure together with a hydrophobic interphase, which results from the backfold of the attached chains is a favourable conformation for the interactions with non-polar domains and evidence for the universal solubility of the CMS molecules.

The scattering intensities deriving from the particle inner structure $I_I(q)$ and the corresponding cross-term $I_{SI}(q)$ are displayed by Fig. 68. The contribution of $I_I(q)$ reveals the expected decrease towards smaller $q$-values, as it does not contribute to the particle shape essentially, confirming that the decomposition procedure is sensitive. The scattering intensities of $I_I(q)$ could not be correlated to distinct structural features of the CMS-structure. This nNotwithstanding, the contribution is supposed to arise from the hPG scaffold microstructure, but also from the attached co-bloc polymer. Here, the isotropic distribution of the hydrogen on short length scales is correlating with the observed scattering in the high-$q$ regime. These aspects could not be resolved in more detail from the measurements.

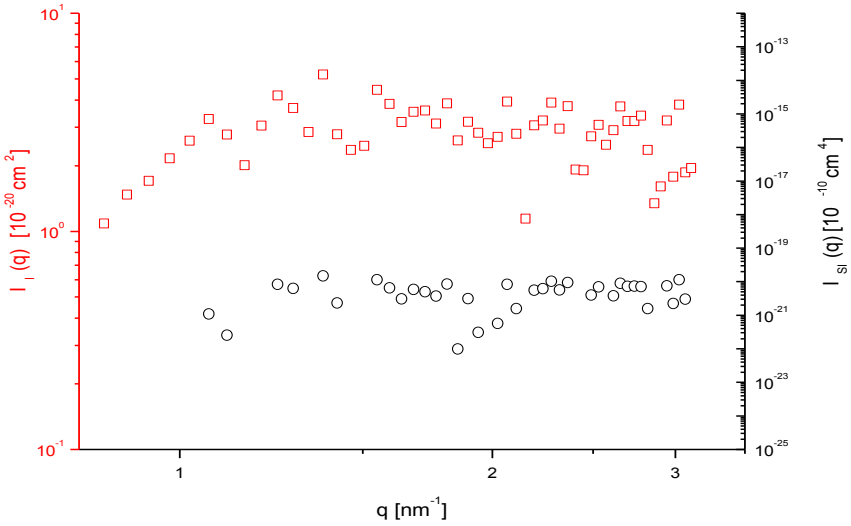


**Fig. 68: Scattering intensities of the inner-term $I_I(q)$ (red squares) and cross-term $I_{SI}(q)$ (black circles) as obtained by the contrast decomposition procedure.**

## Aqueous CMS-nanoparticle dispersions

For the application of the CMS-nanoparticles as a drug delivery platform, their spatial structure in aqueous media is of particular interest. Therefore, the structural characteristics of the CMS-molecules in polar media were a focal point using the analysis of a contrast variation series by SANS. Hence, five different mixtures of $H_2O$ and $D_2O$ with a corresponding $b_m$ of $6.36\ 10^{10}\ cm^{-2} < b_m < 0.30\ 10^{10}\ cm^{-2}$ were utilised to tune the scattering contrast to the dispersed CMS-molecules. The background corrected volume fraction normalised scattering intensities are illustrated in Fig. 69.

The influence of $S(q)$ on the scattering intensities for polar CMS-nanoparticle dispersions could not be analysed in more detail. From complementary SAXS-analyses of concentration series, no distinct trend in the evolution of the scattering intensities with varied particle volume fraction could be verified. Thus, the extrapolation of the intensities at infinite dilution $I_0(q)$ could not be accomplished with the needed accuracy. This issue is discussed in more detail in section 6.2.2.4. Due to the observations made by SAXS, the concentration dependence was not probed by SANS.

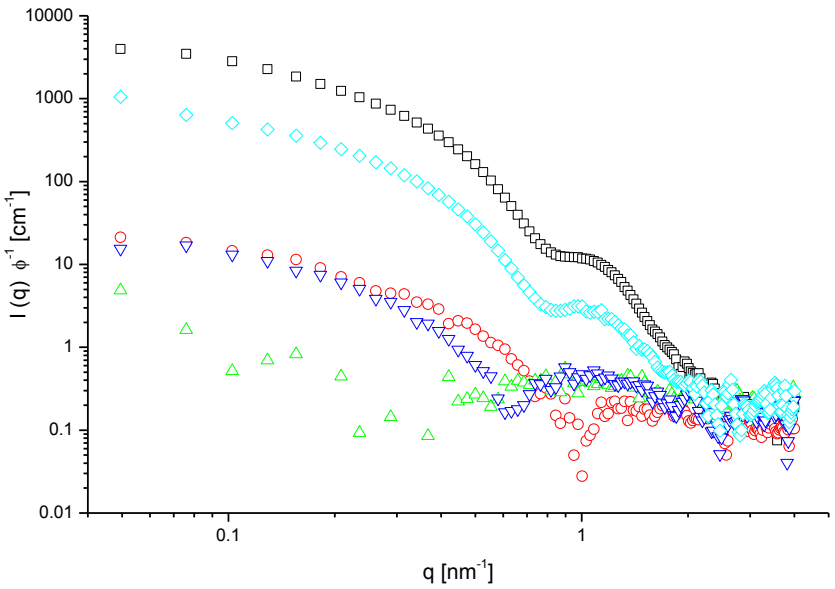


**Fig. 69: SANS-intensities normalised by $\phi$ from the contrast variation series of CMS-nanoparticles dispersed in mixtures of $H_2O$ and $D_2O$ (contrast medium – $D_2O$ : $H_2O$ = 1 : 0 – black squares, 1 : 1 – cyan diamonds, 13 : 90 – red circles, 1 : 3 – blue down-triangles, and 3 : 13 – green up-triangles).**

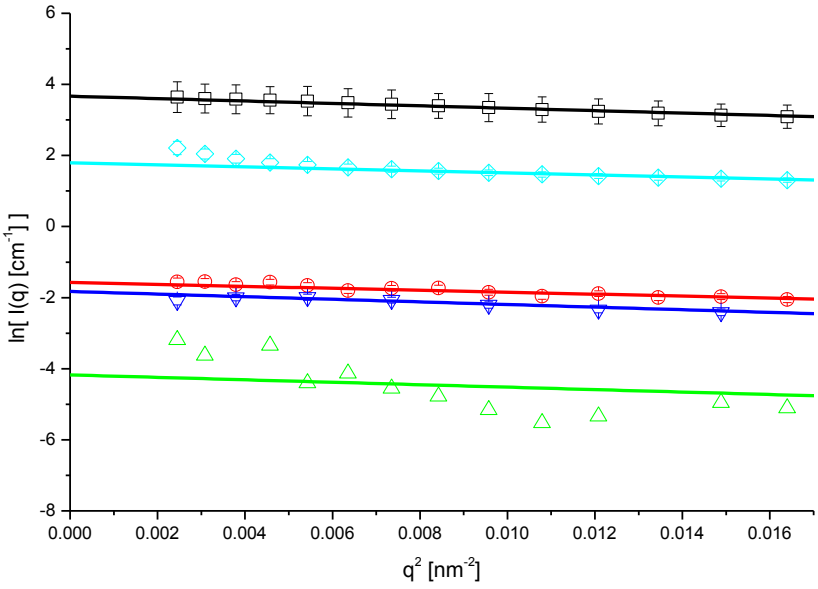


**Fig. 70: *Guinier*-plot: Linearised forward scattering intensities from the contrast variation series of CMS-nanocarriers dispersed in aqueous medium. The respective fits of equation (14) are represented by the solid lines. The colour and symbol code is taken from Fig. 69.**

The values of $R_G$ and respective $I(q \rightarrow 0)$ were obtained from the analysis of the linearised scattering intensities at low $q$-values by equation (14), which is illustrated in Fig. 70. The results and the details of the measured dispersions are provided in Tab. 12. The determination of the average particle volume $V_P$ and the corresponding average scattering length density $b_m$ of the CMS-particles in polar dispersions was done according to equation (27). The correlation illustrated in Fig. 71 revealed $V_P$ = 1260 ± 100 nm$^3$ and $b_P$ = 0.61 ± 0.11 cm$^{-2}$. The particle volume determined hereby is by eightfold higher, just as it is the case for the CMS-structures in non-polar media. This results from the

**Tab. 12: Overview on sample composition for the contrast variation series of CMS-nanoparticles with mixtures of $H_2O$ and $D_2O$. The results from the *Guinier*-analysis are additionally tabulated.**

| $H_2O$ : $D_2O$ | $\omega$ | $\phi$ | $b_m$ | $\rho_m$ | $R_G$ |
|---|---|---|---|---|---|
| | wt% | | $10^{10}$cm$^{-2}$ | g cm$^{-3}$ | nm |
| 0:1 | 0.97 | 0.0096 | 6.36 | 1.1044 | 10.1 ± 0.3 |
| 1:1 | 0.91 | 0.0087 | 3.00 | 1.0535 | 9.2 ± 0.4 |
| 3:1 | 0.84 | 0.0078 | 1.08 | 1.0247 | 10.5 ± 0.7 |
| 13:3 | 0.92 | 0.0085 | 0.71 | 1.0190 | 9.2 ± 4.0 |
| 90:13 | 1.08 | 0.0099 | 0.30 | 1.0129 | 9.1 ± 0.9 |

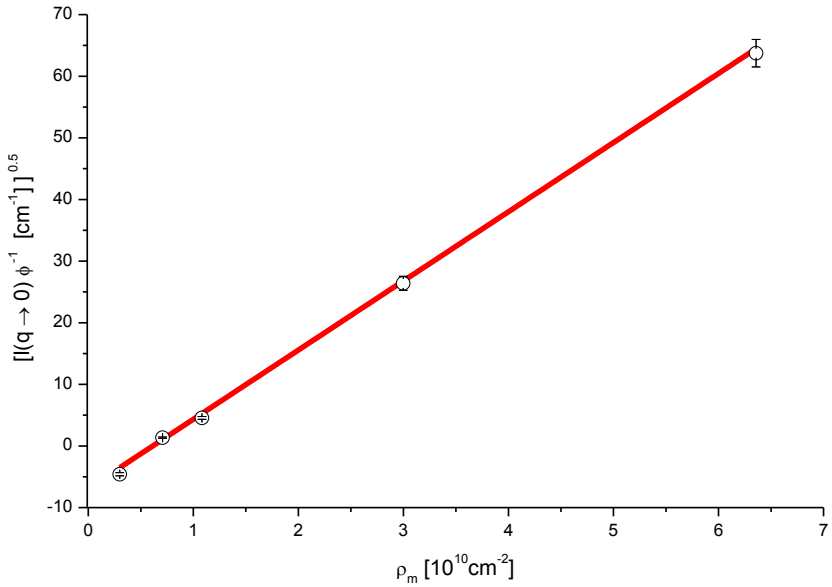


**Fig. 71: *Square root*-plot: Volume fraction normalised forward scattering intensities $I_0(q\rightarrow 0)$ as a function of the scattering length density of the dispersion medium $b_m$.**

formation of non-permanent aggregates by individual CMS-unimers. The general tendency to form respective associates was already observed and discussed for the diluted samples analysed by means of cryo-TEM (refer to chapter 6.2.2.2). Hereinafter, $b_P$ was used for the calculation of the individual scattering contrasts $\Delta b$. The corresponding scattering intensities considering $\Delta b^2$ and $\phi$ as shown in Fig. 72 reveal the influence of the scattering contrast on the small angle scattering. At low $q$-values the scattering intensities appear less influenced by the variation of $b_m$ and can be ascribed to the scattering contribution arising from the shape of the structure. With variation of the scattering contrast the inner structure is accessible, whose scattering contribution reveals a distinct dependence on $\Delta b$. Thus, the internal structure appears to contain small compartments by which the hydrophilic regions are separated from each other (Fig. 76). A distinct core-shell structure of the CMS-particles can be ruled out.

The overall particle dimensions provided by $R_{G\infty}$ were extrapolated from the *Stuhrmann*-relation using equation (29) which is illustrated in Fig. 73. From the respective linear regression $R_{G\infty}$ could be

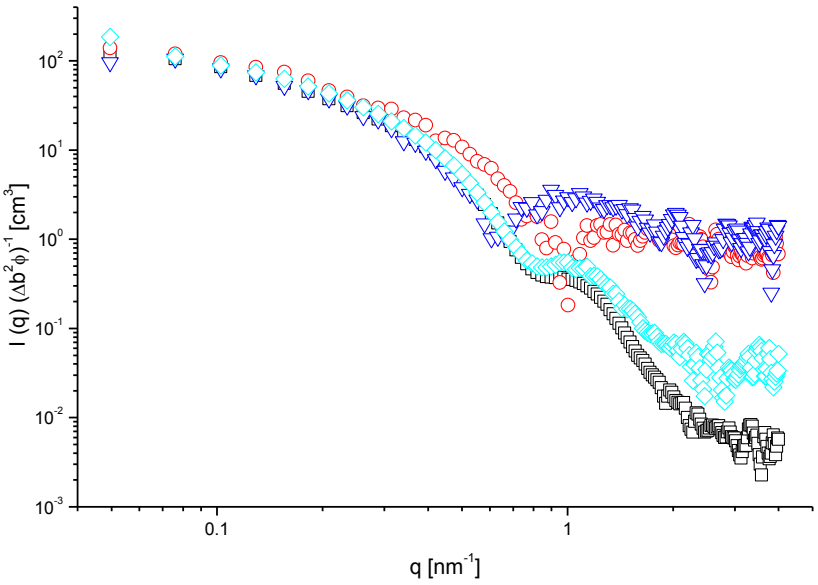


**Fig. 72: SANS-intensities from contrast variation series of the CMS-particles in aqueous media normalised by $\Delta b^2$ and $\phi$. The colour and symbol code is adapted from Fig. 69.**

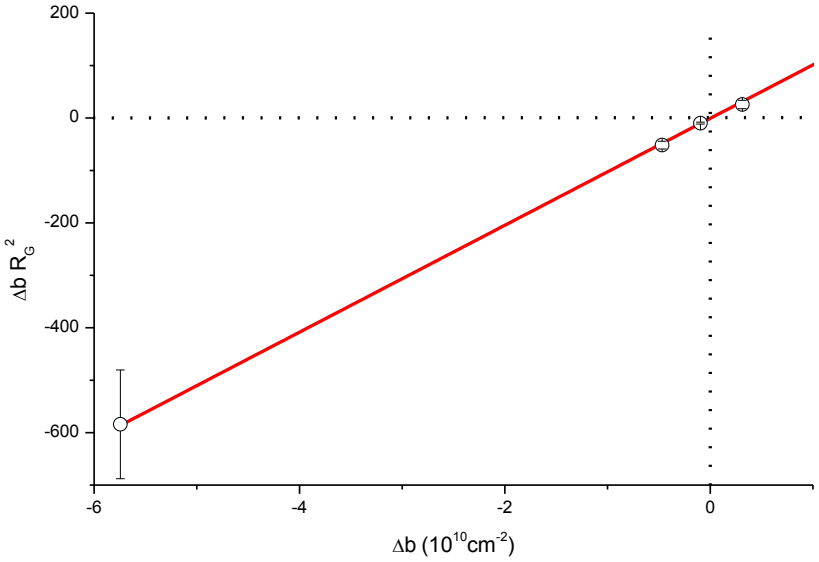


**Fig. 73: *Stuhrmann*-plot: Dependence of the radius of gyration $R_G$ on the contrast $\Delta b$. The solid line shows the linear fit according to equation (29).**

extracted to be $R_{G\infty}$ = 10.1 ± 0.5 nm. These particle dimensions can be addressed to the formation of loose aggregates as the CMS-unimers are expected to be smaller from respective analysis of cryo-TEM micrographs (refer to section 6.2.2.2) and the dynamic light scattering (see section 6.2.2.1). The value of $\alpha$ provided by the intercept of the *Stuhrmann*-relation reveals $\alpha$ = (-0.58 ± 1.07) $10^{-4}$. This value reveals no distinct tendency for the distribution of the scattering length density within the probed structure. The dashed lines provided in Fig. 73 accentuate the contrast inversion obtained due to the variation of $b_m$.

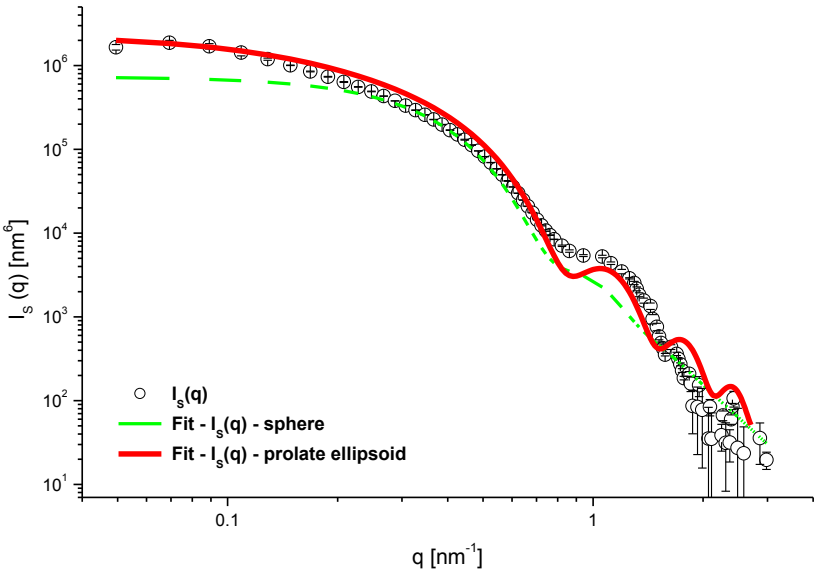


**Fig. 74: Scattering intensity assigned to $I_S(q)$ of the CMS-molecules dispersed in aqueous media as obtained from contrast decomposition according to equation (23). The solid red line represents the best fit a prolate ellipse referring to the formation aggregates by individual unimers. The dashed green line represents the fit of a sphere with a polydisperse mean radius.**

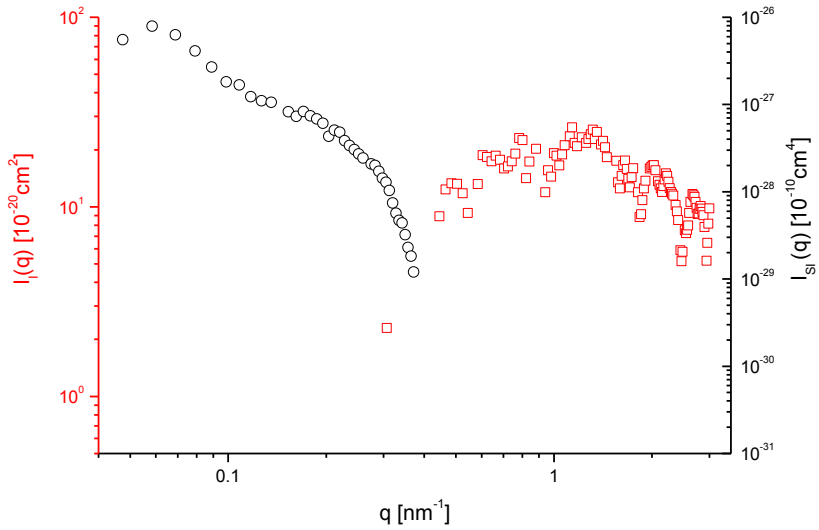


**Fig. 75: Scattering intensities from contrast decomposition according to the contribution of the inner –term $I_I(q)$ (open red squares) and the cross term $I_{SI}(q)$ (open black dots).**

The scattering intensities obtained from the different scattering contrasts served for the decomposition according to formula (23). The scattering intensities corresponding to $I_S(q)$ are provided by the open symbols in Fig. 74. These were modelled with common geometrical bodies with respect to the model independent parameter extracted from the *Guinier*-regime. The dashed green line in Fig. 74 represents the fit according to a sphere having a mean radius of $R_{sphere}$ = 5.4 ± 0.9 nm These dimensions are in the range of the dimensions obtained for the CMS-unimers by cryo TEM (refer to section 6.2.2.2). Nevertheless, this approach did not lead to a sufficient congruence of the

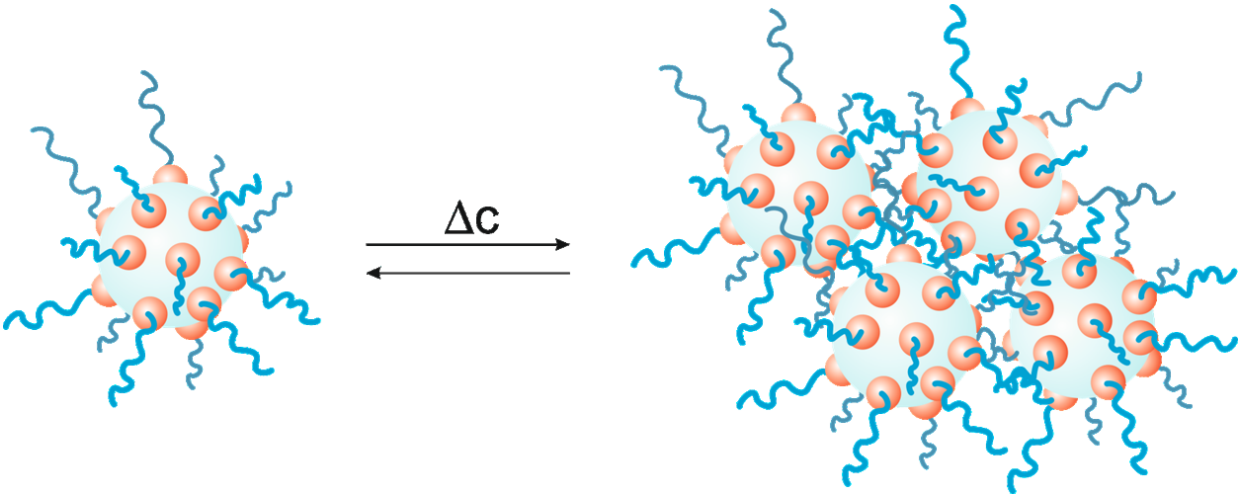


**Fig. 76: CMS-nanoparticles dispersed in aqueous surrounding represented by patchy colloids forming non-permanent associates.**

scattering intensities as especially the scattering intensities in the low-*q* region deviate significantly. This is a further evidence for the suggested formation of aggregates by individual CMS-unimers. The scattering intensities calculated for a prolate-spheroid, revealing the shape of the aggregated CMS-nanoparticles, is provided by the solid red line in Fig. 74 [189,190]. This approach could describe the respective small angle scattering most accurately. The major axis of the ellipsoid was calculated to be $R_{major}$ = 12.6 ± 6.3 nm and the two minor axis with $R_{minor}$ = 5.0 nm. These dimensions refer to a particle volume of $V_P$ = 1260 ± 100 nm$^3$. The scattering intensities of $I_I(q)$ and $I_{SI}(q)$ are provided in Fig. 75.

In contrast to the suggested core-shell structure of the CMS-particles, which is schematically illustrated in Fig. 4, the hydrophobic domains form patches located on the surface of the hydrophilic cores. The hydrophilic PEO-chains stay well dissolved in the aqueous phase. As illustrated in Fig. 76 the single CMS-molecules can be assumed as patchy colloids that show a strong tendency for association upon increasing their concentration. Thus, in the investigated concentration range approximately eight CMS-unimers aggregate due to the contacts of the hydrophobic patches, while the aggregates are stabilised by a layer of PEO-chains. Nevertheless, the CMS-nanotransporter and their respective associates are in a size range that is highly suitable for the in vitro transport of drug molecules, cellular uptake, and skin penetration [52,200].

### 6.2.2.4. Small Angle X-ray Scattering – SAXS

The small angle X-ray scattering of the CMS-nanoparticles was studied at the ASAXS instrument at the BESSY-II in Berlin and at the ID02 beam line at the ESRF in Grenoble. The analysis of the X-ray scattering was supposed to support the findings from neutron scattering and additionally enlarge the accessible set of information on the CMS-nanoparticles from an improved data quality due to the enhanced detection statistics.

## Influence of the dispersion medium

As deduced from the analyses by SANS, the polarity of the surrounding medium plays an important role in the spatial structure of the probed molecules. The SAXS-intensities of the CMS-nanoparticles in polar and non-polar media are shown in Fig. 77. Herein, the scattering intensities of CMS-particles dispersed in water display the characteristic *q*-dependence that was found by neutron scattering as well. The characteristic minimum located at approximately $q \approx 1.2$ nm$^{-1}$ was not resolved by neutron scattering at the highest scattering contrast in pure $D_2O$ (refer to section 6.2.2.3). The scattering of the CMS-particles in non-polar toluene reveals a similar *q*-dependence as it was observed by respective SANS measurements (Fig. 57).

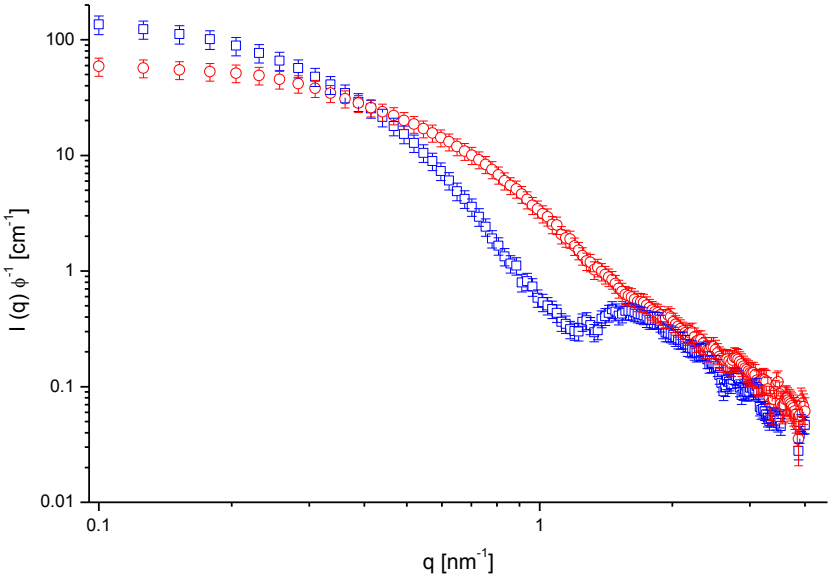


**Fig. 77: SAXS-intensities obtained from CMS-nanoparticles dispersed in toluene (red open circles) and in water (blue open squares) measured at the BESSY-II ASAXS-beamline.**

## Influence of the concentration

A concentration series was analysed for the determination of the influences deriving from the CMS-particle concentration in aqueous media. For this purpose, five concentrations of the polymer in the range between 0.1 wt% < $\omega$ < 1 wt% were investigated (Fig. 78). Higher volume fractions were not tested, as these samples tend to be turbid. For all tested concentrations, the characteristic small angle scattering was preserved. Only for the lowest scattering vectors a variation of the scattering intensities was observed. As illustrated by the inset of Fig. 78, the investigated samples show no distinct trend in the evolution of the scattering intensities at small *q*-vectors. Usually, the concentration dependence is used for the extrapolation of the scattering intensities at infinite volume fractions $I_0(q)$. For the investigated concentration series this could not be realised with the needed accuracy. Thus, $S(q)$ could not be provided for further interpretation of the X-ray data. As already outlined, the analysis of the neutron scattering could not benefit from these investigations either (refer to chapter 6.2.2.3). The limited *q*-range of the experimental setup at the BESSY-II in Berlin does not allow analyses of $q < 0.1$ nm$^{-1}$. Moreover, the data quality at smallest scattering angles and with decreasing polymer volume fraction had to be taken into consideration.

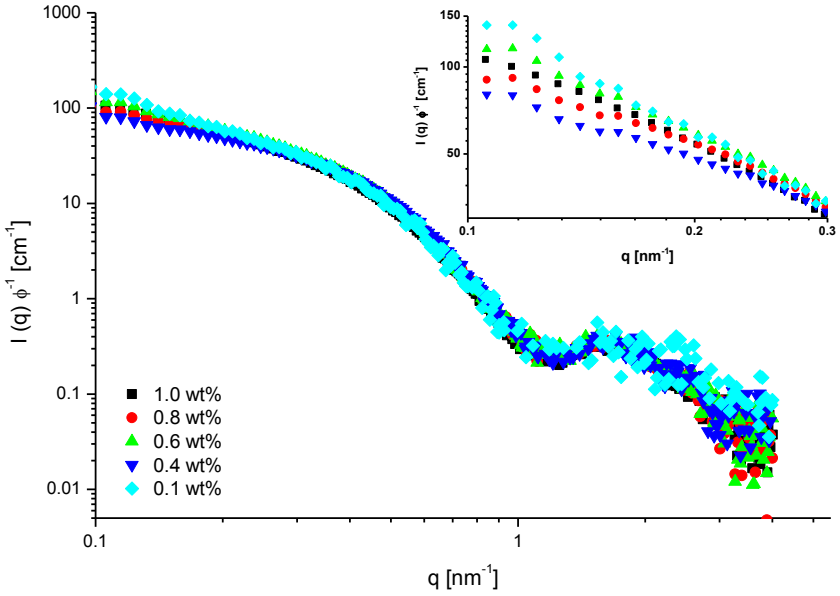


**Fig. 78: Volume fraction normalised scattering intensities of CMS-molecules dispersed in $H_2O$ from a concentration series in the range between 0.1 wt% < $\omega$ < 1 wt% measured at the BESSY-II ASAXS beam line. The inset displays the magnification of the respective low-*q* regime.**

## Variation of the scattering contrast

The CMS-molecules were studied in aqueous media by SAXS in conjunction with contrast variation. Herein, sucrose was used as contrast agent for increasing the scattering length densities of the dispersion media $b_m$. The $b_m$-range is extended by using the disaccharide in contrast to the monosaccharide used for the analysis of the PE-nanoparticles (refer to sections 6.1.1 and 6.1.2.).

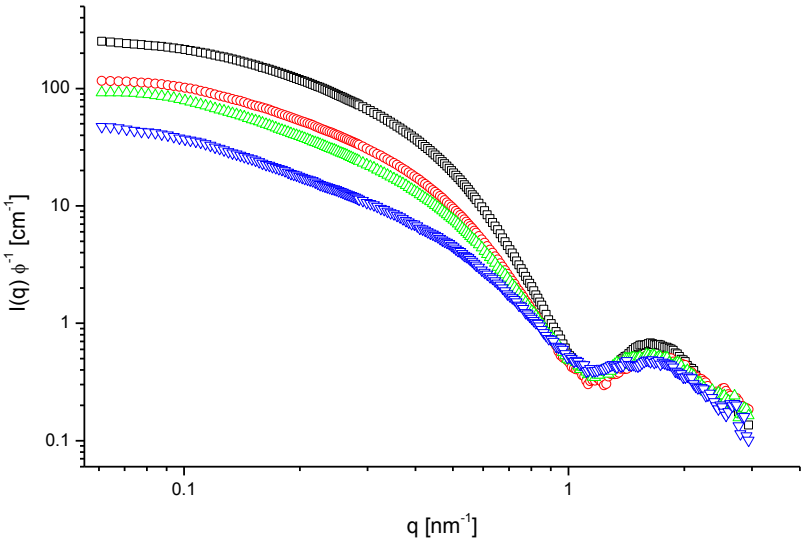


**Fig. 79: SAXS-intensities normalised by $\phi$ obtained from a contrast variation series with CMS-nanoparticles using sucrose as contrast agent (sucrose: 0 wt% – black squares, 4.6 wt% – red circles, 8.4 wt% – green up triangles, and 13 wt% – blue down triangles). The series was measured at the ID02 beam line.**

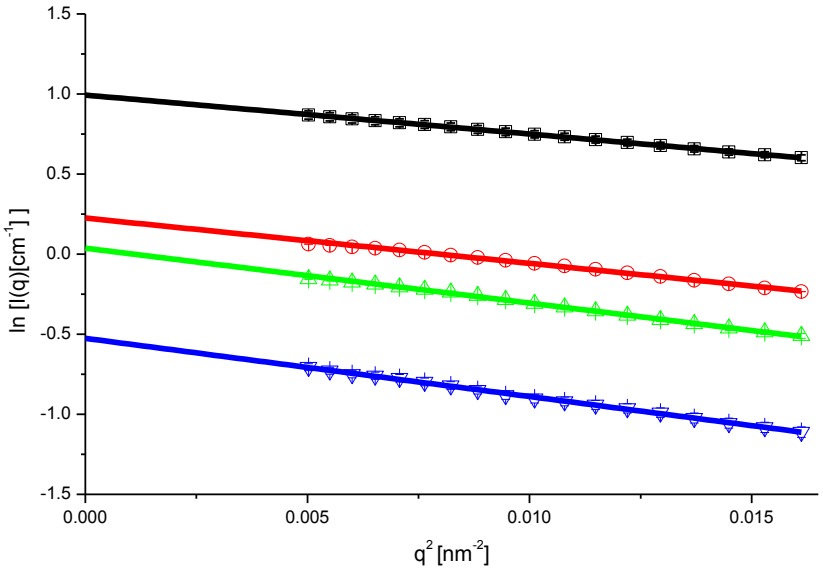


**Fig. 80: *Guinier*-plot of the linearised SAXS-intensities. The colours and symbols are adapted from Fig. 79. The linear regressions represent the fits using the *Guinier*-equation (14).**

**Tab. 13: Overview on the sample composition of a contrast variation series with CMS-nanoparticles. The analysis of the SAXS scattering intensities at vanishing scattering angles from the *Guinier*-equation (14) is tabulated in addition.**

| $\omega$ sucrose | $\omega$ CMS-NP | $\phi$ CMS-NP | $b_m$ | $\rho_m$ | $R_G$ |
|---|---|---|---|---|---|
| wt% | wt% | | $10^{10}$ cm$^{-2}$ | g cm$^{-3}$ | Nm |
| 0 | 1.1 | 0.0099 | 9.42 | 0.9970 | 8.5 ± 0.1 |
| 4.6 | 1.0 | 0.0093 | 9.55 | 1.0164 | 8.8 ± 0.2 |
| 8.4 | 1.0 | 0.0093 | 9.68 | 1.0315 | 10.1 ± 0.1 |
| 13.0 | 1.2 | 0.0110 | 9.84 | 1.0503 | 10.4 ± 0.1 |

Respectively, polymer dispersions were prepared with approximate weight fractions of $\omega \approx 1$ wt%. The dispersion in neat water and three samples having a sugar content of 4.6 wt%, 8.4 wt%, and 13 wt% tune $b_m$ in the range of $9.42 \cdot 10^{10}$ cm$^{-2}$ < $b_m$ < $9.84 \cdot 10^{10}$ cm$^{-2}$ (Tab. 13). The background corrected scattering intensities are plotted in Fig. 79. In comparison to the accessible $b_m$-range for neutron scattering, the $b_m$-range probed by X-ray scattering is relatively narrow.

The radius of gyration and the forward scattering intensities for the contrast variation series were determined from the scattering intensities at vanishing scattering angles using the *Guinier*-equation (14). The respective linearised scattering intensities are illustrated in Fig. 80, whereas the results from the *Guinier*-analysis are tabulated in Tab. 13. From the dependence between $I(q \rightarrow 0)$ and $b_m$ the corresponding $V_P$ and $b_p$ were determined from the correlation provided by equation (27), as illustrated in Fig. 81. This approach reveals $b_P$ to be $b_P = 10.17 \pm 0.49 \cdot 10^{10}$ cm$^{-2}$ and $V_P$ was extrapolated with $V_P = 4800 \pm 120$ nm$^3$. This value is significantly higher than the volume determined by neutron scattering (refer to chapter 6.2.2.3). This observation must be explained by the formation of non-permanent associates of up to 30 CMS-unimers.

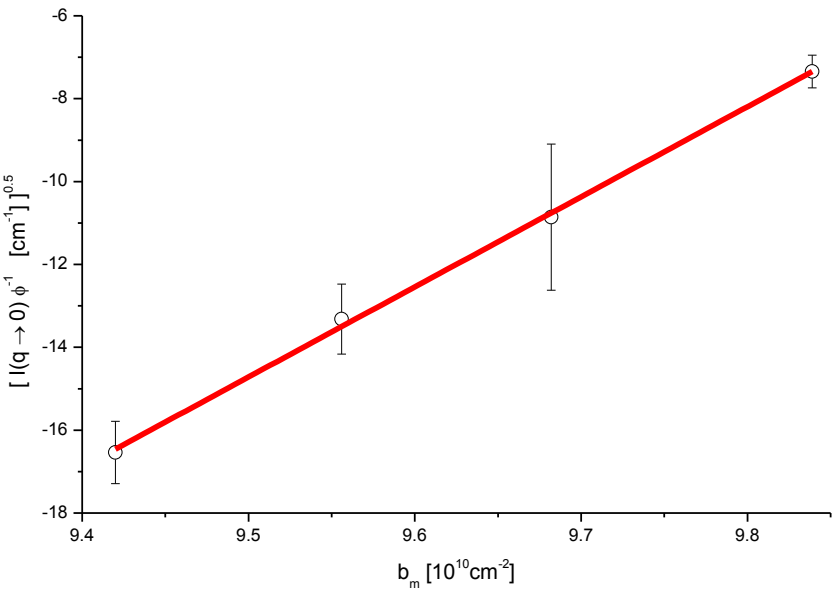


**Fig. 81: *Square root*-plot: *I*(*q*→*0*) normalised by $\phi$ as a function of $b_m$.**

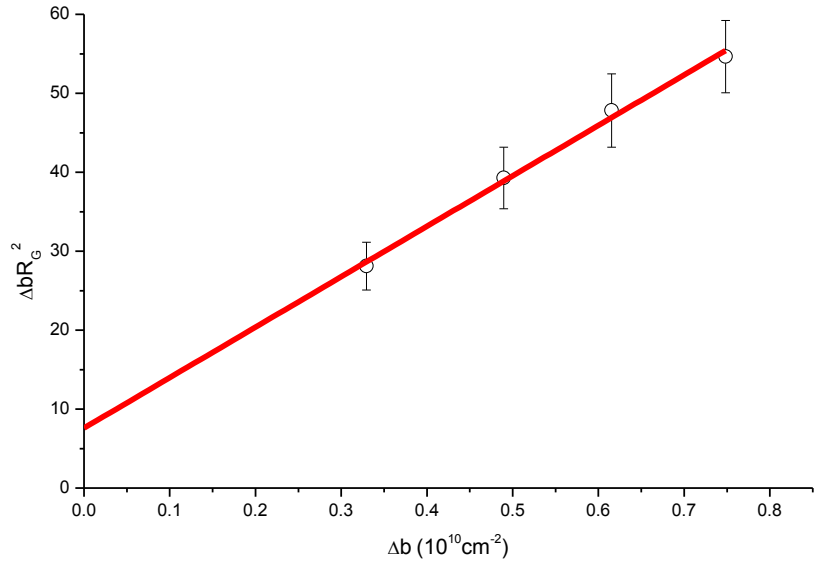


**Fig. 82: *Stuhrmann*-plot: The radius of gyration scales with the scattering contrast and allows the determination of $R_{G\infty}$ at infinite contrast.**

The determination of $b_P$ enables the calculation of the individual scattering contrasts $\Delta b$ of the particles to their respective surroundings. These values serve for the analysis of the *Stuhrmann*-relation provided by equation (29) as this is illustrated in Fig. 82. The radius of gyration at infinite contrast is $R_{G\infty}$ = 8.0 ± 0.4 nm. This value is smaller as the *Guinier*-radii determined from dispersion with higher sugar contents, but smaller as the value determined by neutron scattering, where an association of the CMS-particles was concluded. Moreover, it is in the range of $R_H$ determined from diluted dispersions by respective DLS measurements. The quantity $\alpha$ being a measure for the electron distribution was determined from the relation provided in formula (29) to be $\alpha = (7.6 \pm 1.8) \cdot 10^{-4}$. This indicates an increased electron density at the particles periphery [187]. On the one hand, this can arise from the outermost polar PEO-segments carrying certain amounts of

oxygen (Fig. 2). On the other hand, this can be associated with an increased amount of the contrast agent adsorbed at the particle surface. Therefore, the presence of the polar contrast agent can initialise the well-behaved association of individual CMS-nanoparticles. A further treatment of the scattering data by means of contrast decomposition appeared less meaningful for these reasons. Conclusively, the analysis presented reveals that contrast variation using low-molecular contrast agents acting as mediator for the formation of supramolecular aggregates is not suitable to probe the structural characteristics of individual CMS-nanoparticles by SAXS in more detail.

## Temperature dependent behaviour

As already discussed, with respect to the light scattering experiments in chapter 6.2.2.1, a significant temperature trend of the hydrodynamic radii was found in the temperature range between 25 °C < *T* < 60 °C. A similar observation was made in the analysis of thermostated dispersions by cryo-TEM as discussed in 6.2.2.2. Due to this, the finding was checked using X-ray scattering experiments.

For this purpose, a CMS- nanoparticle dispersion having a weight fraction of approximately $\omega \approx 1$ wt% was slowly tempered to seven discrete temperatures and equilibrated for 30 minutes before measuring the SAXS-intensities (Fig. 83). The scattering contribution of the dispersion medium, which was measured under equivalent conditions was subtracted carefully using equation (51). The comparison of the scattering intensities recorded at different temperatures shows distinct differences above 50 °C. The fluctuations of the scattering intensities in the high *q*-sector appear more dominant and thus correlate with temperature induced internal motions. It was not possible to probe *q*-vectors of $q < 0.1$ nm$^{-1}$, which could reveal further evidence for the formation of larger structures as this was suggested by DLS and cryo-TEM measurements. The analysis of the scattering at low *q*-values using the *Guinier*-relation provided by (14) displays a temperature dependent change of $R_G$ provided in the inset of Fig. 83. Here, the values of $R_G$ drop from around $R_G \approx 8.9$ nm to approximately $R_G \approx 6.7$ nm for temperatures above 50 °C. A temperature

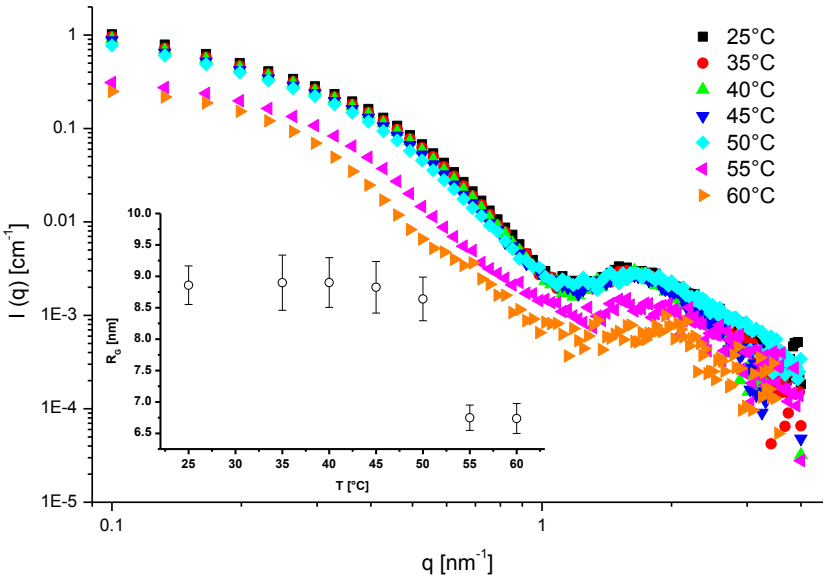


**Fig. 83: SAXS-intensities of CMS-molecules dispersed in $H_2O$ from a temperature series between 25 °C and 60 °C. Inset: $R_G$ as function of *T* determined by the analysis of the *Guinier*-regime by equation (14).**

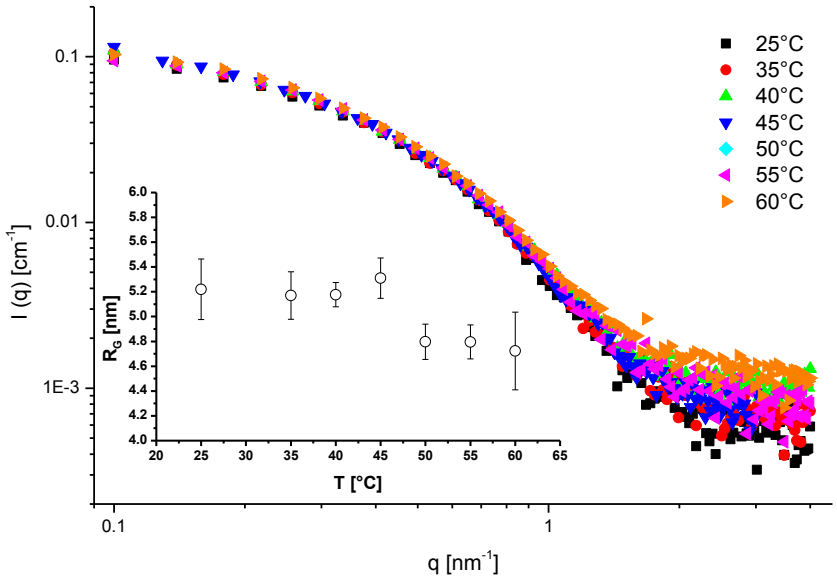


**Fig. 84: Scattering intensities of CMS-nanoparticles dispersed in toluene from a temperature series between 25 °C < *T* < 60 °C. Inset: $R_G$ calculated by equation (14) as a function of *T*.**

dependent size trend is in agreement with the general findings from DLS measurements. This notwithstanding, the DLS measurements revealed the increase of $R_H$ above a critical temperature at around 45 °C. For poly(ethylene oxide) a lower critical solution temperature is observed being a function of the molecular weight and molecular architecture [220,221,222,223,224,225,226]. For polymers carrying oligomeric side chains, a lower LCST is observed [227,228]. The decreasing miscibility of the mPEG at increased temperatures thus induces the formation of supramolecular aggregates.

Temperature dependence was also tested for non-polar dispersions of the CMS-particles. For that purpose CMS-molecules dispersed in toluene ($\omega \approx 1$ wt%) were prepared and measured using the same protocol as for the aqueous samples. The measured scattering intensities corrected from the contribution of the scattering background employing equation (51) are illustrated in Fig. 84. The function of $R_G$ and T determined from the small angle regime by formula (14) is provided in the inset of Fig. 84. Compared to the aqueous dispersions, a less distinctive size trend was observed for the non-polar dispersions. A minor deviation was obtained for temperatures above 45 °C. Here, the values of $R_G$ decrease from approximately 5.2 nm to 4.8 nm. This would correlate with a slight contraction of the CMS-nanoparticles. In the high-*q* expansion, a more prominent variation of the scattering intensities is observed for the higher temperatures. This correlates with the enhanced internal motion of the microscopic structure with increasing temperatures.

# 7. Summary and Conclusion

A combination of complementary methods was applied to conduct detailed structural investigations on different types of nanoparticles. Additionally, small angle scattering analyses were applied as a highly suitable probe to explore structural aspects on the nanometre length scale. The additional variation of the scattering contrast by modifying the composition of the dispersion medium revealed a detailed insight into the structural characteristics of the investigated nanoparticles.

The polymerisation of ethylene in aqueous emulsions using a catalytic active nickel-based complex led to the formation of highly ordered polyethylene nanocrystallites having virtually no branches along the polymer backbone. The detailed analysis by the combination of cryo-TEM and SAXS using contrast variation reveals the formation of platelet-like nanoparticles. The single lamella crystallites are topped by thin amorphous domains on each side and a stabilising layer containing adsorbed surfactant molecules and polyethylene glycol. Investigations using TOF-SANS confirmed the structure of these nanoplatelets. The microstructure of the crystalline domain was investigated by respective WAXS measurements. Hence, the high degree of crystallinity found by SAXS could be verified by the quantitative analysis of the wide angle diffraction. Furthermore, the analysis revealed a fraction of PE in its monoclinic crystal modification. So far, this was not observed for PE-nanoparticles composed of average molecular weight PE and without applying mechanical strain.

The lamella thickening due to an annealing of the nanocrystals could be concluded from SAXS measurements of annealed PE-nanoparticle dispersions. The microstructural changes of the crystallites were followed by accompanying WAXS measurements. With respect to the annealing at moderate temperatures, a constant thickness of the amorphous layers was observed, while the thickness of the crystalline lamella increased. This was discussed in the context of the “pulley mechanism”, as the amorphous domain hosts the chain fold and the consequent adjacent re-entry of the polymer chains into the crystalline phase. Here, the amorphous layers act like a wheel in a pulley leading to a redirection of the chains. This allows a free diffusion of the chains during the thickening of the lamella towards the thermodynamical equilibrium. This mechanism additionally benefits from the absence of chain branches. Moreover, the crystallisation at 10 °C occurs to be faster than the chain growth. The growing chain is directly embedded into the crystal growth front. In turn, this minimises the formation of domains of lower order as for instance chain entanglements leading to high order nanocrystallites. The native PE-nanoparticles being virtually free of defects and disorder can thus be discussed in terms of ideal polymer crystals.

Another aspect of interest is the influence of defects on the crystallisation of polymers and on the formation of nanoparticles. Nanoparticles composed of PE with a precise microstructure were obtained from an ADMET emulsion polymerisation forming semi-crystalline nanoparticles. The embodied polymer carries a single methyl group at every 21$^{st}$ carbon along the polymer chain. The nanoparticle morphology was analysed by means of electron microscopy and complementary SAXS measurements in a contrast variation series. During the evaluation of the scattering data, the presence of free micelles formed by the stabilising surfactant molecules had to be taken into consideration. The particles reveal a core-shell architecture with an oblate-like overall shape, where the crystalline phase is embedded in a voluminous amorphous matrix. This was related to the presence of the methyl branches that hinders the well-behaved redirection of the polymer chain towards the crystalline phase and thus leads to the formation of loops and entanglements.

Furthermore, the crystalline character was analysed by diffraction techniques Thus, a monoclinic arrangement of the polymer chain with a low packing density within the unit cells was identified. This was related to the incorporation of a defect plane formed by the precisely placed methyl groups into the crystalline lattice.

The analyses of a core-multishell architecture based on hyperbranched polyglycerol (hPG) were the second major topic discussed in here. These molecules solubilise polar and non-polar organic structures in various solvents. Therefore, these molecules are a promising system for drug delivery applications. Hence, the hyperbranched scaffold being the major building block of the core-multishell (CMS) molecules became the focus of structural investigations by respective TOF-SANS measurements. The small angle scattering of the hPG was analysed with respect to recent approaches describing the structural details of hyperbranched molecules. Thus, this issue was discussed in the context of the fractal approach with respect to the scattering contribution of the molecular microstructure. The analysis revealed essential parameters for the further investigations on the structure of the CMS-nanoparticles.

The spatial structure of the CMS-molecules composed of the hPG-scaffold structure and attached di-block shell was investigated by small angle scattering in conjunction with contrast variation in polar and non-polar dispersions. To study these issues in detail, neutron and X-ray scattering were used as complementary probes. The differences of the characteristic small angle scattering obtained from aqueous and non-polar dispersions underline the suggestions of crucial structural changes in the spatial structure of the CMS-nanoparticles dispersed in media of different polarity. The general structure of the CMS-molecules in non-polar surroundings was discussed in terms of the fractal approach. The analysis revealed a compact space filling structure due to the poor solvent conditions. The suggested backfold of the outermost polar segments towards the hPG-core and the high degree of functionalisation of the CMS-molecules does support this aspect. For the CMS-particles dispersed in polar surroundings, the molecular parameter and the modelling of the decomposed scattering contributions corroborate the formation of well-defined aggregates by the CMS-unimers. The overall spatial structure was fitted best by a prolate ellipsoid model. The observed small angle scattering could not be related to common core-shell structures. Hereby, the local demixing of the hydrophobic segments leads to hydrophobic patches on the surface of the hPG-core that mediate the formation of the associates. The analysis of the SAXS contrast variation series, with dispersions containing sugar to tune the scattering contrast, revealed the formation of aggregates by the CMS-molecules mediated by sugar molecules. The investigations of the small angle scattering were additionally accompanied by DLS measurements of diluted CMS-particle dispersions. In aqueous dispersions, a temperature-dependent size trend was obtained by a precise heating procedure. Above a certain critical temperature, the formation of superstructures of the CMS-unimers, well-defined in terms of size, was observed. This trend was verified by the analysis of cryo-TEM. The results discussed herein emphasise that the CMS-particles are well-suited for cellular uptake and skin penetration.

# 8. Perspectives

This discussion pursued only some of the issues of recent polymer science and thus might be the basis for further investigations. For instance, the progress in the development of the investigated polymer systems will open access to a deeper understanding of those innovative structures. Moreover, future applications will benefit from the results obtained by following the pathways presented for detailed investigations using a set of complementary techniques.

In addition to the academic progress, the ideal nanocrystals will find their way to further applications. The preparation of ideal crystals led to nanoparticles with tuneable properties. The thermally induced variation of the particle thickness might be applied for the preparation of layered materials with a well-behaved thermal response. Therefore, the utilisation in optical or electronic devices is considered relevant. Recent investigations revealed that crystal engineering can be achieved by preparation of ideal polymers by catalytic emulsion polymerisation. Nevertheless, further refinements of these processes must be taken into account for an upscale towards industrial scales.

The influence of branches on the polymer arrangement will be an aspect of further research using the nanoparticle approach. Refinements of the synthesis routine and the utilisation of various branched monomers will lead to new generations of nanoparticles with precise microstructure. In contrast to studies using respective bulk materials, the analyses should benefit significantly from the almost isolated crystalline phase. The combination of different techniques can be considered an ideal approach to test the properties of those polymer crystals. With respect to this, the stabilisation of the investigated dispersions is of particular importance. Indeed, this aspect should not induce disturbing side effects (refer to chapter 6.1.2). Nanoparticles carrying carboxylic moieties [50] were also tested by SAXS measurements. These dispersions were observed to be less stable under the provided experimental conditions. For this reason, the stability of these dispersions should be improved, as this type of polymer, with precisely placed carboxylic groups, is of particular interest for further investigations. Hence, a useful variance of SAXS is the anomalous small angle X-ray scattering (ASAXS) technique [5,118,229,230,231]. Varying the photon energy near to the absorption edge of metal ions or respective atoms of higher order will open up insight concerning the spatial distribution of the functional groups within the investigated structure. A simple ion exchange, with rubidium, for instance, will yield a breakthrough in the discussion.

Additionally, the presented investigation revealed further insight into the characteristic structure of hyperbranched molecules. The deepened understanding of this kind of architecture is of particular importance, as this type of molecule is more easily accessible by one-step synthesis. This is in contrast to the complex synthesis of regular dendrimers offering similar properties [70,72]. The structural investigations on the core-shell architecture of hyperbranched polyglycerol using a set of complementary techniques were the first of their kind. In addition, the analyses employed recent approaches to model the characteristic small angle scattering and thus reveal the structural characteristics of the hyperbranched architectures. The recent models sufficiently describe the scattering of the hyperbranched scaffold molecules. That notwithstanding, this approach could not completely be adapted to describe the molecules with attached di-block segments representing the CMS-nanoparticles. Hence, this approach needs further refinement as, for instance, the scattering contribution of the hydrophobic patches and thus the scattering in the high-$q$ sector could not be

described in detail. The aggregation in aqueous media might be addressed in succeeding studies as this aspect imped the analysis of individual CMS-unimers. Using different polar media can reduce the tendency to form superstructures. Further investigation might be possible using modification of the CMS-structure itself. Thus, the partial deuteration of specific segments of the CMS-molecules reveals further improvements for investigations by neutron scattering. A partially deuterated CMS-molecule carrying deuterated terminal methyl groups was already synthesised and measured by SANS, but was not an object of the discussion herein presented. The partially deuterated molecules were seen as a helpful tool to study the chain conformation of the CMS-structure and to give insight into the structural changes during a heat treatment or during the embedding of guest molecules. Previous studies predicted the encapsulation of guest molecules by the formation of supramolecular aggregates [58,59,61]. For a more detailed clarification of this issue, the synthesis of deuterium labelled molecules might be a topic for investigation. These molecules ought to resemble recent active agents. The first reports on the encapsulation properties of the CMS-molecules employed common dye molecules. These are readily available and can furthermore be tracked using common lab analytics. For this reason, deuterated dye molecules can provide a suitable probe for testing their respective encapsulation by the CMS-molecules performing further SANS measurements. Moreover, these molecules can be used for other neutron diffraction methods. Here, the interactions of the CMS-particles with membrane tissues might be a focal topic as well.

The temperature dependent behaviour of the CMS-nanoparticles was not focused upon to date. Forming well-defined and narrowly distributed secondary structures by a mild increase of the temperature can play an interesting role in further studies.

The final goal in the development of new CMS-structures is to create CMS-nanoparticles acting as responsive drug delivery systems. Trigger signals such as temperature, pH or electromagnetic fields can be used to induce structural changes within the CMS-particles. For instance, a controlled break-away of shells leads to the release of drugs at the site of action. The ideas of stimulated drug release were recently reviewed by Fleige et al. [52].

Another application of the CMS-particles is the preparation and stabilisation of noble metal nanoparticles acting as catalysts [65,66,67,68,69]. The process guiding the metal nanoparticles formation and the influence of the CMS-structure was a focal point of investigations to date. Thus, the comparison to other systems used for catalysis by metal nanoparticles might be of particular interest [232,233,234]. Probing the spatial distribution of the nanoparticles and respective precursor ions within the CMS-molecules ASAXS measurements is considered a suitable technique.

The discussion herein presented demonstrates that using complementary methods concerning the understanding of structural characteristics ruling the encapsulation and transport mechanism or the preparation of catalytic active nanoparticles is promising. Moreover, the results presented in this discussion will support new approaches in the synthetic work. Thus, further investigations following this path are highly recommended.

# References


[1] Elias, H.G. (2005): An introduction to polymer science, VCH, ISBN: 9783527287901.

[2] Cowie, J.M.G. (2007): Polymers: Chemistry and Physics of Modern Materials, 3nd Edition, Taylor & Francis, ISBN: 0849398134.

[3] Guinier, A. and Fournet, G. (1955): Small-angle scattering of X-rays, Wiley.

[4] Feigin, L.A. ; Svergun, D.I. (1987): Structure analysis by small-angle X-ray and neutron scattering, Plenum Press, New York.

[5] Ballauff, M. (2011): Analysis of Polymer Colloids by Small-Angle X-Ray and Neutron Scattering: Contrast Variation, Advanced Engineering Materials (vol. 13), No. 8, pp. 793-802.

[6] Hagen, J. (2006): Industrial Catalysis: A Practical Approach, John Wiley & Sons, ISBN: 9783527607068.

[7] Keller, A. (1957): A Note on Single Crystals in Polymers - Evidence for a Folded Chain Configuration, Philosophical Magazine (vol. 2), No. 21, pp. 1171-1175.

[8] Keller, A. and Oconnor, A. (1960): A Study on the Relation between Chain Folding and Chain Length in Polyethylene, Polymer (vol. 1), No. 2, pp. 163-168.

[9] Keller, A. (1968): Polymer Crystals, Reports on Progress in Physics (vol. 31), pp. 623-704.

[10] Keller, A.; Organ, S. J. and Ungar, G. (1991): New Trends in Polymer Crystallization Studies .1. From Alkanes to Polyethylene - the Onset of Chain Folding in Polymer Crystallization, Makromolekulare Chemie-Macromolecular Symposia (vol. 48-9), pp. 93-102.

[11] Strobl, Gert-Rèudiger (1997): Physics of polymers concepts for understanding their structures and behavior, Second corrected. ed., Springer, Berlin etc., ISBN: 3-540-63203-4.

[12] Strobl, G. (2006): Crystallization and melting of bulk polymers: New observations, conclusions and a thermodynamic scheme, Progress in Polymer Science (vol. 31), No. 4, pp. 398-442.

[13] Rastogi, S. and Terry, A. E. (2005): Morphological implications of the interphase bridging crystalline and amorphous regions in semi-crystalline polymers, Interphases and Mesophases in Polymer Crystallization I (vol. 180), pp. 161-194.

[14] Pandey, A.; Toda, A. and Rastogi, S. (2011): Influence of Amorphous Component on Melting of Semicrystalline Polymers, Macromolecules (vol. 44), No. 20, pp. 8042-8055.

[15] Cho, T. Y.; Stille, W. and Strobl, G. (2007): Zero growth temperature of crystallizing polyethylene, Macromolecules (vol. 40), No. 7, pp. 2596-2599.

[16] Cheng, S. Z. (2007): Materials science: polymer crystals downsized, Nature (vol. 448), No. 7157, pp. 1006-1007.

[17] Hoffman, J. D. and Lauritzen, J. I. (1961): Crystallization of Bulk Polymers with Chain Folding - Theory of Growth of Lamellar Spherulites, Journal of Research of the National Bureau of Standards (vol. A 65), No. 4, pp. 297-336.

[18] Hoffman, J. D. (1980): Reptation and Chain Folding in Crystallization of Polyethylene, Bulletin of the American Physical Society (vol. 25), No. 3, pp. 250-250.

[19] Hoffman, J. D. and Miller, R. L. (1997): Kinetics of crystallization from the melt and chain folding in polyethylene fractions revisited: Theory and experiment, Polymer (vol. 38), No. 13, pp. 3151-3212.

[20] Sommer, J. U. (2006): The role of the amorphous fraction for the equilibrium shape of polymer single crystals, European Physical Journal E (vol. 19), No. 4, pp. 413-422.

[21] Nilsson, F.; Lan, X.; Gkourmpis, T.; Hedenqvist, M. S. and Gedde, U. W. (2012): Modelling tie chains and trapped entanglements in polyethylene, Polymer (vol. 53), No. 16, pp. 3594-3601.

[22] Gottker-Schnetmann, I.; Korthals, B. and Mecking, S. (2006): Water-soluble salicylaldiminato Ni(II)-methyl complexes: Enhanced dissociative activation for ethylene polymerization with

unprecedented nanoparticle formation, Journal of the American Chemical Society (vol. 128), No. 24, pp. 7708-7709.

[23] Korthals, B.; Gottker-Schnetmann, I. and Mecking, S. (2007): Nickel(II)-methyl complexes with water-soluble ligands L [(salicylaldiminato-kappa N-2,O)NiMe(L)] and their catalytic properties in disperse aqueous systems, Organometallics (vol. 26), No. 6, pp. 1311-1316.

[24] Mecking, S. (2007): Polymer dispersions from catalytic polymerization in aqueous systems, Colloid and Polymer Science (vol. 285), No. 6, pp. 605-619.

[25] Wehrmann, P. and Mecking, S. (2008): Highly active binuclear neutral nickel(II) catalysts affording high molecular weight polyethylene, Organometallics (vol. 27), No. 7, pp. 1399-1408.

[26] Yu, S. M. and Mecking, S. (2009): Variable Crystallinity Polyethylene Nanoparticles, Macromolecules (vol. 42), No. 11, pp. 3669-3673.

[27] Bauers, F. M. and Mecking, S. (2001): High molecular mass polyethylene aqueous latexes by catalytic polymerization, Angew Chem Int Ed Engl (vol. 40), No. 16, pp. 3020-3022.

[28] Bauers, F. M.; Thomann, R. and Mecking, S. (2003): Submicron polyethylene particles from catalytic emulsion polymerization, J Am Chem Soc (vol. 125), No. 29, pp. 8838-8840.

[29] Soula, R.; Novat, C.; Tomov, A.; Spitz, R.; Claverie, J.; Drujon, X.; Malinge, J. and Saudemont, T. (2001): Catalytic polymerization of ethylene in emulsion, Macromolecules (vol. 34), No. 7, pp. 2022-2026.

[30] Weber, C. H. M.; Chiche, A.; Krausch, G.; Rosenfeldt, S.; Ballauff, M.; Harnau, L.; Gottker-Schnetmann, I.; Tong, Q. and Mecking, S. (2007): Single lamella nanoparticles of polyethylene, Nano Letters (vol. 7), No. 7, pp. 2024-2029.

[31] Tong, Q.; Krumova, M. and Mecking, S. (2008): Crystalline polymer ultrathin films from mesoscopic precursors, Angewandte Chemie-International Edition (vol. 47), No. 24, pp. 4509-4511.

[32] Tong, Q. and Mecking, S. (2009): Submicron Films Prepared from Aqueous Dispersions of Nanoscale Polymer Crystals, Journal of Polymer Science Part a-Polymer Chemistry (vol. 47), No. 23, pp. 6420-6432.

[33] Rochette, C. N.; Rosenfeldt, S.; Henzler, K.; Polzer, F.; Ballauff, M.; Tong, Q.; Mecking, S.; Drechsler, M.; Narayanan, T. and Harnau, L. (2011): Annealing of Single Lamella Nanoparticles of Polyethylene, Macromolecules (vol. 44), No. 12, pp. 4845-4851.

[34] Keller, A. and Cheng, S. Z. D. (1998): The role of metastability in polymer phase transitions, Polymer (vol. 39), No. 19, pp. 4461-4487.

[35] Qui, W.; Pyda, M.; Nowak-Pyda, E.; Habenschuss, A.; Wagner, K. B. and Wunderlich, B. (2006): Crystallization and melting of a branched polyethylene with precisely controlled chemical structure, Journal of Polymer Science Part B-Polymer Physics (vol. 44), No. 24, pp. 3461-3474.

[36] Zuluaga, F.; Inci, B.; Nozue, Y.; Hosoda, S. and Wagener, K. B. (2009): Reducing Branch Frequency in Precision Polyethylene, Macromolecules (vol. 42), No. 14, pp. 4953-4955.

[37] Hosoda, S.; Nozue, Y.; Kawashima, Y.; Utsumi, S.; Nagamatsu, T.; Wagener, K.; Berda, E.; Rajas, G.; Baughman, T. and Leonard, J. (2009): Perfectly Controlled Lamella Thickness and Thickness Distribution: A Morphological Study on ADMET Polyolefins, Macromolecular Symposia (vol. 282), pp. 50-64.

[38] Rojas, G.; Inci, B.; Wei, Y. Y. and Wagener, K. B. (2009): Precision Polyethylene: Changes in Morphology as a Function of Alkyl Branch Size, Journal of the American Chemical Society (vol. 131), No. 47, pp. 17376-17386.

[39] Hosoda, S.; Nozue, Y.; Kawashima, Y.; Suita, K.; Seno, S.; Nagamatsu, T.; Wagener, K. B.; Inci, B.; Zuluaga, F.; Rojas, G. and Leonard, J. K. (2011): Effect of the Sequence Length Distribution on the Lamellar Crystal Thickness and Thickness Distribution of Polyethylene: Perfectly Equisequential ADMET Polyethylene vs Ethylene/alpha-Olefin Copolymer, Macromolecules (vol. 44), No. 2, pp. 313-319.

[40] Nozue, Y.; Kawashima, Y.; Seno, S.; Nagamatsu, T.; Hosoda, S.; Berda, E. B.; Rojas, G.; Baughman, T. W. and Wagener, K. B. (2011): Unusual Crystallization Behavior of Polyethylene Having Precisely Spaced Branches, Macromolecules (vol. 44), No. 11, pp. 4030-4034.

[41] Inci, B.; Lieberwirth, I.; Steffen, W.; Mezger, M.; Graf, R.; Landfester, K. and Wagener, K. B. (2012): Decreasing the Alkyl Branch Frequency in Precision Polyethylene: Effect of Alkyl Branch Size on Nanoscale Morphology, Macromolecules (vol. 45), No. 8, pp. 3367-3376.

[42] Wagener, K. B.; Boncella, J. M. and Nel, J. G. (1991): Acyclic diene metathesis (ADMET) polymerization, Macromolecules (vol. 24), No. 10, pp. 2649-2657.

[43] Baughman, T. W. and Wagener, K. B. (2005): Recent advances in ADMET polymerization, Buchmeiser, M. R., Metathesis Polymerization (vol. 176) pp. 1-42, Springer-Verlag Berlin, Berlin.

[44] Opper, K. L. and Wagener, K. B. (2011): ADMET: Metathesis Polycondensation, Journal of Polymer Science Part a-Polymer Chemistry (vol. 49), No. 4, pp. 821-831.

[45] Bunz, U. H.; Maker, D. and Porz, M. (2012): Alkene metathesis - a tool for the synthesis of conjugated polymers, Macromol Rapid Commun (vol. 33), No. 10, pp. 886-910.

[46] Smith, J. A.; Brzezinska, K. R.; Valenti, D. J. and Wagener, K. B. (2000): Precisely controlled methyl branching in polyethylene via acyclic diene metathesis (ADMET) polymerization, Macromolecules (vol. 33), No. 10, pp. 3781-3794.

[47] Rojas, G. and Wagener, K. B. (2007): Precision polyolefin structure: Modeling polyethylene containing methyl and ethyl branches, Metathesis Chemistry: From Nanostructure Design to Synthesis of Advanced Materials (vol. 243), pp. 305-324.

[48] Baughman, T. W.; Chan, C. D.; Winey, K. I. and Wagener, K. B. (2007): Synthesis and morphology of well-defined poly(ethylene-co-acrylic acid) copolymers, Macromolecules (vol. 40), No. 18, pp. 6564-6571.

[49] Kryuchkov, V. A.; Daigle, J. C.; Skupov, K. M.; Claverie, J. P. and Winnik, F. M. (2010): Amphiphilic Polyethylenes Leading to Surfactant-Free Thermoresponsive Nanoparticles, Journal of the American Chemical Society (vol. 132), No. 44, pp. 15573-15579.

[50] Ortmann, Patrick; Trzaskowski, Justyna; Krumova, Marina and Mecking, Stefan (2013): Precise Microstructure Self-Stabilized Polymer Nanocrystals, ACS Macro Letters, pp. 125-127.

[51] Cabral, H.; Nishiyama, N. and Kataoka, K. (2011): Supramolecular nanodevices: from design validation to theranostic nanomedicine, Acc Chem Res (vol. 44), No. 10, pp. 999-1008.

[52] Fleige, E.; Quadir, M. A. and Haag, R. (2012): Stimuli-responsive polymeric nanocarriers for the controlled transport of active compounds: concepts and applications, Adv Drug Deliv Rev (vol. 64), No. 9, pp. 866-884.

[53] Morachis, J. M.; Mahmoud, E. A. and Almutairi, A. (2012): Physical and Chemical Strategies for Therapeutic Delivery by Using Polymeric Nanoparticles, Pharmacological Reviews (vol. 64), No. 3, pp. 505-519.

[54] Gupta, S.; Tyagi, R.; Parmar, V. S.; Sharma, S. K. and Haag, R. (2012): Polyether based amphiphiles for delivery of active components, Polymer (vol. 53), No. 15, pp. 3053-3078.

[55] Lee, J. S. and Jan, F. J. (2012): Polymersomes for drug delivery: Design, formation and characterization, Journal of Controlled Release (vol. 161), No. 2, pp. 473-483.

[56] Rabanel, J. M.; Aoun, V.; Elkin, I.; Mokhtar, M. and Hildgen, P. (2012): Drug-Loaded Nanocarriers: Passive Targeting and Crossing of Biological Barriers, Current Medicinal Chemistry (vol. 19), No. 19, pp. 3070-3102.

[57] Haag, R. (2004): Supramolecular drug-delivery systems based on polymeric core-shell architectures, Angewandte Chemie-International Edition (vol. 43), No. 3, pp. 278-282.

[58] Radowski, M. R.; Shukla, A.; von Berlepsch, H.; Bottcher, C.; Pickaert, G.; Rehage, H. and Haag, R. (2007): Supramolecular aggregates of dendritic multishell architectures as universal nanocarriers, Angewandte Chemie-International Edition (vol. 46), No. 8, pp. 1265-1269.

[59] Quadir, M. A.; Radowski, M. R.; Kratz, F.; Licha, K.; Hauff, P. and Haag, R. (2008): Dendritic multishell architectures for drug and dye transport, Journal of Controlled Release (vol. 132), No. 3, pp. 289-294.

[60] Kuchler, S.; Abdel-Mottaleb, M.; Lamprecht, A.; Radowski, M. R.; Haag, R. and Schafer-Korting, M. (2009): Influence of nanocarrier type and size on skin delivery of hydrophilic agents, International Journal of Pharmaceutics (vol. 377), No. 1-2, pp. 169-172.

[61] Kuchler, S.; Radowski, M. R.; Blaschke, T.; Dathe, M.; Plendl, J.; Haag, R.; Schafer-Korting, M. and Kramer, K. D. (2009): Nanoparticles for skin penetration enhancement - A comparison of a dendritic core-multishell-nanotransporter and solid lipid nanoparticles, European Journal of Pharmaceutics and Biopharmaceutics (vol. 71), No. 2, pp. 243-250.

[62] Haag, S. F.; Fleige, E.; Chen, M.; Fahr, A.; Teutloff, C.; Bittl, R.; Lademann, J.; Schafer-Korting, M.; Haag, R. and Meinke, M. C. (2011): Skin penetration enhancement of core-multishell nanotransporters and invasomes measured by electron paramagnetic resonance spectroscopy, International Journal of Pharmaceutics (vol. 416), No. 1, pp. 223-228.

[63] Wolf, N. B.; Kuchler, S.; Radowski, M. R.; Blaschke, T.; Kramer, K. D.; Weindl, G.; Kleuser, B.; Haag, R. and Schafer-Korting, M. (2009): Influences of opioids and nanoparticles on in vitro wound healing models, European Journal of Pharmaceutics and Biopharmaceutics (vol. 73), No. 1, pp. 34-42.

[64] Treiber, C.; Quadir, M. A.; Voigt, P.; Radowski, M.; Xu, S. J.; Munter, L. M.; Bayer, T. A.; Schaefer, M.; Haag, R. and Multhaup, G. (2009): Cellular Copper Import by Nanocarrier Systems, Intracellular Availability, and Effects on Amyloid beta Peptide Secretion, Biochemistry (vol. 48), No. 20, pp. 4273-4284.

[65] Keilitz, J.; Radowski, M. R.; Marty, J. D.; Haag, R.; Gauffre, F. and Mingotaud, C. (2008): Dendritic polymers with a core-multishell architecture: A versatile tool for the stabilization of nanoparticles, Chemistry of Materials (vol. 20), No. 7, pp. 2423-2425.

[66] Keilitz, J.; Schwarze, M.; Nowag, S.; Schomacker, R. and Haag, R. (2010): Homogeneous Stabilization of Pt Nanoparticles in Dendritic Core-Multishell Architectures: Application in Catalytic Hydrogenation Reactions and Recycling, Chemcatchem (vol. 2), No. 7, pp. 863-870.

[67] Keilitz, J.; Nowag, S.; Marty, J. D. and Haag, R. (2010): Chirally Modified Platinum Nanoparticles Stabilized by Dendritic Core-Multishell Architectures for the Asymmetric Hydrogenation of Ethyl Pyruvate, Advanced Synthesis & Catalysis (vol. 352), No. 9, pp. 1503-1511.

[68] Schwarze, M.; Keilitz, J.; Nowag, S.; Parapat, R. Y.; Haag, R. and Schomacker, R. (2011): Quasi-Homogeneous Hydrogenation with Platinum and Palladium Nanoparticles Stabilized by Dendritic Core-Multishell Architectures, Langmuir (vol. 27), No. 10, pp. 6511-6518.

[69] Nowag, S.; Wang, X. S.; Keilitz, J.; Thomas, A. and Haag, R. (2010): Dendritic Core-Multishell Polymer Templates for the Synthesis of Pt Nanoparticle-Loaded Porous Silica and their Application as Catalysts for the Enantioselective Hydrogenation of Ethyl Pyruvate, Chemcatchem (vol. 2), No. 7, pp. 807-811.

[70] Fischer, Marco and Vögtle, Fritz (1999): Dendrimers: From Design to Application—A Progress Report, Angewandte Chemie International Edition (vol. 38), No. 7, pp. 884-905.

[71] Grayson, S. M. and Frechet, J. M. J. (2001): Convergent dendrons and dendrimers: from synthesis to applications, Chemical Reviews (vol. 101), No. 12, pp. 3819-3867.

[72] Voit, Brigitte I. and Lederer, Albena (2009): Hyperbranched and Highly Branched Polymer Architectures—Synthetic Strategies and Major Characterization Aspects, Chemical Reviews (vol. 109), No. 11, pp. 5924-5973.

[73] Burakowska, E. and Haag, R. (2009): Dendritic Polyglycerol Core-Double-Shell Architectures: Synthesis and Transport Properties, Macromolecules (vol. 42), No. 15, pp. 5545-5550.

[74] Haag, R. (2001): Dendrimers and hyperbranched polymers as high-loading supports for organic synthesis, Chemistry-a European Journal (vol. 7), No. 2, pp. 327-335.

[75] Frey, H. and Haag, R. (2002): Dendritic polyglycerol: a new versatile biocompatible-material, J Biotechnol (vol. 90), No. 3-4, pp. 257-267.

[76] Kakimoto, M.; Grunzinger, S. J. and Hayakawa, T. (2010): Hyperbranched poly(ether sulfone)s: preparation and application to ion-exchange membranes, Polymer Journal (vol. 42), No. 9, pp. 697-705.

[77] Kirkorian, Katerina; Ellis, Adam and Twyman, Lance J. (2012): Catalytic hyperbranched polymers as enzyme mimics; exploiting the principles of encapsulation and supramolecular chemistry, Chemical Society Reviews (vol. 41), No. 18, pp. 6138-6159.

[78] Dong, Zhongmin and Ye, Zhibin (2012): Hyperbranched polyethylenes by chain walking polymerization: synthesis, properties, functionalization, and applications, Polymer Chemistry (vol. 3), No. 2, pp. 286-301.

[79] Turk, H.; Haag, R. and Alban, S. (2004): Dendritic polyglycerol sulfates as new heparin analogues and potent inhibitors of the complement system, Bioconjugate Chemistry (vol. 15), No. 1, pp. 162-167.

[80] Dernedde, J.; Rausch, A.; Weinhart, M.; Enders, S.; Tauber, R.; Licha, K.; Schirner, M.; Zugel, U.; von Bonin, A. and Haag, R. (2010): Dendritic polyglycerol sulfates as multivalent inhibitors of inflammation, Proc Natl Acad Sci U S A (vol. 107), No. 46, pp. 19679-19684.

[81] Licha, K.; Welker, P.; Weinhart, M.; Wegner, N.; Kern, S.; Reichert, S.; Gemeinhardt, I.; Weissbach, C.; Ebert, B.; Haag, R. and Schirner, M. (2011): Fluorescence Imaging with Multifunctional Polyglycerol Sulfates: Novel Polymeric near-IR Probes Targeting Inflammation, Bioconjugate Chemistry (vol. 22), No. 12, pp. 2453-2460.

[82] Reichert, S.; Welker, P.; Calderon, M.; Khandare, J.; Mangoldt, D.; Licha, K.; Kainthan, R. K.; Brooks, D. E. and Haag, R. (2011): Size-Dependant Cellular Uptake of Dendritic Polyglycerol, Small (vol. 7), No. 6, pp. 820-829.

[83] Weinhart, M.; Groger, D.; Enders, S.; Riese, S. B.; Dernedde, J.; Kainthan, R. K.; Brooks, D. E. and Haag, R. (2011): The Role of Dimension in Multivalent Binding Events: Structure-Activity Relationship of Dendritic Polyglycerol Sulfate Binding to L-Selectin in Correlation with Size and Surface Charge Density, Macromolecular Bioscience (vol. 11), No. 8, pp. 1088-1098.

[84] Flory, P. J. (1952): Molecular Size Distribution in Three Dimensional Polymers .6. Branched Polymers Containing a-R-Bf-1 Type Units, Journal of the American Chemical Society (vol. 74), No. 11, pp. 2718-2723.

[85] Burchard, W. (1972): Angular-Distribution of Rayleigh-Scattering from Branched Polycondensates - Amylopectin and Glycogen Types, Macromolecules (vol. 5), No. 5, pp. 604-610.

[86] Burchard, W. (1977): Particle Scattering Factors of Some Branched Polymers, Macromolecules (vol. 10), No. 5, pp. 919-927.

[87] Gelade, E. T. F.; Goderis, B.; de Koster, C. G.; Meijerink, N.; van Benthem, R. A. T. M.; Fokkens, R.; Nibbering, N. M. M. and Mortensen, K. (2001): Molecular structure characterization of hyperbranched polyesteramides, Macromolecules (vol. 34), No. 11, pp. 3552-3558.

[88] De Luca, Edoardo; Richards, Randal W.; Grillo, I. and King, S. M. (2003): Molecular characterization of a hyperbranched polyester. II. Small-angle neutron scattering, Journal of Polymer Science Part B: Polymer Physics (vol. 41), No. 12, pp. 1352-1361.

[89] Garamus, V. M.; Maksimova, T. V.; Kautz, H.; Barriau, E.; Frey, H.; Schlotterbeck, U.; Mecking, S. and Richtering, W. (2004): Hyperbranched polymers: Structure of hyperbranched polyglycerol and amphiphilic poly(glycerol ester)s in dilute aqueous and nonaqueous solution, Macromolecules (vol. 37), No. 22, pp. 8394-8399.

[90] Antonietti, L.; Aymonier, C.; Schlotterbeck, U.; Garamus, V. M.; Maksimova, T.; Richtering, W. and Mecking, S. (2005): Core-shell-structured highly branched poly(ethylenimine amide)s: Synthesis and structure, Macromolecules (vol. 38), No. 14, pp. 5914-5920.

[91] Burchard, W.; Khalyavina, A.; Lindner, P.; Schweins, R.; Friedel, P.; Wiemann, M. and Lederer, A. (2012): SANS Investigation of Global and Segmental Structures of Hyperbranched Aliphatic-Aromatic Polyesters, Macromolecules (vol. 45), No. 7, pp. 3177-3187.

[92] Lieser, G.; Wegner, G.; Smith, J. A. and Wagener, K. B. (2004): Morphology and packing behavior of model ethylene/propylene copolymers with precise methyl branch placement, Colloid and Polymer Science (vol. 282), No. 8, pp. 773-781.

[93] Qiu, W. L.; Sworen, J.; Pyda, M.; Nowak-Pyda, E.; Habenschuss, A.; Wagener, K. B. and Wunderlich, B. (2006): Effect of the precise branching of polyethylene at each 21st CH2 group on its phase transitions, crystal structure, and morphology, Macromolecules (vol. 39), No. 1, pp. 204-217.

[94] Sworen, J. C. and Wagener, K. B. (2007): Linear low-density polyethylene containing precisely placed hexyl branches, Macromolecules (vol. 40), No. 13, pp. 4414-4423.

[95] Alamo, R. G.; Jeon, K.; Smith, R. L.; Boz, E.; Wagener, K. B. and Bockstaller, M. R. (2008): Crystallization of Polyethylenes Containing Chlorines: Precise vs Random Placement, Macromolecules (vol. 41), No. 19, pp. 7141-7151.

[96] Adrian, M.; Dubochet, J.; Lepault, J. and McDowall, A. W. (1984): Cryo-electron microscopy of viruses, Nature (vol. 308), No. 5954, pp. 32-36.

[97] Mcdowall, A. W.; Hofmann, W.; Lepault, J.; Adrian, M. and Dubochet, J. (1984): Cryo-Electron Microscopy of Vitrified Insect Flight-Muscle, Journal of Molecular Biology (vol. 178), No. 1, pp. 105-111.

[98] Dubochet, J.; Adrian, M.; Lepault, J. and Mcdowall, A. W. (1985): Cryo-Electron Microscopy of Vitrified Biological Specimens, Trends in Biochemical Sciences (vol. 10), No. 4, pp. 143-146.

[99] Mortensen, K. and Talmon, Y. (1995): Cryo-TEM and SANS microstructural study of pluronic polymer solutions, Macromolecules (vol. 28), No. 26, pp. 8829-8834.

[100] Egelhaaf, S. U.; Muller, M. and Schurtenberger, P. (1998): Size determination of polymer like micelles using cryo-electron microscopy, Langmuir (vol. 14), No. 16, pp. 4345-4349.

[101] Crassous, J. J.; Rochette, C. N.; Wittemann, A.; Schrinner, M.; Ballauff, M. and Drechsler, M. (2009): Quantitative analysis of polymer colloids by cryo-transmission electron microscopy, Langmuir (vol. 25), No. 14, pp. 7862-7871.

[102] Bolze, J.; Ballauff, M.; Rische, T.; Rudhardt, D. and Meixner, A. (2004): In situ structural characterization of semi-crystalline polymer latex particles by small-angle X-ray scattering\, Macromolecular Chemistry and Physics (vol. 205), No. 2, pp. 165-172.

[103] Potschke, D.; Ballauff, M.; Lindner, P.; Fischer, M. and Vogtle, F. (1999): Analysis of the structure of dendrimers in solution by small-angle neutron scattering including contrast variation, Macromolecules (vol. 32), No. 12, pp. 4079-4087.

[104] Potschke, D.; Ballauff, M.; Lindner, P.; Fischer, M. and Vogtle, F. (2000): Analysis of the structure of dendrimers in solution by small-angle neutron scattering using contrast variation, Journal of Applied Crystallography (vol. 33), No. 1, pp. 605-608.

[105] Rosenfeldt, S.; Dingenouts, N.; Ballauff, M.; Lindner, P.; Likos, C. N.; Werner, N. and Vogtle, F. (2002): Determination of the structure factor of polymeric systems in solution by small-angle scattering: A SANS-Study of a dendrimer of fourth generation, Macromolecular Chemistry and Physics (vol. 203), No. 13, pp. 1995-2004.

[106] Rosenfeldt, S.; Dingenouts, N.; Ballauff, M.; Werner, N.; Vogtle, F. and Lindner, P. (2002): Distribution of end groups within a dendritic structure: A SANS study including contrast variation, Macromolecules (vol. 35), No. 21, pp. 8098-8105.

[107] Likos, C. N.; Rosenfeldt, S.; Dingenouts, N.; Ballauff, M.; Lindner, P.; Werner, N. and Vogtle, F. (2002): Gaussian effective interaction between flexible dendrimers of fourth generation: A theoretical and experimental study, Journal of Chemical Physics (vol. 117), No. 4, pp. 1869-1877.

[108] Dingenouts, N.; Rosenfeldt, S.; Werner, N.; Vogtle, F.; Lindner, P.; Roulamo, A.; Rissanen, K. and Ballauff, M. (2003): Segmental contrast of dendrimers: a small-angle neutron scattering study including contrast variation, Journal of Applied Crystallography (vol. 36), pp. 674-678.

[109] Ballauff, M. and Likos, C. N. (2004): Dendrimers in solution: insight from theory and simulation, Angew Chem Int Ed Engl (vol. 43), No. 23, pp. 2998-3020.

[110] Rosenfeldt, S.; Dingenouts, N.; Potschke, D.; Ballauff, M.; Berresheim, A. J.; Mullen, K. and Lindner, P. (2004): Analysis of the spatial dimensions of fully aromatic dendrimers, Angewandte Chemie-International Edition (vol. 43), No. 1, pp. 109-112.

[111] Rosenfeldt, S.; Karpuk, E.; Lehmann, M.; Meier, H.; Lindner, P.; Harnau, L. and Ballauff, M. (2006): The solution structure of stilbenoid dendrimers: A small-angle scattering study, Chemphyschem (vol. 7), No. 10, pp. 2097-2104.

[112] Rosenfeldt, S.; Ballauff, M.; Lindner, P. and Harnau, L. (2009): Structure and interaction of flexible dendrimers in concentrated solution, Journal of Chemical Physics (vol. 130), No. 24.

[113] Kasai, N. and Kakudo, M. (2005): X-Ray Diffraction by Macromolecules, Kodansha, ISBN: 9783540253174.

[114] Roe, R.J. (2000): Methods of X-Ray and Neutron Scattering in Polymer Science, Oxford University Press, ISBN: 9780195113211.

[115] Ballauff, M. (2001): SAXS and SANS studies of polymer colloids, Current Opinion in Colloid & Interface Science (vol. 6), No. 2, pp. 132-139.

[116] Svergun, D. I. and Koch, M. H. J. (2003): Small-angle scattering studies of biological macromolecules in solution, Reports on Progress in Physics (vol. 66), No. 10, pp. 1735-1782.

[117] Glatter, O. and Kratky, O. (1982): Small angle x-ray scattering, Academic Press, ISBN: 9780122862809.

[118] Zemb, T. and Lindner, P. (2002): Neutrons, X-rays and light: scattering methods applied to soft condensed matter, Elsevier, ISBN: 9780444511225.

[119] Heiderich, M.; Reinartz, R.; Kurz, R. and Schelten, J. (1991): A 2-Dimensional Scintillation Detector for Small-Angle Neutron-Scattering, Nuclear Instruments & Methods in Physics Research Section a-Accelerators Spectrometers Detectors and Associated Equipment (vol. 305), No. 2, pp. 423-432.

[120] Debye, P. and Bueche, A. M. (1949): Scattering by an Inhomogeneous Solid, Journal of Applied Physics (vol. 20), No. 6, pp. 518-525.

[121] Debye, P. (1947): Molecular-weight determination by light scattering, J Phys Colloid Chem (vol. 51), No. 1, pp. 18-32.

[122] Mittelbach, P. (1964): Zur Rontgenkleinwinkelstreuung Verdunnter Kolloider Systeme 8, Acta Physica Austriaca (vol. 19), No. 1, pp. 53-102.

[123] Stuhrman.Hb and Kirste, R. G. (1965): Elimination der intrapartikulaeren Untergrundstreuung bei der Roentgenkleinwinkelstreuung an kompakten Teilchen (Proteinen), Zeitschrift Fur Physikalische Chemie-Frankfurt (vol. 46), No. 3-4, pp. 247-250.

[124] Kirste, R. G. and Stuhrman.Hb (1967): Elimination der intrapartikulären Untergrundstreuung bei der RöntgenkleinWinkelstreuung an kompakten Teilchen. III. Veriflzierung an Lösungen von Myoglobin, Zeitschrift Fur Physikalische Chemie-Frankfurt (vol. 56), No. 5-6, pp. 338-341.

[125] Hickl, P. and Ballauff, M. (1997): Interpretation of the structural parameters derived from the analysis of polymer colloids by small-angle X-ray and neutron scattering, Physica A (vol. 235), No. 1-2, pp. 238-247.

[126] Grillo, I. (2008): Small-Angle Neutron Scattering and Applications in Soft Condensed Matter Soft Matter Characterization, Borsali, Redouane and Pecora, Robert pp. 723-782, Springer Netherlands.

[127] Teixeira, S. C. M.; Zaccai, G.; Ankner, J.; Bellissent-Funel, M. C.; Bewley, R.; Blakeley, M. P.; Callow, P.; Coates, L.; Dahint, R.; Dalgliesh, R.; Dencher, N. A.; Forsyth, V. T.; Fragneto, G.; Frick, B.; Gilles, R.; Gutberlet, T.; Haertlein, M.; Hauss, T.; Haussler, W.; Heller, W. T.; Herwig, K.; Holderer, O.; Juranyi, F.; Kampmann, R.; Knott, R.; Krueger, S.; Langan, P.; Lechner, R. E.;

Lynn, G.; Majkrzak, C.; May, R. P.; Meilleur, F.; Mo, Y.; Mortensen, K.; Myles, D. A. A.; Natali, F.; Neylon, C.; Niimura, N.; Ollivier, J.; Ostermann, A.; Peters, J.; Pieper, J.; Ruhm, A.; Schwahn, D.; Shibata, K.; Soper, A. K.; Strassle, T.; Suzuki, J.; Tanaka, I.; Tehei, M.; Timmins, P.; Torikai, N.; Unruh, T.; Urban, V.; Vavrin, R. and Weiss, K. (2008): New sources and instrumentation for neutrons in biology, Chemical Physics (vol. 345), No. 2-3, pp. 133-151.

[128] Dewhurst, C. D. (2008): D33 - a third small-angle neutron scattering instrument at the Institut Laue Langevin, Measurement Science & Technology (vol. 19), No. 3.

[129] Littrell, Kenneth C. (2004): A comparison of different methods for improving flux and resolution on SANS instruments, Nuclear Instruments and Methods in Physics Research Section A: Accelerators, Spectrometers, Detectors and Associated Equipment (vol. 529), No. 1–3, pp. 22-27.

[130] van Well, A. A. (1992): Double-disk chopper for neutron time-of-flight experiments, Physica B: Condensed Matter (vol. 180–181, Part 2), No. 0, pp. 959-961.

[131] Draper, N. ; Perring, T.; Langridge, S. ; Taylor, J.; Proffen, T. ; Hagen, M.; Shipman, G. and Chown, N. Mantid Project, http://www.mantidproject.org

[132] Lindner, P. (2000): Water calibration at D11 verified with polymer samples, Journal of Applied Crystallography (vol. 33), No. 1, pp. 807-811.

[133] Zimm, B. H. (1948): Apparatus and Methods for Measurement and Interpretation of the Angular Variation of Light Scattering - Preliminary Results on Polystyrene Solutions, Journal of Chemical Physics (vol. 16), No. 12, pp. 1099-1116.

[134] Osichow, Anna; Rabe, Christian; Vogtt, Karsten; Narayanan, Theyencheri; Harnau, Ludger; Drechsler, Markus; Ballauff, Matthias and Mecking, Stefan (2013): Ideal Polyethylene Nanocrystals, Journal of the American Chemical Society.

[135] Trzaskowski, J.; Rabe, C.; Vogtt, K.; Krumova, M.; Goerigk, G.; Ballauff, M. and Mecking, S. (2012): Anisotropic nanoparticles of precise microstructure polyolefins, Chem Commun (Camb) (vol. 48), No. 73, pp. 9153-9155.

[136] Gröger, Dominic; Paulus, Florian; Licha, Kai; Welker, Pia; Weinhart, Marie; Holzhausen, Cornelia; Mundhenk, Lars; Abram, Ulrich; Gruber, Achim D. and Haag, Rainer (2013): Synthesis and Biological Evaluation of Radio and Dye Labeled Amino Functionalized Dendritic Polyglycerol Sulfates as Multivalent Antiinflammatory Compounds, Bioconjugate Chemistry.

[137] Sunder, A.; Mülhaupt, R.; Haag, R. and Frey, H. (2000): Hyperbranched Polyether Polyols: A Modular Approach to Complex Polymer Architectures, Advanced Materials (vol. 12), No. 3, pp. 235-239.

[138] Sunder, A.; Hanselmann, R.; Frey, H. and Mulhaupt, R. (1999): Controlled synthesis of hyperbranched polyglycerols by ring-opening multibranching polymerization, Macromolecules (vol. 32), No. 13, pp. 4240-4246.

[139] Provencher, S. W. (1982): Contin - a General-Purpose Constrained Regularization Program for Inverting Noisy Linear Algebraic and Integral-Equations, Computer Physics Communications (vol. 27), No. 3, pp. 229-242.

[140] Berne, B.J. and Pecora, R. (2000): Dynamic light scattering: with applications to chemistry, biology, and physics, Dover Publications, ISBN: 9780486411552.

[141] Lunkenbein, T.; Kamperman, M.; Li, Z. H.; Bojer, C.; Drechsler, M.; Forster, S.; Wiesner, U.; Muller, A. H. E. and Breu, J. (2012): Direct Synthesis of Inverse Hexagonally Ordered Diblock Copolymer/Polyoxometalate Nanocomposite Films, Journal of the American Chemical Society (vol. 134), No. 30, pp. 12685-12692.

[142] Haas, S. (2010): Nanochemische Zusammensetzungsanalyse mittels anomaler Röntgenkleinwinkelstreuung (ASAXS) - Erbium und Ytterbium dotierte Oxyfluorid-Glaskeramiken, Mathematisch-Naturwissenschaftliche Fakultät I, Humboldt Universität zu Berlin.

[143] Sztucki, M. On-line processing and analysis of SAXS data, http://www.sztucki.de/SAXSutilities/

[144] Keiderling, U. (2002): The new 'BerSANS-PC' software for reduction and treatment of small angle neutron scattering data, Applied Physics a-Materials Science & Processing (vol. 74), pp. S1455-S1457.

[145] Richard, D.; Ferrand, M. and Kearley, G. J. (1996): Analysis and visualisation of neutron-scattering data, Journal of Neutron Research (vol. 4), No. 1-4, pp. 33-39.

[146] Engels, R.; Clemens, U.; Kemmerling, G.; Noldgen, H. and Schelten, J. (2009): Position-sensitive detectors of the detector group at Julich, Nuclear Instruments & Methods in Physics Research Section a-Accelerators Spectrometers Detectors and Associated Equipment (vol. 604), No. 1-2, pp. 147-149.

[147] Kemmerling, G.; Bunten, U. B.; Clemens, U.; Engels, R.; Heiderich, M.; Pykhout-Hintzen, W.; Rongen, H.; Schelten, J.; Schwahn, D. and Zwoll, K. (2004): Performance measurements of a new large-area neutron scintillation detector system, Ieee Transactions on Nuclear Science (vol. 51), No. 3, pp. 1098-1102.

[148] Pipich, V. QtiKWS.

[149] Wittmann, J. C. and Lotz, B. (1982): Crystallization of Paraffins and Polyethylene from the Vapor-Phase - a New Surface Decoration Technique for Polymer Crystals, Makromolekulare Chemie-Rapid Communications (vol. 3), No. 10, pp. 733-738.

[150] Ungar, G.; Putra, E. G. R.; de Silva, D. S. M.; Shcherbina, M. A. and Waddon, A. J. (2005): The Effect of Self-Poisoning on Crystal Morphology and Growth Rates, Interphases and Mesophases in Polymer Crsytallization I (vol. 180) pp. 45-87, Springer Berlin Heidelberg.

[151] Toda, Akihiko (1993): Growth mode and curved lateral habits of polyethylene single crystals, Faraday Discussions (vol. 95), No. 0, pp. 129-143.

[152] Magonov, S. N.; Yerina, N. A.; Ungar, G.; Reneker, D. H. and Ivanov, D. A. (2003): Chain unfolding in single crystals of ultralong alkane C390H782 and polyethylene: An atomic force microscopy study, Macromolecules (vol. 36), No. 15, pp. 5637-5649.

[153] Petrenko, V.F. and Whitworth, R.W. (1999): Physics of Ice, Oxford University Press, USA, ISBN: 9780198518952.

[154] Perkins, S. J.; Nan, R. D.; Li, K. Y.; Khan, S. and Abe, Y. (2011): Analytical ultracentrifugation combined with X-ray and neutron scattering: Experiment and modelling, Methods (vol. 54), No. 1, pp. 181-199.

[155] Prevost, S. and Gradzielski, M. (2009): SANS investigation of the microstructures in catanionic mixtures of SDS/DTAC and the effect of various added salts, Journal of Colloid and Interface Science (vol. 337), No. 2, pp. 472-484.

[156] Bunn, C. W. (1939): The crystal structure of long-chain normal paraffin hydrocarbons. The "shape" of the CH2 group, Transactions of the Faraday Society (vol. 35), pp. 482-491.

[157] Seto, T.; Hara, T. and Tanaka, K. (1968): Phase Transformation and Deformation Processes in Oriented Polyethylene, Japanese Journal of Applied Physics (vol. 7), No. 1, pp. 31-42.

[158] Desper, C. R.; Cohen, S. H. and King, A. O. (1993): Morphological Effects of Ballistic Impact on Fabrics of Highly Drawn Polyethylene Fibers, Journal of Applied Polymer Science (vol. 47), No. 7, pp. 1129-1142.

[159] Russell, K. E.; Hunter, B. K. and Heyding, R. D. (1997): Monoclinic polyethylene revisited, Polymer (vol. 38), No. 6, pp. 1409-1414.

[160] Huang, H. (2000): Structure development and property changes in high density polyethylene during pan-milling, Journal of Applied Polymer Science (vol. 78), No. 11, pp. 2016-2024.

[161] Joo, Y. L.; Han, O. H.; Lee, H. K. and Song, J. K. (2000): Characterization of ultra high molecular weight polyethyelene nascent reactor powders by X-ray diffraction and solid state NMR, Polymer (vol. 41), No. 4, pp. 1355-1368.

[162] Kurelec, L.; Rastogi, S.; Meier, R. J. and Lemstra, P. J. (2000): Chain mobility in polymer systems: On the borderline between solid and melt. 3. Phase transformations in nascent ultrahigh molecular weight polyethylene reactor powder at elevated pressure as revealed by in situ Raman spectroscopy, Macromolecules (vol. 33), No. 15, pp. 5593-5601.

[163] Russell, K. E.; Hunter, B. K. and Heyding, R. D. (1993): Polyethylenes Revisited - Waxs and the Phase-Structure, European Polymer Journal (vol. 29), No. 2-3, pp. 211-217.

[164] Krimm, S. and Tobolsky, A. V. (1951): Quantitative X-Ray Studies of Order in Amorphous and Crystalline Polymers - Quantitative X-Ray Determination of Crystallinity in Polyethylene, Journal of Polymer Science (vol. 7), No. 1, pp. 57-76.

[165] Mcfaddin, D. C.; Russell, K. E.; Wu, G. and Heyding, R. D. (1993): Characterization of Polyethylenes by X-Ray-Diffraction and C-13-Nmr - Temperature Studies and the Nature of the Amorphous Halo, Journal of Polymer Science Part B-Polymer Physics (vol. 31), No. 2, pp. 175-183.

[166] Aggarwal, S. L. and Tilley, G. P. (1955): Determination of Crystallinity in Polyethylene by X-Ray Diffractometer, Journal of Polymer Science (vol. 18), No. 87, pp. 17-26.

[167] Williams, D.B.A. and Carter, C.B. (1996): Transmission Electron Microscopy: A Textbook for Materials Science. Basics, Plenum Press, ISBN: 9780306452475.

[168] Davis, G. T.; Eby, R. K. and Martin, G. M. (1968): Variations of Unit-Cell Dimensions of Polyethylene - Effect of Crystallization Conditions Annealing Deformation, Journal of Applied Physics (vol. 39), No. 11, pp. 4973-4981.

[169] Harnau, L.; Rosenfeldt, S. and Ballauff, M. (2007): Structure factor and thermodynamics of rigid dendrimers in solution, Journal of Chemical Physics (vol. 127), No. 1.

[170] Harnau, L. (2008): Structure and thermodynamics of platelet dispersions, Molecular Physics (vol. 106), No. 16-18, pp. 1975-2000.

[171] Chum, C. P.; Knight, G. W.; Ruiz, J. M. and Phillips, P. J. (1994): Computer Modeling of (110) Adjacent Reentry of Polyethylene Molecules, Macromolecules (vol. 27), No. 3, pp. 656-659.

[172] Dettenmaier, M.; Fischer, E. W. and Stamm, M. (1980): Calculation of Small-Angle Neutron-Scattering by Macromolecules in the Semi-Crystalline State, Colloid and Polymer Science (vol. 258), No. 3, pp. 343-349.

[173] Kavassalis, T. A. and Sundararajan, P. R. (1993): A Molecular-Dynamics Study of Polyethylene Crystallization, Macromolecules (vol. 26), No. 16, pp. 4144-4150.

[174] Sundararajan, P. R. and Kavassalis, T. A. (1995): Molecular-Dynamics Study of Polyethylene Chain Folding - the Effects of Chain-Length and the Torsional Barrier, Journal of the Chemical Society-Faraday Transactions (vol. 91), No. 16, pp. 2541-2549.

[175] Li, C. L.; Choi, P. and Sundararajan, P. R. (2010): Simulation of chain folding in polyethylene: A comparison of united atom and explicit hydrogen atom models, Polymer (vol. 51), No. 13, pp. 2803-2808.

[176] Minoia, Andrea; Chen, Liping; Beljonne, David and Lazzaroni, Roberto (2012): Molecular modeling study of the structure and stability of polymer/carbon nanotube interfaces, Polymer (vol. 53), No. 24, pp. 5480-5490.

[177] Strobl, G. (2005): A thermodynamic multiphase scheme treating polymer crystallization and melting, European Physical Journal E (vol. 18), No. 3, pp. 295-309.

[178] Wunderlich, B. and Czornyj, G. (1977): Study of Equilibrium Melting of Polyethylene, Macromolecules (vol. 10), No. 5, pp. 906-913.

[179] Wang, Y.; Rafailovich, M.; Sokolov, J.; Gersappe, D.; Araki, T.; Zou, Y.; Kilcoyne, A. D. L.; Ade, H.; Marom, G. and Lustiger, A. (2006): Substrate effect on the melting temperature of thin polyethylene films, Physical Review Letters (vol. 96), No. 2.

[180] Metatla, N.; Palato, S.; Commarieu, B.; Claverie, J. P. and Soldera, A. (2012): Melting of polymer nanocrystals: a comparison between experiments and simulation, Soft Matter (vol. 8), No. 2, pp. 347-352.

[181] Loo, Y. L.; Register, R. A. and Ryan, A. J. (2000): Polymer crystallization in 25-nm spheres, Physical Review Letters (vol. 84), No. 18, pp. 4120-4123.

[182] Waheed, N. and Rutledge, G. C. (2005): Crossover behavior in crystal growth rate from n-alkane to polyethylene, Journal of Polymer Science Part B-Polymer Physics (vol. 43), No. 18, pp. 2468-2473.

[183] Ratajski, E. and JaneschitzKriegl, H. (1996): How to determine high growth speeds in polymer crystallization, Colloid and Polymer Science (vol. 274), No. 10, pp. 938-951.
[184] Hickl, P.; Ballauff, M. and Jada, A. (1996): Small-angle X-ray contrast-variation study of micelles formed by poly(styrene)-poly(ethylene oxide) block copolymers in aqueous solution, Macromolecules (vol. 29), No. 11, pp. 4006-4014.
[185] Pedersen, J. S.; Svaneborg, C.; Almdal, K.; Hamley, I. W. and Young, R. N. (2003): A small-angle neutron and X-ray contrast variation scattering study of the structure of block copolymer micelles: Corona shape and excluded volume interactions, Macromolecules (vol. 36), No. 2, pp. 416-433.
[186] Mark, H.F. and Kroschwitz, J.I. (1989): Encyclopedia of polymer science and engineering, Wiley, ISBN: 9780471809487.
[187] Luzzati, V.; Tardieu, A.; Mateu, L. and Stuhrmann, H. B. (1976): Structure of human serum lipoproteins in solution: I. Theory and techniques of an X-ray scattering approach using solvents of variable density, Journal of Molecular Biology (vol. 101), No. 2, pp. 115-127.
[188] Pedersen, J. S. (1997): Analysis of small-angle scattering data from colloids and polymer solutions: modeling and least-squares fitting, Advances in Colloid and Interface Science (vol. 70), pp. 171-210.
[189] Berr, S. S. (1987): Solvent Isotope Effects on Alkyltrimethylammonium Bromide Micelles as a Function of Alkyl Chain-Length, Journal of Physical Chemistry (vol. 91), No. 18, pp. 4760-4765.
[190] Kotlarchyk, M. and Chen, S. H. (1983): Analysis of Small-Angle Neutron-Scattering Spectra from Polydisperse Interacting Colloids, Journal of Chemical Physics (vol. 79), No. 5, pp. 2461-2469.
[191] Shirley, R. The CRYSFIRE System for Automatic Powder Indexing, http://www.ccp14.ac.uk/
[192] Taupin, D. (1968): Une methode generale pour l'indexation des diagrammes de poudres, Journal of Applied Crystallography (vol. 1), No. 3, pp. 178-181.
[193] Werner, P.-E.; Eriksson, L. and Westdahl, M. (1985): TREOR, a semi-exhaustive trial-and-error powder indexing program for all symmetries, Journal of Applied Crystallography (vol. 18), No. 5, pp. 367-370.
[194] Boultif, A. and Louer, D. (1991): Indexing of Powder Diffraction Patterns for Low-Symmetry Lattices by the Successive Dichotomy Method, Journal of Applied Crystallography (vol. 24), No. 6, pp. 987-993.
[195] Laugier, J. ; Bochu B. CHEKCELL, http://www.ccp14.ac.uk/ccp/web-mirrors/lmgp-laugier-bochu/
[196] Favre-Nicolin, V. and Cerny, R. (2002): FOX, 'free objects for crystallography': a modular approach to ab initio structure determination from powder diffraction, Journal of Applied Crystallography (vol. 35), No. 6, pp. 734-743.
[197] Favre-Nicolin, Vincent and Cerny, Radovan FOX - Free Objects for Crystallography, http://vincefn.net/Fox/
[198] Turner-Jones, A. (1962): The triclinic crystal form of polymethylenes and polyethylenes, Journal of Polymer Science (vol. 62), No. 174, pp. S53-S56.
[199] Gutzler, F. and Wegner, G. (1980): Synthesis and Melting Behavior of Poly(Ethylene) Co-Polymers Obtained by Polymeranalogous Reaction, Colloid and Polymer Science (vol. 258), No. 6, pp. 776-786.
[200] Quadir, M. A. and Haag, R. (2012): Biofunctional nanosystems based on dendritic polymers, Journal of Controlled Release (vol. 161), No. 2, pp. 484-495.
[201] Roller, S.; Siegers, C. and Haag, R. (2004): Dendritic polyglycerol as a high-loading support for parallel multistep synthesis of GABA lactam analogues, Tetrahedron (vol. 60), No. 39, pp. 8711-8720.

[202] Roller, S.; Zhou, H. X. and Haag, R. (2005): High-loading polyglycerol supported reagents for Mitsunobu- and acylation-reactions and other useful polyglycerol derivatives, Molecular Diversity (vol. 9), No. 4, pp. 305-316.

[203] Seelenmeyer, S.; Deike, I.; Rosenfeldt, S.; Norhausen, C.; Dingenouts, N.; Ballauff, M.; Narayanan, T. and Lindner, P. (2001): Small-angle x-ray and neutron scattering studies of the volume phase transition in thermosensitive core-shell colloids, Journal of Chemical Physics (vol. 114), No. 23, pp. 10471-10478.

[204] Burchard, W. (1999): Solution properties of branched macromolecules, Branched Polymers Ii (vol. 143), pp. 113-194.

[205] Freltoft, T.; Kjems, J. K. and Sinha, S. K. (1986): Power-law correlations and finite-size effects in silica particle aggregates studied by small-angle neutron scattering, Phys Rev B Condens Matter (vol. 33), No. 1, pp. 269-275.

[206] Teixeira, J. (1988): Small-Angle Scattering by Fractal Systems, Journal of Applied Crystallography (vol. 21), pp. 781-785.

[207] Sorensen, C. M. and Wang, G. M. (1999): Size distribution effect on the power law regime of the structure factor of fractal aggregates, Physical Review E (vol. 60), No. 6, pp. 7143-7148.

[208] Mandelbrot, B.B. (1983): The Fractal Geometry of Nature, Henry Holt and Company, ISBN: 9780716711865.

[209] Bauer, J.; Dingenouts, N. and Ballauff, M. (1994): Small-Angle X-Ray and Light-Scattering from Randomly Branched Polycyanurates, Acta Polymerica (vol. 45), No. 6, pp. 430-434.

[210] Chantler, C. T. (1995): Theoretical Form-Factor, Attenuation and Scattering Tabulation for Z=1-92 from E=1-10 Ev to E=0.4-1.0 Mev, Journal of Physical and Chemical Reference Data (vol. 24), No. 1, pp. 71-591.

[211] Adam, M. and Lairez, D. (1993): Fractal Conformation of Polymers, Fractals-Complex Geometry Patterns and Scaling in Nature and Society (vol. 1), No. 2, pp. 149-169.

[212] Burchard, W. (2004): Angular dependence of scattered light from hyperbranched structures in a good solvent. A fractal approach, Macromolecules (vol. 37), No. 10, pp. 3841-3849.

[213] Trappe, V.; Bauer, J.; Weissmüller, M. and Burchard, W. (1997): Angular Dependence in Static and Dynamic Light Scattering from Randomly Branched Systems, Macromolecules (vol. 30), No. 8, pp. 2365-2372.

[214] de Gennes, P.G. (1979): Scaling concepts in polymer physics, CORNELL University Press, ISBN: 9780801412035.

[215] Sorensen, C. M. (2001): Light scattering by fractal aggregates: A review, Aerosol Science and Technology (vol. 35), No. 2, pp. 648-687.

[216] Sorensen, C. M.; Cai, J. and Lu, N. (1992): Test of Static Structure Factors for Describing Light-Scattering from Fractal Soot Aggregates, Langmuir (vol. 8), No. 8, pp. 2064-2069.

[217] Flory, Paul J. (1953): Principles of Polymer Chemistry, Cornell University Press, ISBN: 9780801401343.

[218] Isaacson, J. and Lubensky, T. C. (1980): Flory Exponents for Generalized Polymer Problems, Journal De Physique Lettres (vol. 41), No. 19, pp. L469-L471.

[219] Fleige, E.; Ziem, B.; Grabolle, M.; Haag, R. and Resch-Genger, U. (2012): Aggregation Phenomena of Host and Guest upon the Loading of Dendritic Core-Multishell Nanoparticles with Solvatochromic Dyes, Macromolecules (vol. 45), No. 23, pp. 9452-9459.

[220] Kim, Moon Suk; Hyun, Hoon; Seo, Kwang Su; Cho, Young Ho; Won Lee, Jung; Rae Lee, Chang; Khang, Gilson and Lee, Hai Bang (2006): Preparation and characterization of MPEG–PCL diblock copolymers with thermo-responsive sol–gel–sol phase transition, Journal of Polymer Science Part A: Polymer Chemistry (vol. 44), No. 18, pp. 5413-5423.

[221] Becer, C. Remzi; Hahn, Sabine; Fijten, Martin W. M.; Thijs, Hanneke M. L.; Hoogenboom, Richard and Schubert, Ulrich S. (2008): Libraries of methacrylic acid and oligo(ethylene glycol) methacrylate copolymers with LCST behavior, Journal of Polymer Science Part A: Polymer Chemistry (vol. 46), No. 21, pp. 7138-7147.

[222] Yoon, Jeong Ae; Gayathri, Chakicherla; Gil, Roberto R.; Kowalewski, Tomasz and Matyjaszewski, Krzysztof (2010): Comparison of the Thermoresponsive Deswelling Kinetics of Poly(2-(2-methoxyethoxy)ethyl methacrylate) Hydrogels Prepared by ATRP and FRP, Macromolecules (vol. 43), No. 10, pp. 4791-4797.

[223] Hu, Zhibing; Cai, Tong and Chi, Chenglin (2010): Thermoresponsive oligo(ethylene glycol)-methacrylate- based polymers and microgels, Soft Matter (vol. 6), No. 10, pp. 2115-2123.

[224] Ward, Mark A. and Georgiou, Theoni K. (2011): Thermoresponsive Polymers for Biomedical Applications, Polymers (vol. 3), No. 3, pp. 1215-1242.

[225] Li, Wen; Zhang, Afang and Schluter, A. Dieter (2008): Thermoresponsive dendronized polymers with tunable lower critical solution temperatures, Chemical Communications, No. 43, pp. 5523-5525.

[226] Kojima, Chie; Yoshimura, Kohei; Harada, Atsushi; Sakanishi, Yuichi and Kono, Kenji (2010): Temperature-sensitive hyperbranched poly(glycidol)s with oligo(ethylene glycol) monoethers, Journal of Polymer Science Part A: Polymer Chemistry (vol. 48), No. 18, pp. 4047-4054.

[227] Lutz, Jean-François and Hoth, Ann (2005): Preparation of Ideal PEG Analogues with a Tunable Thermosensitivity by Controlled Radical Copolymerization of 2-(2-Methoxyethoxy)ethyl Methacrylate and Oligo(ethylene glycol) Methacrylate, Macromolecules (vol. 39), No. 2, pp. 893-896.

[228] Lutz, Jean-François (2008): Polymerization of oligo(ethylene glycol) (meth)acrylates: Toward new generations of smart biocompatible materials, Journal of Polymer Science Part A: Polymer Chemistry (vol. 46), No. 11, pp. 3459-3470.

[229] Sztucki, M.; Di Cola, E. and Narayanan, T. (2012): Anomalous small-angle X-ray scattering from charged soft matter, European Physical Journal-Special Topics (vol. 208), No. 1, pp. 319-331.

[230] Goerigk, G.; Huber, K.; Mattern, N. and Williamson, D. L. (2012): Quantitative anomalous small-angle X-ray scattering - The determination of chemical concentrations in nano-scaled phases, European Physical Journal-Special Topics (vol. 208), No. 1, pp. 259-274.

[231] Waseda, Y. (2002): Anomalous X-Ray Scattering for Materials Characterization: Atomic-Scale Structure Determination, Springer, ISBN: 9783540434436.

[232] Kaiser, J.; Leppert, L.; Welz, H.; Polzer, F.; Wunder, S.; Wanderka, N.; Albrecht, M.; Lunkenbein, T.; Breu, J.; Kummel, S.; Lu, Y. and Ballauff, M. (2012): Catalytic activity of nanoalloys from gold and palladium, Physical Chemistry Chemical Physics (vol. 14), No. 18, pp. 6487-6495.

[233] Lu, Y. and Ballauff, M. (2011): Thermosensitive core-shell microgels: From colloidal model systems to nanoreactors, Progress in Polymer Science (vol. 36), No. 6, pp. 767-792.

[234] Wunder, S.; Lu, Y.; Albrecht, M. and Ballauff, M. (2011): Catalytic Activity of Faceted Gold Nanoparticles Studied by a Model Reaction: Evidence for Substrate-Induced Surface Restructuring, Acs Catalysis (vol. 1), No. 8, pp. 908-916.

[235] Crystallography, International Union of; Shmueli, U. and Hahn, T. (1992): International Tables for Crystallography, International Union of Crystallography.

[236] von Laue, M. (1960): Röntgenstrahlinterferenzen, Akademische Verlagsgesselschaft, Frankfurt a. M.

[237] Cromer, D. T. and Liberman, D. (1970): Relativistic Calculation of Anomalous Scattering Factors for X-Rays, Journal of Chemical Physics (vol. 53), No. 5, pp. 1891-1898.

[238] Koester, L.; Rauch, H. and Seymann, E. (1991): Neutron-Scattering Lengths - a Survey of Experimental-Data and Methods, Atomic Data and Nuclear Data Tables (vol. 49), No. 1, pp. 65-120.

[239] Potschke, D.; Ballauff, M.; Lindner, P.; Fischer, M. and Vogtle, F. (2000): The structure of dendritic molecules in solution as investigated by small-angle neutron scattering, Macromolecular Chemistry and Physics (vol. 201), No. 3, pp. 330-339.

[240] Flory, Paul J. (1952): Molecular Size Distribution in Three Dimensional Polymers. VI. Branched Polymers Containing A—R—Bf-1Type Units, Journal of the American Chemical Society (vol. 74), No. 11, pp. 2718-2723.

[241] Dobson, G. R. and Gordon, M. (1964): Configurational Statistics of Highly Branched Polymer Systems, The Journal of Chemical Physics (vol. 41), No. 8, p. 2389.

[242] Hammouda, B. (1992): Structure Factor for Starburst Dendrimers, Journal of Polymer Science Part B-Polymer Physics (vol. 30), No. 12, pp. 1387-1390.

[243] Hammouda, B. (2012): Small-Angle Scattering From Branched Polymers, Macromolecular Theory and Simulations (vol. 21), No. 6, pp. 372-381.

# Abbreviations

| | |
|---|---|
| ADMET | acyclic diene metathesis |
| AFM | atomic force microscopy |
| ASAXS | anomalous small angle X-ray scattering |
| CAC | critical aggregation concentration |
| CCD | charge-coupled device |
| CD | cadmium reference |
| CMS | core-multishell |
| cryo-TEM | cryogenic transmission electron microscopy |
| DDLS | depolarised dynamic light scattering |
| DLS | dynamic light scattering |
| DSC | differential scanning calorimetry |
| DTAC | dodecyltrimethylammonium chloride |
| EB | empty beam |
| EC | empty cell |
| ESRF | European Synchrotron Radiation Facility, Grenoble (France). |
| EPR | electron paramagnetic resonance |
| GPC | gel permeation chromatography |
| hPG | hyperbranched polyglycerol |
| ILL | Institut Laue-Langevin, Grenoble (France). |
| LS | light scattering |
| LogNorm | logarithmic normal (distribution) |
| MD | molecular dynamics |
| mPEG | monomethyl polyethylene oxide |
| PE | polyethylene |
| PEG | polyethylene glycol |
| PSI | Paul Scherrer Institute, Villigen (Switzerland) |
| rpm | rounds per minute |
| SANS | small angle neutron scattering |
| SAS | small angle scattering |
| SAXS | small angle X-ray scattering |
| SDS | sodium dodecylsulfate |
| SEAD | selected area electron diffraction |

| | |
|---|---|
| SLS | static light scattering |
| TEM | transmission electron microscopy |
| TOF | time of flight |
| TPPTS | 3,3′,3″-Phosphinidynetris(benzenesulfonic acid) trisodium salt |
| UHMW-PE | ultra high molecular weight polyethylene |
| vdW | *van der Waals* |
| VSANS | very small angle neutron scattering |
| WAXD | wide angle X-ray diffraction |
| WAXS | wide angle X-ray scattering |

**Formula symbols**

| | |
|---|---|
| $A$ | scaling constant |
| $A(q)$ | amplitude of scattered wave |
| $b$ | scattering length density |
| $b_m$ | scattering length density of the medium |
| $b_p$ | average scattering length density of the analyst |
| $b_i$ | scattering length |
| $B_{eff}$ | effective bond length |
| $\chi_a$ | fraction of the amorphous phase |
| $\chi_c$ | fraction of the crystalline phase |
| $coh$ | coherent |
| $d$ | distance of the planar crystal plane |
| $D$ | dispersity index |
| $D^*$ | dendritic structure unit |
| $\delta$ | phase difference |
| $DB$ | degree of branching |
| $DP_n$ | degree of polymerisation by number |
| $\Delta b$ | scattering contrast |
| $E_{kin}$ | kinetic energy |
| $\phi$ | volume fraction |
| $\phi_i$ | phase shift of chopper i |
| $f$ | functionality |
| $F(q)$ | form factor |
| $\Gamma$ | relaxation rate |

| | |
|---|---|
| $g(r)$ | pair correlation function |
| $h$ | *Planck*-constant |
| $h(r / \xi)$ | cut-off function |
| *incoh* | incoherent |
| $I(q \rightarrow 0)$ | forward scattering intensity |
| $I_I(q)$ | scattering intensity corresponding to the inner term |
| $I_S(q)$ | scattering intensity corresponding to the shape term |
| $I_{SI}(q)$ | scattering intensity corresponding to the cross term |
| $\varphi$ | phase shift |
| $K$ | scattering constant |
| $K^*$ | scaling constant |
| $\lambda$ | wavelength |
| $L$ | length |
| $L^*$ | linear structure unit |
| $m$ | mass |
| $m_P$ | proton mass |
| $m_n$ | neutron mass |
| $M_n$ | number averaged molecular weight |
| $M_w$ | weight averaged molecular weight |
| $v$ | velocity |
| $v_i$ | chopper rotation frequency |
| $N$ | particle number |
| $p$ | momentum |
| $q$ | scattering vector |
| $\theta$ | scattering angle |
| $\rho$ | mass density |
| $R$ | radius |
| $R_e$ | *Thompson*-radius of the electron |
| $R_G$ | radius of gyration |
| $R_H$ | Hydrodynamic radius |
| $R_{HS}$ | hard sphere radius |
| $\rho(r)$ | radial scattering length density distribution |
| $s_i$ | distance to the pulse source |
| $\sigma$ | cross section |

| | |
|---|---|
| $\sigma_{Log\text{-}Norm}$ | standard deviation of LogNorm distribution |
| $\sigma^*$ | surface free energy of folded polymer chains |
| $S(q)$ | structure factor |
| $t$ | time |
| $\tau$ | time frame of choppers in open state |
| $T$ | temperature |
| $T^*$ | terminal structure unit |
| $T(r)$ | shape function |
| $T(\lambda)$ | transmission as a function of the wavelength |
| $T_c$ | crystallisation temperature |
| $T_m$ | melting temperature |
| $T_m^\infty$ | equilibrium melting temperature of infinite sized crystals |
| $v$ | velocity |
| $V$ | scattering volume |
| $V_m$ | molar volume |
| $V_P$ | particle volume |
| $\omega$ | weight fraction |
| $\Omega$ | solid angle |
| $\xi$ | correlation length |
| $Z$ | atomic number |

# Publications

Parts of this work were published or are in preparation for publication.

Journals

- Trzaskowski J., Rabe C., Vogtt K., Krumova M., Goerigk G., Ballauff M. and Mecking S., **Anisotropic nanoparticles of precise microstructure polyolefins**. *Chemical Communications*, **2012**. 48(73): p. 9153-9155.
- Osichow A., Rabe C., Vogtt K., Narayanan T., Harnau L., Drechsler M., Ballauff M. and Mecking S., **Ideal polyethylene nanocrystals**, *Journal American Chemical Society*, **2013**, 135 (31): p. 11645–11650
- Rabe C., Fleige E., Vogtt K., Szekely N., Lindner P., Burchard W., Haag R., Ballauff M., **The multi-domain nanoparticle structure of a universal core-multi-shell nanocarrier**, Polymer, **2015,** 55(26): p. 6735-6742
- Vogtt K., Siebenbürger M., Clemens D., Prévost S., Rabe C. Russina M., Fromme M., Mezei F. and Ballauff M., **A new time-of-flight small-angle scattering instrument at the Helmholtz-Zentrum Berlin: V16/VSANS**, Journal of Applied Crystallography, **2014**, (47): p. 237-244

Poster presentations

- Rabe C., Fleige E., Vogtt K., Goerigk G., Haag R., Ballauff M. „**Structural Investigations of Core-Multishell Nanoparticles – First results from small angle scattering experiments**“, 25th meeting of the European Colloid and Interface Society, Berlin, Germany, **2011**
- Rabe C., Fleige E., Vogtt K., Goerigk G., Haag R., Ballauff M. „**Structural Investigations of Core-Multishell Nanoparticles – First results from small angle scattering experiments**“, Photons, Neutrons and Ions (PNI) - 2nd joined workshop of the Helmholtz Centers, Potsdam, Germany, **2012**

Publication that are not directly related

Journals

- Rojas O., Tiersch B., Rabe C., Stehle R., Hoell A., Arlt B., Koetz J., **Non-aqueous microemulsions based on N,N'-alkylimidazolium alkylsulfate ionic liquids**, *Langmuir*, **2013**. 29(23): p. 6833-6839.

# Acknowledgments

Abschließend möchte ich allen danken die auf vielfältige Weise am Gelingen dieser Arbeit beteiligt waren. Mein besonderer Dank gilt:

Herrn Prof. Dr. Matthias Ballauff für die Möglichkeit diese Arbeit unter seiner Anleitung anzufertigen und für die stete Unterstützung.

Herrn Prof. Dr. Klaus Rademann für die Übernahme der Aufgaben des Koreferenten.

Dem Helmholtz-Zentrums Berlin für Materialien und Energie für die finanzielle Unterstützung.

Anna Osichow und Justyna Trzaskowski aus der Arbeitsgruppe von Prof. Dr. Stefan Mecking an der Universität Konstanz für die Bereitstellung der Polyethylenproben und die sehr schöne und sich stets ergänzende Zusammenarbeit.

Emanuel Fleige und Florian Paulus aus dem Arbeitskreis von Prof. Dr. Rainer Haag an der Freien Universität Berlin für die Bereitstellung der Proben des hyperverzweigten Polyglycerols und des Kern-Schale Systems, sowie die Überlassung wichtiger Analyseergebnisse zur weiteren Interpretation. Bei Emanuel möchte ich mich darüber hinaus bedanken, dass er meine Arbeit mit großem Interesse verfolgt und mich durch hilfreiche Anregungen von Beginn an unterstützt hat.

Dr. Karsten Vogtt, der für mich ein exzellenter Lehrer war und mir somit den Einstieg in die komplexe Methodik der Kleinwinkelstreuung entscheidend erleichtert hat. Darüber hinaus waren die zahlreichen Diskussionen und Anregungen Grundlage für immer neue Idee und Motivationen.

Herrn Prof. Dr. Walther Burchard für sein sehr großes Interesse an meiner Arbeit. Ihm verdanke ich die Modelle und Ansätze zur Beschreibung der Kleinwinkelstreuung des hyperverzweigte Polyglycerols und des darauf basierenden Kern-Schale-Systems. Darüber hinaus bedanke ich mich für die sehr intensiven fachlichen Diskussionen und die ermutigende Korrespondenz.

Dr. Peter Lindner und Dr. Noemi Szekely für die Unterstützung bei den SANS-Messungen an den Instrumenten D11 am ILL in Grenoble und KWS I am FRM II in Garching.

Dr. Theyencheri Narayanan, Dr. Armin Hoell und Dr. Sylvio Haas für die Unterstützung bei der Vorbereitung und Durchführung der Experimente an den SAXS-Instrumenten ID02 am ESRF in Grenoble und der ASAXS-Anlage am BESSY-II in Berlin.

Dr. Ludger Hanau für die Unterstützung bei der Modellierung der SAXS-Datensätze für die hochkristallinen Polyethylennanopartikel, sowie für die hilfreichen Diskussions- und Interpretationsansätze.

Allen Kollegen des Instituts für weiche Materie und funktionale Materialien am HZB möchte ich für die sehr schöne Zeit in Wannsee danken, an die ich mich gern erinnern werde. Hier sollen allerdings Miriam, Steffanie, Daniel und Matthias ein ganz besonderer Dank gewidmet sein.

Meiner Freundin Maren möchte ich für Ihr Verständnis und Ihren Rückhalt danken und mich für die unzähligen Stunden entschuldigen, in denen ich mich in meiner Arbeit verloren habe.

Bei meiner Familie, der ich diese Arbeit gewidmet habe, möchte ich mich für die stete Unterstützung bei meinem Studium bedanken. Ohne ihre Hilfe hätte auch diese Arbeit nicht entstehen können.

# Appendix

## 1) Scattering of X-rays and Neutrons

The scattering of neutrons and X-rays is similar in many ways. This is why theoretical concepts and experimental techniques can be used for neutron and X-ray scattering in an equivalent way. Notwithstanding, there are differences between the probes that make neutron and X-ray scattering complementary techniques and therefore powerful tools, enlarging the spectrum of information in the analysis of soft matter issues. One of the major differences is that the scattering of X-rays takes place at the atoms electronic shell, whereas the scattering of neutrons results from interactions between the neutrons and the atoms nuclei.

### 1 - a) Scattering of X-rays

X-rays used for soft matter analysis cover wavelengths of the electromagnetic spectrum between 0.5 Å < $\lambda$ < 2.5 Å. Wavelengths of around 1 Å are favoured as they represent the same order of magnitude as it is typical for interatomic distances in soft condensed matter [114].

The scattering of X-rays is phenomenon taking place at the electron shell of atoms. The electron cloud around the atoms nuclei follows a radial density distribution which is quantified by the atomic scattering factor *f(q)*:

$$f(q) = 4\pi \int_V \rho_e(r) r^2 \frac{sin(qr)}{qr} dr \tag{65}$$

The radial distribution $\rho_e(r)$ for different atoms is calculated by quantum mechanics and is tabulated in relevant literature [235]. For the small angle regime *f(q)* only scales with the atomic number *Z* [114].

The quantitative evaluation of X-ray scattering is described by the *Thompson* equation describing the differential scattering cross section of isolated electrons [236]:

$$\frac{d\sigma}{d\Omega} = R_e^2 \frac{1 + cos^2\theta}{2} \tag{66}$$

Here, $R_e$ is the classical electron or *Thompson* radius with $R_e$ = 2.818 $10^{-15}$ m and $\theta$ is the scattering angle. This relation is also valid for bounded electrons. For this case the *Compton* contribution, describing the inelastic scattering, arises in addition to the elastic scattering. This additional term can be neglected for the small angle scattering [3]. The factor (1+cos$^2$ 2$\theta$/ 2) in equation (66) is known as the polarisation factor and becomes unity at small scattering angles as well. This leads to an expression that again only depends on the number of electrons of the atom and thus on the atomic number *Z* [118]:

$$\left(\frac{d\sigma}{d\Omega}\right)_i = r_e^2 Z_i \tag{67}$$

**Tab. S 1: Overview on common agents used for contrast variation experiments with SAXS.**

| | formula | $\rho$ | $b_{X\text{-}ray}$ |
|---|---|---|---|
| | | g cm$^{-3}$ [25 °C] | $10^{10}$cm$^{-2}$ |
| water | $H_2O$ | 0.997 | 9.420 |
| glucose | $C_6H_{12}O_6$ | 1.540 | 16.247 |
| sucrose | $C_{12}H_{22}O_{11}$ | 1.587 | 14.319 |
| glycerine | $C_3H_8O_3$ | 1.261 | 11.619 |
| toluene | $C_6H_5CH_3$ | 0.862 | 6.988 |

The individual scattering length density *b* in this case can be calculated from the sample composition with respect to the atomic numbers $Z_i$ of the incorporated compounds and its respective molar volume $V_m$.

$$b_{X-ray} = \frac{\sum Z_i r_e}{V_m} \tag{68}$$

For contrast variation purpose in X-ray scattering the scattering length density of the dispersions medium $b_m$ can be adjusted by the addition of contrast agents. Sugars and glycerine carrying a large number of oxygen in their molecular structure are commonly used for the increase of $b_m$ [5,118]. The scattering length densities of some agents are listed in Tab. S 1.

The photon energies used for soft matter analysis are mostly apart from the corresponding X-ray adsorption edges of atoms in organic structures. Nevertheless, a variation of the photon energies can be useful for the analysis of the interactions of metal nanoparticles and respective precursor ions with organic molecules by small angle scattering. For this purpose an additional anomalous scattering factor $f_a(E, q)$ arising from the anomalous dispersion around the specific adsorption edges of an element and thus depends on the characteristic adsorption cross section $\sigma_a$ [237]. The method taking advantage of this relation is known as anomalous small angle scattering - ASAXS [5,118,229,230,231].

## 1 - b) Scattering of neutrons

Neutrons are uncharged particles with a mass of $m_p$ = 1.674 10$^{-27}$ kg and a spin of ½ related to their magnetic moment. Their kinetic energy $E_{kin}$ and momentum *p* are defined by their velocity $\nu$. The source of neutrons for science in the classical way is the nuclear fission reaction of uranium $^{235}$U taking place in a nuclear reactor [114]. Nevertheless, spallation sources gained more importance during recent years [114]. Here the release of neutrons follows the bombardment of a heavy metal target by accelerated high energy protons. As target material lead is commonly used. In both cases the generated neutrons a have high velocity and therefore a corresponding small *de Broglie* wavelength of around $\lambda$ = 0.7 Å (*T* = 3000 K, 'hot neutrons'). For this reason, they are used for analysis of hard matter issues. For most of the issues arising from the analysis of soft matter the neutrons have to be moderated. In the so called cold source filled with liquid deuterium at 25 K the neutrons slow down by repeated collision with the moderator to corresponding wavelength of around $\lambda$ = 6 Å. The kinetic energy of neutrons is the range of several meV whereas the energy of

**Tab. S 2: Overview on scattering length *b* and respective scattering cross sections $\sigma$ for coherent ($\sigma_{coh}$) and incoherent contributions ($\sigma_{incoh}$) of selected isotopes for neutron scattering. For comparison the scattering length corresponding to X-ray scattering in the small angle regime and to the *K*-$\alpha$ radiation ($\lambda$ = 1.541 Å ) are listed [238].**

| | Z | $b_{coh}$ | $\sigma_{coh}$ | $\sigma_{incoh}$ | $b_{coh-K\text{-}\alpha}$ |
|---|---|---|---|---|---|
| | | $10^{-12}$cm | $10^{-24}$cm$^{-2}$ | $10^{-24}$cm$^{-2}$ | $10^{-12}$cm |
| $^{1}$H | 1 | -0.374 | 1.76 | 79.9 | 0.28 |
| $^{2}$D | 1 | 0.667 | 5.59 | 2.04 | 0.28 |
| $^{12}$C | 6 | 0.665 | 5.55 | 0.001 | 1.69 |
| $^{16}$O | 8 | 0.580 | 4.23 | 0 | 2.25 |
| $^{26}$Al | 13 | 0.345 | 1.495 | 0.008 | 3.65 |
| $^{28}$Si | 14 | 0.415 | 2.16 | 0.015 | 3.93 |
| $^{56}$Fe | 26 | 0.994 | 12.42 | 0 | 7.29 |

**Tab. S 3: Overview on applied agents for the contrast variation experiments using neutrons. Here, *b* represents the scattering length density and $\rho$ is the mass density.**

| | formula | $\rho$ | $b_{neutrons}$ |
|---|---|---|---|
| | | g cm$^{-3}$ [25 °C] | $10^{10}$cm$^{-2}$ |
| water | $H_2O$ | 0.9974 | -0.561 |
| deuterium oxide | $D_2O$ | 1.1044 | 6.358 |
| toluene | $C_6H_5CH_3$ | 0.8623 | 0.935 |
| toluene D-8 | $C_6D_5CD_3$ | 0.943 | 5.662 |

X-rays is in the range of some keV. Therefore, it is possible to probe atomic movements in matter by neutron scattering in an inelastic scattering experiments [118]. Another advantage of neutrons is their magnetic moment, that allows them to interact with magnetic structures.

An overview on the scattering lengths and the contributions of coherent and incoherent scattering cross sections of different isotopes are given in Tab. S 2. The values of *b* corresponding to the *K*-$\alpha$ radiation are given additionally. These values take into account the approximation being valid for small angle scattering.

The values of *b* can be calculated as already discussed for X-rays from the samples composition and the corresponding molar volume.

$$b_{neutrons} = \frac{\sum b_i}{V_m} \tag{69}$$

Soft matter science takes advantage of the significant difference of the coherent scattering cross section of hydrogen and deuterium. A contrast can either be generated by the utilization of mixtures of deuterated and non-deuterated solvents or by specific deuteration of the analyst. An overview on the corresponding scattering length densities of agents, which were used in the contrast variation series are given in Tab. S 3.

## 1 - c) Consideration of the incoherent scattering contribution

To consider the contribution arising from the incoherent scattered radiation, equation (13) in the main text has to be completed to the following:

$$I(q) = \phi V_P \Delta b^2 F(q) S(q) + \phi V_P I_{incoh} \tag{70}$$

Herein, $I_{incoh}$ represents the incoherent scattering intensity. This value is significant for the probed species as it depends on its molecular composition. For most issues in soft matter science the contribution of incoherently scattered X-rays is vanishing small and is thus neglected. However, in neutron scattering the incoherent scattering cross sections $\sigma_{incoh}$ for different isotopes varies and has to be considered. For selected examples the respective $\sigma_{incoh}$ are given in Tab. S 2. The major share of the incoherent scattered radiation arises due to the $\sigma_{incoh}$ of hydrogen. The individual contribution of $I_{incoh}$ could either be calculated from a known sample composition, or as this contribution is independent of the variation of $\Delta b$ it can also be determined from a contrast variation series. The magnitude of $I_{incoh}$ can be estimated from plots of the forward scattering intensity $I(q \rightarrow 0)$ as a function of $b_m$ [239].

Apart from that the incoherent scattering of hydrogen is exploited for the absolute calibration of the scattering intensities and for the determination of the detectors sensitivity. Here, often water or Plexiglas are used as reference materials [118,132]

## 2) Analysis of polyethylene nanoparticles by SAXS using contrast variation

The SAXS measurements performed with dispersions of crystalline polyethylene nanoparticles (6.1.1) were supplemented by measurements using an analytical ultra-centrifuge.

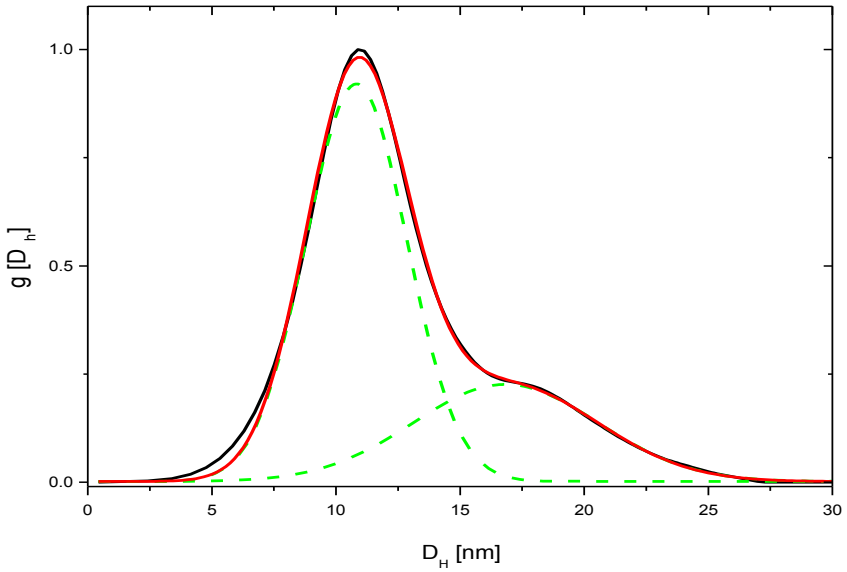


**Fig. S 1: Analytical ultra-centrifugation measurement of PE-nanoparticles dispersed in $D_2O$ (black line). The measurements were realised at 60˙000rpm rotor speed using interference detection.**[1]

The measured hydrodynamic particle dimensions show a bimodal distribution with a major peak at $R_H \approx 5.4$ nm and minor one at $R_H \approx 8.4$ nm. This observation was used for the bimodal distribution used for the calculation of the scattering intensities measured with the contrast variation series of the PE-nanoparticles.

[1] The measurements were performed in the group of Prof. Coelfen from the University of Konstanz.

## 3) Analysis of hyperbranched Polyglycerol by $^{1}H$ and $^{13}C$-NMR

The microstructural analysis of the hyperbranched polyglycerol scaffold was one by analysis of the $^{1}H$ and $^{13}C$ NMR-spectra following the procedure given by Sunder [138].

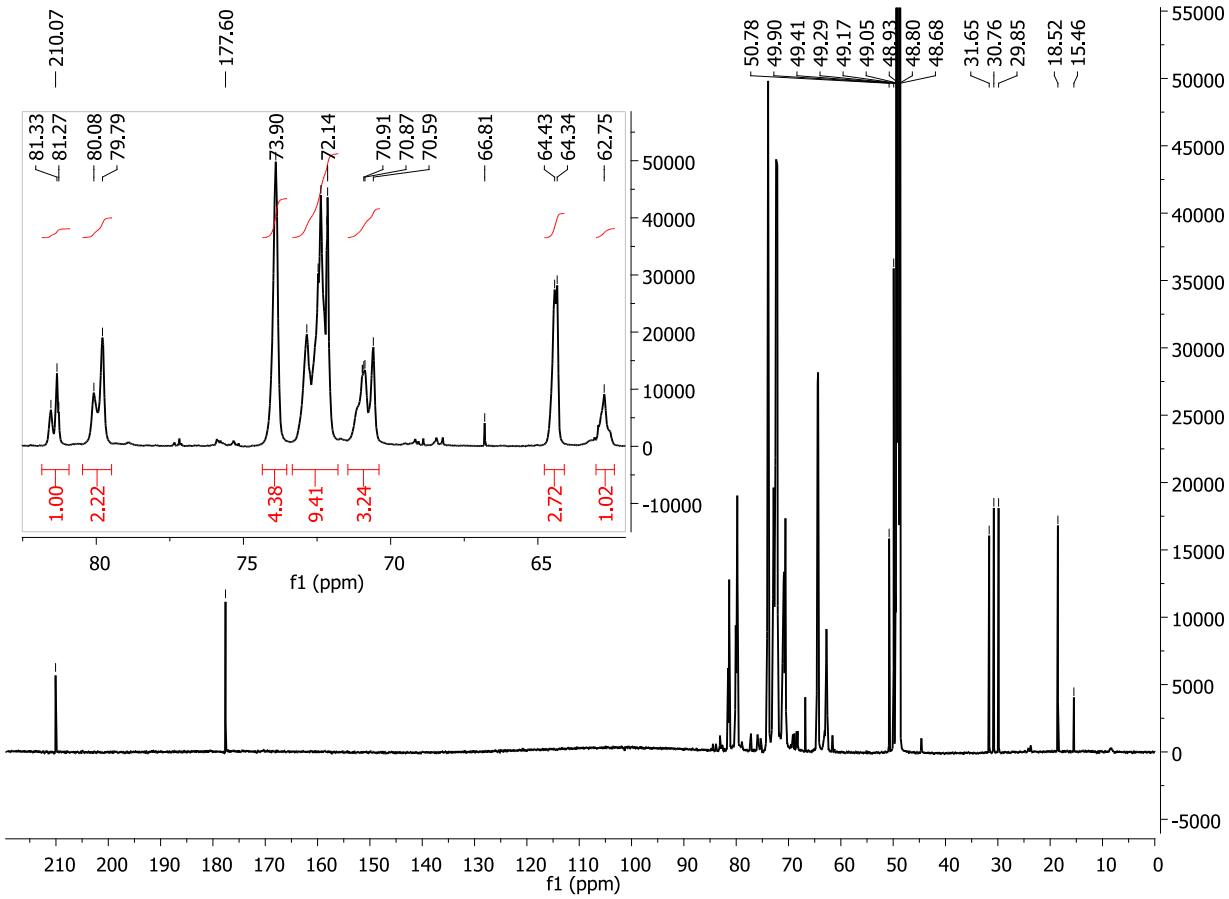


**Fig. S 2: $^{13}C$-NMR spectrum ($CD_3OD$) of hyperbranched polyglycerol obtained by anionic polycondensation using 1, 1, 1-Trimethylolpropane (TMP) for initiation. The inset shows the integrated spectra of the hyperbranched segmental units for the determination of the *DB* and averaged $DP_n$.[2]**

[2] The measurement data were provided by AG Haag from Free University of Berlin.

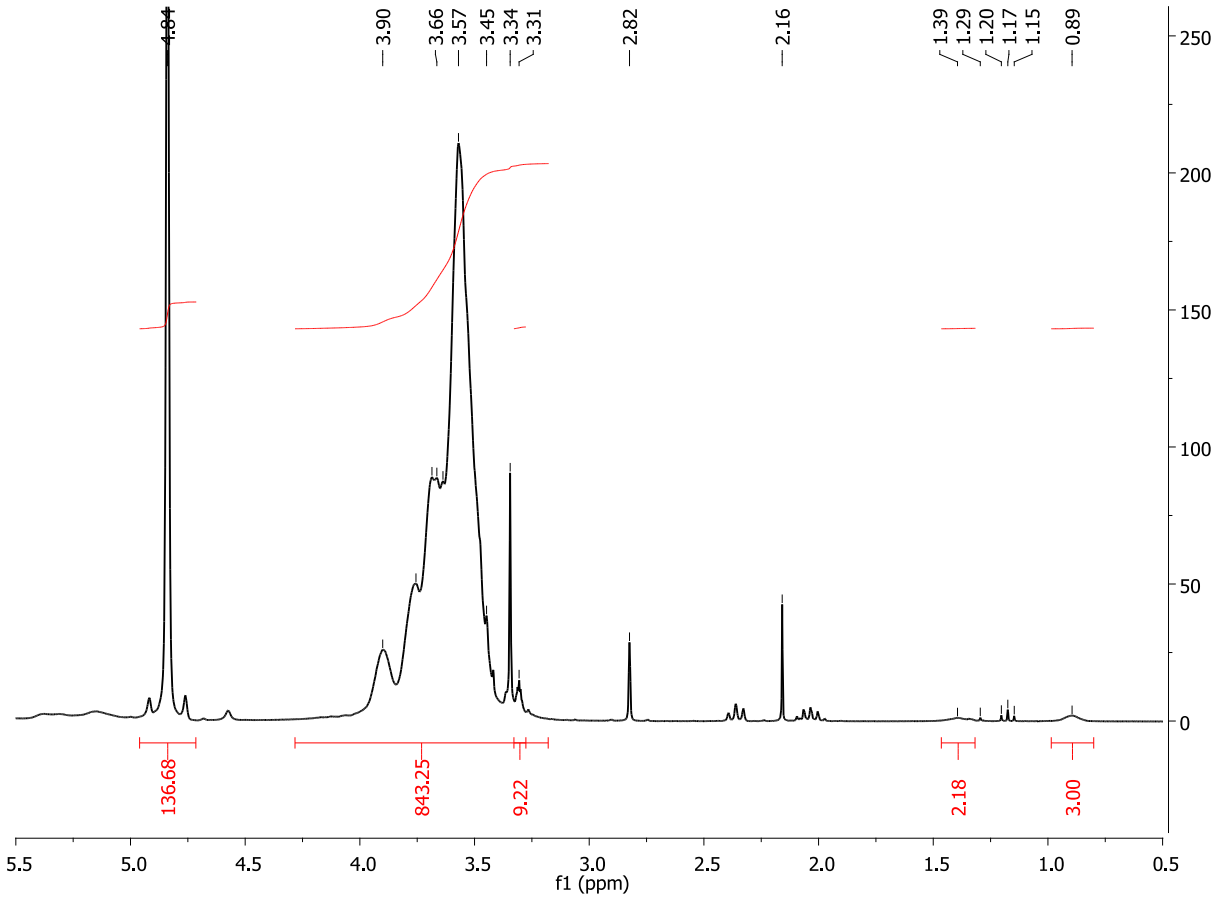


**Fig. S 3: Integrated $^{1}$H-NMR spectrum of hPG measured in methanol D4-**

$^{1}$H-NMR (250 MHz): $\delta$ (ppm) = 4.00 – 3.20 (m, hPG backbone), 1.35 (q, -$CH_2$-$CH_3$, TMP-core), 0.90 (t, -$CH_2$-$CH_3$, TMP-core). $^{13}$C-NMR (175 MHz): $\delta$ (ppm) = 82.0 – 81.0 (PG backbone, $L_{13}$-units), 80.5 – 79.5 (hPG backbone, D-units), 74.5 – 73.5 (hPG backbone, $L_{14}$ units), 73.5 – 72.0 (hPG backbone, T/D-units), 72.0 – 70.5 (hPG backbone, $L_{13}$/ $L_{14}$-units), 65.0 – 64.0 (hPG backbone, T-units), 63.5 – 62.0 (hPG backbone, $L_{13}$-units), 44.7 ($CH_3$-$CH_2$-C-($CH_3OH$)$_3$, TMP-core), 23.7 ($CH_3$-$CH_2$-C-($CH_3OH$)$_3$, TMP-core), 8.2 ($CH_3$-$CH_2$-C-($CH_3OH$)$_3$, TMP-core).

## 4) Alternative Particle Scattering Factor of hyperbranched molecules[3]

The scattering intensities of the hyperbranched polyglycerol were evaluated employing the approach recently reported by Burchard [91]. It takes advantage of fundamental principles from polymer statistics and is thus based on the early work of Flory predicting molecular parameters for branched polymers [217,240]. Following these ideas the degree of polymerisation can be calculated from:

$$DP_w = \frac{1 - \frac{\alpha^2}{2}}{(1-\alpha)^2} \tag{71}$$

The factor $\alpha$ is accessible by solving the parabolic equation (71) using $DP_w$ as discussed in section 6.2.1.2. This value is related to the probability of the reaction of either one of the *f* groups of an $AB_f$ monomer and was calculated to be $\alpha = 0.92099$.

The theory of cascade processes introduced by Gordon [241] was successfully applied by Burchard to the growth of hyperbranched polymers [85,86]. The illustration in Fig. 85 displays the treelike growth of $AB_2$-units emanating from two different initial generations to form the hyperbranched architecture. The reaction probability of either one of the functional groups A and B is given by the parameters $\alpha$ and $\beta$. Hence, $\alpha$ depicts the probability that B reacts with A and $\beta$ for the reaction of B with A to form the new generation $G_n$. Herein, the reaction of A and B of the same unit is not allowed. For an ideal growth $\beta = \alpha / 2$ holds.

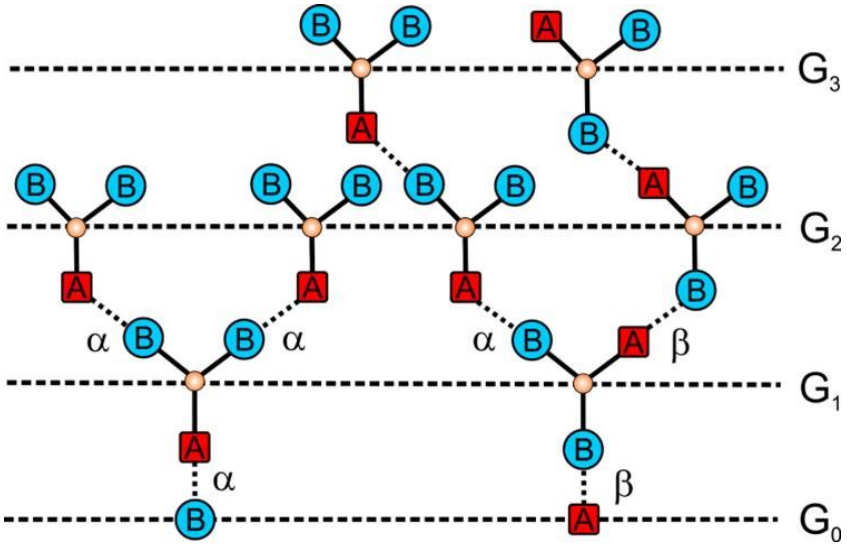


**Fig. 85: Principle of the growth of a hyperbranched scaffold by an $AB_2$-unit based on the concept of cascade processes by Gordon [85]. The respective probabilities for the formation of the next generation $G_n$ are given by $\alpha$ and $\beta$.**

[3] The discussion is based on: Burchard, W., et al.; *Macromolecules*, **2012**; 45; 3177-3187 and further private communications with Prof. Walther Burchard and Dr. Albena Lederer during a meeting at the Leibniz-Institute of Polymer Research on 11th January 2013, which should be gratefully acknowledged here.

These fundamental principles furthermore supplied the development of the particle scattering factor of hyperbranched structures [91].

$$F(q) = \frac{1}{DP_w}\left(\frac{1+\alpha\phi}{1-\alpha\phi} + \frac{\alpha^2\phi^2}{2(1-\alpha\phi)^2}\right) = \frac{1}{DP_w}\left(\frac{1-\frac{\alpha^2\phi^2}{2}}{(1-\alpha\phi)^2}\right) \quad (72)$$

This correlation displays the decomposition into contributions related to the growth of the linear segments and to those correlating with the growth of the branched structure. The linear segments yield from the limited reaction probability of the functional groups of the monomers as already suggested by the scheme displayed in Fig. 41. Furthermore, it becomes obvious from this correlation that the contribution correlating with the branching increases more with $\alpha$ than the contribution related to the linear segments. For this reason the polycondensates of $AB_f$-monomers are structural heterogeneous. Furthermore, this relation embodies the well-known *Debye*-approximation [121]:

$$\phi = \exp\left(\frac{-b_{eff}^{\ 2} q^2}{6}\right) \approx 1 - \left(\frac{b_{eff}^{\ 2} q^2}{6}\right) \quad (73)$$

Herein, the interference between neighbouring units is given by $\phi(q, b_{eff})$, whereas $b_{eff}$ depicts the effective bond length. The individual scattering units are thus simplified to invariant structural elements, whose spatial correlation is given by the respective particle scattering factor. This principle was furthermore applied for computing the spatial structure of dendritic architectures [242,243]. Equation (71) is recovered from equation (72) for $q = 0$ and $\alpha = 1$.

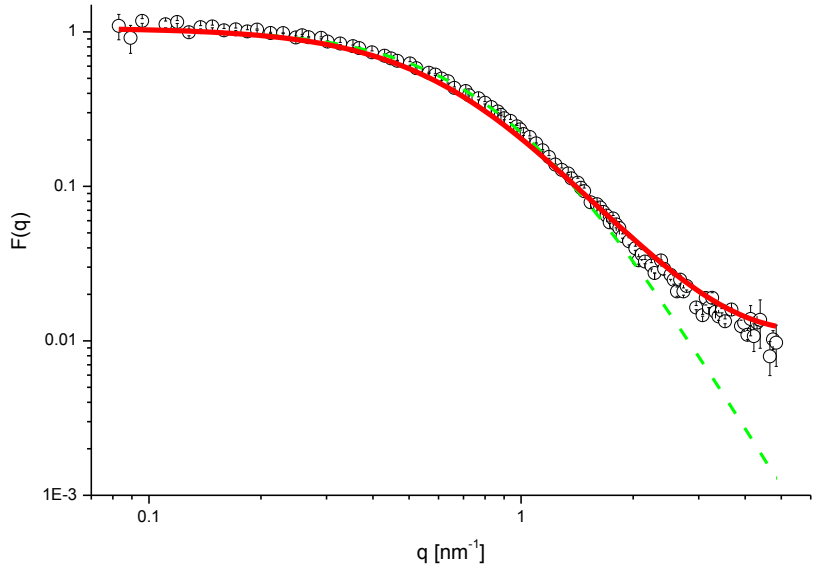


**Fig. 86: Particle scattering factor for hPG dispersed in $D_2O$ and probed by TOF-SANS. The dashed green line represents the fit according to equation (74) related to the global spatial structure of hyperbranched polycondensates. The solid red line corresponds to the fit using equation (72) considering the contribution of the segmental microstructure of the hyperbranched scaffold.**

A simplification describing the global structure of hyperbranched polymers is given by equation (74) [85,86].

$$F_{hb}(q) = \left(1 + \frac{1}{6} q^2 {R_{G-br}}^2\right)^{-2} \tag{74}$$

Here, the global dimension is given by the respective radius of gyration $R_{G\text{-}br}$. This correlation describes the normalised scattering intensities displayed in Fig. 86 at low $q$-values but shows significant deviation in the high-$q$ regime. Similar observation where reported by de Luca and co-worker [88]. Here, $R_{G\text{-}br}$ = 2.75 nm was applied for the calculation of the scattering intensities, which is in the range of the *Guinier*-radius determined from the analysis of $I_0(q)$. The deviation in the high $q$-sector results from the contribution of the segmental microstructure in particular. A good agreement to the particle scattering factor over the total probed $q$-range was obtained using equation (72) and is represented by the solid red line in Fig. 86. The calculation employs an effective bond length of $b_{eff}$ = 0.9 nm, which is in the range expected for the monomer units of the polyglycerol.

The SAXS-intensities were fitted by equation (72) employing an effective bond length of $b_{eff}$ = 0.8 nm, which is in the range of the values determined by neutron scattering.

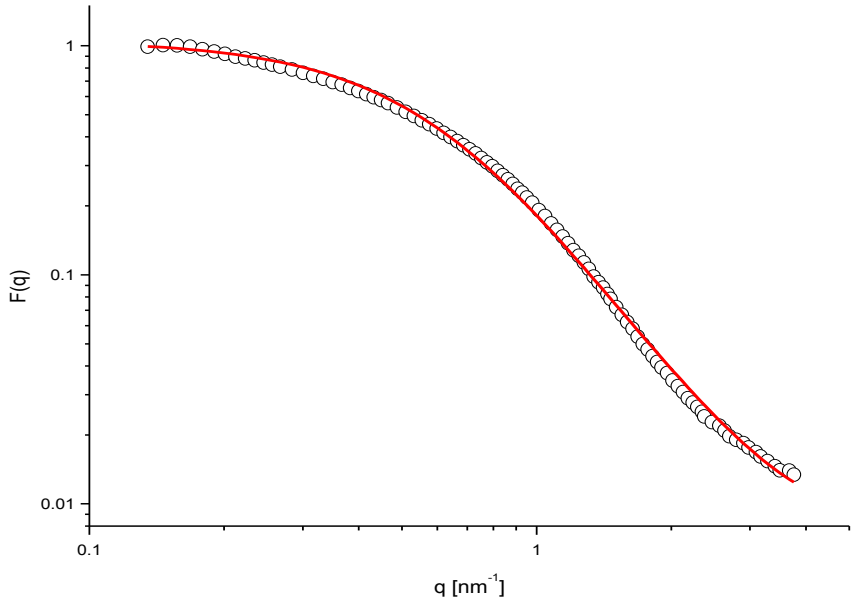


**Fig. 87: Particle scattering factor form experimental data of hPG dissolved in $H_2O$ and measured by SAXS. The solid red line refers to the fit according to the approach given by equation (72).**

## 5) Alternative Approach for the Analysis of the Small Angle Scattering of CMS-nanoparticles[4]

To describe the scattering intensities of the CMS-structures it is meaningful to adapt the approach for hyperbranched molecules given by Burchard.

For this reason the model for hyperbranched polymers can be extended for attached chains to yield:

$$DP_w F(q) = \frac{1+\alpha\phi}{1-\alpha\phi} + \frac{\alpha\beta}{(1-\alpha\phi)^2} + \frac{2\alpha(1-\beta)\phi^2}{1-\alpha\phi}\phi^* + \frac{\alpha(1-\beta)\phi^2}{(1-\alpha\phi)^2}\phi^* \qquad (75)$$

Here, the first two parts of the equation are related to the hyperbranched core-molecule, whereas the second two terms are associated with the attached segments. For this reason $\phi^*$ is related to the structural units, that are subsequently attached to the central molecule by derivatisation of free functional groups. Two cases can be considered for the CMS-molecules. The first case describes the coupling with linear chains.

$$\phi^*_{chain} = \frac{1-\phi^n}{1-\phi} = \frac{1-\exp\left(-\frac{nb^2_{chain}q^2}{6}\right)}{\frac{b^2_{chain}q^2}{6}} \cong n\left(1-\frac{nb^2_{chain}q^2}{12}\right) \qquad (76)$$

The degree of polymerisation, or in other word the number of monomer units within the linear chain, is given by $n$. The effective bond length of the monomer unit of the attached chain is $b_{chain}$. The second term in equation (76) is restricted for small values of $q\, b_{chain}$, which is related to the interference of the segmental units over the total length of the chain. This yields for small $q$-values $\phi^*_{chain}(q = 0) = n$, whereas for the branched scaffold $\phi(q = 0) = 1$ is obtained.

The suggested backfold of chain segments towards the hyperbranched core can be correlated to respective ring formation. Thus, for the chain segments $\phi^*$ can be written as follows:

$$\phi^*_{ring} = n\frac{2}{3}\exp(-X)^2\int_0^X \exp(t^2)dt \qquad (77)$$

Here, $X$ is related to the radius of the formed rings due to the backfold.

$$X^2 = \frac{nb^2_{ring}q^2}{12} = R^2_{ring} \qquad (78)$$

The theoretical description of the ring formation embodies the *Dawson*-integral $D$:

$$D(X) = \exp(-X^2)\int_0^X \exp(t^2)dt \qquad (79)$$

[4] The discussion is based on the private communication with Prof. Walther Burchard of 29th April 2013 following the meeting at HZB on 23th and 24th April 2013.

This allows the calculation of the degree of polymerisation related to the core-shell structure as follows.

$$DP_{w\,core\text{–}shell} = DP_{w\,core} + DP_{w\,shell} = \frac{1+\alpha}{1-\alpha} + \frac{\alpha\beta}{(1-\alpha)^2} + (1-\beta)n\left[2\frac{\alpha}{(1-\alpha)} + \frac{\alpha^2}{(1-\alpha)^2}\right] \quad (80)$$

Considering the interferences of the neighbouring segments $\phi(q, b_{eff})$ thus yields equation (75).

Notwithstanding, this general approach does not consider contrast aspects that are given from the different composition of the segments within the core-shell architecture. This aspect has to be considered in a further discussion.

# Selbständigkeitserklärung

Ich erkläre, dass ich die vorliegende Arbeit selbständig und nur unter Verwendung der angegebenen Literatur und Hilfsmittel angefertigt habe.

Berlin, den 20.01.2014

Christian Rabe